



**HAL**  
open science

# Optical spectroscopy of hexagonal boron nitride: from bulk to monolayer

Christine Elias

► **To cite this version:**

Christine Elias. Optical spectroscopy of hexagonal boron nitride: from bulk to monolayer. Optics [physics.optics]. Université Montpellier, 2020. English. NNT : 2020MONT054 . tel-03538149

**HAL Id: tel-03538149**

**<https://theses.hal.science/tel-03538149>**

Submitted on 20 Jan 2022

**HAL** is a multi-disciplinary open access archive for the deposit and dissemination of scientific research documents, whether they are published or not. The documents may come from teaching and research institutions in France or abroad, or from public or private research centers.

L'archive ouverte pluridisciplinaire **HAL**, est destinée au dépôt et à la diffusion de documents scientifiques de niveau recherche, publiés ou non, émanant des établissements d'enseignement et de recherche français ou étrangers, des laboratoires publics ou privés.

# THÈSE POUR OBTENIR LE GRADE DE DOCTEUR DE L'UNIVERSITÉ DE MONTPELLIER

En Physique

École doctorale Information, Structures et Systèmes (I2S)

Unité de recherche UMR5221

## Optical spectroscopy of hexagonal boron nitride: from bulk to monolayer

Présentée par Christine ELIAS

Le 1 décembre 2020

Sous la direction de Guillaume CASSABOIS  
et Bernard GIL

Devant le jury composé de

M. Eric TOURNIE, Professeur, UM, IES, Montpellier

M. Christophe VOISIN, Professeur, ENS-Paris, Paris

M. Julien BRAULT, CR, CNRS-CRHEA, SOPHIA ANTIPOLIS

M. Alberto ZOBELLI, Maître de conférences, Université Paris-sud, LPS, Orsay

M. Bernhard URBASZEK, DR, CNRS, INSA-Toulouse

M. Sergei NOVIKOV, Professeur, University of Nottingham, UK

M. Guillaume CASSABOIS, Professeur, UM, L2C, Montpellier

M. Bernard GIL, DR, CNRS, L2C, Montpellier

Président du jury

Rapporteur

Rapporteur

Examineur

Examineur

Examineur

Directeur de thèse

Co-directeur de thèse



UNIVERSITÉ  
DE MONTPELLIER



*À mes parents.*



---

---

# REMERCIEMENTS

Tout d'abord, je remercie sincèrement mes directeurs Guillaume Cassabois et Bernard Gil de m'avoir accueillie dans leur équipe et de m'avoir fait confiance pour travailler sur ce sujet de thèse et de découvrir la belle physique du h-BN. J'ai beaucoup apprécié le travail avec vous durant ces trois années. Vous m'avez toujours soutenue et vous m'avez offert beaucoup de liberté tout au long de cette thèse. En même temps, vous m'avez poussée autant que possible pour bien comprendre la physique, en n'hésitant pas à vous montrer très exigeants lorsque je pouvais faire mieux. Je vous en suis très reconnaissante.

Guillaume tu t'es montré très patient envers moi, surtout lors de la rédaction de mon manuscrit. Je te remercie. Je te remercie aussi pour ta gentillesse tout au long de ces trois années et d'avoir m'aider pour trouver le post-doc, je suis très reconnaissante.

Bernard, toi et Monique vous m'avez été un vrai soutien durant ces trois années. Merci pour votre générosité et pour votre gentillesse.

Je remercie Pierre Valvin, avec qui j'ai beaucoup travaillé pendant ces trois années. Pierre, tu étais le "magicien" de la pico room. T'avais toujours le sourire et la confiance qu'on va y arriver malgré toutes les difficultés de la spectroscopie dans l'UV. Je te remercie beaucoup. Merci aussi pour ta bonne humeur pendant les longues journées de manipes.

Je remercie l'ensemble des membres du jury: Eric Tournié, Alberto Zobelli, Bernhard Urbaszek, Sergei Novikov, Julien Brault et Christophe Voisin, d'avoir accepté d'y être dans mon jury de thèse. Merci aussi pour vos remarques et la riche discussion scientifique le jour de la soutenance. Merci en particulier à Christophe Voisin et Julien Brault pour leurs rapports. Un grand merci à Sergei Novikov pour la fabrication des échantillons de monocouche de BN par épitaxie sur graphite. Ces échantillons étaient la clé pour le succès de ma thèse. Merci aussi Sergei pour ton attention et tes remarques sur le manuscrit de thèse.

Ensuite, je remercie nos collaborateurs à Kansas State University: l'équipe de James Edgar pour la fabrication des échantillons massifs de h-BN. En particulier je remercie Jiahan Li, avec qui j'ai beaucoup discuté pendant ces trois années. Merci pour la fabrication des nombreux échantillons en particulier pour les larges cristaux de h-BN qui m'ont permis d'étudier les propriétés optiques du bulk h-BN en réflectivité. J'espère que nous pourrons publier ces beaux résultats bientôt.

Pendant ma thèse j'ai travaillé aussi avec Ryan Page de *Cornell University* qui était venu en France avec une bourse *Chateaubriand* pour travailler dans notre équipe sur les propriétés optiques de h-BN. Nous avons travaillé ensemble pendant 6 mois. Merci Ryan pour cette belle collaboration et pour toutes les discussions sur la physique du h-BN.

Je tiens à remercier tous les membres de l'équipe S2QT: Vincent Jacques, Anais Dréau et Isabelle Philippe pour les discussions. Anais Dréau, merci bien aussi pour tes délicieux gâteaux que j'attendais avec impatience d'une semaine à l'autre. Isabelle, merci pour tes conseils et ton aide avec les papiers administratifs.

Je remercie chaleureusement Béatrice Tomberli, Christelle Eve et Jean-Christophe art pour

---

les dossiers administratifs. Béatrice, merci d'avoir galérer avec moi pour tous les papiers... Merci aussi pour ton soutien. Jean-Christophe, merci d'avoir s'en occuper de toutes mes missions durant ces trois années. Christelle, merci pour ton soutien et pour les beaux moments qu'on a partagé ensemble et avec Manon.

Ensuite je remercie mes collègues de l'équipe S2QT, post-doc et thésards: Aurore Finco, Phuong Vuong, Thomas Pelini, Walid Redjem, Saddem Chouaieb, Alrik Durand, Florentin Fabre (Jeannot), Yoan Baron, Maxime Rollo (Pikachu), Rana Tanos et Angela Haykal. Merci pour votre belle ambiance et pour tous les moments que nous avons partagés ensemble.

Walid, tu étais de très bonne humeur. On a beaucoup rigolé. On a aussi beaucoup discuté, et nos discussions m'ont permis de mieux comprendre la physique. Merci Walid.

Florentin et Maxime, vous étiez les meilleurs amis pour partager un café avec. Nous avons beaucoup rigolé de tout et de rien. Je vous souhaite le meilleur pour vos thèses.

Je tiens à remercier chaleureusement Angela Haykal et Rana Tanos que je connais depuis huit ans. On étaient rencontrées en 2012 à la fac de Beyrouth. Merci pour toutes ces années que nous avons partagées ensemble. Je vous souhaite le meilleur pour les années qui suivent. Rana, merci pour ta générosité et pour la délicieuse cuisine libanaise qui me manquait pendant ces années d'éloignement. Angela, l'heure du sport tous les jours pendant la "supper" période de confinement et pendant laquelle on rédigeait nos thèses était vitale pour moi. Merci pour ta gentillesse et pour ton soutien. Merci aussi d'avoir être "l'ingénieur du son et de l'image" le jour de ma soutenance.

Je n'oublie pas Thomas Pelini et Phuong Vuong, avec qui j'ai travaillé au début de ma thèse. Avec thomas, on a eu de beaux résultats sur les défauts dans h-BN. Je souhaite à vous deux une bonne continuation pour les années qui suivent.

Un grand Merci à Christophe Chaubet, Leatitia Doyenette et Olivier Richard qui m'ont permis d'enseigner. C'étaient des belles expériences et j'ai pris beaucoup de plaisir à partager cette passion.

Parmi les membres de l'équipe technique Christian l'Hénauret m'a été d'une aide précieuse surtout pour la fabrication de pièces mécaniques pour la réflectivité. Merci à Guilhem Taly de m'avoir préparer chaque semaine pendant 3 ans une bouteille d'azote liquide prête à être utilisée.

Merci beaucoup à mes deux chères amies Leyla Barakat et Manon Rodrigo que j'ai rencontré sur Montpellier pendant ces 3 années de thèse. Nous avons partagé de très beaux moments ensemble. Vos soutiens étaient primordiales pour moi pendant ces trois années. Je vous souhaite le meilleur pour les années qui viennent.

Enfin, j'arrive aux membres de la famille. Premièrement, mes parents: Joumana et Georges. Vous avez toujours chercher à nous donner tout ce qu'il faut pour que nous puissions étudier dans les meilleurs conditions et à nous soutenir pour chaque pas. Si je suis arrivée là, c'est grace à vous.

Mes deux frères et ma soeur: Toni, Charbel et Hanadi, vous m'avez manqué pendant ces années. Je vous souhaite le meilleur pour votre futur et je croise les doigts pour que puissiez accomplir vos rêves.

---

# TABLE OF CONTENTS

<b>Remerciements</b>	<b>iii</b>
<b>Introduction</b>	<b>1</b>
<b>1 Boron Nitride</b>	<b>5</b>
1.1 The crystal . . . . .	6
1.1.1 Identification of the geometric structure of h-BN . . . . .	6
1.1.2 Allotropes . . . . .	6
1.1.3 Reciprocal lattice and first Brillouin zone . . . . .	9
1.2 Electronic properties of h-BN . . . . .	10
1.2.1 Electronic band structure for mBN . . . . .	10
1.2.2 Electronic band structure for bulk h-BN . . . . .	11
1.2.3 Excitons . . . . .	14
1.3 Phonon band structure . . . . .	18
1.3.1 Phonon modes in mBN . . . . .	18
1.3.2 Phonon modes in bulk h-BN . . . . .	20
1.4 Emission spectrum in bulk h-BN . . . . .	21
1.5 Conclusion . . . . .	24
<b>2 Experimental aspects</b>	<b>25</b>
2.1 Experiments . . . . .	25
2.1.1 Reflectance . . . . .	26
2.1.2 Photoluminescence spectroscopy . . . . .	38
2.2 Samples . . . . .	41
2.2.1 Samples grown by Molecular Beam Epitaxy . . . . .	41
2.2.2 Bulk h-BN . . . . .	43
2.3 Conclusion . . . . .	46
<b>3 Monolayer Boron Nitride</b>	<b>49</b>
3.1 Direct band gap in monolayer boron nitride . . . . .	49
3.1.1 Modification of the band gap nature in 2D materials . . . . .	49
3.1.2 State of the art for h-BN monolayer . . . . .	52
3.2 Boron nitride monolayer grown by MBE . . . . .	59
3.2.1 Control of the coverage by the temperature of the boron source $T_B$ . . . . .	60
3.2.2 Control of the coverage by tuning the growth time $t_g$ . . . . .	63
3.2.3 Growth of mBN by MBE . . . . .	65
3.3 Experimental results . . . . .	67
3.3.1 Photo-luminescence spectroscopy . . . . .	67
3.3.2 Reflectance spectroscopy . . . . .	78
3.4 Interpretation . . . . .	82
3.4.1 PL emission in mBN . . . . .	82
3.4.2 Temperature dependence of the photoluminescence . . . . .	85
3.4.3 Secondary reflectance minimum at 5.98 eV in mBN . . . . .	90
3.4.4 Quantitative modeling of the lineshape fitting of the reflectance in mBN . . . . .	92

---

3.5 Conclusion . . . . .	99
<b>General conclusion</b>	<b>101</b>
<b>A Reflectivity of bulk h-BN</b>	<b>105</b>
A.1 Motivation . . . . .	105
A.2 Reflectance spectra from two different h-BN crystals . . . . .	106
A.3 Reflectance versus emission in bulk h-BN . . . . .	108
A.4 Temperature-dependent measurements . . . . .	110
A.5 Conclusion . . . . .	111
<b>B T-dependence of reflectance measurements in mBN</b>	<b>113</b>
<b>C Theoretical model used to fit our reflectance data: quantum approach</b>	<b>115</b>
<b>D Epitaxial h-BN with sub-monolayer thickness</b>	<b>119</b>
D.1 Motivation . . . . .	119
D.2 Morphology of the samples . . . . .	120
D.3 Experimental results . . . . .	122
D.3.1 PL measurements . . . . .	122
D.3.2 Reflectance measurements . . . . .	124
D.4 Conclusion . . . . .	125
<b>References</b>	<b>127</b>

---

## Publications

- **Direct band-gap crossover in epitaxial monolayer boron nitride.**  
Nature Communications, **10**, 2639 (2019).  
C. Elias<sup>1</sup>, P. Valvin<sup>1</sup>, T. Pelini<sup>1</sup>, A. Summerfield<sup>2</sup>, C. J. Mellor<sup>2</sup>, T. S. Cheng<sup>2</sup>, L. Eaves<sup>2</sup>, C. T. Foxon<sup>2</sup>, P. H. Beton<sup>2</sup>, S. V. Novikov<sup>2</sup>, B. Gil<sup>1</sup>, and G. Cassabois<sup>1</sup>.
- **Shallow and deep levels in carbon-doped hexagonal boron nitride crystals.**  
Phys. Rev. Materials, **3**, 094001 (2019).  
T. Pelini<sup>1</sup>, C. Elias<sup>1</sup>, R. Page<sup>2</sup>, L. Xue<sup>3</sup>, S. Liu<sup>3</sup>, J. Li<sup>3</sup>, J. H. Edgar<sup>3</sup>, A. Dréau<sup>1</sup>, V. Jacques<sup>1</sup>, P. Valvin<sup>1</sup>, B. Gil<sup>1</sup> and G. Cassabois<sup>1</sup>.
- **Single crystal growth of monoisotopic hexagonal boron nitride from a Fe–Cr flux.**  
J. Mater. Chem. C, **8**, 9931-9935 (2020).  
J. Li<sup>1</sup>, C. Elias<sup>2</sup>, G. Ye<sup>3</sup>, D. Evans<sup>1</sup>, S. Liu<sup>1</sup>, R. He<sup>3</sup>, G. Cassabois<sup>2</sup>, B. Gil<sup>2</sup>, P. Valvin<sup>2</sup>, B. Liu<sup>1</sup> and J. H. Edgar<sup>1</sup>.
- **Hexagonal Boron Nitride Single Crystal Growth from Solution with a Temperature Gradient.**  
Chemistry of Materials, **32**, 5066–5072 (2020).  
J. Li<sup>1</sup>, C. Yuan<sup>2</sup>, C. Elias<sup>3</sup>, J. Wang<sup>4</sup>, X. Zhang<sup>6</sup>, G. Ye, C. Huang<sup>1</sup>, Martin Kuball<sup>2</sup>, G. Eda<sup>4</sup>, J. M. Redwing<sup>6</sup>, R. He, G. Cassabois, B. Gil, P. Valvin, T. Pelini, B. Liu, and J. H. Edgar.
- **Spontaneous emission of color centers at 4eV in hexagonal boron nitride under hydrostatic pressure.**  
Superlattices and Microstructures, **131**, 1-7 (2019).  
K. Koronski<sup>1</sup>, A. Kaminska<sup>1,2</sup>, N. D. Zhigadlo<sup>3,4</sup>, C. Elias<sup>5</sup>, G. Cassabois<sup>5</sup> and B. Gil<sup>5</sup>.

## Conferences

- **Oral:** Direct band gap crossover in epitaxial monolayer boron nitride.  
IWUMD 2019, September 8-13 2019, St Petersburg, Russia.
- **Poster:** Reflectivity of hexagonal boron nitride in Deep UV.  
CSW 2019, May 19-23 2019, Nara, Japan.

---

# LIST OF TABLES

1.1	<b>Excitons in mBN:</b> the first column summarizes the 4 states for valley degree of freedom. Here, 0 and K correspond to momentum of the center-of-mass; the second column summarizes the 4 states for total spin degree of freedom where S is singlet state and T the triplet. . . . .	15
2.1	Growth parameters of the h-BN samples grown by Molecular Beam Epitaxy under ultra-high vacuum conditions in Nottingham University and the approximative thickness of each sample. . . . .	43
2.2	Growth parameters of the h-BN samples grown from a metal molten solution under high temperature and atmospheric pressure conditions in Kansas State University. . . . .	46
3.1	Growth parameters of the h-BN samples grown by Molecular Beam Epitaxy under ultra-high vacuum conditions in Nottingham University and their thickness estimated by VASE. . . . .	67

---

# LIST OF FIGURES

1.1	Allotropes of Boron Nitride. . . . .	7
1.2	Allotropes of Boron Nitride . . . . .	8
1.3	Reciprocal space and first Brillouin zone for 2D BN . . . . .	9
1.4	First Brillouin zone of bulk h-BN (3D lattice) . . . . .	10
1.5	Electronic band structure for mBN . . . . .	11
1.6	Electronic band structure for bulk h-BN . . . . .	12
1.7	Valence band structure of bulk h-BN . . . . .	13
1.8	Dispersion of excitons in mBN . . . . .	17
1.9	Dispersion of excitons in h-BN . . . . .	18
1.10	Phonon dispersion relation of mBN . . . . .	19
1.11	Phonon dispersion in h-BN . . . . .	20
1.12	PL emission of h-BN at cryogenic temperature . . . . .	22
1.13	PL emission of h-BN at cryogenic temperature . . . . .	23
1.14	Emission in bulk h-BN . . . . .	24
2.1	Schematic plot showing partial reflection, and refraction of an electromagnetic wave with a linear polarization at an interface between two different media . . . . .	27
2.2	Configuration used to build our reflectance experiment . . . . .	28
2.3	Comparison between the irradiance spectrum of the two lamps used to build our reflectance setup . . . . .	29
2.4	Scheme of the reflectance setup . . . . .	31
2.5	Principle of synchronous detection . . . . .	32
2.6	Simulation of our experiment using Zemax . . . . .	33
2.7	Illumination diagrams after the exit slit of the monochromator simulated using Zemax . . . . .	34
2.8	Intensity of the reflected light in the spectral range of the Schumann–Runge bands plotted in semi-log scale . . . . .	36
2.9	Reflectance of our reference sample . . . . .	37
2.10	Normalization of our reflectance spectra . . . . .	38
2.11	Principle of photoluminescence spectroscopy for semiconductors . . . . .	39
2.12	Scheme of our experimental setup used for PL measurements of h-BN samples . . . . .	40
2.13	Hot-Pressed BN (HPBN) boat crucible for h-BN crystal growth . . . . .	45
2.14	h-BN bulk crystals grown by metal flux method . . . . .	45
3.1	Direct band gap in monolayer MoS <sub>2</sub> . . . . .	49
3.2	Calculations showing the variation of the band structure for h-BN as a function of the number of layers . . . . .	50

---

3.3	Variation of the emission spectrum of h-BN as a function of the number of layers	52
3.4	Shape dependence of the h-BN grains on the growth conditions	54
3.5	Growth of h-BN single layer on the surface of a molten Au	54
3.6	Atomic force microscopy images of h-BN by MBE at high temperature	57
3.7	Raman spectra of atomically thin BN	58
3.8	Variation of the h-BN thickness versus $T_B$	60
3.9	Tapping-mode AFM images measured under ambient conditions on h-BN samples grown by MBE on HOPG substrates for increasing boron cell temperatures	61
3.10	Same as figure 3.9 (c)	62
3.11	AFM images of MBE-grown h-BN on HOPG for $t_g=1$ h	63
3.12	AFM images of MBE-grown h-BN on HOPG for different growth times	64
3.13	Surface morphology of epitaxial monolayer BN on graphite	66
3.14	Photoluminescence of epitaxial monolayer BN on graphite	68
3.15	Photoluminescence of epitaxial monolayer BN on graphite	69
3.16	Emission of mBN	71
3.17	PL spectrum for MoSe <sub>2</sub>	72
3.18	PL emission of mBN for different values of the excitation energy	73
3.19	Excitation of mBN	75
3.20	Photoluminescence spectroscopy of h-BN epilayers at 8 K	77
3.21	Photoluminescence spectroscopy of h-BN epilayers at 8 K	78
3.22	Optical response of graphite in the DUV	79
3.23	Reflectance of epitaxial monolayer BN on graphite	80
3.24	DUV reflectance spectrum for several mBN samples measured at 8 K, obtained for different MBE boron cell temperatures ( $T_B$ ) and growth times	81
3.25	Doublet origin in the photo-luminescence spectrum of mBN	83
3.26	Reflectance versus PL in mBN	85
3.27	PL spectra in mBN as a function of temperature	86
3.28	Temperature dependence of the emission in mBN	87
3.29	Temperature dependence of the emission in mBN	88
3.30	Temperature dependence of the emission in mBN	89
3.31	Fit of the reflectance spectrum in mBN taking into account one oscillator at 6.12 eV	95
3.32	Fit of the reflectance spectrum in mBN taking into account two oscillators at 6.12 and 5.98 eV	96
3.33	Fit of the reflectance spectrum in mBN taking into account 4 Gaussian distributions centered at $\Omega_1 = 6.12$ eV, $\Omega_2 = 5.98$ eV, $\Omega_3 = 6.29$ eV and $\Omega_4 = 6.39$ eV	97
3.34	Reflectance spectrum in mBN for samples N <sub>2</sub> and N <sub>6</sub>	98

---

A.1	<b>Reflectance of BN:</b> (a) Reflectance spectrum measured from pyrolytic BN at room temperature. These data are taken from Ref. [128]; (b) Reflectance measurements from high quality h-BN at 8K. These data are taken from Ref. [129]. . . . .	106
A.2	Reflectivity of bulk h-BN . . . . .	108
A.3	Reflectance versus PL in bulk h-BN . . . . .	109
A.4	Reflectance spectra in bulk h-BN as a function of temperature . . . . .	110
B.1	Temperature dependance of reflectance in mBN . . . . .	113



---

# INTRODUCTION

Semiconductors are the building block of today's electronic and opto-electronic devices. They have played a key role in the development of our society as they have largely contributed in diverse applications that have become an indispensable part of our daily lives such as computing, telecommunications, light emitting devices, health care, military systems, transportation, etc.. Innovative materials are increasingly demanded for a high-performance industry that is based on miniaturization, robustness and lightweight of future devices. For that, modern growth techniques such as epitaxial growth play a key role in the semiconductor technology. They allow the deposition of thin layers at the surface of a substrate and they control the growth of the material at the atomic scale. These methods have allowed the reduction of size of transistors and diodes and permitted to obtain smart-computer devices with the size of our pockets.

The development of such technology requires the understanding of the physical properties of a material at the atomic scale. Quantum effects play a key role in the properties of a material and the understanding of these properties is the main challenge of today's science.

The emergence of nanomaterials over the past seventy years has been marked by silicon and III-N compounds that have been largely studied in order to develop integrated circuits and efficient light emitting devices. The growth of these materials by modern epitaxial methods led to the development of light emitting diodes and semiconductor laser diodes that are largely used in the modern information technology and communication. Moreover, the development of efficient blue light emitting diodes in the nineties opened up a new technology for white light emitters.

However, the saturation of Moore's law imposes the development of alternative technology that combines performance and functionality. The traditional materials used (such as silicon) have shown their limits within these parameters and the need is to develop a new semiconductor technology based on these two parameters.

Over the past decade, the discovery of graphene [1] and many other layered crystals of atomic thickness, that integrated the family of two-dimensional crystals, have been highly marked in semiconductor science and it opened up a new avenue of research in order to develop a new technology based on van-der-Waals heterostructures and which consist of stacking different layered semiconductor often as thin as one atomic plane. These layers are weakly bound together by van-der-Waals-type forces. It is expected that this technology will allow to go beyond the limits of traditional materials and that it will enable the easy growth of materials with extreme thinness of the order of single atomic layers.

In graphene, the carbon atoms are assembled in a 2D network of honeycombed hexagons. Its zero-gap gives an excellent electrical and thermal conduction owing it to be used for many applications such as fast electronics, ultra-sensitive sensors, etc.. In parallel to graphene, 2D transition metal dichalcogenides display a finite energy gap in the visible spectral range.

---

Among these materials molybdenum disulfide ( $\text{MoS}_2$ ) and tungsten diselenide ( $\text{WSe}_2$ ) are very well known, in particular their forbidden bandgap which depends on the number of layers. In exfoliated ultrathin crystals of these two materials, it was demonstrated a transition from indirect bandgap in the bulk crystal to direct gap in a single monolayer [2, 3]. The highly efficient light–matter coupling in a direct-gap monolayer makes the family of semiconducting transition metal dichalcogenides a promising platform for optoelectronics and valleytronics.

Hexagonal boron nitride (hBN) is an insulating analogue of graphite with a 2D hexagonal crystal structure. It is called white graphite and it has a small lattice mismatch ( $\sim 1.7\%$ ) with graphite. This property additionally to its large bandgap ( $\sim 6$  eV) makes it a key building block in van-der-Waals heterostructures to be an ideal dielectric substrate for graphene. Additionally, h-BN is a III-N material owing very interesting properties for emitting light in the deep-ultraviolet and competing with nitride semiconductors of the AlGaN family that are widely used for blue and ultraviolet lighting.

The development of semiconductor light sources operating at short wavelengths (200 nm) is now motivating researchers in relation with a wide variety of applications. Such light sources are expected to be used in sterilization applications [4], medicine, water purification, biochemistry, etc... One of the basic building block for the development of compact solid-state UV technology could be hexagonal boron nitride which has a band-gap value sitting at 6 eV.

We point out that the applications of h-BN go beyond deep-ultraviolet emission and van-der-Waals heterostructures, it can be used for applications in 5G and terahertz communication systems [5], as well as in quantum technologies [6] and photovoltaics detectors [7].

An isolated monolayer of hexagonal boron nitride is theoretically predicted to be a direct-gap semiconductor with a bandgap of around 6 eV and with an indirect–direct crossover similar to that of  $\text{MoS}_2$  and  $\text{WSe}_2$  when passing from a several-layer stacking to the monolayer [8, 9]. The investigation of the direct gap properties of monolayer boron nitride is very important for applications in DUV optoelectronics, with an exciting perspective of using it as an active layer with highly efficient light–matter coupling.

In this context, the goal of this thesis is to study the opto-electronic properties of monolayer boron nitride, in particular to demonstrate the direct gap properties. This work relies on the scalable growth of monolayer boron nitride by Molecular Beam Epitaxy at high temperatures using graphite substrates.

## Outline of the manuscript

In the first chapter of this thesis we present the structural properties of h-BN in his monolayer and bulk forms, and additionally the first Brillouin zone for both structures. Then, we will

---

present the electronic properties of h-BN in monolayer and bulk forms. Moreover, we will describe the excitonic states existing in monolayer boron nitride (mBN) and we will compare their dispersion relations with those of bulk h-BN. Later, we will give a description of the vibrational properties. Finally, we will present a state of the art on the experiments performed before my thesis in our group in order to understand the emission processes in bulk h-BN.

In the second chapter of this manuscript, we will present the experimental setups and samples studied during my PhD. This chapter will be split into two parts, the first one is dedicated to the experimental techniques (reflectance and photoluminescence) that have been implemented in deep-ultraviolet ( $\lambda < 350$  nm). These two experiments are complementary and will allow us to study the existence of a direct gap in mBN. We will present as well the difficulties we faced while implementing these spectroscopy techniques. The second part of this chapter will be devoted to describe the samples that we used for this work and their different growth methods.

Chapter 3 will present the main experimental results that we obtained during my thesis. It is divided into 4 sections: section 3.1 will expose the problematic of the chapter and the strategy we used in order to solve it. Additionally, we will give a brief state of the art on the experimental studies on mBN before this thesis. In section 3.2, we will explain how to control the growth of h-BN by Molecular Beam Epitaxy, and we will describe further how our collaborators achieved the growth of mBN on a large scale using their Molecular Beam Epitaxy system. Our discussion will be accompanied with Atomic Force Microscopy images and Variable Angle Spectroscopic Ellipsometry measurements performed at Nottingham University in order to describe the morphological properties of our samples.

In section 3.3, we will present our experimental results. We will start by presenting the emission measured from mBN samples and the condition that controls the excitation processes in mBN. Then we will study how the emission process in mBN compares to the one in bulk h-BN and to other thick samples. Finally, we will end this section by comparing the emission of mBN to its reflectance in order to examine whether the bandgap nature in mBN is direct or not.

In the last section 3.4, we will present our interpretation of the different experimental results and we will give a quantitative analysis of photoluminescence and reflectance measurements in mBN samples grown under different conditions.

This last chapter will be followed by a general conclusion and appendices including a collection of complementary studies not presented in these three chapters.



---

# BORON NITRIDE

In 1842, William H. Balmain combined melted boric acid and cyanide potassium in a covered porcelain crucible. The outcome was a white porous substance allowing him to declare: **“the white solid is evidently a distinct and stable compound, a more interesting object of study”** [10]. Meanwhile, the compound of Balmain was not stable and it demanded many trials to be possibly synthesized as a powder.

The synthesis of large-size and high-quality crystals of BN demands high pressure and high temperature conditions (HPHT) [11]. In the nineteenth century the requirement of such conditions was difficult to achieve from the technical point of view. The breakthrough in the synthesis of BN came in 2004, when Takashi Taniguchi and Kenji Watanbe grew high-quality hexagonal boron nitride (h-BN) crystals offering very interesting optical properties for deep ultraviolet (DUV) light emission at room temperature [11, 12]. Their synthesis method was developed in order to grow cubic-BN (c-BN) using solvent growth techniques based on the temperature-gradient method under HPHT conditions. The residues of the chemical reaction in their crucible were crystals of h-BN with few millimeters size. The optical properties measured from this residual product has opened up a new avenue of research for h-BN as being a potential material for developing light emission devices in the DUV. Nowadays, many methods have been developed and adapted for the synthesis of h-BN crystals, some of them are at atmospheric pressure condition [13, 14, 15, 16, 17].

BN was largely used as a powder in the industry of electronics, metallurgy, ceramics, cosmetics, etc... The interest for this material in the industry is due to many reasons: its chemical inertness, its heat resistance (melting point 2967°C for ambient pressure) and its whiteness. In parallel to the industrial interest, many efforts have been endowed in order to understand the physical properties of this material. However, since the synthesis of high-quality h-BN crystals is very recent, the understanding of its fundamental optical properties is also very recent and the knowledge of its intrinsic properties is not fully established yet.

In this thesis work, we are interested in the optical properties of h-BN and the target of this chapter of my dissertation is to recall the existing literature on h-BN and the scientific context of my thesis. We will start by defining the main structural properties of h-BN and its

reciprocal lattice. Then we investigate the electronic properties of this material by presenting the electronic band structures for monolayer BN (mBN) and bulk h-BN with their corresponding excitonic states. We present as well the phonon modes in both cases. Finally, we end this chapter by recalling the optical properties, in particularly the carrier recombination processes that occur in bulk h-BN.

## 1.1 The crystal

In this section we recall the crystallographic structure of h-BN and its existing allotropes. Then, we present the reciprocal lattice and the first Brillouin zones for 2D and 3D lattices of h-BN.

### 1.1.1 Identification of the geometric structure of h-BN

The geometric structure of h-BN was studied about hundred years ago by Hassel [18]. He performed X-ray measurements on BN powders and he identified a bi-molecular material consisting of a stacking of hexagonal layers. He considered an AB stacking of the two-dimensional layers along the z-axis (as later detailed in figure 1.2 b). However, the model elaborated by Hassel did not give a complete picture about the crystalline structure of h-BN and one had to wait until 1952, when Pease extended the work of Hassel and gave a consolidated model about the crystalline structure of h-BN [19]. The re-crystallization of a commercial powder after heating at 2050°C allowed him to investigate X-ray measurements and then to identify the crystalline structure of h-BN. Pease evidenced the AA' stacking in the crystalline structure of h-BN by analyzing the intensities of the lines from the measured diffraction patterns [19] (see figure 1.2 a). His work has been confirmed later by many theoretical and experimental papers [20, 21, 22, 23].

### 1.1.2 Allotropes

Boron nitride is a binary III-V compound, with boron ( $Z = 5$  *i.e.* 3 electrons in the outer shell) and nitrogen ( $Z = 7$  *i.e.* 5 electrons in the outer shell) atoms located on each side of carbon ( $Z = 6$ ) in the periodic classification table, with various crystallographic structures like carbon. The electronic configurations of B and N are  $1s^2 2s^2 2p^1$  and  $1s^2 2s^2 2p^3$ , respectively. The valence electrons are described by the atomic orbitals 2s,  $2p_x$ ,  $2p_y$  and  $2p_z$ . The atomic orbitals of B and N can hybridize either in  $sp^3$  or in  $sp^2$  wavefunctions. Depending on the growth conditions such as pressure, temperature and cooling process, BN can crystallize into different structures having different total energies. There are six different phases: 2 phases are formed with  $sp^3$  covalent bonds and 4 other lamellar phases are formed with  $sp^2$  covalent bonds.

- **Cubic (c-BN) and wurtzite (w-BN)** are four-fold coordinated crystals with perfect  $AB_3$  tetrahedron where the 2s and 2p orbitals are in  $sp^3$  hybridization. c-BN is known to be one of the hardest crystals with diamond, while w-BN is metastable and less interesting to study. Schematic diagrams of the atomic arrangements in both phases are given in figures 1.1 (a) and (b).

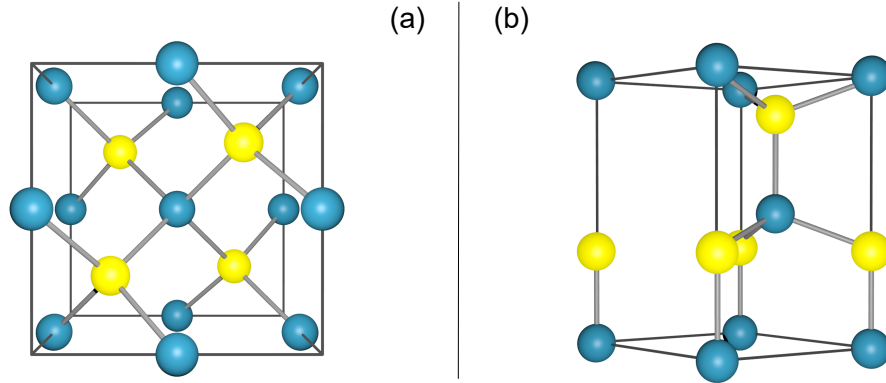


**Figure 1.1: Allotropes of Boron Nitride:** (a) schematic diagram presenting the crystalline structure of cubic BN (c-BN); (b) schematic diagram presenting the crystalline structure of wurtzite BN (w-BN). In both schemes: yellow spheres are Boron atoms and blue spheres are Nitrogen atoms.

- The atomic orbitals of the four other phases arrange in  $sp^2$  scheme and give a lamellar structure composed of planes with hexagons ( $B_3N_3$ ) forming a honeycomb network. The planes are stacked along a high symmetry direction (c-axis) and they are interconnected by van-der-Waals forces (weak bonds). They can stack in different sequences and all of them have stable phases. Three stackings strictly obey to specific space group symmetries (figure 1.2): **hexagonal (h-BN)** (a), **bernal (b-BN)** (b) and **rhombohedral (r-BN)** (c) with h-BN being the best known among them. In h-BN the positions of boron and nitrogen atoms alternate at the junctions of the honeycomb lattice from a given plane to another. This stacking is known as  $AA'$  (figure 1.2 a). In  $AB$  and  $ABC$  stackings the periodic vectors between adjacent planes are not parallel to the c-axis as in  $AA'$  (figure 1.2 b and c). We note the existence of an additional lamellar structure, the turbostratic phase (t-BN), with random arrangement of the planes in the c-direction. Among the four lamellar phases,  $AA'$  stacking has the highest cohesive energy.

The common properties among all existing allotropes of BN are thermal resistance, chemical inertness and wide energy gap. Each of the existing structure presents different electronic and optical properties due to the differences in their atomic arrangements. In this thesis we study the optical properties of h-BN ( $AA'$  stacking) going from the bulk to the monolayer limit.

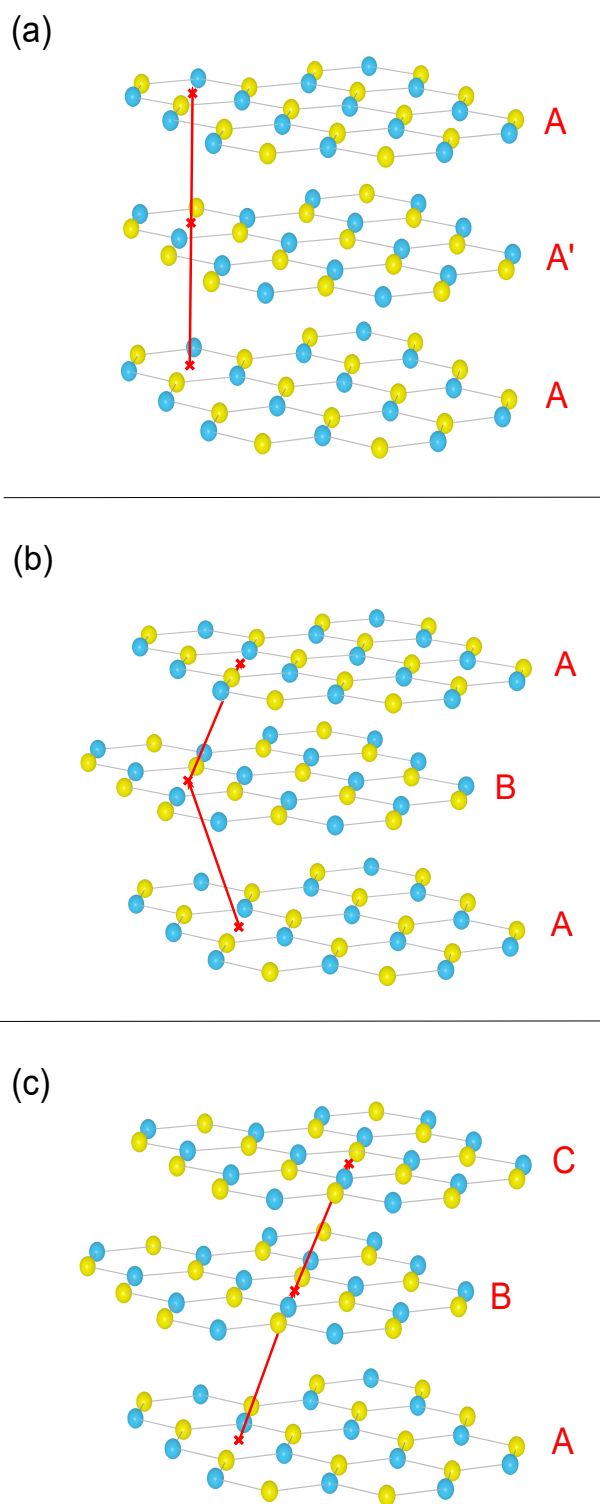


**Figure 1.2: Allotropes of Boron Nitride:** schematic diagrams presenting (a) the crystalline structure of hexagonal BN (h-BN) in AA' stacking; (b) the crystalline structure of bernal BN (b-BN) in AB stacking; (c) the crystalline structure of rhombohedral BN (r-BN) in ABC stacking. The red lines joining the centers of  $B_3N_3$  hexagons highlight the periodic stacking of the different structures. In all schemes: yellow spheres are Boron atoms and blue spheres are Nitrogen atoms.

### 1.1.3 Reciprocal lattice and first Brillouin zone

In the previous part, we have shown that the crystalline structure of h-BN is formed by the stacking of hexagonal honeycomb layers along the high-symmetry  $c$ -axis. Here, in this part, we will show how to construct the first Brillouin zone (BZ) for a hexagonal network in order to describe later the electronic and vibration properties of h-BN. We will start by a single layer (2D case), and then bulk h-BN (3D case).

#### 2D h-BN

In figure 1.3 (a) is presented a top view of a single atomic layer of h-BN. Boron and nitrogen atoms are distinguished from each other using spheres of different colors, B in yellow and N in blue. The positions of N and B atoms (highlighted by a circular dashed line in red) are chosen respectively as:  $(0,0)$  and  $(a_0,0)$ , with  $a_0 = 1.4 \text{ \AA}$  being the distance between boron and nitrogen nodes.

Relatively to the  $(x,y)$  axes, the primitive lattice wave-vectors are given by:  $\mathbf{T}_1 = a(\frac{\sqrt{3}}{2}, \frac{1}{2})$  and  $\mathbf{T}_2 = a(\frac{\sqrt{3}}{2}, -\frac{1}{2})$ , with  $a=a_0\sqrt{3}$  being the lattice parameter.

The reciprocal vectors are defined by:  $\mathbf{T}_1^* = \frac{2\pi}{a}(1, \frac{1}{\sqrt{3}})$  and  $\mathbf{T}_2^* = \frac{2\pi}{a}(1, -\frac{1}{\sqrt{3}})$  with  $\mathbf{T}_i\mathbf{T}_j^* = 2\pi\delta_{ij}$ ,  $\delta_{ij}$  being the Kronecker symbol.

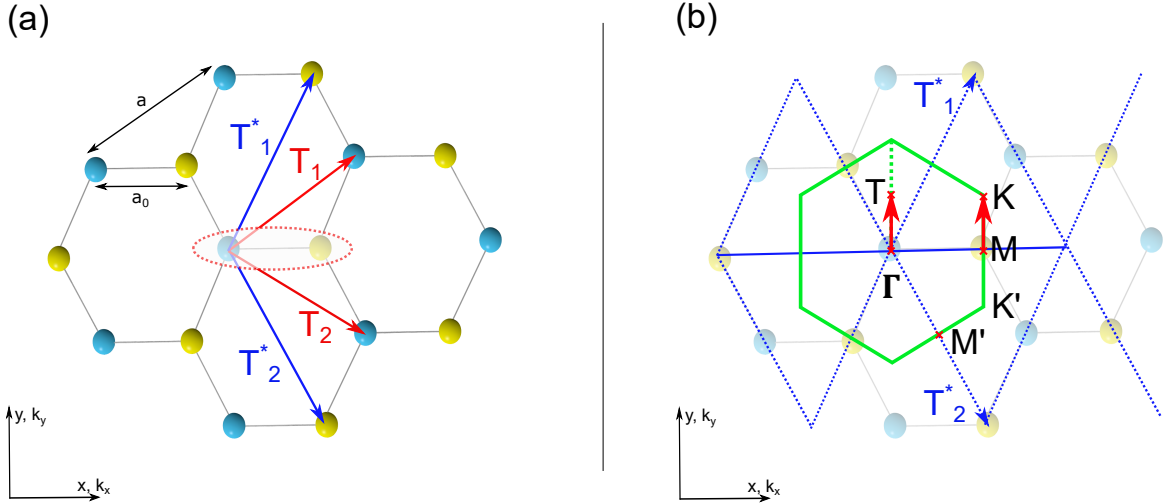


**Figure 1.3: Reciprocal space and first Brillouin zone for 2D h-BN:** schematic diagrams presenting (a) Bravais lattice of single layer BN;  $\mathbf{T}_1$  and  $\mathbf{T}_2$  being the primitive wave-vectors,  $\mathbf{T}_1^*$  and  $\mathbf{T}_2^*$  being the reciprocal wave-vectors; (b) the reciprocal lattice of single layer h-BN, superposed to the crystal. The first BZ for monolayer BN is sketched in green and it presents different high symmetry points:  $\Gamma$ ,  $\mathbf{K}$ ,  $\mathbf{M}$ ,  $\mathbf{K}'$  and  $\mathbf{M}'$ . In both schemes: yellow spheres present Boron atoms and blue spheres Nitrogen atoms.

In Figure 1.3 (b), the reciprocal lattice of the h-BN network is reconstructed in blue vectors, and superposed to the direct lattice of 2D h-BN. The first BZ is presented in green lines. It takes a hexagonal form and involves the critical points:  $\Gamma$ ,  $\mathbf{K}$ ,  $\mathbf{M}$ ,  $\mathbf{K}'$  and  $\mathbf{M}'$ , which correspond to high symmetry points.

### 3D h-BN

The 3D lattice is obtained by adding a second layer in the  $AA'$  stacking and repeating this double layer arrangement along the  $c$ -axis. The primitive cell is then obtained from a third vector  $\mathbf{T}_3=c(0,0,1)$  orthogonal to the plane constructed by  $(\mathbf{T}_1,\mathbf{T}_2)$  with  $c = 2c_0$  being the lattice constant in the  $z$  direction, and  $c_0=0.33$  nm being the distance between Nitrogen and Boron nodes along the  $c$ -axis. The reciprocal vector along this direction is given by:  $\mathbf{T}_3^* = \frac{2\pi}{c}(0,0,1)$ .

The BZ for the 3D lattice is presented in figure 1.4 : it involves 8 critical points:  $\Gamma$ ,  $\mathbf{M}$ ,  $\mathbf{K}$ ,  $\mathbf{A}$ ,  $\mathbf{L}$ ,  $\mathbf{H}$ ,  $\mathbf{K}'$  and  $\mathbf{M}'$ .

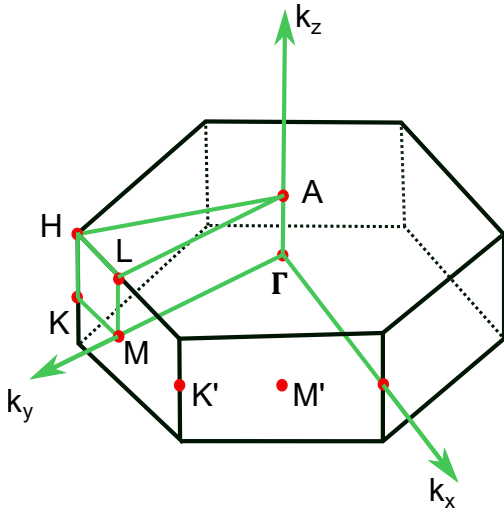


Figure 1.4: First Brillouin zone of bulk h-BN (3D lattice) with 8 critical points:  $\Gamma$ ,  $\mathbf{M}$ ,  $\mathbf{K}$ ,  $\mathbf{A}$ ,  $\mathbf{L}$ ,  $\mathbf{H}$ ,  $\mathbf{K}'$  and  $\mathbf{M}'$ .

## 1.2 Electronic properties of h-BN

In this section we present the electronic properties of mBN (2D case) and h-BN bulk (3D case). We will present the dispersion relation of the electronic band structure with the properties of excitons in mBN and then in bulk h-BN.

### 1.2.1 Electronic band structure for mBN

The electronic band structure for an isolated h-BN layer has been calculated using different *ab initio* methods and tight binding theory. All of them indicate that the monolayer displays a direct band gap at the  $\mathbf{K}$  point (figure 1.5) [21, 24, 25, 8, 9].

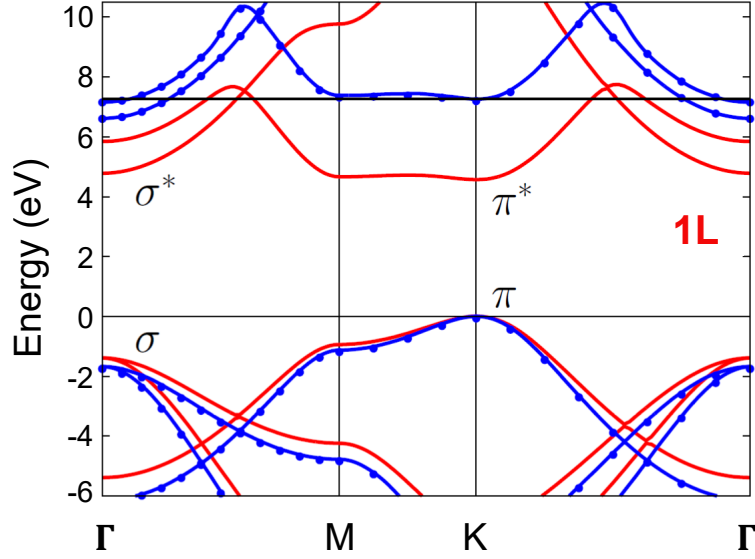


**Figure 1.5: Electronic band structure for mBN:** this figure is taken from Ref.[8]. It indicates the presence of a direct gap at the K point in mBN. Red curves have been calculated using DFT-LDA method and blue curves using GW approximation.

From the experimental point of view, few studies investigated the electronic band structure of mBN [26, 27] using XPS (*X-ray Photoelectron Spectroscopy*) and ARUPS (*Angle-Resolved Ultraviolet PhotoElectron Spectroscopy*). The mBN layers were grown on metal substrates using CVD (*Chemical Vapor Deposition*) growth methods. They measured the valence and conduction bands from mBN/Ni. Their results showed an agreement between their measurements of the valence band structure of mBN and the theoretical calculations done by Catellani *et al.* in 1985. In 2010, another work [28] reported the intercalation of Au to decouple the h-BN layer from Ni substrate. They obtained a quasi-freestanding mBN layer and they observed its valence band structure through ARPES (*Angle Resolved PhotoEmission Spectroscopy*). However, no experimental work has determined the nature of the electronic band gap in monolayer BN neither its energy.

### 1.2.2 Electronic band structure for bulk h-BN

The electronic band structure of h-BN was first calculated by Doni and Parravicini [21] in 1969 within tight-binding method which is based on the linear combination of atomic orbitals in a crystal. Their result indicated the presence a direct fundamental bandgap of h-BN at the K point of the first BZ.

In 1985, Catellani *et al.* recalculated the electronic band structure of h-BN using other calculation methods such as DFT (*Density functional theory*) and LDA (*local density approximation*) [29, 30]. Their results demonstrated an indirect nature for the fundamental bandgap in bulk

h-BN with an energy about 5 eV. In 1995, the nature of bandgap in bulk h-BN was confirmed to be indirect by Blase *et al.* [24]; their results provided an energy of about 5.4 eV in bulk h-BN.

After 2000's, several groups calculated the electronic band structure for h-BN [31, 32, 33, 34, 35, 36]. They all found an indirect bandgap in bulk h-BN (Figure 1.6) with the minimum of the conduction band at the M point and the maximum of the valence band near the K point of the first BZ, with KM equal to  $\frac{\Gamma K}{2}$ . The energy of the fundamental gap was estimated about 6 eV in bulk h-BN. The electronic band structure for bulk h-BN shows the presence of direct gap at K and H points with energies close to the one of the fundamental gap (direct gap estimated about 6.5 eV).

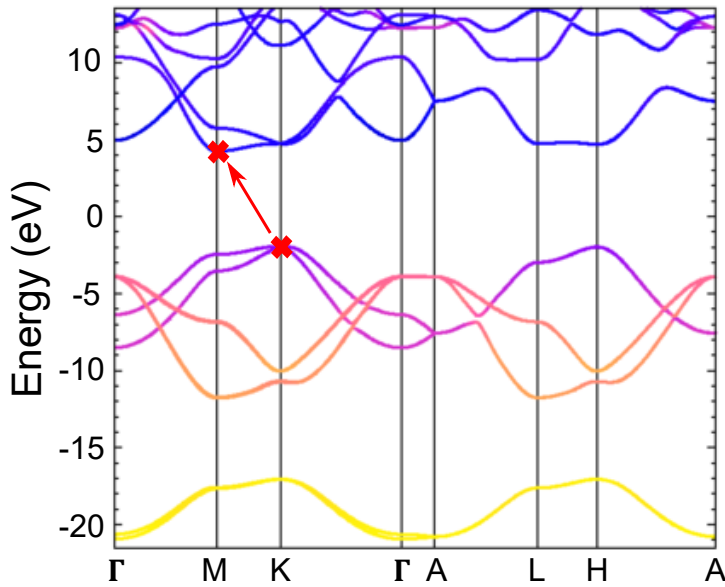


**Figure 1.6: Electronic band structure for bulk h-BN:** adapted from Ref. [35] and calculated using GW approximation. The valence band maximum (K) point and the conduction band minimum (M) are indicated by red crosses.

<sup>1</sup> In 2017, Koskelo *et al.* calculated the band structure for bulk h-BN by increasing the inter-layer distance [37]. Their results showed that the increase of the interlayer distance decreases the coupling between the layers ( $\pi$  bands) and consequently the nature of the bandgap asymptotically reaches the monolayer case and becomes direct at the K point. The reason for that change is that  $\pi$  bands are formed by the  $p_z$  orbitals oriented out of the plane making their overlap to vanish with the increase of  $c$ . Consequently, the electronic states are very sensitive to the interlayer distance *i.e.* the interaction between the layers, which increases the screening effect in the vertical direction and results in lowering the energy gap in h-BN by

<sup>1</sup>The GW approximation is usually used in order to calculate the self-energy of a many-body system of electrons with G standing for the single particle Green's function and W for the screened Coulomb interaction.

moving the minimum of the conduction band (M point in the case of bulk h-BN). When the interaction between the layers is weak or absent (as in mBN) the bandgap increases and the conduction band minimum lies at the K point.

We point out that the electron in the valence state at K point is localized on the nitrogen site and the one in the conduction state at M point is localized on the boron site. This is due to a larger electronegativity for N compared to B *i.e.* the electronic excitation  $\pi \rightarrow \pi^*$  at the bandgap energy occurs when an electron jumps from a nitrogen site to a boron site [8]. We have also to note that along the  $MK$  direction, the curves appear flat in the electronic band structure, and more importantly the one corresponding to the conduction band which indicates the presence of a large density of electronic states along this direction.

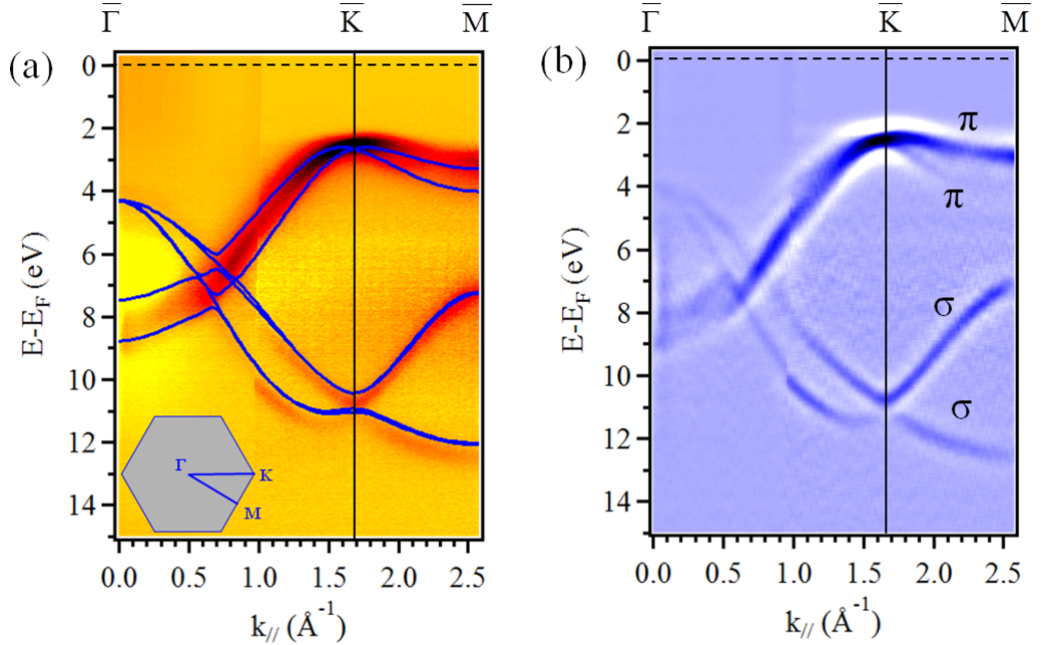


**Figure 1.7: Valence band structure of bulk h-BN:** (a) nano-ARPES spectra of h-BN and calculated band structure (blue lines) of bulk h-BN with modern methods (GW); the inset of (a) shows the Brillouin zone of h-BN; (b) to enhance the visibility of the bands in (a). This figure is taken from Ref. [38].

From the experimental point of view, Henck *et al.* reported Nano ARPES measurements on h-BN crystals (Figure 1.7) [38]. Their results were compared to GW calculations of the electronic band structure. They showed that the maximum of the valence band is located near the K point of the first BZ, in agreement with theoretical calculations.

What is fundamentally original in h-BN is that neither the conduction band minimum, nor the valence band maximum are at the zone center of the first BZ. In other indirect

semiconductors like diamond or silicon, etc... the valence band maximum is at the zone center and the conduction band minimum is at high symmetry points of the BZ. This originality in h-BN has an important impact on the optical properties of h-BN that will be discussed later in the chapter.

### 1.2.3 Excitons

When a semiconductor is excited (by light for example) with an energy greater than the gap, electrons from the valence band jump into the conduction band and the system ends up with electrons in the CB and absence of electrons in the valence band (holes). The properties of the electron and the hole can be derived from the band structure within the one-electron approximation. In order to understand the optical properties of a semiconductor, one has to describe the excited states of a N particle problem. The quanta of the excitations in semiconductors are called *excitons*. They can be separated in two types:

- For strong electron–hole attraction, the electron and the hole are tightly bound to each other *i.e* the Bohr radius is of the order of the lattice constant: the exciton is called of Frenkel type. These excitons cannot be described within the effective mass approximation and they are usually present in ionic crystals.
- If the Coulomb interaction of the e-h pair is strongly screened due to a large dielectric constant, electrons and holes are only weakly bound and the Bohr radius extends over several inter-atomic distances: the exciton is called of Wannier-Mott type. The properties of these excitons can be calculated within the effective mass approximation for which the electron and the hole are considered as two particles moving with the effective masses of the conduction and valence bands. Usually in inorganic semiconductors, the excitons are of Wannier-Mott type.

As in any two-particle system, the exciton motion is decomposed into a center-of-mass (CM) motion and a relative motion of the two particles. Within the effective mass approximation, the exciton CM behaves like a free particle with mass  $M=m_e+m_h$ . The kinetic energy of the exciton is related to  $q$  by:  $E(q) = \frac{\hbar q^2}{2M}$ , with  $q=k_e+k_h$  being the wavevector of CM. Thus exciton levels are represented by parabolas in the two-particle energy diagram and their wavefunction is a linear combination of many electron–hole pair wavefunctions satisfying the condition  $q=k_e+k_h$ .

The exciton levels present discrete states depending on the quantum number  $n$  and given by:

$$E(n) = E_\infty - \frac{\mu_{eff}}{m_0} \frac{R_H}{\epsilon^2} \frac{1}{n^2} \quad (1.1)$$

$E_\infty$  being the minimum energy of the continuum state or the energy of the gap,  $R_H$  is Rydberg

constant for hydrogen atom (13.6 eV);  $\mu_{eff}$  is the effective mass of the e-h pair,  $\epsilon$  is the dielectric constant of the system,  $m_0$  is free electron mass. The upper levels of the exciton ( $n>1$ ) exhibit decreasing binding energies as  $\frac{1}{n^2}$  [39, 40]. In the case of Frenkel exciton, the center of mass motion departs from the parabolic scheme.

In this section we will present the excitonic states in mBN and the calculated dispersion relations, then we will give the dispersion relations of the excitons in bulk h-BN.

### Excitons in mBN

In section 1.2.1 we presented the electronic band structure of mBN: the fundamental bandgap is direct at the K point of the first BZ.

Here in this section we present the excitonic states for mBN based on the simple description given by Ando for excitons in carbon nanotubes [41, 42]. In both cases: mBN and graphene, the crystalline structure has a honey-comb lattice with identical hexagonal Brillouin zones. The electronic band extrema in both cases are situated at K and K' points, with a finite gap for mBN and a zero gap for graphene. In our case, an exciton is an electron-hole pair formed from two bands with valley and spin degrees of freedom: the electron (hole) can be spin-up  $\uparrow$  ( $\uparrow$ ) or spin-down  $\downarrow$  ( $\downarrow$ ) and can be located either in K or K' valley.

Valley	Spin
$ 0_+\rangle = \frac{1}{\sqrt{2}}( KK\rangle +  K'K'\rangle)$	$ S\rangle = \frac{1}{\sqrt{2}}( \uparrow\downarrow\rangle -  \downarrow\uparrow\rangle)$
$ 0_-\rangle = \frac{1}{\sqrt{2}}( KK\rangle -  K'K'\rangle)$	$ T_0\rangle = \frac{1}{\sqrt{2}}( \uparrow\downarrow\rangle +  \downarrow\uparrow\rangle)$
$ K_+\rangle =  KK'\rangle$	$ T_+\rangle =  \uparrow\uparrow\rangle$
$ K_-\rangle =  K'K\rangle$	$ T_-\rangle =  \downarrow\downarrow\rangle$

**Table 1.1: Excitons in mBN:** the first column summarizes the 4 states for valley degree of freedom. Here, 0 and K correspond to momentum of the center-of-mass; the second column summarizes the 4 states for total spin degree of freedom where S is singlet state and T the triplet.

Neglecting spin-orbit interaction for the light B and N atoms, spin and valley are treated separately. There are four states for the spin and four states for the valley. For the valley degrees of freedom, four combinations are possible following Ando:  $|KK\rangle$ ,  $|K'K'\rangle$ ,  $|KK'\rangle$

and  $|K'K\rangle$  and they can be re-written in a more symmetric way as summarized in the first column of table 1.1 with (0) is for direct excitons ( $q=k_e+k_h=0$ ) and K for indirect excitons ( $q=k_e+k_h=KK' \neq 0$ ).

$|K_+\rangle$  and  $|K_-\rangle$  are dark in the electric dipole approximation.  $|0_+\rangle$  and  $|0_-\rangle$  states have opposite parity, and only  $|0_+\rangle$  is allowed.

For the total spin, there is one singlet  $|S\rangle$  and three triplet  $|T\rangle$  states. We summarize them in the second column of table 1.1.

From table 1.1 one gets 16 different possibilities in the (valley, spin) representation for the excitonic states in mBN:

- 1 out of the 16 exciton states is bright:  $|S, 0_+\rangle$
- 1 spin-singlet state is dark because of parity:  $|S, 0_-\rangle$
- 2 spin-singlet states are dark because the excitons are indirect:  $|S, K_+\rangle$  and  $|S, K_-\rangle$
- 12 states are dark because of the forbidden character of the transition involving spin-triplet states:  $|T, 0_+\rangle$ ,  $|T, 0_-\rangle$ ,  $|T, K_+\rangle$  and  $|T, K_-\rangle$ . T being the triplet states presented in table 1.1: either  $|T_+\rangle$  either  $|T_-\rangle$  or  $|T_0\rangle$ .

In 2017, Koskelo *et al.* [37] calculated the dispersion relation of excitons in h-BN from bulk to monolayer along  $\Gamma M$  direction, with  $q$  being the momentum of CM. The excitonic dispersion in mBN for singlet and triplet states are respectively plotted in figures 1.8 (a) and (b) where "Singlet" refers to spin-singlet and "Triplet" refers to spin-triplet. In the dispersion curves presented in figures 1.8 (a) and (b), at  $q = 0$  one can identify the A singlet with  $|S, 0_+\rangle$ , which is a bright state, and the B singlet with  $|S, 0_-\rangle$ , which is dark (figure 1.8 a). In the triplet case (figure 1.8 b), the A triplet is 3-times degenerate and it corresponds to  $|T, 0_+\rangle$  and the B triplet is 3-times degenerate and it corresponds to  $|T, 0_-\rangle$ .

We point out that in figure 1.8 (a) and for a momentum  $q$  close to zero, the dispersion relation of the singlet A is linear. We highlight that by a green line. This excitonic dispersion is unusual in inorganic semiconductors and it highlights the fact that the singlet A ( $|S, 0_+\rangle$ ) in mBN does not follow the dispersion of a Wannier-Mott exciton ( $E(q) \neq \frac{\hbar q^2}{2M}$ ).

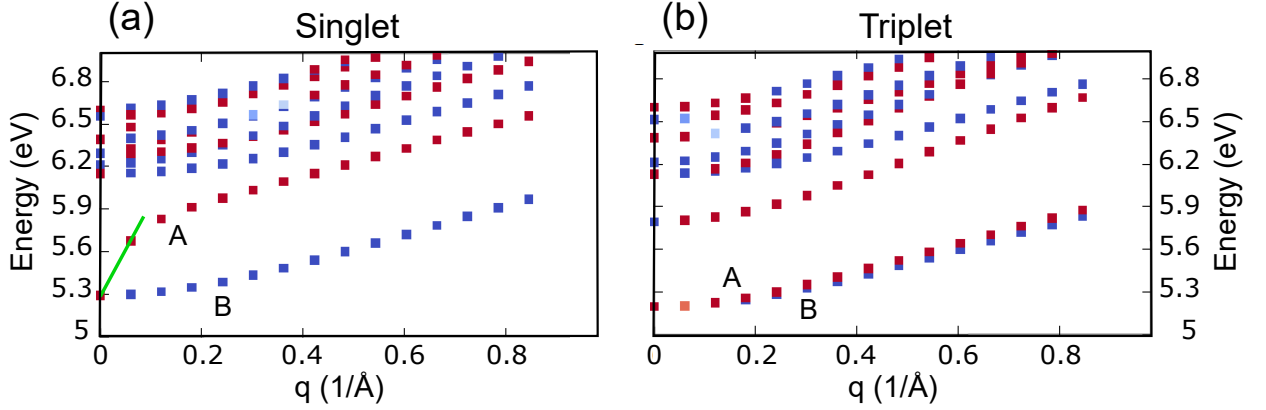


**Figure 1.8: Dispersion of excitons in mBN:** (a) dispersion of singlet excitons; (b) dispersion of triplet excitons in the BN single layer. The calculations are performed for in-plane momentum  $q$  along the  $\Gamma M$  direction [37], with  $q$  being the momentum of CM. Red squares correspond for states that have a visible peak in the absorption spectrum of mBN, while blue squares are dark exciton states with no intensity in the absorption spectrum.

Following Ando, the long range Coulomb interaction splits the triplet and singlet states, and the short range Coulomb interaction splits the singlet states between  $|S, 0_{\pm}\rangle$  and  $|S, K_{\pm}\rangle$  [41, 42].

### Excitons in bulk h-BN

For bulk h-BN, the dispersion relation for a non-interacting electron-hole pair using the GW method is compared with the exciton dispersion relation by taking into account the Coulomb interaction in figure 1.9 (a). These dispersion relations were reported by Schué *et al.* [43] in 2018. They used GW with the BSE method in order to solve the two-body problem by taking into account the Coulomb interaction (Figure 1.9 a, red line). In figure 1.9 (a) the momentum  $q$  corresponds to  $k_e+k_h$  *i.e.*  $\Gamma$  corresponds to  $q=0$ . In the electronic band structure of bulk h-BN, the electron and the hole of the fundamental exciton are situated at M and K points respectively (Figure 1.6). Since  $MK=\frac{\Gamma K}{2}$ , the lowest energy of the independent e-h dispersion (black curve) is in the middle of  $\Gamma K$  and it lies 0.5 eV below the direct transition (at  $\Gamma$ , figure 1.9 a). By considering the Coulomb interaction, the minimum of the exciton energy (red curve) stays close to the middle of  $\Gamma K$  at 5.97 eV with a binding energy  $E_b(iX)=250 \pm 50$  meV. Around  $\Gamma$  and  $K$ , the comparison between the two curves shows that the red parabola is flattened in comparison with the black one. This means that after taking into account the Coulomb interaction, the effective mass of the CM ( $M=m_e+m_h$ ) was larger than for the black curve. The two curves are not parallel along  $\Gamma K$  whereas they would be in the case of Wannier excitons. The energy of the direct exciton ( $q=0$ ) is 6.1 eV with a binding energy  $E_b(dX)=670$  meV (more than twice of  $E_b(iX)$  in the middle of  $\Gamma K$ ). This figure highlights the complexity of

the properties of excitons in h-BN, which are different from what is usually observed in other inorganic semiconductors.

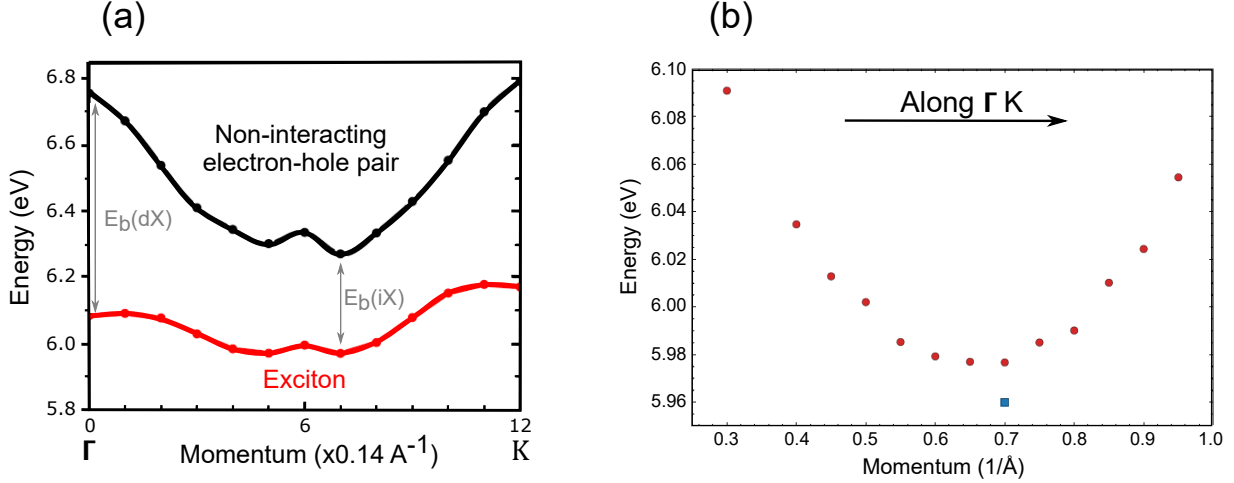


**Figure 1.9: Dispersion of excitons in h-BN:** (a) dispersion of excitons in h-BN compared to the noninteracting electron-hole pair along the  $\Gamma K$  line, with the momentum  $q$  corresponding to CM. The vertical arrows indicate the binding energy  $E_b$  for the direct (dX) and indirect (iX) excitons [43]; (b) dispersion energy of the fundamental exciton in bulk h-BN along  $\Gamma K$  direction, determined from EELS (*Electron Energy Loss Spectroscopy*) measurements [44].

From the experimental point of view, we cite the work done by Schuster *et al.* in 2018 [44]. They performed EELS (*Electron Energy Loss Spectroscopy*) measurements on bulk h-BN crystals. Their measurements have been performed along the  $\Gamma K$  and  $\Gamma M$  directions. Along  $\Gamma K$ , their measurements revealed the excitonic dispersion between 5.98 and 6.1 eV as a function of the momentum (Figure 1.9 b). It shows that the exciton minimum energy is at  $5.96 \pm 0.06$  eV, which confirms the energy of the fundamental exciton measured by PL in our team [45].

## 1.3 Phonon band structure

In this section we present the phonon modes in mBN and in bulk h-BN in order to investigate later the optical properties of this material. In h-BN, one could expect 12 different phonon modes in the bulk ( $3 \times 4$  because there are 4 atoms in the unit cell) and 6 phonon modes in mBN (2 atoms in the unit cell).

### 1.3.1 Phonon modes in mBN

The phonon modes in mBN were investigated in 1997 by the group of Nagashima in Japan [46]. They performed high resolution EELS measurements on epitaxial mBN grown by CVD

methods on metal substrates. Their results revealed for the first time the phonon dispersion relation along  $\Gamma K$  direction in the first BZ. These results have been complemented later by theoretical calculations [47, 48].

In figure 1.10, we present the phonon band structure calculated by Wirtz [48] for mBN. There are three acoustic phonons: two in-plane modes  $LA$  and  $TA$  and one out-of-plane mode  $ZA$ . The optical phonons in mBN are  $LO$ ,  $TO$ : two in-plane modes, and  $ZO$ : along the  $z$  axis.

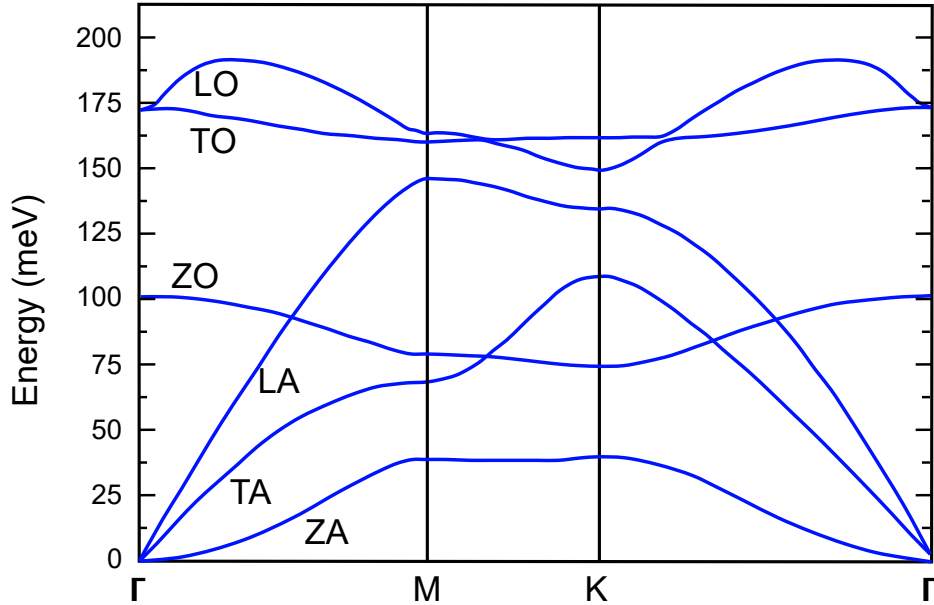


**Figure 1.10: Phonon dispersion relation of mBN:** calculated using local density theory ( $LDA$ ) by Wirtz *et al.* [48].

In mBN, the maximal phonon energy does not occur neither at the  $\Gamma$  point nor at zone edges, but at intermediate points away from the Brillouin zone edges (along  $\Gamma M$  and  $\Gamma K$ ). This is known in terms of over-bending, and it has been largely studied in diamond for the LO phonon mode [49].

From the experimental point of view, besides the experiments performed in Japan on mBN [46], few reports have investigated the phonon modes in mBN. Gorbachev *et al.* measured the Raman mode (LO) from exfoliated mono-, bi- and tri-layers of h-BN [50] deposited on a  $\text{SiO}_2/\text{Si}$  wafer. The energy of the LO phonon was measured about 169 meV in mBN. This energy value was dependent of the number of layers. Later Cai *et al.* [51] measured again the LO phonon mode from mono-, bi- and tri-layers of h-BN. He concluded that the energy of the LO phonon mode depends on the substrate used to deposit the layers on it and that the LO mode is not influenced by the number of layers. More details about these two reports are given within chapter 3.

### 1.3.2 Phonon modes in bulk h-BN

Phonon modes in bulk h-BN were studied for the first time in 1966 by Geik *et al.* [52]. In their work, they proposed the presence of twelve different phonon modes in h-BN. In figure 1.11 we present the phonon band structure [53] calculated 4 years ago and in which the 12 phonon branches can be identified. We note that the phonon dispersion relation for h-BN was calculated by many groups [54, 48, 20, 55, 56]. Almost all of them have a good agreement with each other.

For  $q$  in the plane of the layer, there are three acoustic phonons: two in-plane vibration modes noted  $LA$  and  $TA$ , the third one is an out-of-plane mode noted  $ZA$ . The nine remaining phonons are optical modes: three Infrared active modes and two silent-Infrared modes; two twice-degenerated Raman active modes  $E_{2g}^{high}$  and  $E_{2g}^{low}$  (Figure 1.11).

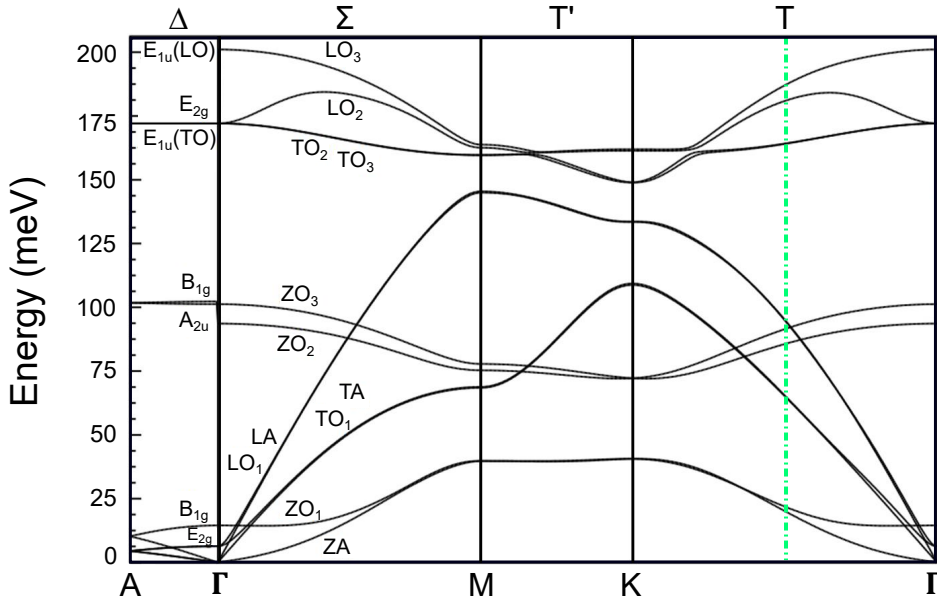


**Figure 1.11: Phonon dispersion in h-BN:** obtained from DFT calculations in Ref. [53]. The green dashed line highlight the phonon branches investigated at T point and involved the recombination process of the indirect exciton along KM.

The high-frequency Raman-active mode ( $E_{2g}^{high}$ ) was detected by Geik *et al.* and they measured an energy around 169.8 meV ( $1369\text{ cm}^{-1}$ ) at room temperature. This mode is analogous to the G mode in graphene and it corresponds to the vibrations of B and N atoms in opposite directions in the plane. The low-frequency Raman mode ( $E_{2g}^{low}$ ) was measured for the first time in 1978 [57] by Kuzuba *et al.* and later by Nemamich *et al.* in 1981 [22], they

found an energy around 6.4 meV ( $51.8 \text{ cm}^{-1}$ ). This second mode corresponds to the shear movements between the layers, it is usually present in lamellar materials. It was studied in multi-layer graphene by varying the number of layers [58] and it was demonstrated that its frequency decreases with the reduction of the number of layers. However, in h-BN it was never measured as function of the number of layers. The maximal phonon energy in h-BN is the one of the Infrared active-mode ( $\text{LO}_3$ ) for which the energy is 199.6 meV ( $1609 \text{ cm}^{-1}$ ) at the zone center.

The recombination processes in bulk h-BN involve phonons of  $MK$  wavevector, which is equal to  $\frac{\Gamma K}{2}$ . These phonons are situated at the T point (indicated by green dashed line in figure 1.11). The originality in h-BN comes from the fact that the valence band maximum (K) is away from the zone center ( $\Gamma$ ). Therefore, the relevant phonons for indirect exciton recombination are located in another valley (T) than the conduction band minimum. Their group velocity is then non-null since they are far from the high symmetry points. This originality has an important effect on the optical properties in h-BN and that we discuss below.

## 1.4 Emission spectrum in bulk h-BN

The optical properties of a material depend of the interaction of light (photon) with the material (electrons and phonons). These properties are governed by the dispersion relations of electrons and phonons. In the previous sections 1.2 and 1.3, we displayed the electronic and vibrational properties in h-BN for bulk and monolayer. In this section, we will discuss the recombination processes in bulk h-BN.

As mentioned previously, the calculations of the band structure lead to an indirect configuration for the fundamental bandgap in bulk h-BN and a direct configuration for the bandgap in mBN. The luminescence of mBN was never measured before this PhD thesis, while for bulk h-BN, experiments investigating the luminescence in high quality crystals have been performed in 2004 by Watanabe *et al.* [11]. An unexpected and intense photoluminescence (PL) spectrum around 200 nm was reported at room temperature in their h-BN crystals. This intense luminescence is due to a high internal quantum efficiency estimated about 50% in h-BN [43]. Such an effect exceeds what is commonly observed in indirect semiconductors and led them to conclude that the gap of h-BN is of a direct nature. This controversy between a direct bandgap claim and the theoretical calculations lasted during twelve years.

In 2016, experiments by two-photon spectroscopy performed in our group [59] demonstrated that the band gap of bulk h-BN is of indirect nature and that the PL spectrum consists of emission lines corresponding to phonon-assisted recombination for the spectral range between 5.75 and 6 eV (figure 1.12). The involved phonons are lying at the T point of the BZ (section

1.3.2). In Ref.[59], they identified 5 phonon replicas (blue lines in figure 1.12). Later within the thesis of T.P.Q. Vuong [60] and after the calculations done by Cuscó [53] all the involved replicas have been identified (green lines in figure 1.12) as following  $LO_3$ : 5.76 eV,  $TO_3/TO_2$ : 5.79 eV,  $LA/LO_1$ : 5.86 eV,  $ZO_3$ : 5.87 eV,  $TA/TO_1$ : 5.89 eV, and  $ZO_1$ : 5.93 eV. The zero-phonon-line (ZPL) at 5.955 eV corresponds to a weak luminescence of the indirect exciton (iX).

The phonons  $ZA/ZO_1$  and  $ZO_3$  were identified using polarization-resolved measurements with the pointing vector of the emitted phonon being orthogonal to the c-axis (Figure 1.12 spectrum in green) [60].

The interaction between excitons and phonons in bulk h-BN has been identified to be in a strong coupling regime [61] and the temperature dependence of phonon replicas linewidth is ruled by quasi-elastic scattering of acoustic phonons (ZA) and inelastic scattering by absorption of optical phonons ( $ZO_1$ ).

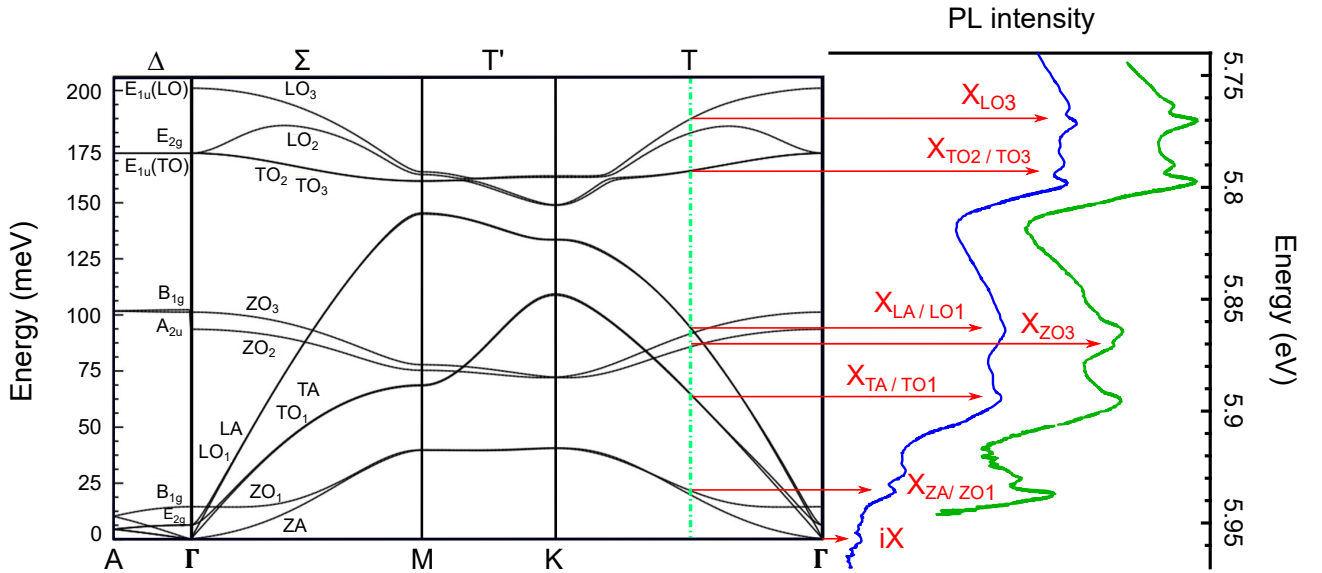


**Figure 1.12: PL emission of h-BN at cryogenic temperature:** (right side) PL spectra of bulk h-BN [59, 60] plotted at the same scale as the phonon dispersion relation [53] (left side); the energy of the indirect exciton (iX) coincides with the zero-phonon energy.

Our team studied also the effect of isotope purification on the properties of bulk h-BN. Isotopes of a given element have the same number of electrons, but their atomic mass and nuclear spin differ through the number of neutrons in their nucleus. The trivial effect of isotope exchange within a material is the change of its vibrational properties. The natural composition of h-BN is made of 20%  $^{10}BN$ , 80%  $^{11}BN$  and 99.6%  $^{14}N$ . Our group has studied the isotope effect on the optical properties of h-BN by performing PL, Raman and X-ray measurements

on B-purified crystals:  $^{10}\text{BN}$  and  $^{11}\text{BN}$ . Their properties have been compared to the one of  $^{\text{Nat}}\text{BN}$  (Figure 1.13) [23].

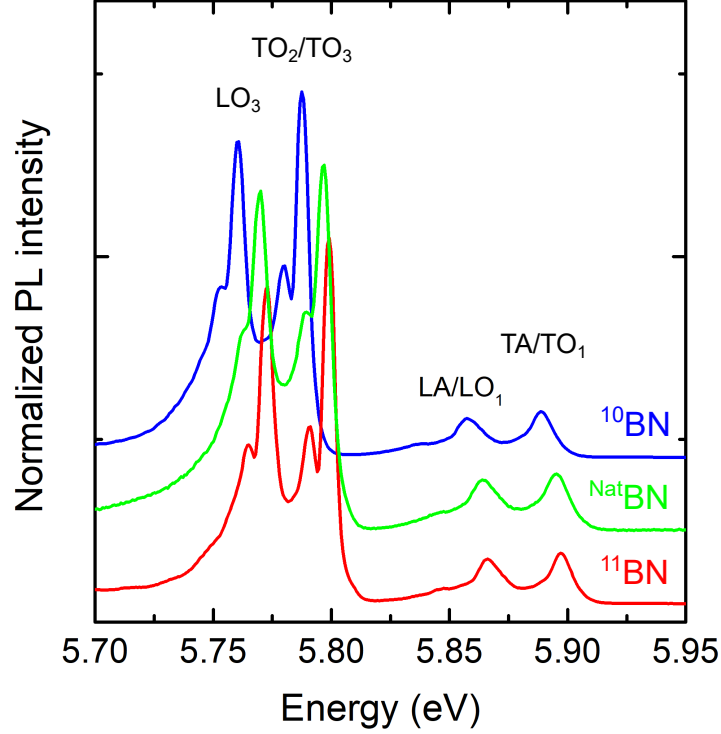


**Figure 1.13:** PL emission of h-BN at cryogenic temperature: for samples purified isotopically:  $^{10}\text{BN}$  and  $^{11}\text{BN}$  and  $^{\text{Nat}}\text{BN}$ .

A global red-shift from  $^{11}\text{BN}$  to  $^{10}\text{BN}$  was observed in the PL spectra of h-BN since the PL energy of phonon replicas depends of the reduced mass; the larger is the reduced mass, the lower the phonon energy, and the higher is the energy of the emitted photon (the energy of the emitted photon being  $h\nu = E_{iX} - E_p$  with  $E_{iX}$  the energy of the indirect exciton and  $E_p$  the phonon energy).

Besides the emission resulting from the recombination processes of the fundamental bandgap, the luminescence spectra in h-BN presents a series of intense emission lines in the spectral range between 5 and 5.65 eV (Figure 1.14, box in a darker blue). The lines labeled  $D_2$  and  $D_6$  come from extrinsic recombination processes, they are attributed to a boron-nitrogen divacancy ( $V_{BN}$ ) and a nitrogen vacancy ( $V_N$ ) [62], respectively. In parallel, there is phonon-related emission at 5.32, 5.47 and 5.62 eV. These emission lines are involving intervalley scattering assisted by optical phonons (TO) between K and K' points [63]. It was demonstrated that

the observation of these emission lines is related to the existence of stacking faults in h-BN crystals [64].

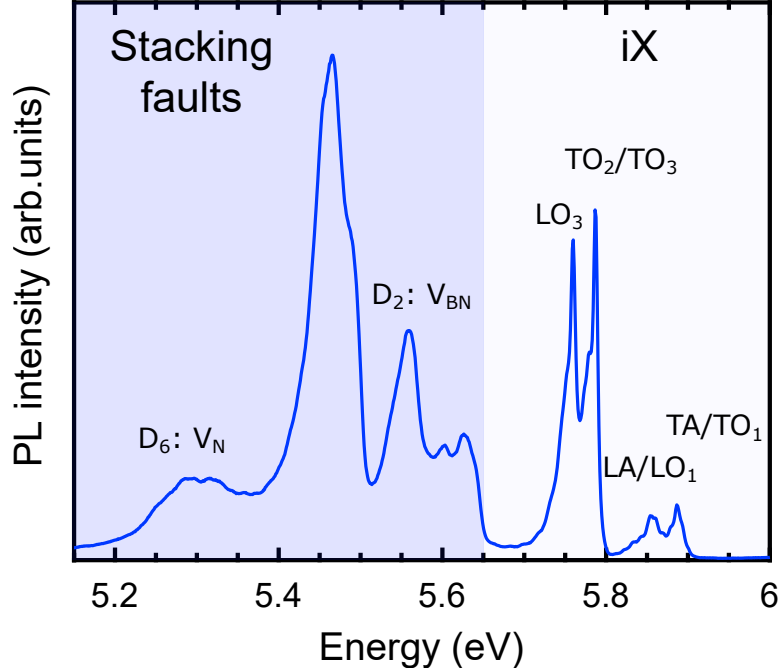


**Figure 1.14: Emission in bulk h-BN:** PL spectrum measured from bulk h-BN at cryogenic temperature for an excitation energy of 6.3 eV and plotted in a linear scale. The emission of stacking faults is in the spectral range 5-5.65 eV and the phonons replicas resulting from the recombination of indirect exciton (iX) in h-BN are in the spectral range 5.65-5.95 eV.

## 1.5 Conclusion

In this chapter we discussed the main properties of hexagonal boron nitride. We recalled the structural properties of h-BN. Within the plane of the layer, the atoms are tightly bound by covalent bonds while the layers are interconnected by weak van der Waals forces. We discussed later the electronic properties of h-BN by describing the band gap structure for 3D and 2D lattices. In the bulk form, the fundamental gap is indirect with an indirect excitonic transition at 5.955 eV and it undergoes from indirect to direct when thinned to a monolayer. We presented later the excitonic properties of bulk h-BN and we discussed the states involved in monolayer. Finally we displayed the phonon band structure in mBN and bulk h-BN in addition to the optical properties studied in our team.

---

## EXPERIMENTAL ASPECTS

The target of this chapter is to present the experimental techniques and the samples used during my thesis. This chapter is split into two parts, the first one is devoted to the description of the reflectance and photo-luminescence setups built in the DUV range ( $<350\text{nm}$ ), and the difficulties we faced while implementing these techniques. The second section will be devoted to the description of the samples studied during this work and to present the different growth methods.

### 2.1 Experiments

Optical spectroscopy is a powerful tool for understanding the physics of semiconductors. Here, we utilize PL and reflectance spectroscopy techniques in order to explore the opto-electronic properties of h-BN. PL is a basic method that probes the radiative recombination processes of a considered material after laser excitation. However, the emitted photons result from the recombination of charge-carriers having thermalized into the lowest energy states. This fact makes PL an insufficient technique to examine the opto-electronic properties for the energy levels situated higher than the fundamental energy gap. During my thesis, I built a reflectance setup in order to complement the PL experiments and analyze the response of the material for a deeper understanding of its opto-electronic properties. Reflectance spectroscopy probes the refractive index of a material and more specifically it investigates the dielectric function which takes into account all the optical transitions involving the fundamental and excited energy states. This technique probes a system at thermodynamic equilibrium, while PL is controlled by the relaxation dynamics in the system brought out of equilibrium by the laser excitation. For that reason, the need to build this technique was primordial to expand our understanding of the opto-electronic properties of h-BN.

In this section, we will provide a detailed explanation of both setups.

## 2.1.1 Reflectance

### Optical constants

Before considering the reflectance principle, let us resume the optical constants useful to understand quantitatively the optical properties of the solid and its optical response. The dielectric function of a material is given by:  $\tilde{\epsilon}(\omega) = \epsilon_1(\omega) + i\epsilon_2(\omega)$ ,  $\epsilon_1$  and  $\epsilon_2$  being the real and imaginary parts, respectively, which are interdependent under the Kramers-Krönig transformation.

The dielectric function is linked to the refractive index by:  $\tilde{\epsilon}(\omega) = \tilde{n}^2$ . The refractive index of a material is defined by:  $\tilde{n} = n + ik$ . The real part  $n$  gives the ratio between the vacuum speed of light and the phase velocity of an electromagnetic wave propagating through the material ( $n = \frac{c}{v}$ ), while the imaginary part  $k$  is known as the *extinction coefficient* and it characterizes the attenuation of the electric field in a medium.

### Principle of Reflectance

Reflectance spectroscopy examines the interaction of an electromagnetic field with a material and probes the electromagnetic field reflected by an interface with the medium.

We consider an incident electromagnetic wave with a linear polarization at an interface between two media having complex refractive indices  $n_1$  and  $n_2$ , respectively.  $\theta_1$  and  $\theta_2$  are the angles between the normal to the interface and the propagation direction of the electromagnetic waves in each medium (Figure 2.1). The incident, reflected and transmitted waves are given by the following equations, respectively :

$$\begin{aligned}\vec{E}_i &= \vec{E}_{0i} e^{i(\omega t - \vec{k}_i \cdot \vec{r})} \\ \vec{E}_r &= \vec{E}_{0r} e^{i(\omega t - \vec{k}_r \cdot \vec{r})} \\ \vec{E}_t &= \vec{E}_{0t} e^{i(\omega t - \vec{k}_t \cdot \vec{r})}\end{aligned}\tag{2.1}$$

$\vec{E}_{0i,r,t}$  are the respective amplitudes for the incident/reflected/transmitted waves and  $\vec{k}_{i,r,t}$  their respective wave-vectors.  $\vec{r}$  being the position vector and  $\omega$  the frequency.

The Fresnel's coefficients correspond to the reflection and refraction amplitudes which are respectively defined by:  $r = \frac{E_r}{E_i}$  and  $t = \frac{E_t}{E_i}$ .

Here we are interested by the reflection case. Depending on the waves polarization s or p<sup>1</sup>, the

---

<sup>1</sup>The two orthogonal linear polarization states are referred to as p- and s-polarization. P-polarized (from the German parallel) light has an electric field polarized parallel to the plane of incidence, while s-polarized (from the German senkrecht) light is perpendicular to the plane of incidence.

Fresnel's coefficient in reflection are defined as following:

$$r_s = \frac{n_1 \cos(\theta_1) - n_2 \cos(\theta_2)}{n_1 \cos(\theta_1) + n_2 \cos(\theta_2)} \quad (2.2)$$

$$r_p = \frac{n_2 \cos(\theta_1) - n_1 \cos(\theta_2)}{n_2 \cos(\theta_1) + n_1 \cos(\theta_2)}$$

$n_1$ ,  $n_2$ ,  $\theta_1$  and  $\theta_2$  are related by the Snell-Descartes law given by:  $n_1 \sin(\theta_1) = n_2 \sin(\theta_2)$ .

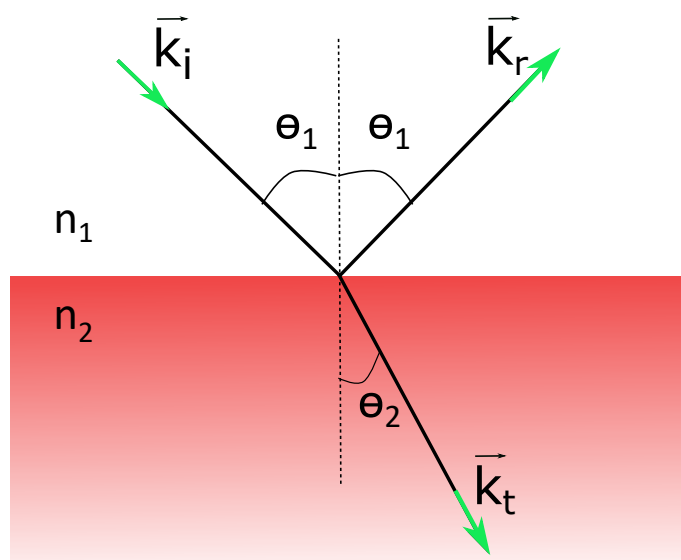


**Figure 2.1: Schematic plot showing partial reflection, and refraction of an electromagnetic wave with a linear polarization at an interface between two different media:**  $\theta_1$  is the angle between the normal and the incident/reflected wave in the medium (1);  $\theta_2$  is the angle between the normal and the refracted wave in the medium (2);  $\vec{k}_{i,r,t}$  are the corresponding wave-vectors.

The reflection coefficient is defined by:  $R = |r|^2$ . If we consider that the medium (1) is the air, its refractive index is real and equal to one ( $n_1 = 1$ ). Medium (2) is the material with a complex refractive index  $n_2 = \tilde{n} = n + ik$ . For normal incidence ( $\theta = 0^\circ$ ), the reflection coefficient is given by:

$$R = \left| \frac{1 - \tilde{n}}{1 + \tilde{n}} \right|^2 \quad (2.3)$$

In our case, we performed reflectance experiments with an incidence angle close to the normal, ( $\theta_1 = 4^\circ$ ) as detailed in the following parts of this section.

### Experimental setup

Reflectance spectroscopy consists in measuring the spectrum of the light reflected by a sample. There are many possibilities to build the platform for the reflectance setup and to realize

such measurements. One can send directly the light emitted by the source (covering a large spectral range) to the sample surface, then one filters spectrally the light reflected by the sample surface in order to record the spectrum. To analyze spectrally the reflected light, one can use a monochromator or a spectrometer<sup>2</sup>.

Another configuration can be used which consists to directly filter the light emitted by the source using a monochromator and then send the spectrally-filtered source to the sample surface.

We used the second case (Figure 2.2) because in the first configuration, simultaneous processes could occur in the material under white-light illumination, while in the second configuration, we can avoid the simultaneous excitation of competing processes that could occur at energies/wavelengths other than those of interest like PL.

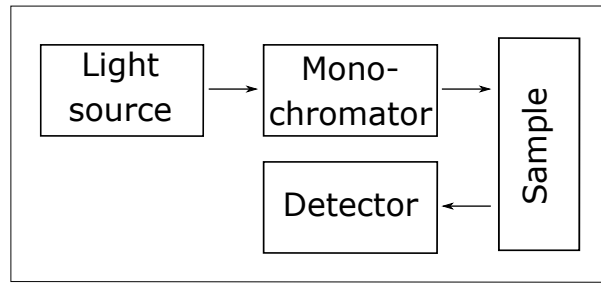


**Figure 2.2: Configuration used to build our reflectance experiment:** The light emitted by the source is filtered spectrally by a monochromator before reaching the sample surface. The reflected light from the sample surface is directly detected by a photo-detector.

### Light sources:

As mentioned before, my thesis has consisted in the study of the opto-electronic properties of h-BN in the DUV range. We are especially interested in doing reflectance measurements up to 7 eV ( $\sim 177$  nm) in order to examine the electronic properties of h-BN above 5.95 eV. For that, our choice was first to use a deuterium lamp (*63163 Newport*) with an arc size of  $0.5 \times 0.5$  mm<sup>2</sup>. This lamp produces a broadband emission from 160 to 800 nm, with an ultraviolet radiation of  $\sim 1$  mW/mm<sup>2</sup>/nm around 200 nm. This irradiance decreases by more than a factor 10 between 200 and 400 nm. The spectrum of the light emitted by the lamp presents emission lines for wavelengths higher than 400 nm (Figure 2.3).

Afterwards, we have bought another lamp with higher performances that could replace our

---

<sup>2</sup>The monochromator, as its name indicates, permits the transmission of selected wavelengths of light chosen from a wider range of wavelengths available at the input. A spectrometer has an output with a wide spectral range and is equipped with a multi-channel detection device.

Deuterium lamp. It is a Xenon-plasma light source (LDLS EQ-99X EnergetiQ) based on laser-driven bulb technology that directly heats the plasma to the temperatures necessary to get an efficient DUV discharge. This technology results in an arc size of the order of  $100\mu\text{m} \times 100\mu\text{m}$ , 5 times smaller than that of the Deuterium one. Another important consequence of the use of this light source is the absence of noise in the broad spectral range (170-750 nm) which permits us to do reflectance measurements for longer wavelengths if needed. The irradiance is  $\sim 1 \text{ mW}/\text{mm}^2/\text{nm}$  and approximately constant over all the spectrum range. The irradiance spectrum of the two lamps are taken from the published data by the lamps producers and are plotted in the figure 2.3.

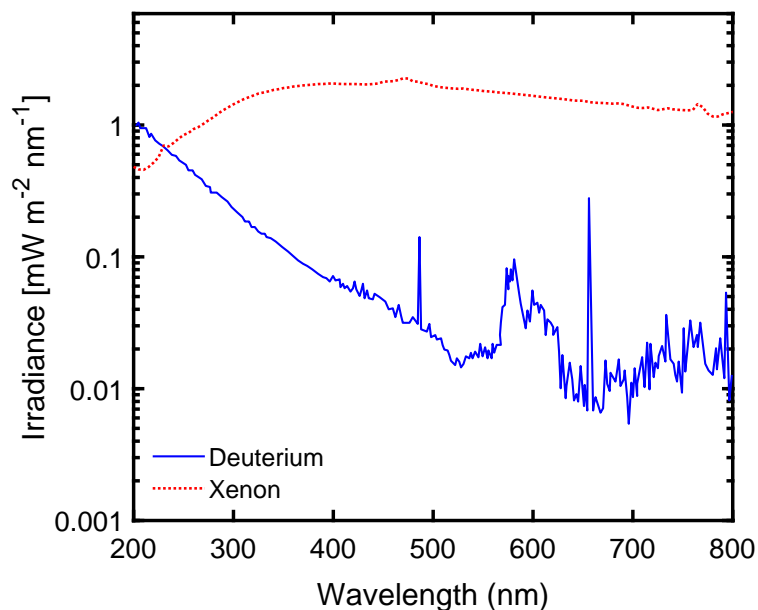


**Figure 2.3: Comparison between the irradiance spectrum of the two lamps used to build our reflectance setup:** the curve plotted in solid blue line corresponds to the irradiance of the Deuterium lamp; the dashed red line corresponds to the one of Xenon-plasma light source.

As mentioned above, the size of the Xenon-plasma light source is 5 times smaller than the one of the Deuterium Lamp. Later when doing experiments, the size of the spot focused on the sample surface will be delimited vertically by the arc size of the lamp and horizontally by the width of the monochromator slits  $e$ , it is given by:  $arcsize \times e$ . Using the Xenon-plasma source has allowed us to measure reflectance by exciting a smaller region on the sample surface and then to reduce the inhomogeneous broadening from our reflectance spectrum which can be caused by morphological defects and some surface inhomogeneity.

The results obtained using the Deuterium lamp are presented in the third chapter while the ones obtained after we bought the Xenon-plasma light source are described in Appendix A.

### Description of the setup:

Our home-made reflectance setup is sketched in figures 2.4 (a) and (b). As it is mentioned in the paragraph before, we used two different light sources to build our setup. The light emitted by the lamp is spectrally filtered through a mono-chromator (*Cornerstone CS130*), equipped with three diffraction gratings (Figure 2.4 (a)): a 2400 *grooves/mm* grating blazed at 275 nm, a 1200 *grooves/mm* grating blazed at 350 nm, and a 150 *grooves/mm* grating blazed at 800 nm. We used the 2400 *grooves/mm* grating for all my measurements as it presents the higher groove density, providing the higher dispersion and therefore the best spectral resolution for our measurements. Both the input and output slits of the monochromator are opened with widths of 100  $\mu\text{m}$  providing a spectral resolution of the order of 10 meV (that is calculated later). The filtered light is collected at the exit slit through a spherical mirror (SM2), and then focused on the sample surface with an incidence angle close to the normal (equal to  $4^\circ$ ). The sample is held on a cold finger of a closed-cycle cryostat, in order to perform temperature-dependent measurements from 8K to room temperature (Figure 2.4 (b)). The reflected light is focused on a photo-multiplier (PM) detector, adapted for a spectral range scaling from 160 nm to 900 nm (*R955 tube, Hamamatsu photonics*). The signal is amplified through a pre-amplifier and then detected using a synchronous detection method that is explained later.

All the optical elements are reflective mirrors with a special coating for the DUV: aluminium protected by  $\text{MgF}_2$  film, that gives an anti-reflective film for 180 nm.

In order to visualize the image of the sample surface, we installed an imaging system using a source which emits visible light. It was mounted in front of the cryostat window to light up the sample holder. The image of the sample holder is formed by a lens on a CCD camera (Thorlabs DCC1545M). The spot position on the sample surface is visualized when setting the grating of the monochromator to the zero-order in which there is no diffraction, and the spot is visible<sup>3</sup>. For clarity of the scheme, the imaging system is not presented in figure 2.4.

All the instruments used to build our setup are controlled by a central unit. The computers programs were developed by our engineer P.Valvin using Lab-view interface to communicate with the different instruments, to acquire and save the measured data.

Under ambient conditions, light sources with emission wavelength below 242 nm produces toxic  $\text{O}_3$  (ozone) gaz, so that we use an *Ozone Eater (66087 Oriel)* that converts the toxic ozone produced by the lamp into oxygen.

---

<sup>3</sup>At the zero-order the grating acts like a mirror, and the light coupled to the monochromator which contains visible wavelengths, exits the monochromator in a non-dispersed light beam. One can see a visible spot of light, thanks to the component of the source in the visible range

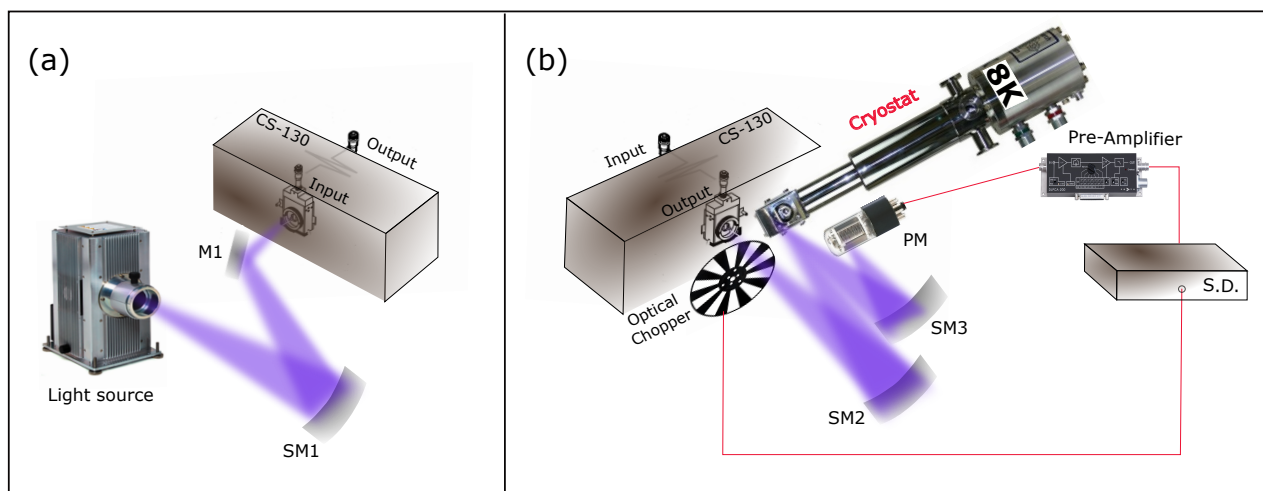


**Figure 2.4: Scheme of the reflectance setup:** (a) Before the input slit of the monochromator, the light source is coupled with the monochromator through reflective mirrors; (b) after the exit slit of the monochromator, the light beam is focused on the sample surface and the reflected beam is collected by the photo-multiplier detector (PM); an optical chopper, a pre-amplifier and a Synchronous Detection (S.D.) system provide a synchronous detection of the signal. All the elements are placed in  $N_2$  environment.

### Spectral resolution:

The spectral resolution of our system is determined by the monochromator slit widths ( $e = 100\mu\text{m}$ ) and the reciprocal dispersion ( $r_d = 3\text{nm}/\text{mm}$ ) of the grating used (Newport 74021):  $\Delta\lambda = e \times r_d = 0.3\text{nm}$ . In terms of energy and for a wavelength  $\lambda = 200\text{nm}$ ,  $\Delta E \sim 10\text{meV}$ .

### Synchronous detection:

In order to detect the reflectance signal, we use a photo-multiplier (PM), a pre-amplifier and a lock-in amplifier (5210 Princeton) that is indicated in figure 2.4 (b) by S.D. (for synchronous detection).

The principle of synchronous detection consists firstly, to modulate the signal we want to measure with a reference signal of a known frequency and secondly, to de-modulate and integrate the signal of interest using a lock-in amplifier. The modulation is given by turning repeatedly on and off the excitation signal. In our case, an optical chopper with a frequency of  $\sim 1\text{kHz}$  is used. The lock-in amplifier first amplifies the input signal, then multiplies the input and the reference signals (the reference signal is given by the optical chopper and the detected signal by the PM at the same frequency) and finally integrates with a low-pass filter that removes all frequencies except the one of interest. This is resumed in figure 2.5.

For a good accuracy with a noise level  $\leq 0.2\%$  we should increase the gain (which represents the overall amplification of the signal before injection into the S.D.) at the maximum with a

condition on the entry not to be saturated. In our case we use a gain of  $10^4 \text{ V.A}^{-1}$ . However, to improve the signal to noise ratio, one has also to choose the time constant  $\tau$ , which defines the lock-in amplifier's low-pass band-width. It ranges between  $300\text{ms}$  and  $1\text{s}$  depending on the sample. The measurement is carried out over a time equal to  $3 \times \tau$ , for each wavelength. Finally, the measured signal is detected, and saved on the computer through a Lab-View interface.

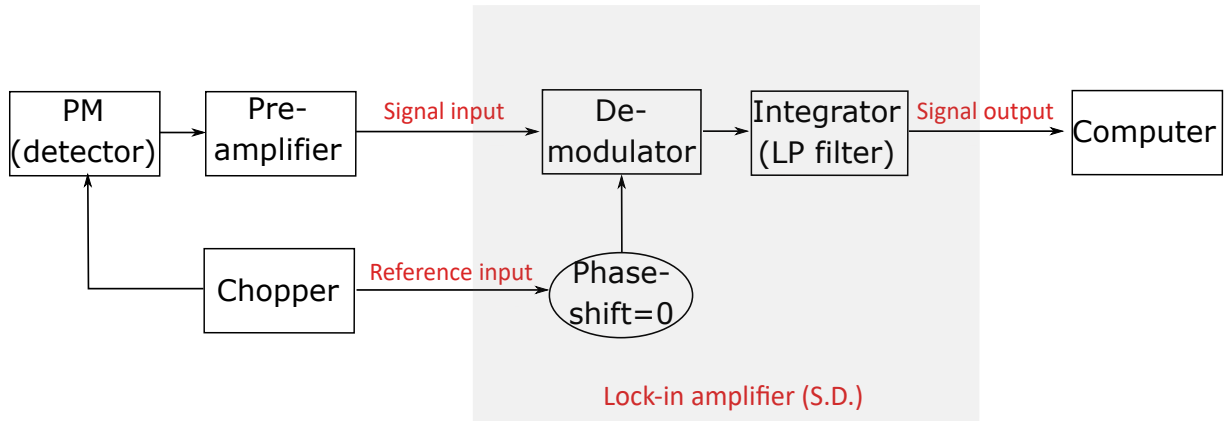


**Figure 2.5: Principle of synchronous detection:** scheme resuming the process of synchronous detection in our setup with a phase shift chosen to maximize the modulated signal.

### Complications of the setup

Doing reflectance experiments seems to be basic and easy to realize. In the DUV, the presence of optical aberrations makes the alignment of the optics complicated. Moreover, we are dealing with energies/wavelengths overlapping with the absorption bands of oxygen. In this part, we will discuss the main difficulties we faced while building our reflectance setup.

#### Optical aberrations:

In the previous section, we presented the platform of our reflectance setup and the detection of our signal, but we did not discuss the alignment of the optics when building our setup. Here we will discuss especially the alignment of the monochromator and the optical aberrations that are present in our system.

We note that the alignment of our setup is realized with visible light: the grating of the monochromator is set at the zeroth-order.

In an ideal case, when no aberration exists in the system and if the grating is tilted to the zeroth-order, one can see a rectangular form for the illuminating beam after the exit slit, with a homogeneous intensity among the surface. The light intensity decreases homogeneously on the rectangular surface when closing both the input and output slits and the form of the

image should remain the same. However, in practice, for widths narrower than  $150\mu\text{m}$ , the monochromator output shows two separated "bean shapes" of light, suggesting the presence of optical aberrations in our system.

Optical aberrations exist in different forms, we separate them between chromatic aberrations and geometrical aberrations. Chromatic aberrations are usually observed when using lenses which fail to focus all colors on the same convergence point, due to the different refractive indices of the glasses for different wavelengths of light. While aberrations with monochromatic light are caused by the geometry of the optics and include spherical aberration, coma, astigmatism<sup>4</sup>, field curvature and image distortion. In our system, all the optics we used are reflective mirrors (flat and spherical mirrors), and the monochromator is a Fastie-Ebert instrument<sup>5</sup> composed of one large spherical mirror and one plane diffraction grating. Then, the presence of optical aberrations in our system is limited to the geometrical family.

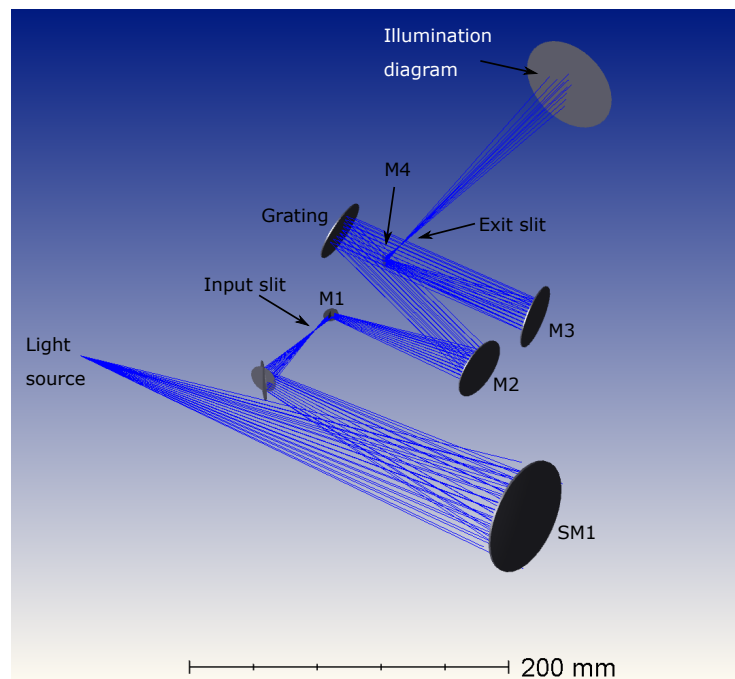


**Figure 2.6: Simulation of our experiment using Zemax:** The input and output slits of the monochromator are presented by two converging points. The dispersion of light by the monochromator is simulated by 3 mirrors and one grating with M2 being the one collimating the beam and M3 the one focusing the beam and giving the image at the exit plane; M4 is a flat mirror.

<sup>4</sup>Coma is produced when rays from an off-axis object point are imaged by different zones of the optical element, one sees the images are circular in shape and of varying size, displaced with respect to each other. While astigmatism results from the failure of a single zone of an optical element to focus the image of an off-axis point at a single point, and the rays that propagate in two perpendicular planes have different focal points on the plane.

<sup>5</sup>In a Fastie-Ebert instrument, a portion of the spherical mirror firstly collimates the light and then reflects the beam upon the grating. A separate portion of the spherical mirror focuses the dispersed light from the grating into images of the entrance slit in the exit plane.

In order to understand the shape of the illumination spot after the exit slit of the monochromator, we performed an optical simulation of our setup using Zemax<sup>6</sup>, that we present in figures 2.6 and 2.7.

Firstly, we considered that the light is perfectly focused on the entrance slit of the monochromator. The results of this simulation is presented in the illumination diagram shown in figure 2.7 (a). The illumination diagram shows the form of a cross for slit width of about  $30\mu m$ , suggesting the presence of off-axis aberrations in our system, like astigmatism. This is in agreement with the suggestions of the producer proposing not to work for widths less than  $50\mu m$ .

As a second step, we took into account the impact of the focusing element at the entrance of the monochromator. To align our setup, we use a spherical mirror to couple the light at the entrance slit of the monochromator. This induces the presence of spherical aberrations<sup>7</sup> at the input of the monochromator. The result of such type of aberration is that all the rays emerging from the pupil will not cross at the same point on the focal plane. When closing the input slit of the monochromator, some rays are cut resulting in dark shapes in the pupil, after the exit slit. Moreover, the relatively high aperture of the monochromator (F/4) enhances the effect of these aberrations when a tiny off-center misalignment is present.

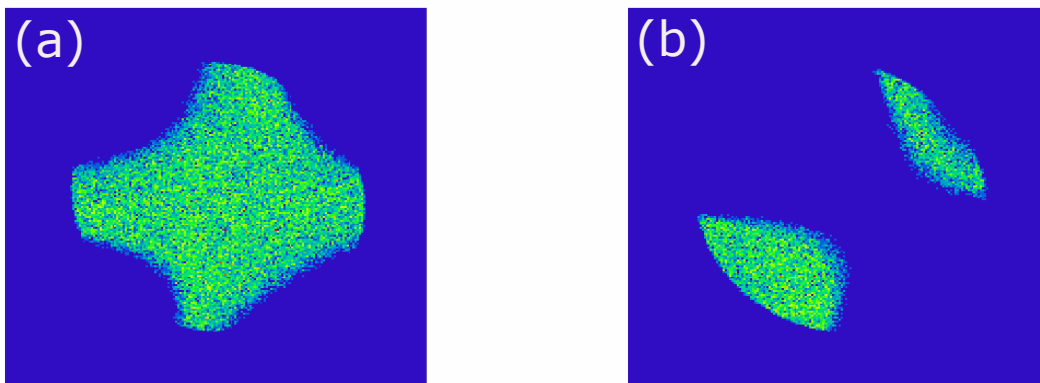


**Figure 2.7: Illumination diagrams after the exit slit of the monochromator simulated using Zemax:** (a) result of the simulation for slit width of about  $30\mu m$  ; (b) result obtained for slit width of  $150\mu m$  and by adding to the previous simulation a tiny off-center misalignment at the input slit of the monochromator.

We added to our simulation a small misalignment at the entrance of the monochromator: the result is presented in figure 2.7(b). The illumination diagram shows two separated spots with "bean shapes" for slit widths of  $150\mu m$ . The spot form corresponds perfectly to what we

<sup>6</sup>Zemax is a professional optical design program that serves to design and analyze imaging and illumination systems by modeling the propagation of rays through an optical system.

<sup>7</sup>Spherical aberrations are caused by spherically shaped optics. Parallel light rays that pass through the central region focus farther away than those that pass through the edges. The result is many focal points.

observe in practice when aligning our setup, and we can remark that the two forms presented in (a) and (b) are complementary.

From what we presented here, one can conclude that at the exit slit of our monochromator the light beam is affected by many types of geometrical aberrations which came from the spherical shapes of the mirrors used but mostly from the off-axis design of the monochromator which exhibits of a limited ability to maintain an image without aberrations.

In order to resolve this problem, one can either de-center the spot on the entrance slit of the monochromator in order to get the same form as in the case (a) or work with the case (b) by selecting one of the two beams. As we had enough intensity on our detector, we decided to cut one of the two spots in case (b) using a spherical iris/pinhole before the sample surface and the spot selected was the one with the higher intensity.

### **Oxygen absorption:**

As it is mentioned in the beginning of this section, we are interested in measurements of reflectance up to 7 eV ( $\sim 177$  nm). In this spectral range, the absorption of oxygen is inconvenient and is due to the Schumann–Runge bands<sup>8</sup>. In order to resolve this issue and do measurements without being disturbed by oxygen absorption, we decided to work in a nitrogen-gas environment. For that, we covered the optical table by a plastic film and we built a box covering the setup with a scaling keeping the nitrogen gas inside it.

The nitrogen flux was provided by a cryogenic liquid container that allows to extract the gaseous nitrogen through an internal vaporizer and then inject it inside the box. The percentage of oxygen inside the box was measured using an oxygen-meter.

In figure 2.8 (a), we plotted in red solid line the intensity of the reflected signal from the surface of a flat mirror (aluminum) as a function of the energy (eV). The graph is plotted in log scale. The spectrum was recorded using our Deuterium lamp under ambient conditions and it shows a series of bands between 6.2 and 6.8 eV. We compared our data with a reference spectrum of reflectance [65] plotted in a green dotted line, and recorded using a deuterium lamp too. The comparison between the two spectra shows that the bands present in our data correspond perfectly to the ones attributed to the absorption of the UV light by the oxygen existent in the air.

Figure 2.8 (b) shows the plot of the intensity of the reflected signal from the surface of the same flat mirror. The box is purged by a nitrogen flux, and the oxygen percentage inside the box is null with an uncertainty of the oxygen-meter about 0.1%.

---

<sup>8</sup>Set of absorption bands of oxygen that occur at wavelengths between 176 and 192.6 nm.

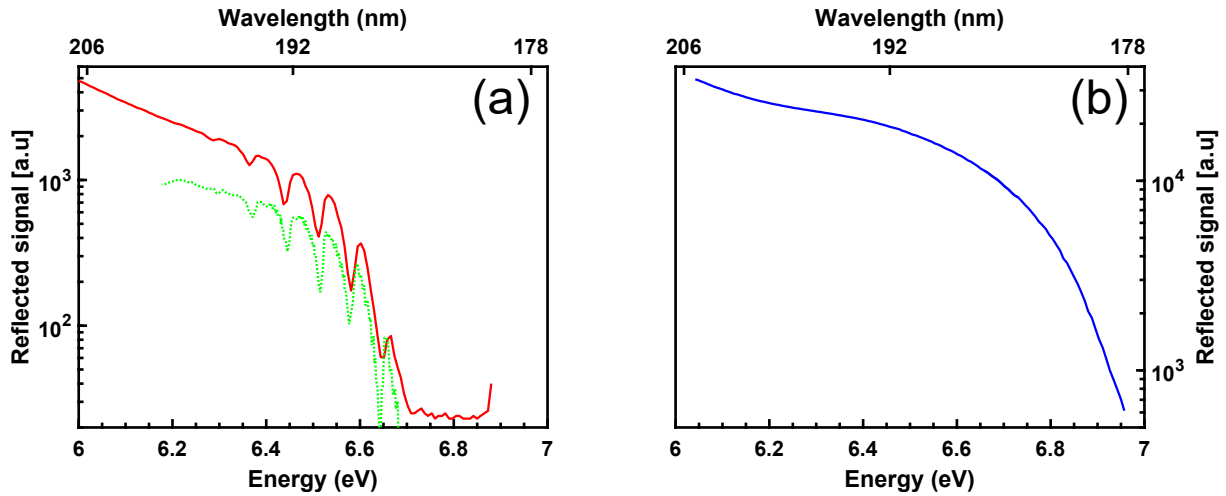


**Figure 2.8: Intensity of the reflected light in the spectral range of the Schumann–Runge bands plotted in semi-log scale:** (a) In red solid line is the spectrum measured by our setup from a reference sample, using a deuterium lamp and under ambient conditions; in green dotted line is plotted a spectrum of reflectance showing the Schumann-Runge bands from Ref.[65]. (b) The spectrum measured by our setup from a reference sample, using a deuterium lamp and under nitrogen-gas conditions.

The spectrum under nitrogen-gas conditions shows the total disappearance of the oxygen absorption bands. In addition, the intensity of the signal increases by a factor of 8 for energies around 6 eV and by a factor of 28 for energies higher than 6.6 eV.

### Normalization of our measurements

A reflectance spectrum shows for each wavelength/energy, the ratio between the intensity of the light reflected by the sample and the intensity of the incident light, given by:

$$R(\lambda) = \frac{I_r(\lambda)}{I_0(\lambda)} \quad (2.4)$$

$I_0(\lambda)$  and  $I_r(\lambda)$  being the intensities of the incident and reflected light from a sample surface respectively.  $I_r(\lambda)$  is directly measured from the reflected signal of the considered sample's surface, it is given by:  $I_r(\lambda) = I_0(\lambda) \times R_{sample}(\lambda) \times \eta$ , with  $\eta$  being the sensitivity of the PM detector.  $I_0(\lambda)$  cannot be directly measured due to the experiment conditions: the presence of cryogenic conditions in our experiments and the need to pass the light by the cryostat window leads to the impossibility of measuring directly  $I_0(\lambda)$ . For that, we use a reference mirror that permits us to measure  $I_{ref}(\lambda) = I_0(\lambda) \times R_{ref}(\lambda) \times \eta$ . Consequently,  $\frac{I_r(\lambda)}{I_{ref}(\lambda)} = \frac{R_{sample}(\lambda)}{R_{ref}(\lambda)}$ . The reflectance of the sample is then given by  $R_{sample}(\lambda) = \frac{I_r(\lambda) \times R_{ref}(\lambda)}{I_{ref}(\lambda)}$ .

As mentioned, we use as a reference a mirror with a diameter size of 5mm, held next to the sample inside the cryostat, it permits us to measure  $I_{ref}$ . The mirror used is covered

with an aluminum coating and protected by a thin film of  $MgF_2$  (the same coating as the one of the optics used to align our setup) providing a reflectivity  $R_{ref}$  sufficiently flat for the wavelength/energy domain that we use which allows us to normalize our measurements. The reflectivity spectrum of the mirror we use is given by the producer (Acton optics), it is re-plotted in figure 2.9.

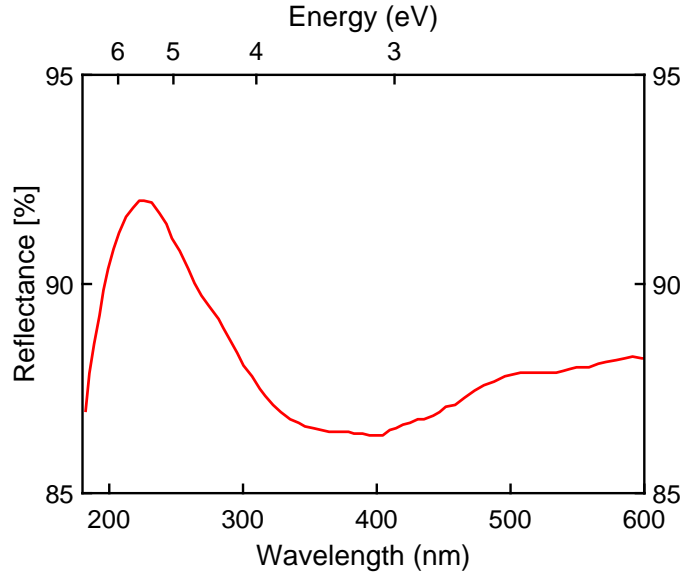


**Figure 2.9: Reflectance of our reference sample:** curve presenting the reflectance spectrum given by our reference mirror for a spectral range between 180 and 600 nm. These data are provided by the producer (Acton optics).

It shows that for the spectral range between 180 and 600 nm, the reflectance of the mirror is constant (of about 87%) all over the spectrum, with the absence of any oscillation, so that the mirror can be used as a good reference in order to normalize our measurements. The reflected signal from the mirror surface was measured for each set of data, at the beginning and at the end of the acquisition of the spectrum of the h-BN sample.

In order to validate the reflectance measured by our setup, we used a graphite sample. We measured the intensity of the reflected beam by the graphite surface  $I_r(\lambda)$  (presented in figure 2.10 (a)), then the intensity of the reflected beam by the mirror  $I_{ref}(\lambda)$  (presented in figure 2.10 (b)). The normalization between the intensity of the reflected signal from the sample surface and the intensity of the reflected signal from the surface of the reference mirror,  $\frac{I_r \times R_{ref}}{I_{ref}}$  is plotted in figure 2.10 (c) with blue solid line. The reflectance of graphite shows a smooth variation between 4.5 and 7 eV with a maximum of about 35% at around 5.2 eV. We compared our data with the calculated reflectance of graphite (dotted red line). The calculated spectrum is evaluated from the optical constants of graphite published in Ref [66].

The comparison between the two curves shows an overall agreement between the variation of

our spectrum and the maximal reflectance of graphite in the literature. The relative deviation of the reflectance varies between 14% and 30% for the spectral range between 5.2 and 6.7 eV. For energies lower than 5.2 eV and higher than 6.7 eV, the deviation is more than 50% and we do not have any explanation for this except the possible influence of the graphite fabrication conditions, our graphite being HOPG (*Highly Oriented Pyrolytic Graphite*).

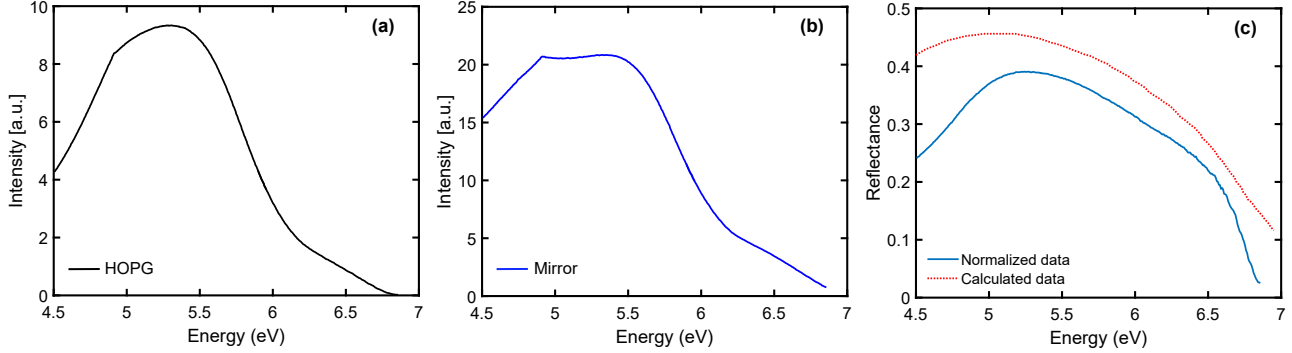


**Figure 2.10: Normalization of our reflectance spectra** (a) Intensity of the reflected signal from the surface of a HOPG sample as a function of energy; (b) intensity of the reflected signal from the surface of reference mirror as a function of energy; (c) Normalization of  $\frac{I_r(\lambda) \times R_{ref}(\lambda)}{I_{ref}(\lambda)}$  in solid blue line compared with the calculated reflectance of graphite (dotted red line).

## 2.1.2 Photoluminescence spectroscopy

### Principle of photoluminescence

PL spectroscopy is a non-contact method, that probes directly the opto-electronic properties of materials. It occurs when photons induce the emission of other photons from a medium. When a light beam excites a medium, photons are absorbed by the matter, generate carriers that recombine, a process called PL. The photo-generated carriers remain in their excited state for a short time ( $\sim 10^{-12}$ s), before relaxing to lower states by non-radiative processes. When the carriers return to their equilibrium states, the excess energy is released and a radiative process occurs which causes the emission of a photon.

In the case of a semiconductor, the radiative recombination process usually occurs between the states located in the conduction and valence bands extrema and the energy of the emitted photon depends on the band gap energy of the material. However, radiative transitions may also involve energy levels located inside the band gap. The latter are due to the presence of localized defects or impurities in the semiconductor.

The principle of PL is summarized in figure 2.11 below.

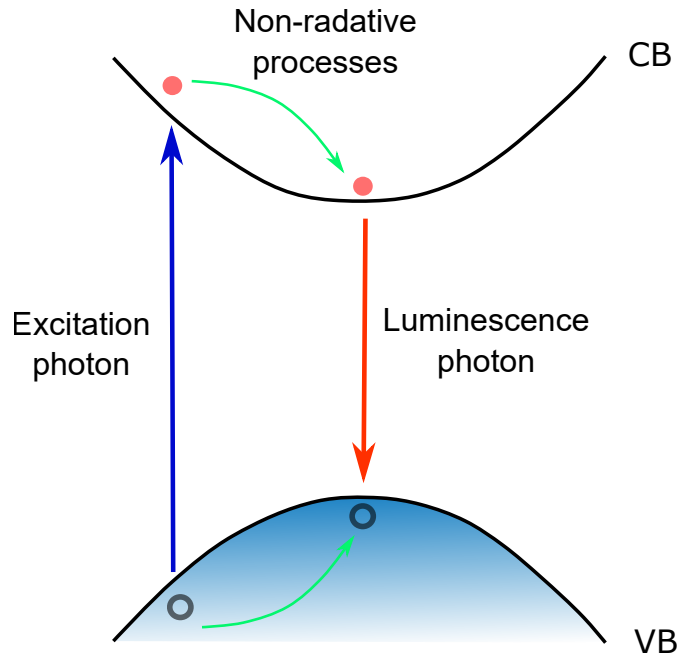


Figure 2.11: Principle of photoluminescence spectroscopy for semiconductors.

### Experimental Setup

**A brief history about our PL setup:** Our PL setup was firstly built in 1994 in order to perform time-resolved photo-luminescence spectroscopy for materials with high energy gap like nitrides (GaN) and oxides (ZnO) using the third-harmonic of a Ti-Sa oscillator (260-270 nm). Later our engineer P. Valvin has upgraded this setup and in 2012-2013 a fourth-harmonic generator was installed in order to perform PL spectroscopy for wavelengths around 195 nm and a cryostat to realize temperature-dependent measurements. In 2014-2015 our group started to study the optical properties of h-BN [45, 63, 60].

During my PhD, we only changed the configuration of the collecting system using new reflective mirrors (parabolic and spherical) with  $MgF_2$  coating for the DUV. The actual configuration of the PL setup is described in the following section.

**Description of the setup:** The experimental setup for our PL spectroscopy is displayed in figure 2.12. The excitation beam is provided by the fourth harmonic of a cw mode-locked Ti:Sa oscillator with a repetition of 82 MHz. The latter is pumped by a cw pump laser at 532 nm. The fourth harmonic is given by the addition of  $3\omega$  and  $1\omega$ . The wavelength of the excitation pulse varies in the spectral range between 192 nm and 196 nm.

The sample is held on a cold finger of a closed-cycle cryostat for which the temperature can be controlled between 8K and 300K in order to perform temperature-dependent measurements.

## 2.1. EXPERIMENTS

The excitation beam is focused on the sample surface through a lens (L) tilted by a small angle about  $3^\circ$ , in order to avoid the mixing between the reflected beam by the cryostat window and the PL signal. The spot diameter is of the order of  $50 \mu\text{m}$ , with a power of  $30 \mu\text{W}$ .

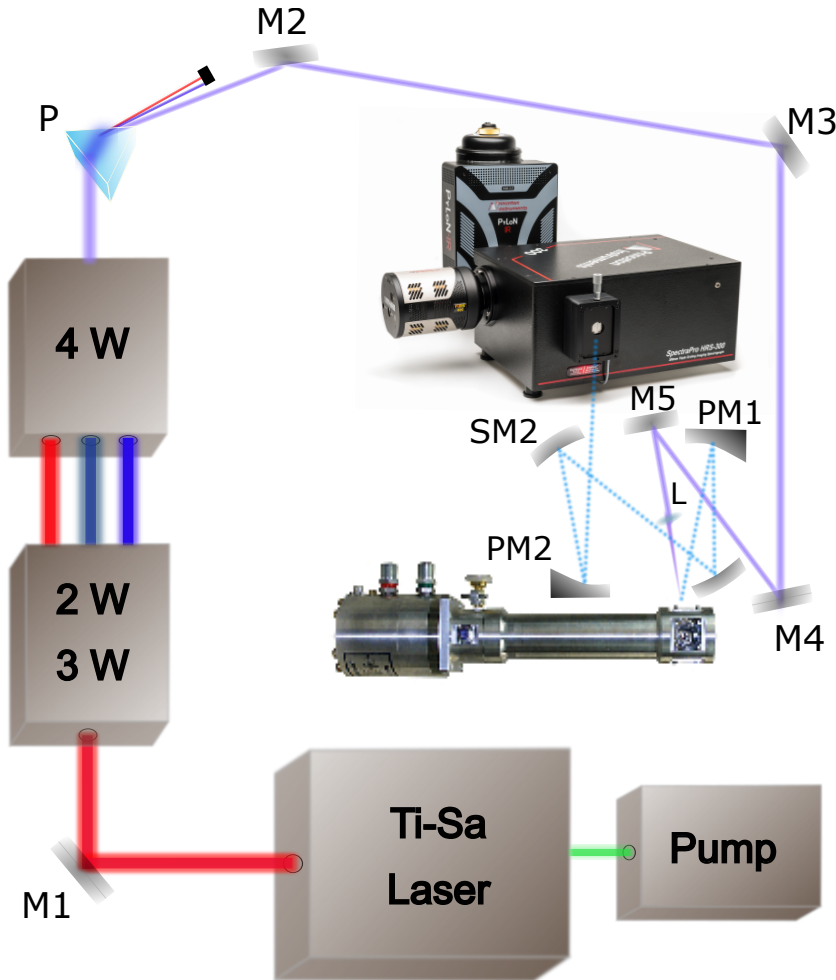


**Figure 2.12: Scheme of our experimental setup used for PL measurements of h-BN samples:** cryostat for temperature-dependent measurements, excitation beam provided by the fourth-harmonic of a Ti-Sa laser with wavelength varying from 192 and 196nm; (PM) = Parabolic mirrors; (SM) = Spherical mirrors; (M) = flat mirrors, (P) = prism and (L) = lens.

An achromatic optical system which is composed of parabolic and spherical mirrors, couples the emitted signal to our detection system. All mirrors are coated with aluminium and protected by  $MgF_2$  film, that gives an anti-reflective film for 180nm. The detection system is composed of a Czerny–Turner monochromator with a focal distance  $f = 300\text{mm}$ , equipped with three diffraction gratings: a 1800 grooves. $\text{mm}^{-1}$  grating blazed at 250nm, a 1200 grooves/mm grating blazed at 250nm, and a 300 grooves/mm grating blazed at 250 nm. We usually used

the 1800 grooves. $mm^{-1}$  grating for all my measurements in order to get the highest possible resolution. The detector is a back-illuminated CCD camera (Andor Newton 920) that gives a quantum efficiency of 50% at 210nm. The camera is operated over different integration times varying between 1 and 5 mins. For measurements with wavelengths higher than 260nm, we use a long-pass filter (266RU Semrock) at the input slit of the spectrometer in order to avoid the second and third orders of diffraction from our PL spectrum. The spectral resolution provided by our system is about 2.5 meV for 200nm.

## 2.2 Samples

During my thesis, I used h-BN samples from two different sources: Nottingham University in the UK and Kansas state University (KSU) in the USA. The samples grown in Nottingham are epitaxial layers having a thickness around one monolayer. These samples were grown using Molecular Beam Epitaxy on graphite substrates. The samples grown in KSU are bulk crystals synthesized using a metal flux method at atmospheric pressure.

In this section we will present the different samples used during this thesis and their growth methods.

### 2.2.1 Samples grown by Molecular Beam Epitaxy

Our h-BN epilayers samples were grown in the group of Prof. Sergei Novikov, at the University of Nottingham in the UK. These samples were grown by the Molecular Beam Epitaxy (MBE) technique at high temperature and using graphite as a substrate.

In the MBE approach, the crystalline growth is performed by the reaction between molecular or atomic beams on a heated substrate. The beams are turned out of heated effusion cells which are spatially separated and thermally isolated. The temperature of each cell controls the intensity of the projected beam. The deposition is assisted layer by layer and the process occurs under ultra-high vacuum (UHV) environment.

In order to grow high quality h-BN samples, the need is to have an environment under high temperature conditions. When using the MBE process, one has to manage very high temperatures at the surface of the substrate, while the intrinsic properties of metals such as high thermal conductivity makes the thermal exchange between the substrate holder and the rest of the metallic growth chamber very high. This fact makes the development of such growth technology very difficult in the high temperature range. Our collaborators in Nottingham managed to solve these difficulties by building a specific and expensive design of MBE system in order to grow h-BN under high temperature conditions.

The system used is a dual-chamber Veeco GENxplor MBE, capable of achieving growth temperatures of up to **1850 °C** under UHV conditions. Their system is equipped by a rotating

substrate holder of 3 inches in diameter in order to get a homogeneous growth on the substrate surface, provided with a high temperature heater. The substrate temperature is provided by a thermo-couple reading. A high-temperature effusion cell provides the evaporation of boron, and a standard Veeco RF plasma source delivers the active nitrogen flux.

### Substrate used

The substrate used to grow thin films by MBE has to be stable at high temperatures ( $\geq 1500^\circ\text{C}$ ), easily available, and of relatively low cost. The best candidates for these conditions are sapphire, templates of AlN on sapphire and silicon carbide (SiC). While graphite is isostructural to h-BN, the choice to use it as a substrate for growing h-BN epilayers provides several potential advantages since the lattice mismatch between h-BN and graphite is very small (1.7%). Our collaborators in Nottingham have shown the possibility to grow high quality epitaxial h-BN using a substrate of highly oriented pyrolytic graphite (HOPG) [67]. The substrates are highly ordered along the c-axis and display a tilt between the domains of about  $0.4^\circ$ . The surface of the substrates is  $10\times 10\text{mm}^2$ .

Before introduction into the MBE growth chamber, the substrates are exfoliated using an adhesive tape to obtain a fresh surface before the growth. Then they are cleaned in toluene overnight to remove any remaining residue, and finally thermally cleaned at  $200^\circ\text{C}$  in a flow of Ar:H<sub>2</sub> (95:5).

### Quality of h-BN grown by MBE

As mentioned above, in 2017, our collaborators in Nottingham reported the growth of h-BN on HOPG substrates [67].

In their paper, they demonstrated that the h-BN deposited on the growth surface was dependent on the growth temperature  $T_G$  and that the surface coverage was reduced when  $T_G$  was increased higher than  $1390^\circ\text{C}$ . In order to grow h-BN using MBE,  $T_G$  has to be fixed at  $1390^\circ\text{C}$ .

Samples grown within this condition showed the emission of intrinsic phonon-assisted recombination in the PL spectra and attesting the high quality of their epilayers [67]. Moreover, X-ray and angle resolved photo-emission spectroscopy (XPS and ARPES) performed on their samples [68] demonstrated the high quality of their h-BN layers after the observation of the valence band dispersion. They demonstrated also that their h-BN layers grow parallel to the graphite layers, and that the two materials are hold together by Van-der-Waals interactions [68].

## Samples studied during this thesis

The h-BN epilayers were grown using a fixed RF power of 550W and a nitrogen ( $N_2$ ) flow rate of 2 sccm. The h-BN coverage is reproducibly controlled by the growth time, substrate temperature and boron to nitrogen flux ratios. The substrate temperature for all the sample used in this thesis was fixed at 1390°C. The characteristics of the samples studied during this thesis are summarized in the table 2.1 below with the different growth conditions and their thicknesses <sup>9</sup>.

Sample	B cell temperature	Growth time	Coverage thickness
N1	1875°C	3 hrs	$\leq$ monolayer
N2	1888°C	3 hrs	$\geq$ monolayer
N3	1900°C	3 hrs	multilayers
N4	1925°C	3 hrs	multilayers
N5	1950°C	3 hrs	multilayers
N6	1875°C	5 hrs	$\geq$ monolayer

**Table 2.1:** Growth parameters of the h-BN samples grown by Molecular Beam Epitaxy under ultra-high vacuum conditions in Nottingham University and the approximative thickness of each sample.

The MBE-grown layers were studied by atomic force microscopy (AFM) and spectroscopic ellipsometry under ambient conditions. From our side, we have performed PL and reflectance spectroscopy using the experiments detailed in the previous section 2.1 under cryogenic conditions. All the results obtained from these measurements will be detailed in the next chapter 3.

### 2.2.2 Bulk h-BN

#### Growth method

Our bulk h-BN crystals were produced in the group of Prof. J. H. Edgar, at the department of Chemical Engineering, Kansas State University, USA. The amalgamation of these samples is obtained from a molten metal solution at atmospheric pressure. This growth method is derived from the paper of Yoichi Kubota *et al.* [13], where they exhibited the feasibility of synthesizing BN at atmospheric pressure. This method allows to grow crystals at temperatures lower than their melting points. h-BN has a melting temperature around 3000 °C, while it can be grown at a temperature of 1500°C when using a Ni-Cr metal flux for example [69]. This is interesting since it permits to grow crystals with lower density of defects due to the lower thermal stress.

<sup>9</sup>More details about the coverage will be given in chapter 3, with the AFM characterization.

The metal flux crystal growth method is based on dissolving the source material in a molten metal or what we call a metalloid flux: the metal is heated to a high temperature in order to dissolve and then kept for an enough time up to the saturation. After that the metal is cooled down. This cooling process decreases the solubility and permits to produce the precipitation of the desired crystal on the metal surface.

In the case of h-BN crystal growth, boron is highly soluble in Ni and Fe (melting points  $\sim 1455/1538^{\circ}\text{C}$  respectively), with maximum solubilities of 18.5 % and 17 %, respectively, while nitrogen has a good solubility in chromium (melting point  $\sim 1907^{\circ}\text{C}$ ). However, utilizing Fe is of a paramount benefit in reducing the production cost, since it is abundantly obtainable on earth. Regardless, nickel is found in Earth's crust only in tiny amounts, fact that classifies it among expensive materials for synthesizing h-BN.

The crystal growth process consists of placing the metal powders (Ni-Cr or Fe-Cr with a proportion of 50-50wt%) in a hot-pressed BN (HPBN) boat<sup>10</sup> (Figure 2.13), then loading the crucible into an alumina furnace providing two heating zones. The system is placed under nitrogen flux (850 Torr) with a small amount of hydrogen in order to remove any oxides from the source materials. After that, both zones of the furnace are heated at high temperatures (about  $\sim 1600^{\circ}\text{C}$ ) with a rate of  $200^{\circ}\text{C}/\text{h}$ , and then kept at this temperature for a period of 24 hours, in order to melt the metals and dissolve the h-BN from the crucible until saturation and allowing the time for mixing.

After that, two cooling processes can be performed: the first one is a uniform cooling process while the other one is a temperature-gradient process. In the first case, both zones are cooled to the same temperature  $1400^{\circ}\text{C}$  with a rate of  $4^{\circ}\text{C}/\text{h}$  (the cooling rate can be changed). During this process, h-BN crystals precipitate on the metal surface, since the solubility decreases with the temperature. After that the furnace reaches a temperature of  $1400^{\circ}\text{C}$ . The whole system is cooled down to room temperature with a rate of  $200^{\circ}\text{C}/\text{h}$ .

In the second case corresponding to the temperature-gradient process, one zone is cooled to  $1400^{\circ}\text{C}$  with a rate of  $4^{\circ}\text{C}/\text{h}$ , while the other is kept at  $1600^{\circ}\text{C}$  in order to apply the temperature-gradient on the boat placed in between the two heating zones. During this cooling process, the h-BN source dissolves continually in the high temperature zone (maintained at  $1600^{\circ}\text{C}$ ) whereas h-BN crystals precipitate in the other zone during the cooling process (Figure 2.13).

After the temperature of the second zone reaches  $1400^{\circ}\text{C}$ , the whole system is cooled down to room temperature with a rate of  $200^{\circ}\text{C}/\text{h}$  to produce a metal ingot.

---

<sup>10</sup>In this case, the boat serves as the material source for growth. However, another material source can be used: pure BN powder and in this case the boat used is made of alumina

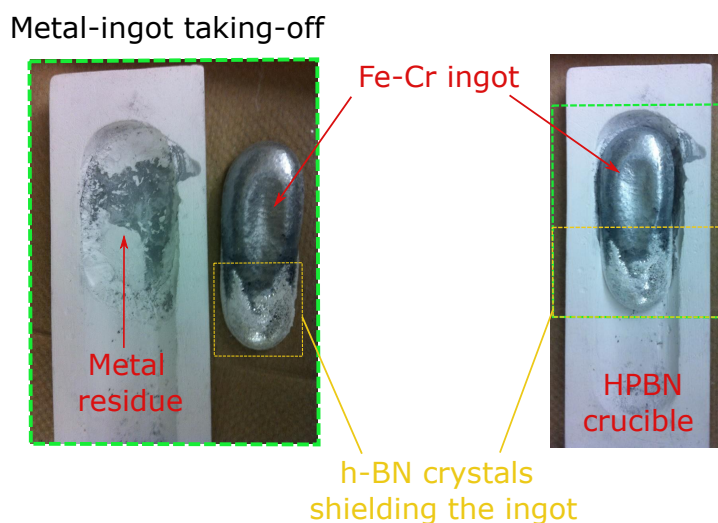


**Figure 2.13: Hot-Pressed BN (HPBN) boat crucible for h-BN crystal growth:** this crucible is used in the metal flux method with a temperature-gradient cooling process (left-side); Metal-ingot taken off from the crucible (right-side); both pictures show the h-BN crystals covering the metal-ingot.

A picture of the ingot produced in the HPBN boat after a temperature-gradient cooling process, is presented in figure 2.13 and it shows the precipitation of h-BN crystals on one side of the ingot corresponding to the cooler zone, while on the high temperature side, we don't see precipitation of h-BN crystals.

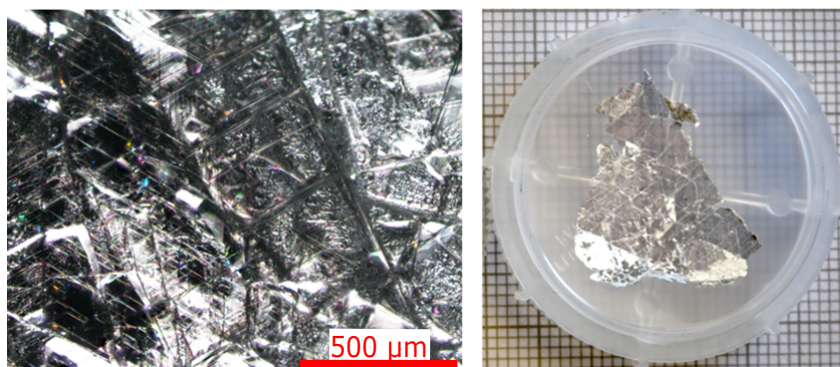


**Figure 2.14: h-BN bulk crystals grown by metal flux method:** on the left side is an image taken by an optical microscope; on the right side is a macro image of the peeled h-BN flake with a size of about 3 cm placed in the wafer carrier.

In order to remove the crystals from the metal surface, our collaborators in KSU use a heated release tape (130 °C) in order to peel-off the crystals from the ingot surface. Large crystal domains (about  $\sim 3$ cm) are obtained with their growth method with a single crystal size about  $\sim 3$ mm (Figure 2.14) [17, 16]. Their samples are of high-crystalline quality presenting narrow linewidths of Raman modes ( $\sim 7.8$  cm<sup>-1</sup>) [69, 70].

### Studied samples

The h-BN crystals that I studied during my thesis and for which the data are presented in the appendix A of this manuscript are resumed in the following table 2.2.

Sample	BN source material	Solvents	Cooling rate	Cooling process
K1	HPBN	Fe-Cr	4°C/h	uniform
K2	pure BN powder	Fe-Cr	1°C/h	uniform

**Table 2.2:** Growth parameters of the h-BN samples grown from a metal molten solution under high temperature and atmospheric pressure conditions in Kansas State University.

## 2.3 Conclusion

In this chapter we presented the experimental aspects on which the results of this thesis are based and the growth methods used to produce the h-BN samples we studied.

We presented the experimental setups used during this thesis in order to perform optical spectroscopy on h-BN samples in DUV. We firstly detailed the reflectance setup that was built during my PhD, in addition to the difficulties related to the spectral range in which we work and that we faced when building our setup. The built reflectance setup can perform experiments for energies up to 7 eV after the elimination of oxygen by purging nitrogen gas in the experimental environment. The absorption of oxygen is inconvenient in this spectral range, since the reflectance spectra measured in an oxygen environment are noisy and could hide important information about the optical properties of the material in study. We detailed the optical aberrations that exist in our setup as well and their effect on our operating system. In order to normalize our reflectance measurements we used a reflective mirror coated with a MgF<sub>2</sub> film and that gives a flat spectrum in the DUV spectral range. The spectral resolution provided by our reflectance setup is about 10 meV.

The PL setup for the DUV range was built a few years before my PhD. The laser is provided by the fourth harmonic of a Ti-Sapphire laser, allowing measurements for wavelengths up to 192 nm. The system provides a spectral resolution of about 2.5 meV.

Both experiments are complementary when studying the optical properties of solids since reflectance probes the dielectric function comprising all the optical transitions in solids while PL probes the recombination processes.

In the second part of this chapter, we have exposed the different growth techniques used by our collaborators for the growth of the h-BN samples we studied. The first method used by our collaborators in Nottingham University is Molecular Beam Epitaxy realized under very

high temperature. For this method h-BN monolayers are produced. The second method is the metal-flux technique, used by our collaborators in the KSU in order to grow bulk h-BN crystals. Within this growth method, large domain crystals were obtained ( $\sim 3$  cm) with a single crystal-size (about 3 mm).



---

# MONOLAYER BORON NITRIDE

## 3.1 Direct band gap in monolayer boron nitride

### 3.1.1 Modification of the band gap nature in 2D materials

The exfoliation of graphene by Novoselov and Geim in 2004 [1] and the discovery of its remarkable electronic properties have opened up a new avenue of research with a new type of materials having a potential for revolutionizing electronics. The band structure of graphene and its zero-gap at the K point of the first Brillouin zone lead to unique physical and electronic properties [71, 72]. In parallel to graphene, two-dimensional (2D) transition metal dichalcogenides (TMDs) have been discovered as a new class of semiconductors, for atomically thin electronics and opto-electronics, with a finite energy gap and they have emerged as new optically active materials for developing novel 2D light emitters [73, 74]. Of particular interest are exfoliated ultrathin monolayers from TMD crystals, which have demonstrated a change in the band gap nature from the bulk crystal to the single monolayer [2, 3]. Most of them demonstrated a cross-over from an indirect to a direct band gap in the monolayer limit [75, 76].

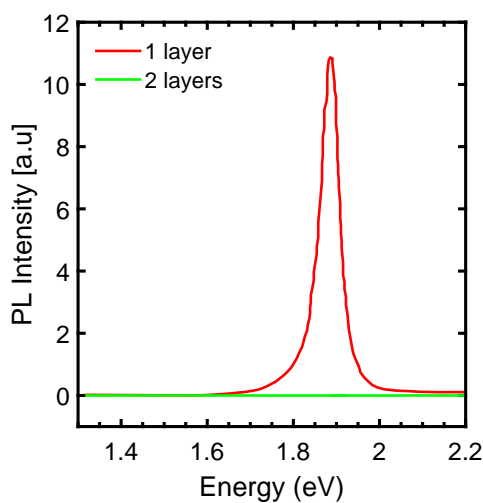


**Figure 3.1: Direct band gap in monolayer MoS<sub>2</sub>:** PL spectra for mono- and bi-layer MoS<sub>2</sub> samples in the photon energy range from 1.3 to 2.2 eV. These data are taken from Ref.[2] and they were measured at room temperature for an excitation energy at 2.33 eV.

The most known among TMDs is molybdenum disulphide  $\text{MoS}_2$ . Mak *et al.* studied the optical properties of  $\text{MoS}_2$  as a function of the number of layers [2]. The measurement of the PL intensity from suspended mono- and bilayer samples showed that the PL intensities were very different (see figure 3.1). They demonstrated that a transition occurs from an indirect band gap for samples thicker than two layers to a direct gap in the single monolayer [2, 77]. In 2D monochalcogenides, the inverse transition can occur: for example GaSe has a direct band gap in the bulk crystal and an indirect gap in the monolayer case [78, 79, 80].

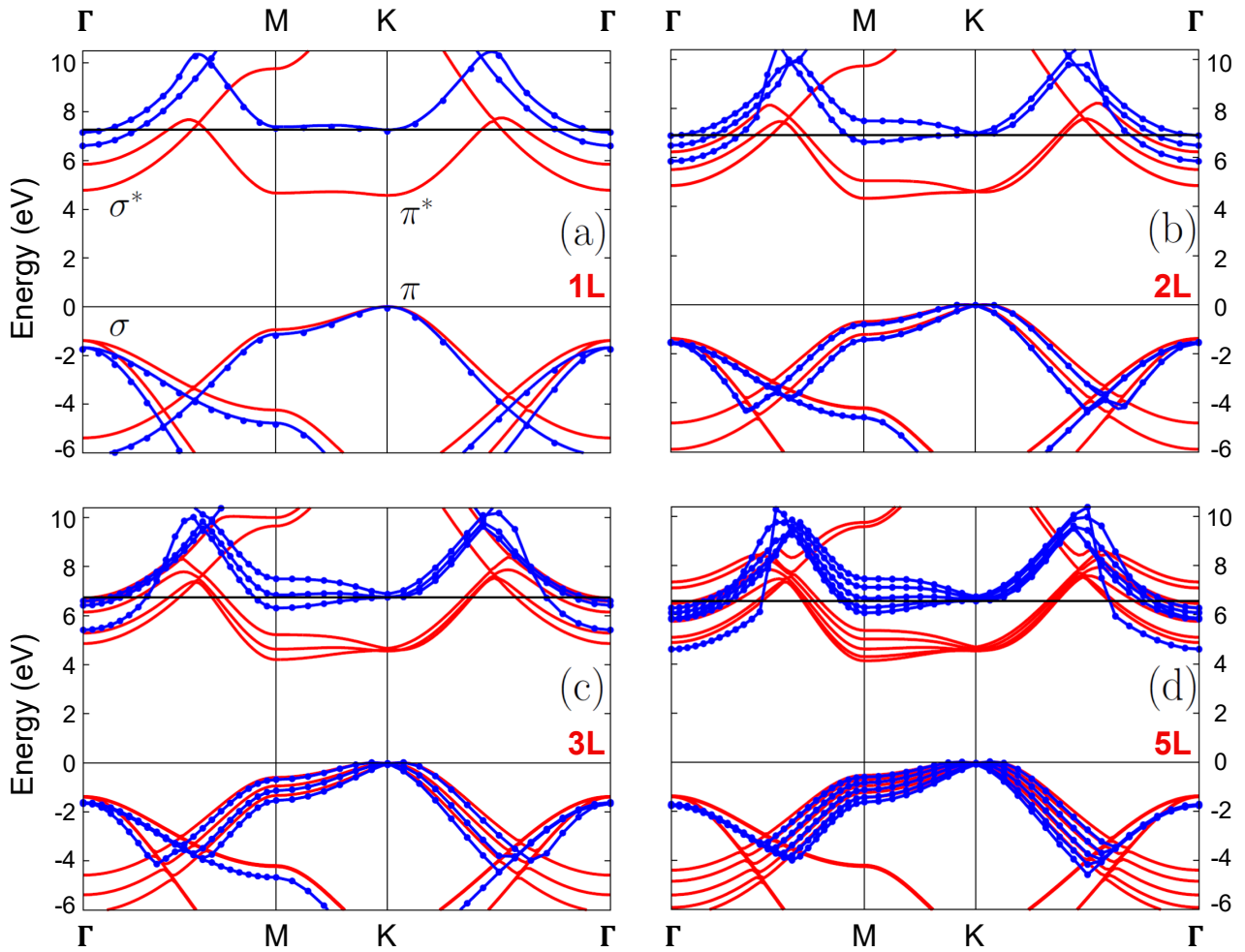


**Figure 3.2:** Calculations showing the variation of the band structure for h-BN as a function of the number of layers: (a) for monolayer; (b) for bilayer; (c) for trilayer and (d) for pentalayer. The band extrema for monolayer are situated at the K point of the first Brillouin zone (BZ). For the number of layers higher than 2, the band extrema are situated along the  $MK$  direction [8].

The current interest in 2D materials and the development of techniques to handle few-layer materials motivated the study of h-BN as a function of the number of layers, as done for graphene, TMDs and monochalcogenides. Similarly to the other 2D materials, the gap nature

of h-BN depends also on the number of layers (see figures 3.2), and the theoretical calculations predict a transition from an indirect gap in bulk h-BN to a direct gap in monolayer BN (mBN) [8]. In 2016, it was experimentally demonstrated that bulk h-BN has an indirect band gap between the M and K points of the first Brillouin zone (BZ) [59]. The opto-electronic properties of bulk h-BN were discussed and detailed in the first chapter of this thesis.

On the other hand, an isolated monolayer of hexagonal boron nitride is predicted theoretically to be a direct-gap semiconductor with a band gap energy around 6 eV [8, 9, 24, 25]. So an indirect–direct transition is expected as in MoS<sub>2</sub> [2] with band extrema situated at the K point of the first BZ (see figure 3.2 (a)). As soon as a second layer is added, the band gap nature of bilayer h-BN becomes indirect between the M and K points (see figure 3.2 (b)), and the recombination process is predicted to occur at roughly the same energies as in bulk h-BN (see figures 3.2 (b), (c) and (d)).

The issue of the indirect-direct band gap transition in h-BN was unresolved at the beginning of this PhD for many reasons:

From one side, the lateral size of exfoliated flakes is around tens of micrometers, which makes the study of exfoliated layers using a macro-PL setup (like the one presented in the second chapter of this thesis) unfeasible. The need is either to use a microscope setup operating at 200 nm, or to study crystals with a larger size.

From the fabrication point of view, the possibility to grow large h-BN crystals with mono-crystal domains larger than 100  $\mu\text{m}$  is technologically very difficult<sup>1</sup> and growers were not able to produce such samples at the beginning of my thesis (large crystals with  $\sim 3$  mm mono-crystals were obtained very recently: see chapter 2, section 2.2.2).

In parallel, the operation of a microscope at 200 nm is very difficult due to the optical aberrations in the system and the dispersion of light which becomes detrimental in this spectral regime. Such a microscope was developed in our team during the thesis of T. Pelini [81, 82] and just a short time ago it came to be operational at 200 nm [83].

From the other side, cathodo-luminescence (CL) has shown that it is not able to resolve the emission spectrum from samples with a thickness lower than 6 monolayers [84]. CL measurements have been done by Schué *et al.* in order to understand the optical properties of h-BN as a function of the number of layers [84]. Their experiments were performed on samples of bulk h-BN and flakes with thicknesses going from 100 down to 6 layers (figure 3.3). Their results showed the presence of the phonon replicas in all the emission spectra. For few h-BN layers, the phonon replicas are at the same energies as in the emission spectrum of bulk h-BN but with different intensities of the PL lines.

These experiments were inconclusive to understand the optical properties of the h-BN

---

<sup>1</sup>The difficulty of growing large h-BN crystals is due to the high melting temperatures of boron and to the low solubility of nitrogen in liquid boron, which leads to a low growth rate and an easy formation of defects.

bulk-mBN system. Much remained to be done and a precise knowledge on the optical properties of mBN was still required at the beginning of my PhD.

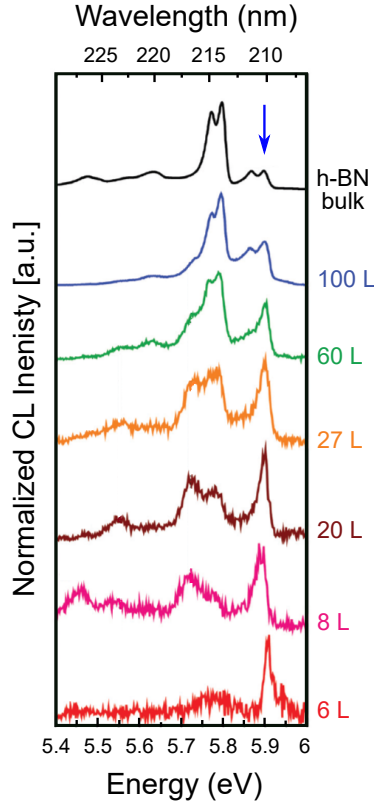


**Figure 3.3: Variation of the emission spectrum of h-BN as a function of the number of layers:** CL spectra measured at 8K from bulk h-BN and flakes of 100, 60, 27, 20, 8 and 6L. The blue vertical arrow shows the position of the LA-TA phonon replicas in the emission spectra of h-BN. These data are taken from Ref. [84].

All the difficulties discussed above had left the question about the emission of mBN unanswered and motivated an original approach within this thesis in order to study this issue. We have used a strategy which is different from the standard methods documented in the literature and used to demonstrate the band gap modification in TMDs and other 2D materials. Here, we take advantage of the progress achieved in growing high-quality h-BN films in Nottingham using the MBE epitaxial method at high temperatures [67]. This strategy relies on the scalable growth of mBN which enables the use of macroscopic PL and reflectance measurements in the DUV to demonstrate a band gap crossover from indirect in bulk h-BN to direct in the monolayer.

### 3.1.2 State of the art for h-BN monolayer

**Growth of h-BN:** The production of atomically thin layers from h-BN crystals by mechanical exfoliation induces chemical contamination, in addition to the reduction of the lateral size of

the exfoliated sheets. The limited size hinders their application in large devices. Additionally, industrial applications require progresses of h-BN growth using epitaxial methods such as CVD or MBE. These growth methods provide controllable thicknesses of the deposited layers and avoid their chemical contamination.

The growth of materials by epitaxial methods requires many processes: firstly, the adsorption of the precursors on the substrate surface; secondly, the decomposition of the precursors and the formation of mobile species on the substrate surface; thirdly, the diffusion of these species and finally the nucleation and the incorporation of these species into the growing layer. These successive processes are mainly affected by the choice of the reactants, the process conditions (temperature, time and reactant flux rates or ambient gas conditions) and the choice of the substrate.

Many efforts have been done in order to grow h-BN by epitaxial methods using substrates such as metals, dielectrics or 2D materials. Considerable advances have been obtained on the fabrication of h-BN by CVD methods since they are less expensive and can be performed at low pressure conditions. The precursors in CVD methods can be gaseous, liquid or solid. Gaseous precursors such as  $\text{BF}_3/\text{NH}_3$ ,  $\text{BCl}_3/\text{NH}_3$ , and  $\text{B}_2\text{H}_6/\text{NH}_3$ , face the problem of their toxicity [85], while liquid and solid precursors are largely used to grow h-BN layers [86, 87, 88, 89, 90]. Usually, to grow h-BN by CVD methods, metal substrates are preferred, with Ni and Cu being the main used substrates.

The growth of mBN on Ni substrate has been achieved since 1995 in Japan using CVD methods [26, 27, 46]. But generally, the grown h-BN films on metal substrates are made of small grains (about tens of micro-meters) with different shapes varying from an equilateral triangle to a hexagonal form [86, 87, 88]. The shape of the h-BN grains depends on the ratio between the B and N fluxes (figure 3.4). It was demonstrated that it takes a triangular form when the edge of the domain is N-terminated. In contrast, it takes either a truncated triangular shape or semi-hexagonal shape when the samples are grown in a B-rich environment [91].

The size of the h-BN grains and the roughness of the deposited film depend on the surface morphology of the substrate. For example, the size of the h-BN layers grown on Cu and Ni surfaces is typically less than  $100 \mu\text{m}$ . In order to get h-BN grains with larger size, it is required to use a substrate with a low nucleation density and a smooth surface.

Many studies reported the effect of the substrate surface on the roughness and the size of the h-BN grown films [92, 93, 94]. Lu *et al.* reported that the use of a Ni-Cu alloy rather than Cu for the substrate plays a crucial role on the grain size indicating that the Ni decreases the nucleation density on the surface of the Cu and permits to obtain a larger domain size for the grown h-BN grains [92].

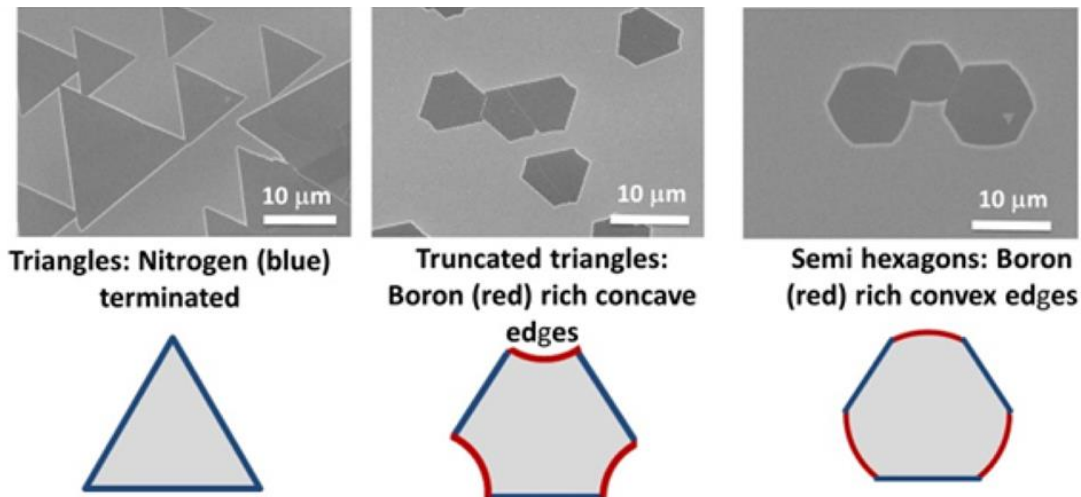


**Figure 3.4: Shape dependence of the h-BN grains on the growth conditions:** first line: SEM images of the h-BN domains grown at 1065°C by CVD method on Cu foils; second line: Sketch of the resulting h-BN crystal shapes and corresponding to N-termination in blue and B-termination in red. Form left to right the N:B ratio was decreased during the growth. These figures are taken from Ref. [91].

In 2018, large h-BN single layers have been produced on a flat surface of molten gold (figure 3.5) [89]. In that work, the grains take circular shapes rather than triangular due to the diffusion of the atoms on a molten metal surface at high temperature (the triangular forms are only observed in the case of solid substrates).

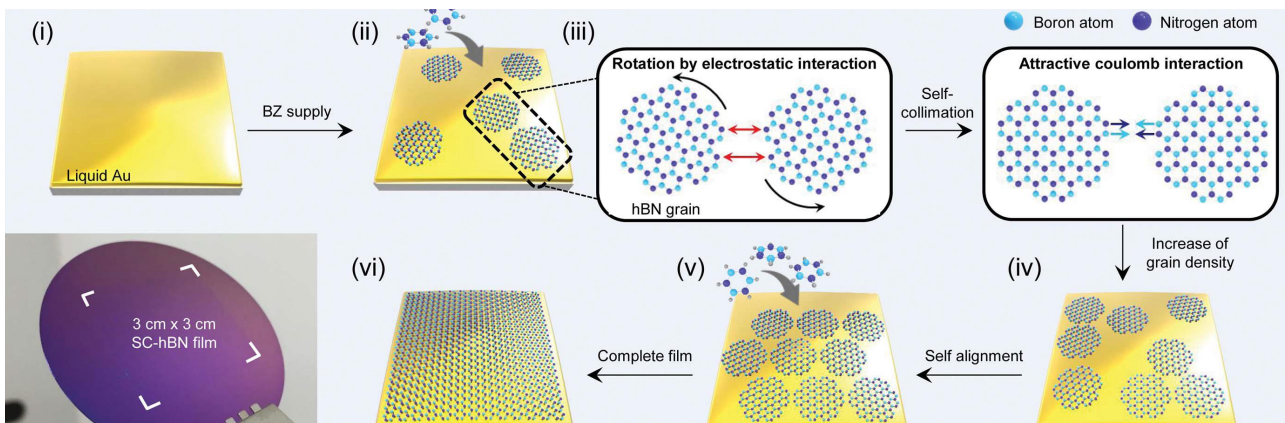


**Figure 3.5: Growth of h-BN single layer on the surface of a molten Au:** Schematic illustration for the growth of h-BN film by means of circular h-BN grains with a rotation invoked by the attractive Coulomb interaction of B and N edges between grains (i to vi). And a photograph of the wafer-scale h-BN film on a SiO<sub>2</sub>-Si wafer. This figure is taken from Ref. [89].

The existence of Coulomb interaction between B and N atoms at the grains edges led to the coalescence of the h-BN domains and resulted in a continuous h-BN layer (see figure 3.5). This process is referred to by the authors as *self-collimation* of the h-BN grains. After a sufficient growth time, the grains transform into a hexagonal structure giving a crystalline h-BN film with a surface about  $3 \times 3 \text{ cm}^2$ . The h-BN films are transferred later onto a  $\text{SiO}_2/\text{Si}$  wafer as indicated in figure 3.5. However, no measurements investigating the optical properties of these samples have been reported yet.

The issue with all these methods allowing the growth of h-BN on metal surfaces is that they require further transfer steps for any practical application. This may induce a damage of the grown layer and a contamination by some residues of the transferred layers. In order to avoid the transfer-induced contamination, it is required to use a substrate different from metals and which permits to use directly the h-BN layer grown on it. Some papers reported the growth of h-BN using Si,  $\text{SiO}_2/\text{Si}$  and quartz as tentative substrates in order to avoid transfer stages [95, 96, 97, 98]. However, most of the studies reporting the growth of h-BN on these substrates have shown a broad peak in the measured Raman spectra (FWHM  $40\text{-}50 \text{ cm}^{-1}$  compared to  $8 \text{ cm}^{-1}$  in high quality crystals) indicating that the crystalline structure of the grown layers is lower.

For devices based on III-N materials, usually sapphire and SiC are used as substrates. Few studies have investigated the growth of h-BN on SiC substrate [99]. Most of the h-BN growth efforts have been done on sapphire as being a dielectric substrate with a less expensive choice for future applications. Moreover, it can be used for growing h-BN by avoiding transfer stages. In order to grow h-BN, sapphire has been largely used in both CVD [100, 101, 102, 103] and MBE methods [104, 67, 86, 105]. The nitridation of  $\text{Al}_2\text{O}_3$  induces the formation of a buffer AlN layer on the surface of the substrate before h-BN starts to grow. The reported Raman measurements on these samples usually indicate the presence of a peak at  $1370 \text{ cm}^{-1}$  with a FWHM varying from  $40$  to  $50 \text{ cm}^{-1}$  (which is broad in comparison with h-BN crystals  $8 \text{ cm}^{-1}$ ), similarly to what is usually reported on Si or  $\text{SiO}_2/\text{Si}$ .

Usually, the luminescence spectra measured from h-BN layers grown on sapphire substrates demonstrate that the emission is dominated by a broad emission band at around  $5.5 \text{ eV}$ , in addition to an emission line coming from the AlN buffer layer at  $6.05 \text{ eV}$  [106, 107]. The emission band at  $5.5 \text{ eV}$  is attributed to the presence of stacking faults in bulk h-BN (Chapter 1 section 1.4), and it indicates that the layers grown on sapphire present an important amount of defects in their crystalline structure, especially the N-vacancy defect [62]. The presence of an important amount of defects in the crystalline structure induces non-radiative recombination processes and may not allow the observation of phonon replicas related to the intrinsic optical properties of h-BN (chapter 1, section 1.4).

Furthermore, the formation of an AlN buffer layer between  $\text{Al}_2\text{O}_3$  and the grown h-BN is not

favorable in the case of growing h-BN as an active layer. AlN is a direct band gap material with an energy about 6.12 eV very close to the energy gap of h-BN. Consequently, the interpretation of the optical properties of h-BN will be complicated by the presence of an AlN buffer layer. The need is to find an alternative substrate to sapphire which permits to grow h-BN without the requirement to transfer steps after the growth and which allows to obtain h-BN films with less defects in their structure.

Besides the efforts done for growing h-BN using metal and dielectric substrates, the group of Prof. Novikov in Nottingham University reported in 2016 the growth of graphene on sapphire substrate and on h-BN flakes using MBE [104]. The reason for growing graphene on h-BN flakes is the small lattice mismatch between the two materials (about 1.7%). In Nottingham, they use MBE at high temperature and under UHV conditions. This technique permits to control the thickness of the grown layers, additionally the UHV environment offered by the MBE and the high purity of sources provide crucial advantages for films grown over large areas. The work reported in the Ref. [104] is based on previous studies indicating that high growth temperatures are needed in order to grow high quality graphene films. The results in Ref. [104] demonstrated that the quality of graphene layers is significantly improved when growing on h-BN layers rather than on sapphire substrates. This publication demonstrated the existence of a *high compatibility* between these 2 materials for epitaxial growth and opened up a new direction for growing 2D materials. It was an important step toward the development of graphene-BN van-der-Waals heterostructures and devices.

Few months later, the group of Prof. Novikov adopted the opposite strategy by using graphite as a substrate for growing h-BN. This approach allows to get rid of any influence of AlN formed by the nitridation of sapphire on the emission spectrum of the grown h-BN layers. They used HOPG (*Highly Oriented Pyrolytic Graphite*) as a substrate, for which the graphite domains are highly ordered along the c-axis with a tilt between the domains about  $0.4^\circ$ .

In order to compare the epitaxy of h-BN on graphite to the one on sapphire, they have grown h-BN simultaneously on sapphire and on HOPG substrates under the same conditions [67] and under high growth temperatures ( $T_G$  between  $1200^\circ\text{C}$  and  $1700^\circ\text{C}$ ).

The morphology of the samples grown on HOPG was completely different from those grown on sapphire (figure 3.6): the h-BN films grown on sapphire are poly-crystalline (figure 3.6 a) while those grown on HOPG present flat mono and multi-layer domains (figure 3.6 b). The PL measurements showed the presence of a large emission band centered at 5.5 eV in the samples grown on sapphire, very similar to what was observed on the h-BN layers grown by CVD methods. Nevertheless, the PL spectra measured in the samples grown on HOPG substrates showed the presence of bright emission at 5.9 eV in addition to a large emission band at 5.5 eV. This emission band is similar to what is usually observed on epitaxial h-BN samples. While the emission at 5.9 eV was never measured before in h-BN epilayers and is characteristic of

intrinsic phonon-assisted recombination in high quality crystals. The presence of these phonon replicas in the PL spectra from h-BN grown on HOPG is a direct proof of the high quality of the epilayers [67].

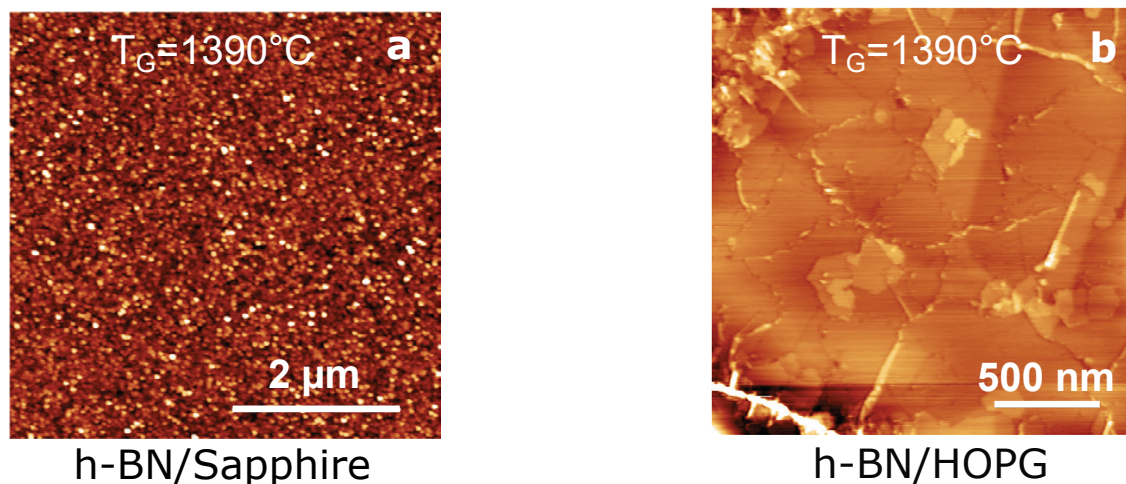


**Figure 3.6: Atomic force microscopy images of h-BN by MBE at high temperature:** (a) AFM image of h-BN grown on sapphire; (b) AFM image of h-BN grown on HOPG. Both samples were grown for 3 h, at  $T_G=1390^\circ\text{C}$  and a boron cell temperature  $T_B=1875^\circ\text{C}$ . These data are taken from Ref.[67].

These results indicated that growing h-BN/HOPG heterostructures could be the solution for studying the optical properties of mBN on a large scale (HOPG surface:  $10 \times 10 \text{ mm}^2$ ) and that could allow the use of our macro-PL and reflectance techniques in order to perform optical spectroscopy.

**Optical experiments performed on mBN:** The electronic and vibrational properties of single mBN layer are not fully explored. In this part we will give a brief summary of the optical experiments that have been performed on mBN. We will start by presenting experiments performed using Raman spectroscopy on mBN and later we will recall absorption measurements done on thin BN layers.

Gorbachev *et al.* [50] were the first to measure vibrational properties of mBN. They performed Raman spectroscopy on mono-, bi- and tri-layers h-BN. The sheets were exfoliated from single h-BN crystals, and then deposited on  $\text{SiO}_2/\text{Si}$  substrate. The measured spectra have been compared to the one measured from a bulk h-BN crystal (see figure 3.7). The data showed the presence of a peak at  $1366 \text{ cm}^{-1}$  (169.36 meV) in the spectrum corresponding to bulk h-BN and which corresponds to the  $E_{2g}^{high}$  Raman-active mode (chapter 1, section 1.3). The comparison between this spectrum and the ones measured from exfoliated layers showed that the intensity of the Raman peak at  $1366 \text{ cm}^{-1}$  decreases progressively with the decrease

of the number of layers. Additionally, the energy of the detected peak blue-shifts with the decrease of the number of layers. For mono-layer, it was detected at  $1370\text{ cm}^{-1}$  ( $169.86\text{ meV}$ ), and the FWHM increased from  $9\text{ cm}^{-1}$  for bulk h-BN to  $12\text{ cm}^{-1}$  for mBN [50].

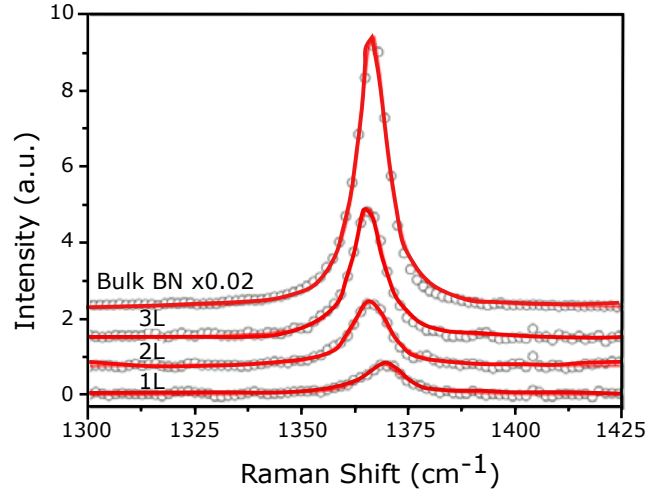


**Figure 3.7: Raman spectra of atomically thin BN:** Dependence of the Raman spectra on the thickness of h-BN exfoliated layers. The layers have been deposited on  $\text{SiO}_2/\text{Si}$  substrate. These data have been measured using a green laser with an excitation wavelength of  $514.5\text{ nm}$ . The data are taken from Ref.[50].

Cai *et al.* reported later another work investigating the phonons of mBN by Raman spectroscopy [51]. They demonstrated that the blue-shift of the Raman peak observed in the case of mBN is not related to the thickness or to the number of layers but rather to the strain caused by the substrate on which the layers are deposited. In that work, they compared Raman spectra measured from layers deposited on  $\text{SiO}_2/\text{Si}$  substrate to spectra measured from suspended mono-, bi- and tri-layers h-BN. The results showed that the spectral position of Raman peak measured from all the suspended layers was the same as the one detected from bulk h-BN crystal. Their results gave an indication of the dependence of the phonon modes on the interaction between mBN and the substrate and which causes some strain on the deposited h-BN layer [51].

The optical properties of h-BN thin films are not very well known. Here, we mention the work reported in 2010 by Song *et al.* and in which they measured the absorption spectrum from h-BN films with a thickness of about  $1.3\text{ nm}$  ( $\sim 3\text{MLs}$ ) [108]. Their films were grown using CVD method on a Cu substrate and then transferred on quartz plates. The absorption spectrum measured from their h-BN films showed a peak at  $\sim 6.1\text{ eV}$  ( $203\text{ nm}$ ). However, this is the only work reporting optical experiments on thin BN layers. In the following pages of this manuscript we will present our optical experiments performed for the first time

on a single mBN layer in order to understand its opto-electronic properties.

## 3.2 Boron nitride monolayer grown by MBE

In chapter 2 we explained that in the MBE approach, the crystalline growth is performed between reactants beams provided by effusion cells and a heated substrate and that the flux of reactants is controlled by the temperature of the effusion cell. The high temperature condition is crucial for growing wide gap semi-conductors and it gives high mobility for the atoms on the growth surface.

In order to grow III-nitride materials by MBE, the group III-elements are typically provided by effusion cells while the active nitrogen flux is provided by either a radio-frequency plasma source or ammonia. The ratio between the two reactants is very important for the quality of III-N materials. For example, the growth of high-quality GaN has to be realized in a III-rich condition, since it allows the migration of Ga atoms all over the growth surface in order to give flat and uniform epilayers [109, 110]. In the case of h-BN, the opposite condition is required, and a N-rich environment has to be present in the growth conditions.

In this section we will discuss how our collaborators in Nottingham control the h-BN coverage by MBE. We will examine the effect of the different parameters that affect the growth of h-BN in order to achieve the scalable growth of a mBN layer on HOPG substrate.

The control of the h-BN coverage and of the thickness of deposited layers is achieved by adjusting the following parameters: the growth temperature  $T_G$ , the temperature of the boron source  $T_B$  and the MBE growth time  $t_g$ . The growth temperature  $T_G$  has to be maintained at 1390°C [67]. The effect of this parameter was discussed in chapter 2, section 2.2.1. In this section, we show the effect of the other two parameters ( $T_B$  and  $t_g$ ) by fixing  $T_G$  at 1390°C. We display variable angle spectroscopic ellipsometry (VASE) measurements and we present Atomic Force Microscopy (AFM) measurements, both performed in Nottingham in order to study the surface morphology and the thicknesses of the grown samples.

We note that AFM and VASE measurements were acquired under ambient conditions. VASE was carried out using a M2000-DI instrument made by J.A. Woollam Inc. The results were obtained over a wavelength range from 192 to 1690 nm [111]. For AFM they use an Asylum Research Cypher-S AFM and Multi75A1-G cantilevers (Budget Sensors, stiffness  $\sim 3\text{N/m}$ , Resonant frequency = 70 kHz). The grown samples were also studied by RHEED <sup>2</sup> [111].

---

<sup>2</sup>Reflection high-energy electron diffraction (RHEED): An electron beam strikes the sample at a small angle relative to the sample surface. Incident electrons diffract from atoms at the surface of the sample, and the diffracted electrons interfere constructively and form regular patterns on the detector. The diffraction pattern at the detector is a function of the sample surface.

### 3.2.1 Control of the coverage by the temperature of the boron source $T_B$

The growth of high quality h-BN samples requires high temperature of the source effusion cells and high growth temperature  $T_G$  in order to give a high mobility of the atoms on the growth surface. For h-BN, the growth is performed for a boron cell temperature  $T_B$  higher than  $1800^\circ\text{C}$ . The increase of the temperature of the boron source  $T_B$  results in the increase of the boron flux and in an increase of the growth rate on the substrate surface.

Five different h-BN samples were grown on HOPG substrates. The growth temperature was  $T_G=1390^\circ\text{C}$ , the growth time was  $t_g=3$  hours and the Nitrogen flow rate was fixed at 2 sccm.  $T_B$  was the only parameter that changes in the growth conditions from one sample to another, with the following values:  $1875^\circ\text{C}$ ,  $1888^\circ\text{C}$ ,  $1900^\circ\text{C}$ ,  $1925^\circ\text{C}$  and  $1950^\circ\text{C}$ .

VASE was used to estimate the thickness of the h-BN deposited on HOPG. The estimated thicknesses are presented in figure 3.8 as a function of  $T_B$ . The results show that the thicknesses of the samples grown for temperatures  $T_B$  between  $1875^\circ\text{C}$  and  $1900^\circ\text{C}$  are less than 1 nm (3 ML) with an uncertainty of  $\pm 0.5$  nm. For the samples grown at  $T_B=1925^\circ\text{C}$  and  $1950^\circ\text{C}$ , the thicknesses are about 3 nm and 32 nm, respectively. This indicates that the thickness of the deposited h-BN increases in an abrupt way for  $T_B \geq 1925^\circ\text{C}$ . In order to achieve the growth of mBN,  $T_B$  should be taken  $\leq 1900^\circ\text{C}$ .

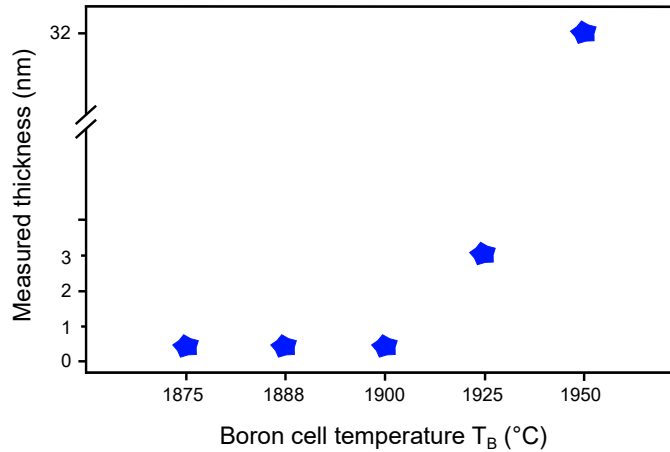


**Figure 3.8: Variation of the h-BN thickness versus  $T_B$ :** the thickness of the grown layers has been estimated by the mean of VASE measurements performed by the group of Prof. Mellor in Nottingham.

The surface morphology of the grown samples was studied using AFM, in Nottingham. The measurements have been done in tapping mode AFM and are presented in figure 3.9 as a function of  $T_B$ . The upper row presents height images, and the bottom one presents the

corresponding phase images. In the height ones, the bright spots correspond to the thickest regions, while the darkest ones correspond to the lowest thickness. In the phase images, it is the reverse case: the bright regions correspond to the thinnest h-BN while the dark ones correspond to thicker h-BN.

Figure 3.9 (a) shows a smooth and rather homogeneous h-BN film deposited on the growth surface with the presence of bright spots along the HOPG step edges corresponding to 3D aggregates. Figure 3.9 (f) corresponds to the phase image of figure 3.9 (a). In this figure one can see the h-BN plates in grey, deposited homogeneously on the surface with some uncovered HOPG regions (bright regions indicated by white arrows).

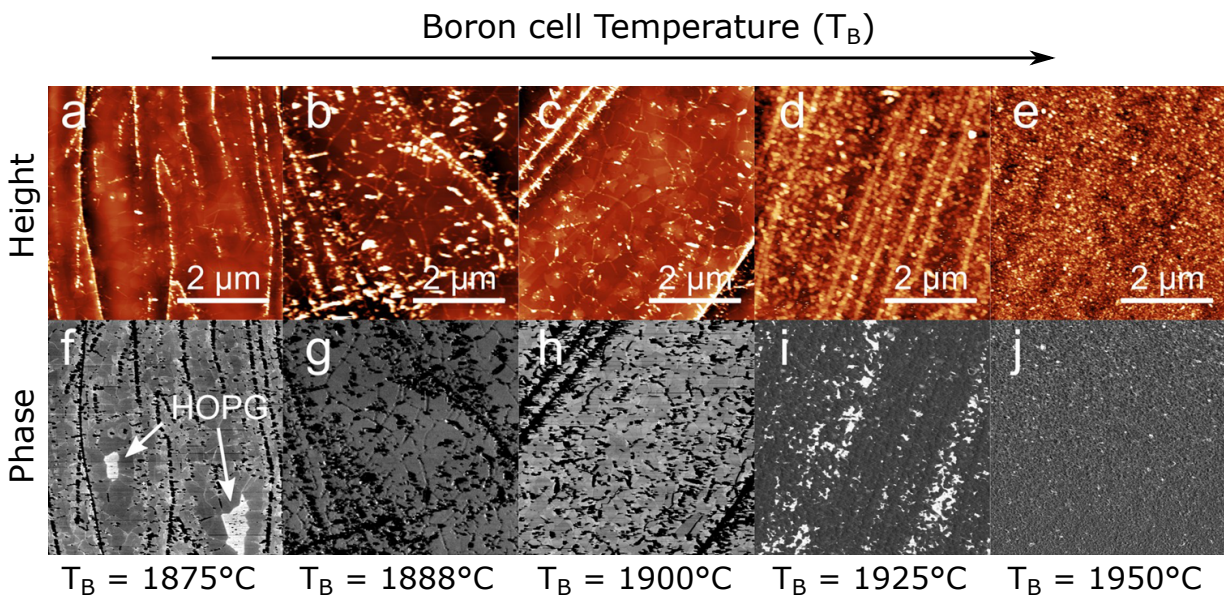


**Figure 3.9: Tapping-mode AFM images measured under ambient conditions on h-BN samples grown by MBE on HOPG substrates for increasing boron cell temperatures:** the boron cell temperature increases from left to right; (a-e) are topographic height-channel images showing the evolution of the surface morphology with the increase of the boron cell temperature; (f-j) phase images corresponding to the height ones shown in (a-e). The white arrows in image (f) indicate the regions of HOPG that remain uncovered during the growth and which present a bright contrast in comparison with the rest of the surface. These samples were labeled in chapter two by N1-N5.

The increase of the boron cell temperature induces a higher boron flux. In figures 3.9 (b and g) we can see that the surface is completely covered by h-BN with no identifiable gaps in the h-BN film (no bright spot corresponding to uncovered HOPG is identified in the phase image (g)). This increase in boron flux is accompanied by a simultaneous increase of the amount of 3D aggregates deposited on the surface (bright and dark spots in figures (b) and (g), respectively). In figure 3.9 (c), we see some hexagonal domains with a brighter color than

the rest of the sample surface, in addition to the high density of 3D aggregates (bright and dark spots respectively in (b) and (g)). We displayed figure 3.9 (c) in a bigger size in order to distinguish the regions with a brighter color (figure 3.10), and that we highlight by white dashed arrows. These regions are attributed to bi-layers that start to form on the growth surface [112].

For temperatures  $\geq 1925^\circ\text{C}$ , the samples are much thicker (figure 3.9) and the surface presents only bright spots (see figures 3.9 d and e) indicating the predominance of 3D clusters. This is shown also in the phase images (figures 3.9 i and j).

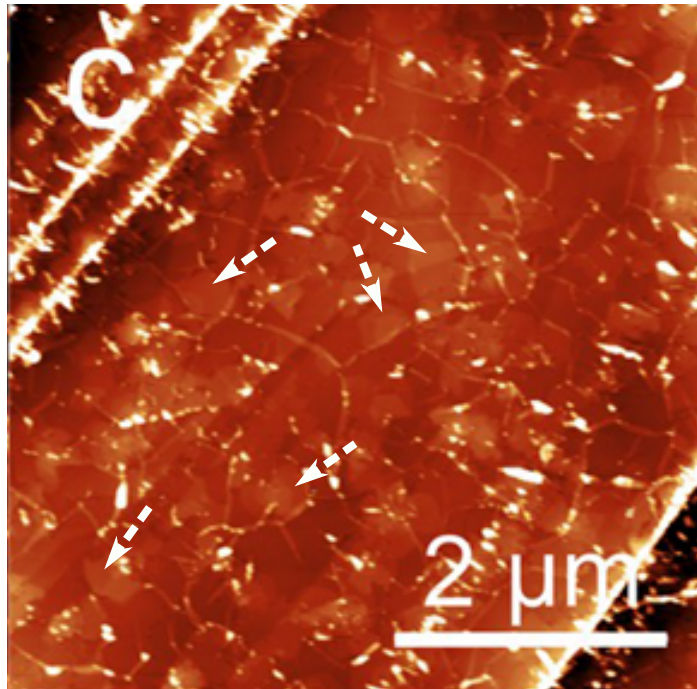


**Figure 3.10:** The same figure presented above corresponding to figure 3.9c, but sketched this time in a bigger size in order to distinguish multi-layer regions: white dashed arrows indicate the regions of bi-layer coverage.

The VASE and AFM measurements for samples grown as a function of  $T_B$  indicate that the formation of 3D clusters is probably caused by the decrease of reactants (N:B) ratio; when increasing the boron flux ( $T_B$ ), the formation of 3D clusters was highly marked. For the lowest (N:B) ratio the morphology of the samples was completely different and the deposited h-BN is polycrystalline (figures 3.9 (d), (e), (i) and (j)).

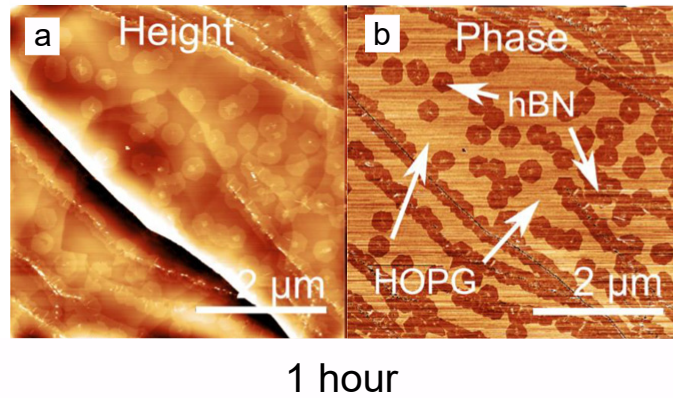
B has a high sticking coefficient, when it arrives to the growth surface it sticks on the nucleation sites. N has a low sticking coefficient, when it arrives to the growth surface it can re-evaporate and leaves the growth surface with an excess of B. The excess of boron on the growth surface is responsible of the formation of 3D clusters. In order to get homogeneous h-BN films and avoid the formation of 3D clusters, the growth has to be performed with low B and high N fluxes. Based on our topographic images, the lowest density of 3D aggregates is observed in

figure 3.9 (a and f) corresponding to  $T_B=1875^\circ\text{C}$ . For this temperature the 3D clusters are only observed along the HOPG step edges, where the nucleation density is the highest and B atoms firstly stick when arriving to the growth surface.

### 3.2.2 Control of the coverage by tuning the growth time $t_g$

Another way to control the MBE growth of h-BN layers is to change the MBE growth time  $t_g$ . In this part, we will show the effect of  $t_g$  on the growth of h-BN. AFM measurements have been performed in Nottingham on samples grown for different growth times:  $t_g$ : 1, 3 and 5 h. All the other growth parameters were fixed as following: growth temperature  $T_G = 1390^\circ\text{C}$ , nitrogen flux : 2 sccm and temperature of the boron source  $T_B = 1875^\circ\text{C}$ . The AFM images are presented in figures 3.11 and 3.12.

AFM images for the sample grown during 1 hour shows h-BN islands formed along the HOPG step edges and on the HOPG plates with an average size of  $\sim 250$  nm [112].



**Figure 3.11:** AFM images of MBE-grown h-BN on HOPG for  $t_g=1$  h: (a) height image; (b) phase image [112].

The AFM measurements corresponding to the samples grown for deposition times of 3 and 5 h are presented in figures 3.12. The upper row presents images for the sample grown for 3 hours, while the bottom row shows AFM images for the sample grown for 5 hours. The first column shows the topographic AFM images for both samples, the second row presents a zoom in regions indicated by white boxes in the first column, and the third one corresponds to the phase-channel images.

The surface of the sample grown for 3 hours shows that the h-BN islands have coalesced and form one monolayer with almost a homogeneous coverage (figures 3.12 a, b and c) except some bright/dark (height/phase-channel) spots along the HOPG step edges. The phase image (c) reveals the presence of small areas of uncoated HOPG (bright region highlighted by a white arrow). This means that after 3 h of growth, the h-BN coverage is still slightly below one ML.

It shows also the appearance of bi- and tri-layer regions near the HOPG step edges (hexagons which appear in a brighter grey in comparison with the rest of the surface). These regions are highlighted by white dashed arrows.

With a further increase of the growth time up to five hours, the h-BN islands achieve a complete coalescence (no identifiable bright regions in the phase image (f) *i.e.* uncoated HOPG), accompanied by an increase of the density of 3D clusters (bright spots in (d) and (e) and dark ones in (f)). In figure (f), we can distinguish the presence of different domains (we highlight them by white lines). They appear bright in figure (e) (we highlight them by black lines), and they correspond to multilayer regions at the edges of the HOPG plates. They are due to the twist between the HOPG plates [112].

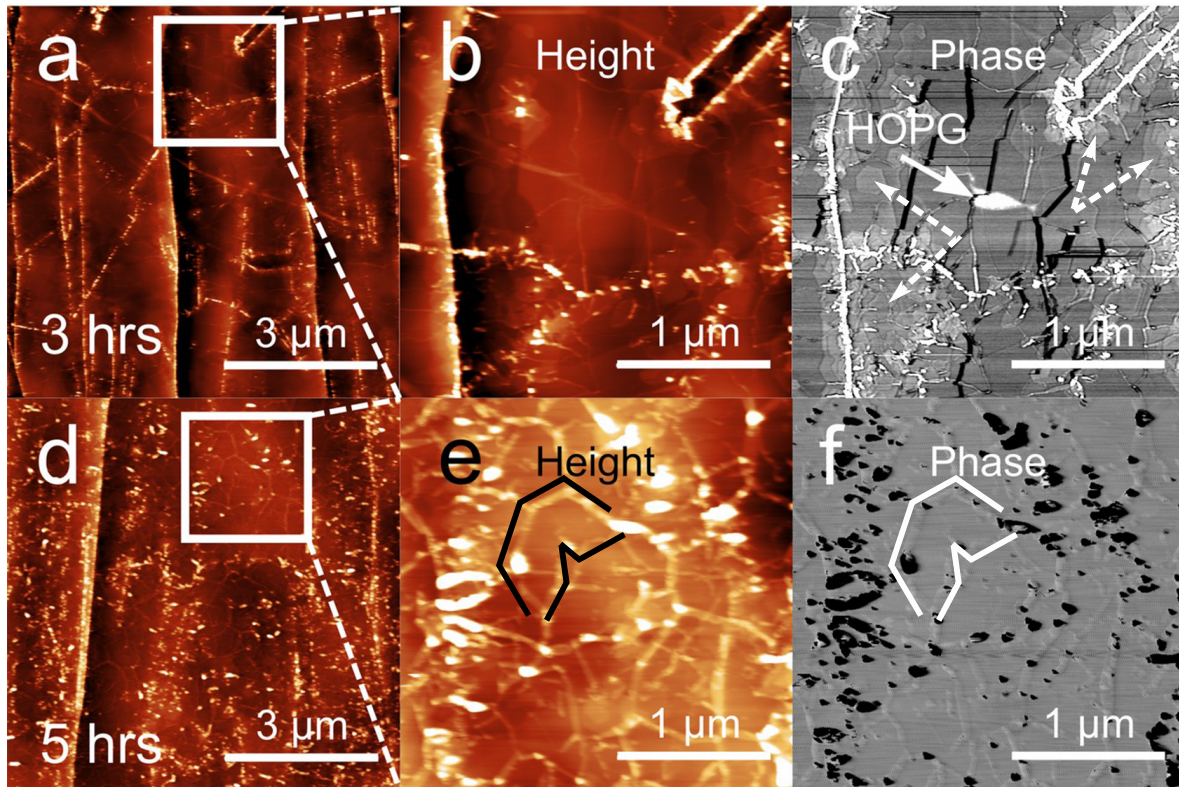


**Figure 3.12: AFM images of MBE-grown h-BN on HOPG for different growth times:** The growth temperature and the boron cell temperature are  $T_g = 1390^\circ\text{C}$  and  $T_B = 1875^\circ\text{C}$ , respectively. (a) Topography image for h-BN growth after 3 hours; (b) zoom of the region indicated by the white box in (a); (c) phase-channel data for image (b), and the white arrow indicates the position of an exposed region of HOPG or uncovered by mBN growth and the white dashed arrows indicate multilayer regions; (d) topography image for h-BN growth after 5 hours; (e) zoom of the region indicated by the white box in (d); (f) phase-channel data for image (e), the black dots correspond to the bright aggregates in the topography images.

The comparison between these AFM images shows for  $t_g$  greater than 3 hours, the surface

morphology of the grown samples becomes dominated by 3D clusters. With a further increase of  $t_g$ , the h-BN film becomes poly-crystalline and the surface morphology becomes comparable to what was observed for samples grown at  $T_B \geq 1925^\circ\text{C}$  in the previous section.

This study shows that the formation of continuous films of given thicknesses (1, 2, 3 MLs) is still not possible by MBE. Once a second layer starts to grow, the density of the 3D clusters increases, and the film becomes by polycrystalline. On the contrary, the fabrication of a single monolayer can be achieved with a moderate  $T_B$  and short growth time  $t_g$ .

### 3.2.3 Growth of mBN by MBE

In the previous sections, we have seen how the growth parameters modify the h-BN coverage and the morphology of the deposited film. For a growth time of 3 hours and a temperature  $T_B$  of  $1875^\circ\text{C}$ , the grown h-BN gives a smooth and rather homogeneous film except few regions covered by 3D clusters that originate from the high nucleation density on the HOPG step edges. Consequently, in order to grow h-BN samples as close as possible to a single monolayer, our collaborators in Nottingham chose the following set of parameters:  $T_G = 1390^\circ\text{C}$ ;  $T_B = 1875^\circ\text{C}$ ;  $t_g = 3$  h and a nitrogen flux = 2 sccm.

Figures 3.13 (a-e) present AFM images for the sample on which we performed macro-PL and reflectance in the DUV in order to study the opto-electronic properties for mBN. The first column shows height images with (d) being the zoom of the region denoted by a white box in (a). The second column presents the phase images corresponding to the ones presented in the first column. Figure (c) presents AFM measurements performed in contact mode at the interface between the mBN grown layer and uncovered HOPG.

The analysis of the phase-channel data performed on our mBN sample indicates that there is an overall coverage of  $\sim 95\%$  of mBN on the surface of our sample. Only about  $\sim 5\%$  are uncovered HOPG. About  $\sim 87\%$  from the covered surface is predominated by mBN and the rest  $\sim 13\%$  are shared between regions of bi- and tri-layers coalesced near the 3D clusters which deposit at the HOPG step edges.

The monolayer height of the grown mBN layer at the interface with the uncovered HOPG surface is shown in figure 3.13 (c). The line profile associated to the region indicated by a white line is presented in figure (f). It indicates a step height of about  $3.5 \text{ \AA}$ . This value is expected for mBN (chapter 1: interlayer distance  $c_0 = 3.3 \text{ \AA}$ ).

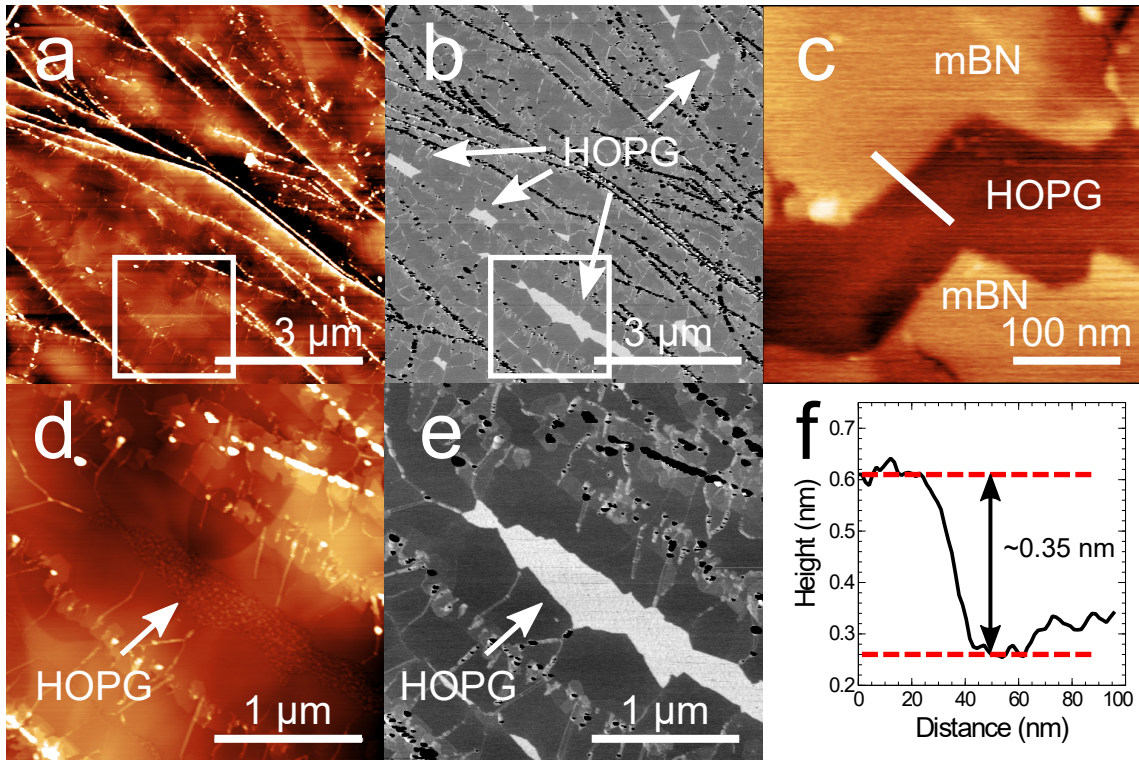


**Figure 3.13: Surface morphology of epitaxial monolayer BN on graphite:** Atomic force microscopy (AFM) of mBN grown on HOPG (boron cell temperature  $T_B = 1875$  °C, growth temperature  $T_g = 1390$  °C and growth time of 3 h); (a) large-area AC-mode AFM topography of mBN growth on HOPG; (b) phase-channel data for image (a) and the white arrows indicate regions of exposed HOPG; (c) small area contact-mode AFM image of the mBN boundary next to an exposed region of HOPG, showing the characteristic monolayer BN step height; (d) zoom of the region indicated by the white box in (a). (e) phase-channel image for image (d) and the zoom of the region indicated by the white box in (b); (f) line-profile along the interface between mBN and exposed HOPG as indicated by the white line in image (c) showing the characteristic monolayer BN step height.

**Conclusion:** In this part we presented how our collaborators in Nottingham control the h-BN growth by MBE. We showed how the growth of h-BN changes with the variation of N:B ratio. In order to get a monolayer coverage and a low density of 3D clusters, the growth has to be formed in low B and high N fluxes. The morphology of the grown h-BN films can be affected also by the increase of the growth time.

We highlighted how the growth of mBN can be achieved on a large scale ( $10 \times 10$  mm<sup>2</sup>) using MBE at high temperature. The growth of this mBN sample enabled us to perform PL and reflectance in the DUV and allowed us to demonstrate the presence of a direct band gap transition in monolayer boron nitride as we will see in the next sections of this chapter.

We summarize in table 3.1 the h-BN samples that we studied in this chapter together with

their estimated thickness.

Sample	Growth temperature	B cell temperature	Growth time	Estimated thickness
N1	1390°C	1875°C	3 hrs	<1 nm
N2	1390°C	1888°C	3 hrs	<1 nm
N3	1390°C	1900°C	3 hrs	<1 nm
N4	1390°C	1925°C	3 hrs	~ 3 nm
N5	1390°C	1950°C	3 hrs	~ 32 nm
N6	1390°C	1875°C	5 hrs	<1 nm

**Table 3.1:** Growth parameters of the h-BN samples grown by Molecular Beam Epitaxy under ultra-high vacuum conditions in Nottingham University and their thickness estimated by VASE.

### 3.3 Experimental results

In this section we present our results on the opto-electronic properties of mBN. First, we display the photo-luminescence spectrum measured from mBN and we show how it compares to the one of bulk h-BN. We exhibit the conditions on the excitation energy of mBN and we explain how the excitation process occurs. We also compare PL measurements from thick samples to the emission of mBN. Second, we present reflectance measurements on mBN samples and we show how these measurements compare to the PL spectra. This allows us to conclude on the direct nature of the optical transition in mBN.

#### 3.3.1 Photo-luminescence spectroscopy

##### PL of monolayer BN

In order to study the optical properties of mBN, we first performed PL measurements using our experimental setup optimized for the DUV, described in chapter 2 (section 2.1.2).

The PL spectrum measured on our mBN sample was recorded at a cryogenic temperature of 8K and for an excitation energy of 6.37 eV (194.47 nm) and it is plotted in figure 3.14 (blue solid line). We compare this PL spectrum to the signal recorded from the surface of HOPG, on the back-side of one of our samples, where no BN was deposited.

The signal recorded from the HOPG surface corresponds to the diffusion of the laser (centered at 6.37 eV). The PL spectrum of mBN on HOPG exhibits a broadband emission centered at 5.55 eV and two sharp lines at 6.05 eV and 6.08 eV, superimposed on the signal coming from the laser diffusion. We observe also that the emission in mBN for energies higher than 5.8 eV is not limited to this doublet. We can distinguish the presence of a weak emission peak at 5.98

eV and a broad band of width  $\sim 90$  meV, centered at 5.9 eV. On the high-energy side of the doublet we detect the presence of weak emission lines at 6.16 eV.

The broadband emission at 5.55 eV is attributed to defects in h-BN epilayers [100, 67] because it overlaps with the emission of the stacking faults identified in bulk crystals (chapter 1, section 1.4), while the emission of the doublet at 6.05 eV and 6.08 eV is a totally new feature as detailed below.

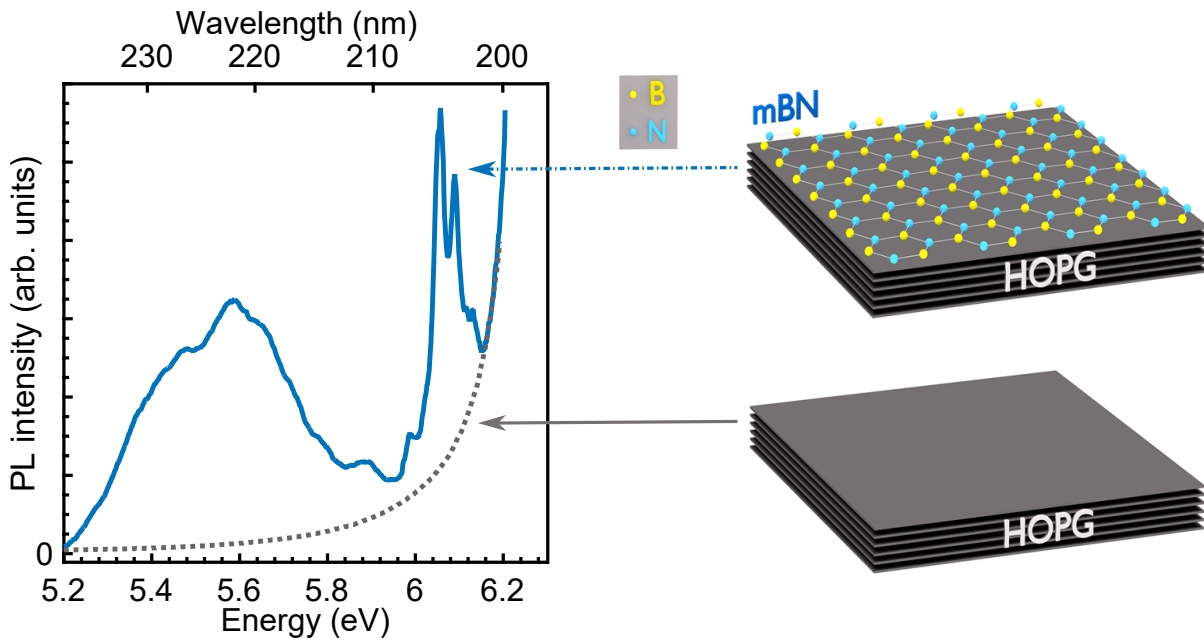


**Figure 3.14: Photoluminescence of epitaxial monolayer BN on graphite:** left-side: in blue solid line is the PL spectrum recorded from mBN; in dotted grey line is the signal recorded from HOPG; both spectra are recorded at 8K, with a laser excitation of 6.375 eV (194.47 nm); right side: schematics of the mBN-graphite heterostructure synthesized by van-der-Waals epitaxy, and HOPG substrate. HOPG stands for highly oriented pyrolytic graphite.

**How does the emission of bulk h-BN compare to the one of mBN?** In order to understand the origin of the emission lines in the PL spectrum measured from the mBN sample, we begin by comparing the emission of mBN to the one of a bulk h-BN crystal. In figure 3.15 we plot in a linear scale the PL spectrum of mBN (blue solid line) in comparison with the normalized PL spectrum recorded from a h-BN bulk crystal bought from HQ-graphene company (red dashed line). Both spectra are measured at a cryogenic temperature of 8K. We use one-photon excitation for mBN at an energy of 6.37 eV and two-photon excitation for bulk h-BN at an energy of 3.03 eV. We indicate the position of the band gap in bulk h-BN by a black vertical arrow located at 5.95 eV.

As discussed previously, bulk h-BN is an indirect band-gap semiconductor with the fundamental

indirect exciton at 5.95 eV. Consequently, the PL emission is red-shifted with respect to this energy and the phonon replicas corresponding to the optical transitions appear at energies lower than 5.95 eV. The PL spectrum shows emission lines at the energies of 5.87 eV and 5.76 eV corresponding to the LA/TA and LO/TO phonon replicas in addition to emission lines at lower energies coming from the emission of defects in h-BN. No PL emission is detected at energies higher than the fundamental gap.

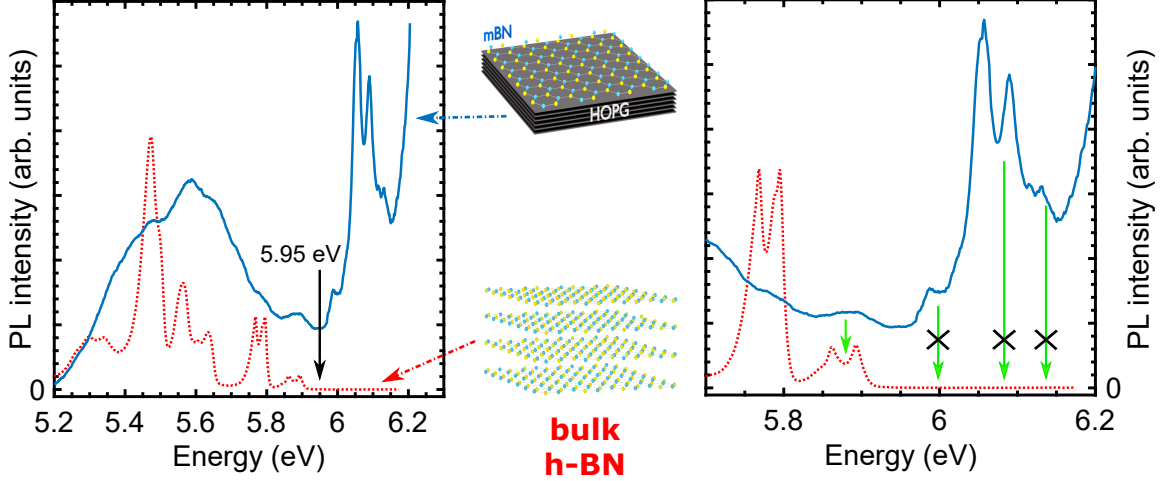


**Figure 3.15: Photoluminescence of epitaxial monolayer BN on graphite:** (left-side) in the blue solid line is the PL spectrum recorded from mBN; in the red dashed line is the normalized PL spectrum in bulk h-BN at 8 K. It is plotted for comparison and the energy of the indirect gap of bulk h-BN is presented by a vertical arrow at 5.95 eV; both spectra are recorded at 8K, the laser excitation for the mBN sample is 6.375 eV (194.47 nm) while for bulk h-BN we use two-photon excitation at 3.03 eV; (right-side) zoom of (left-side) in the spectral region between 5.7 eV and 6.2 eV. Schematics of the mBN-graphite heterostructure synthesized by van-der-Waals epitaxy and the crystalline structure of h-BN bulk crystal are displayed between (left) and (right) plots.

In figure 3.15 (left-side), we compare the emission spectrum of bulk h-BN with the one detected from our mBN sample. The comparison shows that the broad band emission centered at 5.5 eV in the case of mBN overlaps with the emission of the stacking faults in the case of bulk h-BN. In agreement with what was mentioned previously, the emission band at 5.5 eV is attributed to defects in h-BN. In figure 3.15 (right-side), we plotted the same data but in a smaller spectral region (between 5.7 and 6.2 eV). We highlighted the emission lines from mBN by green arrows for the comparison with bulk h-BN. It shows that the emission band at 5.9 eV in the PL spectrum of mBN overlaps with the LA/TA phonon replicas detected from bulk h-BN. Nevertheless, all the other emission lines detected from the mBN sample at energies higher than 5.95 eV do not overlap with any emission of bulk h-BN. We interpret the detection of the emission at 5.9 eV as originating from the multi-layer h-BN regions that coalesce near the step edges of HOPG. At 5.76 eV, we also observe a small modulation in the PL spectrum

of mBN, which overlaps with the LO/TO phonon replicas for bulk h-BN.

The comparison of the spectra in figures 3.15 shows that there is no possible overlap between the phonon replicas in bulk h-BN and the doublet at 6.05 and 6.08 eV in mBN. This comparison rules out any misinterpretation of the doublet as being due to carrier recombination in the indirect-gap of bulk h-BN and it indicates that the emission of these lines is a new feature specific to the emission of mBN.

**Selective excitation:** In order to detect the PL doublet that we presented previously, a selective excitation is necessary in mBN. We present below PL spectra for different excitation energies and we show that a selective optical pumping is mandatory to detect the emission of mBN.

In figure 3.16 (a), we display the PL spectra between 6 eV and 6.16 eV, for 4 different excitation energies. These spectra are measured at a cryogenic temperature of 8K and excitation energies of (i) 6.4 eV, (ii) 6.39 eV, (iii) 6.375 eV and (iv) 6.345 eV. We plot them after the subtraction of the stray light coming from the laser diffusion. They are plotted in a linear scale and are vertically shifted for clarity. We observe a strong modification in the intensity of the PL doublet when changing the excitation energy. Particularly, for  $E_{ex}=6.345$  eV (orange line (iv)) there is barely any emission of the PL doublet, while for the three other excitation energies the PL lines are detected with a strong intensity. We note that for excitation energies less than 6.345 eV no emission line can be detected around 6.1 eV. Moreover, the comparison of the four spectra in figure 3.16 (a) shows that for  $E_{ex}=6.4$  eV (magenta line (i)), a strong modification in the intensity of the two lines in the doublet occurs in comparison to the other spectra. This modification inverses the intensity ratio between the two lines. We point out the existence of a supplementary component for which the energy varies linearly with the variation of the excitation energy. This component is situated at about  $\sim 318$  meV below the energy of the laser, and it is indicated by vertical arrows in figure 3.16 (a) for each spectrum.

The measurements plotted in figure 3.16 (a) reveal two important facts. Firstly, in order to detect the PL doublet, a selective excitation is required: for the 4 spectra shown here, we observe that an efficient excitation pathway exists for  $E_{ex}$  between 6.375 eV to 6.4 eV *i.e*  $\sim 318$  meV above the emission doublet. Secondly, there is an additional component that modifies the form and the intensity of the PL spectrum, suggesting a Raman-related process.

Let us compare the PLE(*Photoluminescence Excitation*)<sup>3</sup> spectra in bulk h-BN and in mBN. In figure 3.16 (b) we plot the PL intensity as a function of the excitation energy for bulk h-BN in red dotted line monitored at an emission energy of 5.78 eV. The black solid line indicates the spectral position of the fundamental gap at 5.95 eV for bulk h-BN. These data are taken

---

<sup>3</sup>In this spectroscopy method, the energy/wavelength of the excitation light is varied and the luminescence is monitored at a typical emission energy/wavelength of the material studied.

from Ref.[113] and have been recorded using a mono-chromatized UV synchrotron-radiation excitation in vacuum and at a cryogenic temperature of 10K. We compare the normalized PLE data of bulk h-BN to the ones extracted from figure 3.16 (a) corresponding to mBN. The PL intensities corresponding to mBN are extracted at the energy 6.07 eV *i.e.* at the minimum situated between the PL lines of the doublet.

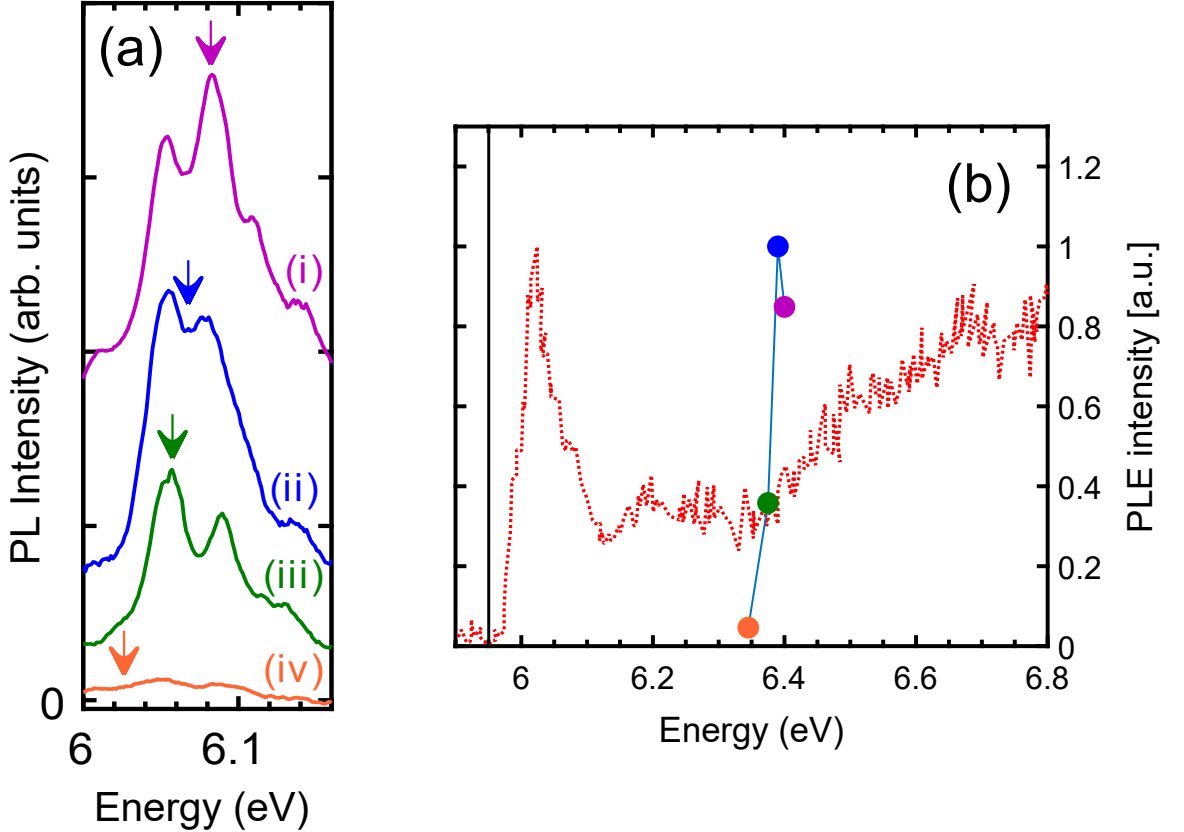


**Figure 3.16: Emission of mBN:** (a) emission of mBN (after subtraction of laser stray light) for different values of the excitation energies  $E_{ex}$ : (i) 6.4, (ii) 6.39, (iii) 6.375, and (iv) 6.345 eV from top to bottom (the three top spectra are shifted vertically for clarity); the vertical arrows indicate the Raman-shifted energy  $E_{ex} - 2\Delta$ , with  $\Delta = 159$  meV, corresponding to the energy of the LA(M) phonon in mBN. The vertical arrows point at: (i) 6.088, (ii) 6.078, (ii) 6.063, and (iv) 6.033 eV; (b) in red dotted line PL signal intensity as a function of the excitation energy for bulk h-BN from Ref. [113], compared to the PLE measured from our mBN sample. The black solid line shows the spectral position of the fundamental band gap of bulk h-BN at 5.95 eV.

The PLE spectrum of bulk h-BN displays a peak at 6.02 eV, followed by a lower plateau and then a continuous increase above 6.4 eV. The PLE spectrum in bulk h-BN shows that an intense PL signal can be detected for any excitation energy higher than 6 eV. In particular, the PLE for the bulk shows that for an energy of 6.3-6.4 eV, an intense PL can be recorded

in bulk h-BN, while in the case of mBN, the PL intensity is very sensitive to the excitation energy (orange point in figure 3.16 (b)). The comparison between the two PLE spectra shows that for mBN, an efficient excitation is limited to a narrow spectral range: it is forbidden for energies lower than 6.345 eV and it is maximal for 6.375 eV.

Our data show that h-BN bulk and mBN systems are distinct systems because their PL and their PLE spectra are strongly different.

**Resonant Raman Scattering (RRS):** In the previous paragraph, we highlighted the distortion of the emission spectrum when varying the excitation energy  $E_{ex}$ . In particular, for  $E_{ex} = 6.4$  eV, the intensity ratio between the two lines at 6.05 eV and 6.08 eV reverses. An efficient pathway is present when the excitation energy is situated at  $\sim 318$  meV above the PL doublet. This energy matches perfectly to the energy of two LA phonons at the M point of the first BZ in mBN (the phonon band structure has been presented in chapter 1, section 1.3.1 it shows that the LA(M) phonon has an energy of about  $\sim 150$  meV [47, 48]). It suggests the presence of a resonant raman scattering (RRS) process that occurs after the emission of 2 LA(M) phonons and which overlaps with the PL emission.

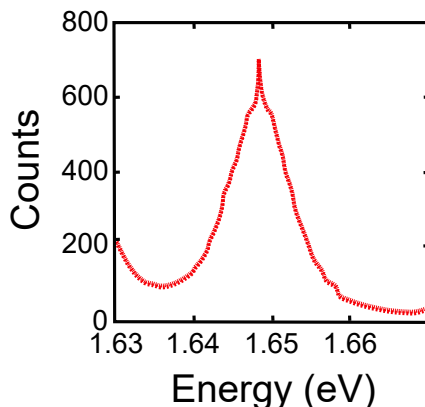


**Figure 3.17: PL spectrum for MoSe<sub>2</sub>:** showing a narrow Raman line superimposed on the broader emission that corresponds to the X<sup>0</sup> exciton in MoSe<sub>2</sub> [114].

The contribution of RRS was first observed by Chow *et al.* when performing PL measurements on MoSe<sub>2</sub> monolayers (figure 3.17) [114]. Their spectra showed a narrow line (corresponding to RRS) that superposes to the PL line which takes a broader linewidth. For MoSe<sub>2</sub>, the distinction between RRS and PL lines was easier than our case because the excitation of MoS<sub>2</sub> ML has been performed using a tunable cw laser, so the RRS linewidth was much smaller than that of the PL [114]. In our experiments, the mBN sample is excited with a femtosecond laser (the fourth harmonic a Ti:Sa laser). This excitation source gives a broad line with a FWHM of  $\sim 9$  meV. Since the RRS arises here from the emission of two LA(M)

phonons, which means that we are dealing with second-order Raman scattering, we expect a FWHM equal approximately to twice the FWHM of Rayleigh scattering  $\sim 18$  meV. This value is comparable to the FWHM of the PL doublet lines ( $\sim 32$  meV). Consequently, one cannot easily discriminate between RRS and PL from their linewidth.

In figures 3.18, the comparison between the linewidth of the laser diffusion and the PL spectra is given. We re-plot the four spectra presented previously (figure 3.16 a) in separate panels: figure 3.18 (a) for  $E_{ex} = 6.345$  eV, figure 3.18 (b) for  $E_{ex} = 6.375$  eV, figure 3.18 (c) for  $E_{ex} = 6.39$  eV and figure 3.18 (d) for  $E_{ex} = 6.4$  eV. Rayleigh scattering of the laser is shifted in energy by 2 LA(M) phonons ( $\sim 318$  meV) and superposed to each of the spectra in the different panels. It is displayed in a black dotted line. Its intensity is normalized with respect to the signal of each spectrum in order to compare them easily.

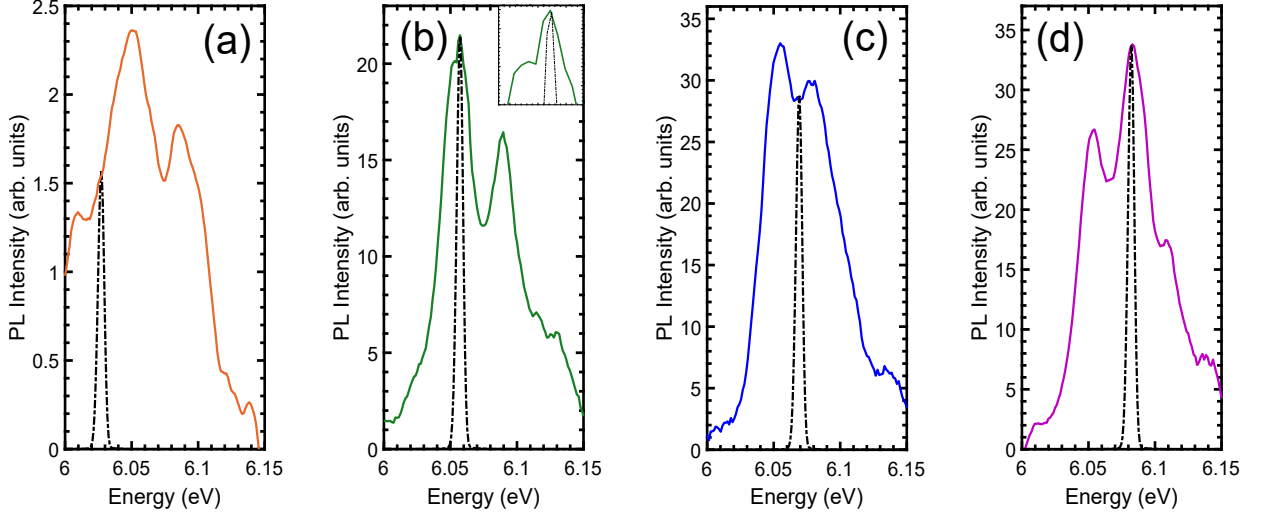


**Figure 3.18: PL emission of mBN for different values of the excitation energy:** data are plotted after subtraction of stray laser light; the excitation energies are  $E_{ex}$  : (a) 6.345 eV; (b) 6.375 eV, (c) 6.39 eV, (d) 6.4 eV; Rayleigh scattering of the laser is plotted in black dotted lines and shifted by the Raman energy  $2\Delta$ , with  $\Delta = 159$  meV, corresponding to the energy of the LA(M) phonon in mBN.

In figure 3.18 (a) (orange line), the spectrum is measured under off-resonance conditions with a weak signal intensity which is lower by one order of magnitude in comparison to the other spectra (panels b, c and d). It is dominated by the contribution of the PL signal without any indication for the presence of RRS. The intensity ratio between the 6.05 and 6.08 eV lines is 1.29 for this spectrum.

For  $E_{ex} = 6.375$  eV (green line in panel (b)), the position of the second order Raman line overlaps with the PL line at 6.05 eV. We point out the observation of a narrow line that superimposes to the PL peak (see inset). This line is comparable to what was observed in

MoSe<sub>2</sub> (figure 3.17). It corresponds to second-order RRS in mBN and its linewidth corresponds to the double of the one of Rayleigh scattering (black dashed line). The ratio between the doublet PL lines is 1.32, it is comparable to the one in figure 3.18 (a) (orange line) indicating that the contribution of the RRS in this spectrum is low, and is limited to the small modulation highlighted in the inset.

For  $E_{ex}=6.39$  eV (panel c), the RRS line is positioned at 6.072 eV. It changes slightly the emission of the PL doublet, and gives a ratio of 1.15 between the intensities of the PL lines at 6.05 and 6.08 eV. Nevertheless, it changes strongly the PL intensity at 6.07 eV (the minimum between the lines of the doublet) and gives a doublet less contrasted in comparison to the other spectra. For  $E_{ex}=6.4$  eV (magenta line in panel (d)), the form of the spectrum is importantly changed and the intensity ratio between the two lines reverses from 1.3 to 0.8. An important contribution from the RRS modifies the form of the PL spectrum for this excitation energy.

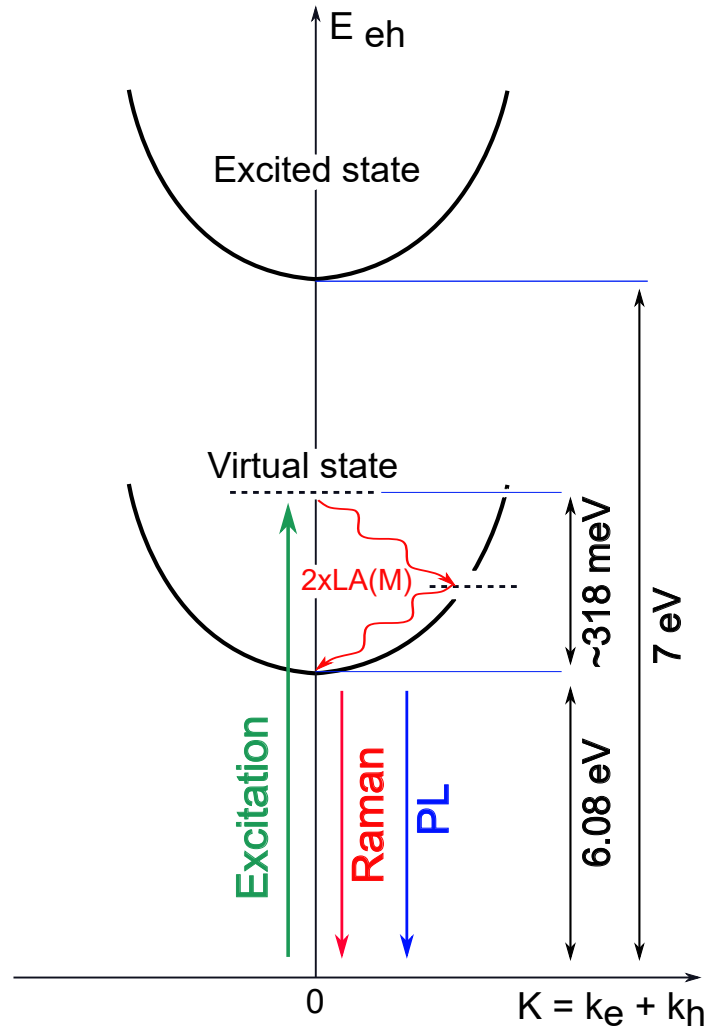


**Figure 3.19: Excitation of mBN:** Scheme explaining the optical process investigated in mBN and which allows the detection of the PL emission.

In order to understand in a clearer way how the optical process excitation occurs when exciting mBN, we sketched in figure 3.19 the scheme resuming the optical process that permits us to detect the PL lines in the emission spectrum of mBN.

Calculations predict a huge exciton binding energy in the case of mBN, and the first excited state is calculated to be at  $0.9\text{ eV}$  above the fundamental exciton, *i.e.* at about  $7\text{ eV}$  [8]. This energy level is situated beyond the reach of our laser source with a maximum excitation energy of  $6.45\text{ eV}$ . In order to excite mBN optically, a resonant excitation of phonon modes is required. The optical pumping has to be performed with a detuning between excitation and detection given by the energy of  $2LA(M)$  phonons. This resonant excitation leads to an efficient pathway at  $\sim 6.38 \pm 0.03\text{ eV}$  ( $\lambda = 194.5 \pm 1\text{ nm}$ ).

### PL of thick samples

The transition from a direct to an indirect band gap in h-BN is expected to occur between 1ML and 2ML, as discussed at the beginning of this chapter. In principle, one would like to perform PL in a 2ML sample grown by MBE. It was explained that the MBE technique is so far limited to a film with a mono-layer thickness, while it is still not possible to produce continuous epilayers of 2ML, 3ML... The reason comes from the high density of 3D clusters which prevents the growth of a complete second layer, as discussed previously in section 3.2.

We have studied the PL signal of our set of samples with an increasing amount of deposited h-BN. In figure 3.20 (a), we present the PL spectra for the samples grown at different  $T_B$ . All the measurements are performed at cryogenic temperature and under the same excitation energy 6.375 eV (194.47 nm). The spectra are plotted in a semi-log scale and we note that they correspond to the absolute PL signal intensity (they are not vertically shifted).  $T_B$  is indicated for each spectrum.

Figure 3.20 (a) shows that the PL spectra of the five samples present a broad emission band centered at 5.5 eV. The intensity of this emission band, which corresponds to defects in h-BN, increases from one sample to another with  $T_B$ , except for sample  $N_5$  grown at the highest  $T_B$ . In that case, the whole PL spectrum is weaker than in  $N_3$  and  $N_4$ .

On the high energy side, more specifically at energies higher than 5.8 eV, the spectra of samples  $N_1$ (1875°C) and  $N_2$ (1888°C) reveal the presence of the PL doublet at 6.05 eV and 6.08 eV. For sample  $N_3$  ( $T_B=1900^\circ\text{C}$ ), there are no strong PL lines at the energies 6.05 eV and 6.08 eV (just a weak modulation in the spectrum). For samples  $N_4$  and  $N_5$  (grown at  $T_B=1925^\circ\text{C}$  and  $T_B=1950^\circ\text{C}$ ), no emission line can be detected for energies higher than 5.8 eV. Still, we observe that the intensity of the laser diffusion strongly changes and that in samples  $N_3$  and  $N_4$  (orange and black lines) it is higher than in the 3 other samples. This increase may be due to the morphology of sample surface and to the presence of defects on the surface.

In order to get rid of the influence of laser diffusion on the doublet visibility, we re-plot the spectra presented in figure 3.20 (a) after the subtraction of the laser diffusion, in a narrow spectral range (between 5.95 eV and 6.15 eV). In figure 3.20 (b), the spectra are plotted in a linear scale and are vertically shifted for clarity. The subtraction of laser diffusion shows that for the samples  $N_1$ ,  $N_2$  and  $N_3$ , the emission of a doublet at 6.05 and 6.08 eV is present in the spectrum. The emission of the doublet was obvious for samples  $N_1$  and  $N_2$  before the subtraction of the laser diffusion, while it was hidden by laser scattering and it appeared only as a weak modulation in the spectrum of sample  $N_3$  (orange line). For samples  $N_4$  and  $N_5$ , no emission line is present in this spectral range after the subtraction of the laser diffusion.

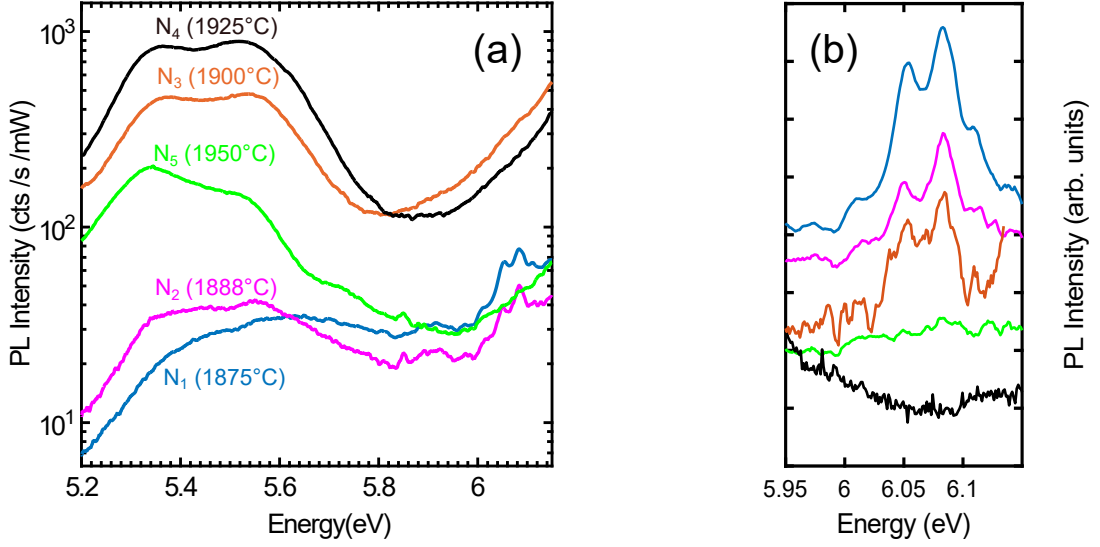


**Figure 3.20: Photoluminescence spectroscopy of h-BN epilayers at 8 K:** (a) raw PL data plotted in a semi-log scale. The spectra are not vertically shifted; (b) after subtraction of the laser diffusion. The spectra are vertically shifted. The samples are grown with five different MBE boron source temperatures  $T_B$ :  $N_1$ :1875°C,  $N_2$ : 1888°C,  $N_3$ :1900°C,  $N_4$ : 1925°C and  $N_5$ : 1950°C. The surface morphology of these samples is presented in figures 3.9.

Figure 3.20 (b) shows firstly, that the presence of a high diffusion level can hide the emission of the doublet at 6.05 and 6.08 eV, secondly, that the emission of the doublet is only detectable in the samples with a thickness less than 1nm, which have more or less a complete mono-layer coverage and a density of 3D clusters that increases with  $T_B$  (section 3.2). However, we note that the intensity of the PL doublet decreases with the increase of  $T_B$ . The emission of the doublet disappears in the samples having thicknesses of 3 nm (10 ML) and 32 nm (100 ML) respectively.

We have extracted the intensity of the PL doublet after subtraction of the laser diffusion and we have plotted them in green as a function of  $T_B$  in figure 3.21 (a). We compare them to the variation of the PL intensity corresponding to the defects emission at 5.5 eV (red circles), and to the variation of the thickness of the deposited h-BN (blue stars) measured by VASE.

Figure 3.21 (a) shows that for samples  $N_1$ ,  $N_2$  and  $N_3$ , the intensity of the PL doublet varies in opposite way to the PL intensity at 5.5 eV: it decreases by a factor of 2 between  $N_1$  and  $N_3$  before disappearing for  $N_4$  and  $N_5$ . The PL intensity at 5.5 eV increases for  $T_B = 1875^\circ\text{C}$  to  $1925^\circ\text{C}$  consistently with the increase of defects density pointed out in figure 3.9. The low PL intensity in the thickest sample  $N_5$  suggests efficient non-radiative recombination process in this highly polycrystalline sample.

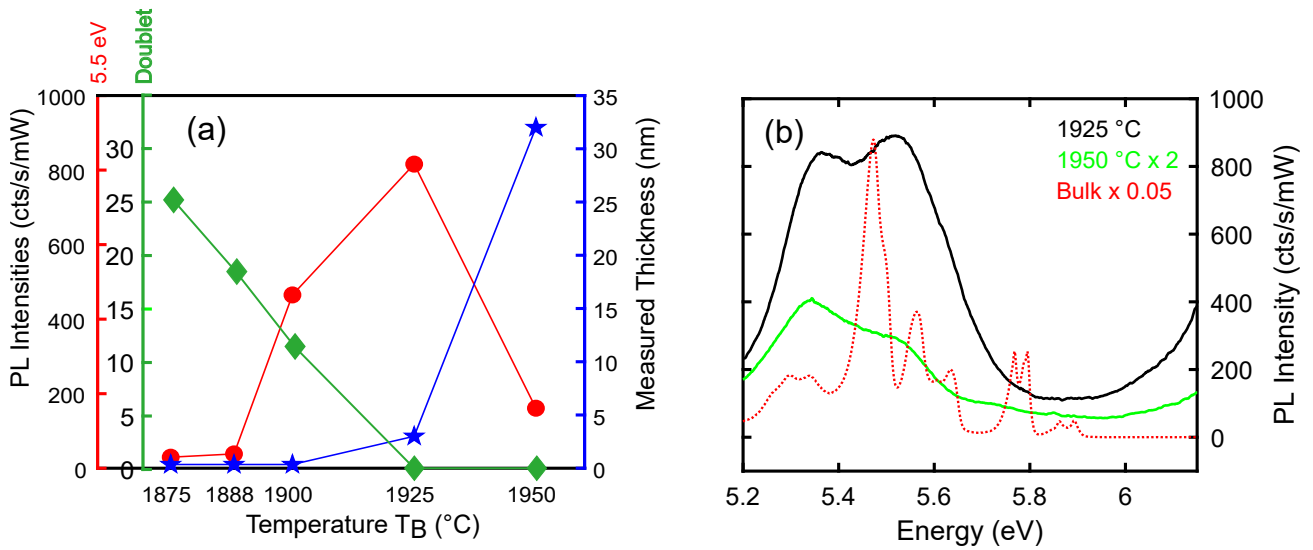


**Figure 3.21: Photoluminescence spectroscopy of h-BN epilayers at 8 K:** (a) The PL intensities for the band emission at 5.5 eV (red circles) and for the PL doublet (green diamonds) as a function of  $T_B$ . The blue stars present the thickness of the h-BN deposited, provided by VASE measurements. The y scale for each of the data is presented in the same color as the symbols. (b) PL spectra for samples  $N_4$ : 1925 °C (black line) and  $N_5$ : 1950 °C (green line) compared to the PL spectrum measured from bulk crystal of h-BN (red dotted line).

In figure 3.21 (b), we compare the PL spectra measured in the thick samples  $N_4$  and  $N_5$  with the PL emission in bulk h-BN (red dotted line). The comparison between the PL spectra shows that the emission band centered at 5.5 eV overlaps with the emission lines related to stacking faults in h-BN. However, in the PL spectra measured from our samples  $N_4$  and  $N_5$ , we do not observe any signature of the phonon replicas around 5.8 eV. The PL signal of these samples is dominated by the emission of the defects.

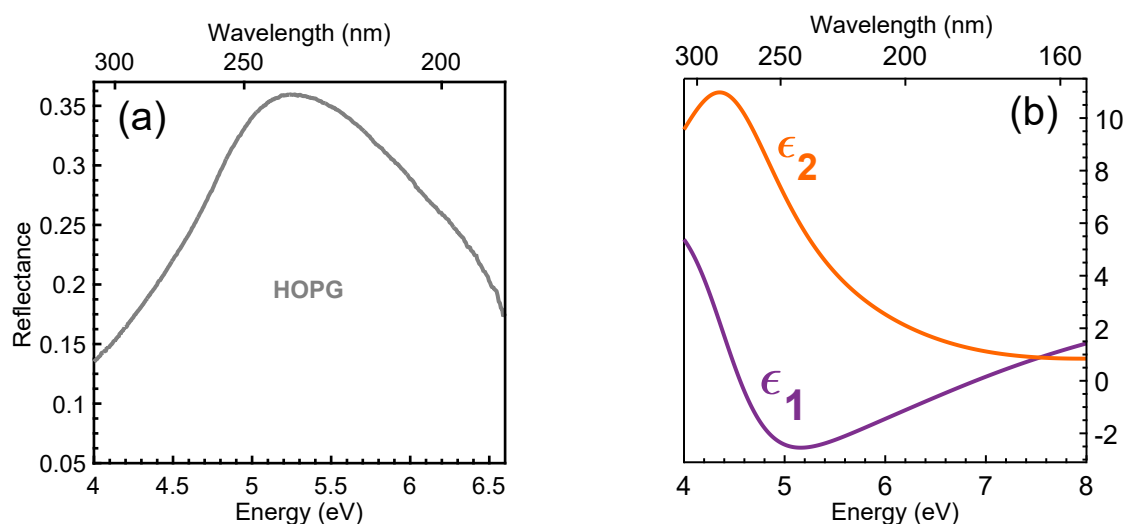
### 3.3.2 Reflectance spectroscopy

In section 3.3.1, the emission of mBN grown by MBE has shown the existence of a new PL doublet at 6.05 eV and 6.08 eV. These lines were never detected before and they do not correspond to any transition related to bulk h-BN. They are a unique feature specific to mBN. However, PL spectroscopy is controlled by the relaxation dynamics in a semiconductor and it probes the recombination process of the states of lowest energy. In order to study the existence of a direct gap transition in mBN, we performed reflectance spectroscopy using the setup described in chapter 2 (section 2.1.1). Reflectance spectroscopy probes the dielectric function of a material, which takes into account all the optical transitions and examines their oscillator strength. In the case of a direct transition, reflectance spectroscopy and PL emission are usually in resonance. In this section, we will show reflectance measurements performed on the samples presenting the emission of the PL doublet at 6.05 eV and 6.08 eV in order to examine

if they correspond to a direct transition in mBN.

### Reflectance of mBN on HOPG

**Reflectance of HOPG:** Before presenting the reflectance measurements performed in mBN samples, we show the reflectance spectra on HOPG, since our samples are made of a single atomic layer of BN deposited on a HOPG substrate with a thickness of about  $\sim 1.5$  nm. The reflectance spectrum measured on HOPG is presented in figure 3.22 (a) for a spectral range between 4 eV and 6.5 eV (185-300 nm). It was measured at the cryogenic temperature of 8K, in a nitrogen environment using the deuterium lamp as a source of light. These data have been shown in chapter 2. We re-plot them here, in order to compare the optical response of HOPG with the one of mBN on HOPG.



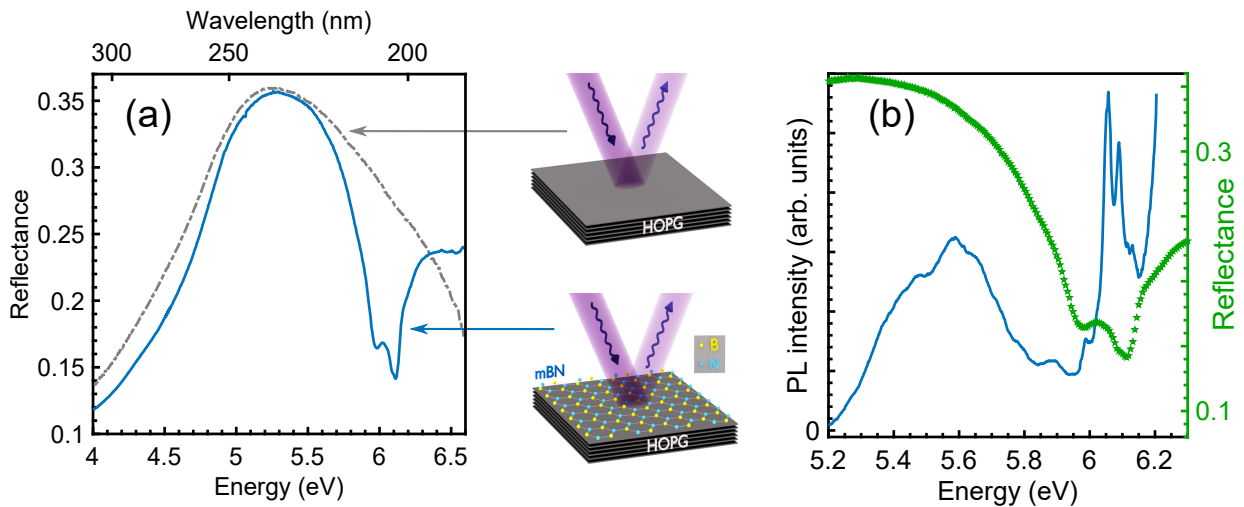
**Figure 3.22: Optical response of graphite in the DUV** (a) reflectance spectrum in the deep ultraviolet for the bare graphite substrate, measured at 8K, under nitrogen environment and using Deuterium lamp; (b) real ( $\epsilon_1$ ) and imaginary ( $\epsilon_2$ ) parts of the dielectric permittivity of graphite: these data are taken from ref. [66].

Figure 3.22 (a) shows a smooth variation of the reflectance spectrum as a function of the energy, with the presence of a maximum of about 35% of reflectivity at around 5.2 eV. This non-monotonic behavior in the response of HOPG results from a key property of its dielectric function in the DUV range.

The dispersion of the real and imaginary parts ( $\epsilon_1$  and  $\epsilon_2$ , respectively) of the dielectric permittivity of graphite were measured in Ref. [66]. We re-plot them in figure 3.22 (b):  $\epsilon_1$  is displayed in violet line while  $\epsilon_2$  is shown in orange solid line.  $\epsilon_1$  and  $\epsilon_2$  show a smooth variation between 4 eV and 7 eV, with the absence of any particular resonance in this spectral range. Of particular interest is the decrease of  $\epsilon_2$  for energies higher than 4.5 eV, corresponding to

a reduction in the optical absorption of graphite in the DUV range. The behavior of  $\epsilon_2$  is of particular interest for an active layer on the top of graphite, since it does not show any resonance that could affect the optical properties of mBN.

**Reflectance of mBN on HOPG:** Here, we compare the reflectance spectra of mBN/HOPG (sample N<sub>1</sub>) with the one recorded from HOPG, as displayed in figure 3.23 (a). The reflectance of mBN/HOPG is displayed in blue solid line and the one from HOPG is shown in a grey dashed line.



**Figure 3.23: Reflectance of epitaxial monolayer BN on graphite:** (a) reflectance spectrum in the deep ultraviolet for the bare graphite substrate (grey dashed line) and mBN on graphite (blue solid line), both at 8K; (b) comparison between PL (blue solid line) and reflectance (green symbols) spectra of mBN/HOPG; in the middle: schematics of the reflectance experiment performed on HOPG and on the mBN/HOPG heterostructure synthesised by van-der-Waals epitaxy; HOPG stands for highly oriented pyrolytic graphite.

The reflectance of mBN/HOPG shows a smooth variation between 4 eV and 5.2 eV, with an increase of reflectance from 10% to 35%. This variation is comparable to the one of HOPG with a relative deviation between 0.5% and 18% in this spectral range. For energies higher than 5.2 eV, we observe a pronounced dip of 15% reflectivity at 6.1 eV for the reflectance of mBN/HOPG. We observe two minima: one at 6.11 eV and a secondary minimum less contrasted at 5.98 eV.

The comparison between HOPG and mBN/HOPG shows that the epitaxy of a single atomic layer of h-BN on HOPG changes drastically the reflectance spectrum of HOPG with a decrease of its reflectance by a factor of 2 (from 30% to 15%).

In figure 3.23 (b), we replot the reflectance spectra of mBN/HOPG between 5.2 eV and 6.3 eV and we compare it to the PL spectrum that we measured in the same sample. The comparison between the two spectra shows that the width of the reflectance lines are very large

(110-150 meV: section 3.4.4) compared to the width of the PL lines (32 meV). However, we observe a resonance between the reflectance minima and the PL emission in mBN indicating the presence of a direct gap at 6.1 eV in mBN.

**Reflectance spectra of  $N_1$ ,  $N_2$  and  $N_6$  samples:** In figures 3.24, we compare in separated panels the reflectance spectra for samples  $N_1$ ,  $N_2$  and  $N_6$  on which we detected the emission of the PL doublet. In each panel we compare the reflectance spectrum to the one of HOPG (grey dashed line).

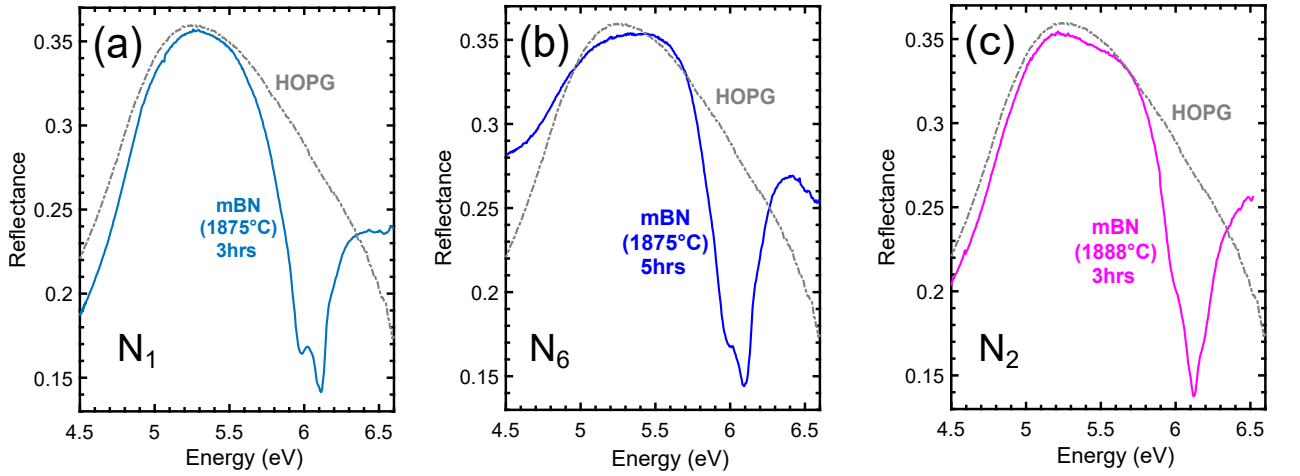


**Figure 3.24: DUV reflectance spectrum for several mBN samples measured at 8 K, obtained for different MBE boron cell temperatures ( $T_B$ ) and growth times:** (a)  $T_B=1875^\circ\text{C}$ , 3 hours, (b)  $T_B=1875^\circ\text{C}$ , 5 hours, (c)  $T_B=1888^\circ\text{C}$ , 3 hours. The solid grey line is the reflectance spectrum of the bare HOPG substrate for reference.

The comparison between the data plotted in figures 3.24 (a, b and c) shows that the overall shape of the reflectance spectra is robust for samples grown with slightly different growth conditions and all getting a coverage close to mBN. Moreover, the absolute reflectance minimum is positioned at 6.11 eV for the three samples. Meanwhile, the visibility of the secondary minimum at 5.98 eV changes from one sample to another. It is well resolved for  $N_1$  (panel (a)) and still apparent for  $N_6$  (panel (b)) but with a lower contrast in comparison with  $N_1$ . For  $N_2$  the 5.98 eV-minimum is hardly observable and appears as a shoulder on the low energy side of the main resonance at 6.11 eV.

The comparison between these spectra suggests that the resonance at 6.11 eV is intrinsic and that it corresponds to the direct optical transition in mBN, while the secondary minimum has an extrinsic origin depending on the growth conditions as discussed below.

Temperature-dependent reflectance measurements are presented in appendix B. They

complement our measurements at low temperature without any significant new physical insight due to the large width of the reflectance lines.

## 3.4 Interpretation

### 3.4.1 PL emission in mBN

#### PL doublet

In the previous sections, we have presented PL and reflectance measurements in mBN samples grown by MBE. The PL spectra showed two emission lines at 6.05 eV and 6.08 eV, while the reflectance measurements showed a pronounced minimum at 6.1 eV, approximately in resonance with the PL emission, supporting the existence of a direct optical transition in mBN. However, the observation of a doublet structure rather than a singlet in the PL spectrum seems puzzling for the emission of a direct-gap transition. In the case of MoSe<sub>2</sub> monolayers, Lindlau *et al.* [115] reported the emission of a PL doublet and their measurements showed features of two bright PL peaks, closely analogous to the doublet we observe in our data on mBN samples. In this part, we will present our interpretation for the emission of a doublet in the PL spectrum of mBN.

The excitonic states in mBN have been described in chapter 1 (section 1.2.3) of this thesis. In mBN as in graphene and TMDs, the band extrema are lying at K and K' points of the first BZ [115, 41, 42]. However, K and K' are two non-equivalent points of the first BZ, since they cannot be connected by a wave-vector of the reciprocal lattice. As a result, four types of excitons can be constructed by the combination of an electron and a hole situated either at K or K': two zero-momentum excitons are obtained if both electron and hole are situated in the same valley; and two momentum-dark excitons are obtained if the electron and the hole are situated in two different valleys (chapter 1: section 1.2.3). These excitons are specific to the valley-physics in hexagonal lattices and their recombination requires the emission of a phonon at the K point. As a result, a doublet may arise in the PL emission with one line emerging from the recombination of a direct exciton ( $|S, 0_+\rangle$ , chapter 1, p.16) in the same valley (K or K'), and a second line at a lower energy, from an indirect transition of the momentum-dark exciton ( $|S, K_\pm\rangle$ ).

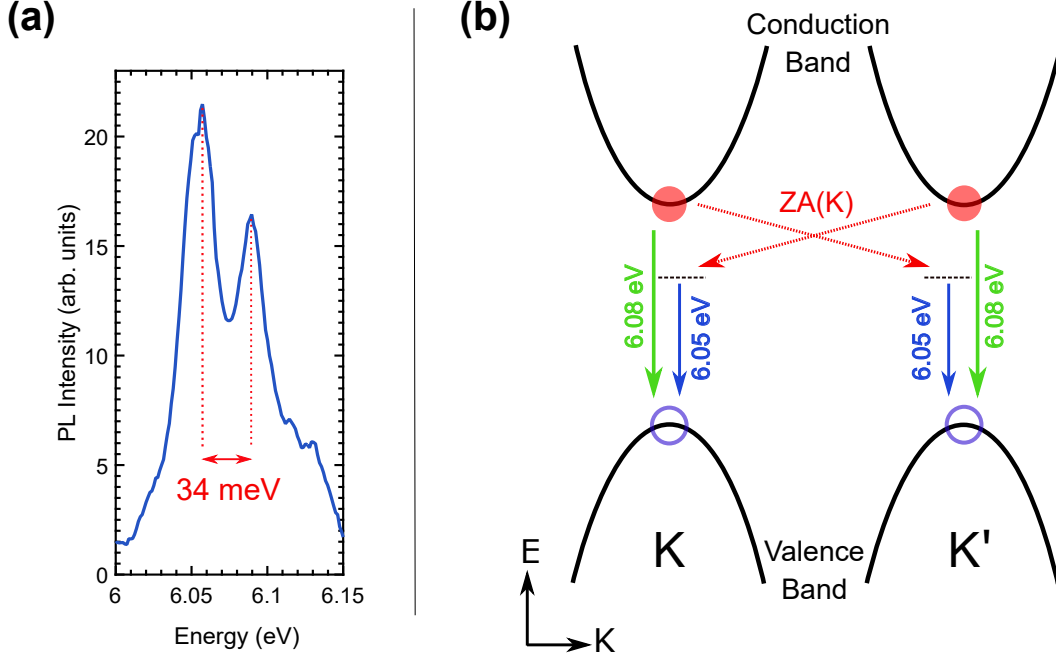


**Figure 3.25: Doublet origin in the photo-luminescence spectrum of mBN:** (a) PL spectrum after subtraction of the laser diffusion presented in the spectral range from 6 to 6.15 eV, with the energy splitting of the doublet being 34 meV; (b) scheme of the band structure at K and K' points of the first Brillouin zone in a one-particle configuration; the green arrows illustrate the recombination of the electron and hole in the same valley ( $k_e = k_h$ ) and the blue arrows illustrate the photon after recombination of the electron and hole in different valleys ( $k_e \neq k_h$ ); dotted red arrows illustrate the phonon emission.

We have observed in section 3.3.1 that there is no significant contribution of RRS with an excitation energy of 6.375 eV (Figure 3.18 b), suggesting the absence of a real exciton state at 6.05 eV, but probably a virtual state. While for the line at 6.08 eV, we have seen that RRS changes drastically the spectrum for  $E_{ex} = 6.4$  eV indicating the presence of a real excitonic state at 6.08 eV. Consequently, we interpret the luminescence line at 6.08 eV as the direct recombination of an exciton with both electron and hole in the same k-valley (singlet  $|S, 0_+\rangle$ ), and the line at 6.05 eV as the phonon-assisted emission of a dark-exciton in mBN (singlets  $|S, K_\pm\rangle$ ).

The splitting in energy between the two lines is equal to 34 meV. This energy splitting matches the energy of the out-of-plane phonon ZA at the K point (phonon band-structure in chapter 1, section 1.3.1). In this case the emission process of both excitons can be represented as in figure 3.25 (b). However, there may be a splitting due to the presence of a Coulomb interaction between the excitons  $|S, 0_+\rangle$  and the other excitons  $|S, K_-\rangle$  and  $|S, K_+\rangle$ . Consequently, the 34

meV could be the sum of the Coulomb interaction and phonon energy making the identification of the phonon mode tricky.

Finally, we note the PL spectrum goes beyond a simple doublet at 6.05 eV and 6.08 eV, since it presents additional lines on the lower (5.98 eV) and higher (6.16 eV) energy sides of the dominant doublet. The origin of these emission lines is not clear at the present.

#### Reflectance versus emission in mBN

We have interpreted the doublet in the PL spectrum as being the result of two different transitions: a direct transition at 6.08 eV resulting from the direct bright exciton in mBN and the phonon-assisted emission at 6.05 eV of a momentum-dark exciton. However, the reflectance spectrum displays only one transition at 6.11 eV, approximately in resonance with the PL emission. For direct transitions, the PL and reflectance are resonant. For indirect transitions, the phonon-assisted absorption and phonon-assisted emission are mirror processes occurring at different energies as sketched in figure 3.26 (a).

In this part, we compare the emission and the reflectance spectra in the context of a possible mirror effect between PL and reflectance for the indirect transition at 6.05 eV in the PL spectrum. Assuming that the emission of a photon at 6.05 eV results from the emission of a phonon (ZA(K)) having an energy of 34 meV, there should be an absorption at 6.118 eV (Figure 3.26 (a)).

In figure 3.26 (b), the energy of the absorbed photon of 6.118 eV is indicated by the blue dashed line on the high energy side of the fundamental exciton (6.084 eV). The energy of the emitted photon of 6.05 eV is shown in red dashed line on the low-energy side of the fundamental exciton. The splitting in energy between the emitted and absorbed photons is twice the phonon energy. This energy splitting is lower than the linewidth of the reflectance minimum at 6.11 eV (100-150 meV section 3.4.4) preventing any analysis about a mirror effect that could occur between the emission and the absorption processes in mBN. Still, the broad reflectance minimum at 6.11 eV appears fully consistent with both direct and indirect optical transitions in mBN.

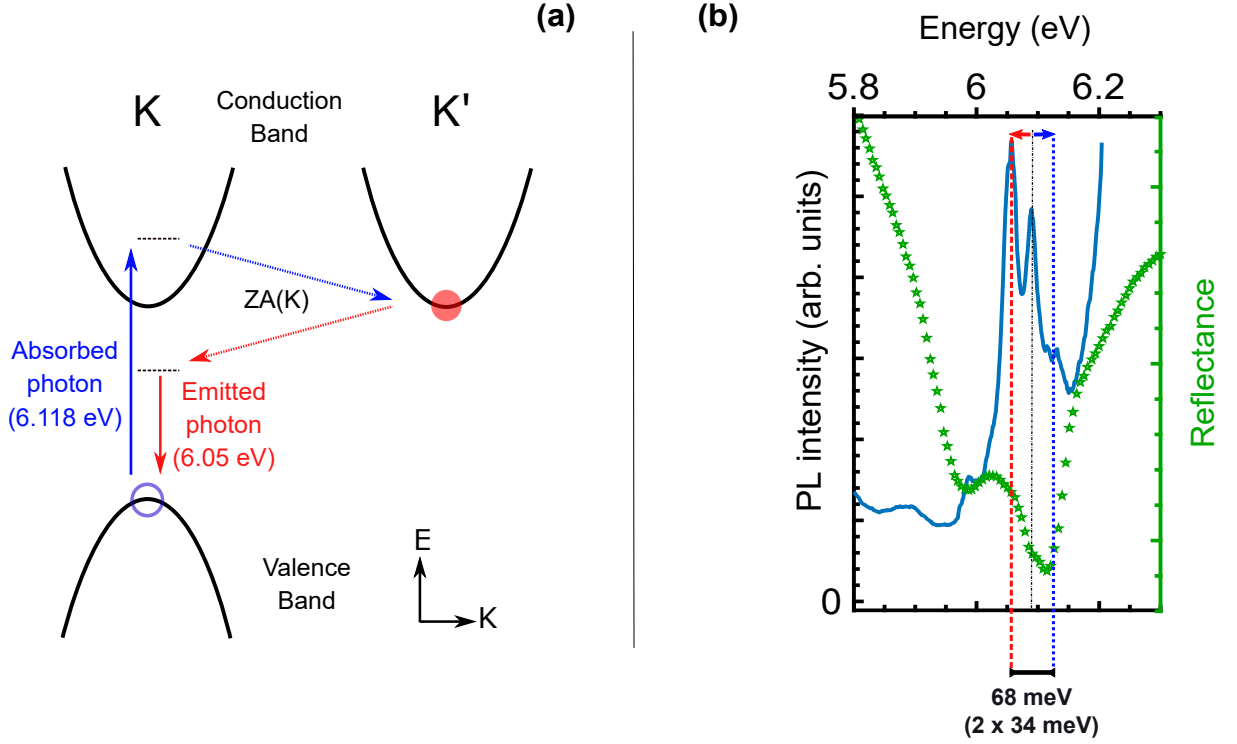


**Figure 3.26: Reflectance versus PL in mBN:** (a) Scheme presenting the emission and absorption processes for an indirect optical transition; (b) reflectance spectrum (green symbols) and photo-luminescence (PL) spectrum (blue solid line) of mBN on graphite at 8K.

### 3.4.2 Temperature dependence of the photoluminescence

In the previous sections, we have seen that the emission in mBN is conditioned by a selective excitation giving rise to RRS, which is completely different from the excitation of bulk h-BN. Moreover, the emission of mBN at cryogenic temperature showed a PL doublet with a spectral separation between the lines equal to 34 meV. In this part, we study the influence of temperature on the direct-gap emission in mBN. This dependence could be characterized by three aspects: (i) a red-shift of the emission energy; (ii) a broadening of the doublet lines and (iii) a decrease in the intensity of the PL. The analysis of these three aspects provides us information on the phonon-exciton interaction in mBN. We will in particular compare the exciton-phonon interactions in both systems: mBN and bulk h-BN.

#### PL measurements depending on the temperature of the sample:

Here, the PL measurements are realized by varying the temperature from 8K to room temperature. The excitation energy is 6.375 eV (194.47nm). Our data are presented in figure 3.27 (a) with open circles after the subtraction of laser diffusion. The temperature is indicated on the

right side for each spectrum. The spectra are vertically shifted for clarity.

Figure 3.27 (a) shows that when increasing the temperature from 8K to room temperature the lines of the PL doublet broaden and the PL intensity decreases. We observe that the spectral positions of  $L_1$  and  $L_2$  shift toward lower energies.

In order to analyze quantitatively the change in the PL spectra as a function of temperature, we fitted our data by using the sum of two Lorentzian functions centered at  $E_1=6.05$  eV and  $E_2=6.08$  eV (dark blue solid line in figure 3.27 (b) with L for Lorentzian). We also used the sum of two Gaussian functions centered at  $E_1=6.05$  eV and  $E_2=6.083$  eV (see solid line in magenta with G for Gaussian). The comparison between our data and two curves given by G and L fits are presented in figure 3.27 (b). Both functions fit more or less the PL doublet present in our data. We used Gaussian functions for our quantitative analysis because of inhomogeneous broadening that is present in our data. Inhomogeneous broadening usually leads to a Gaussian line.

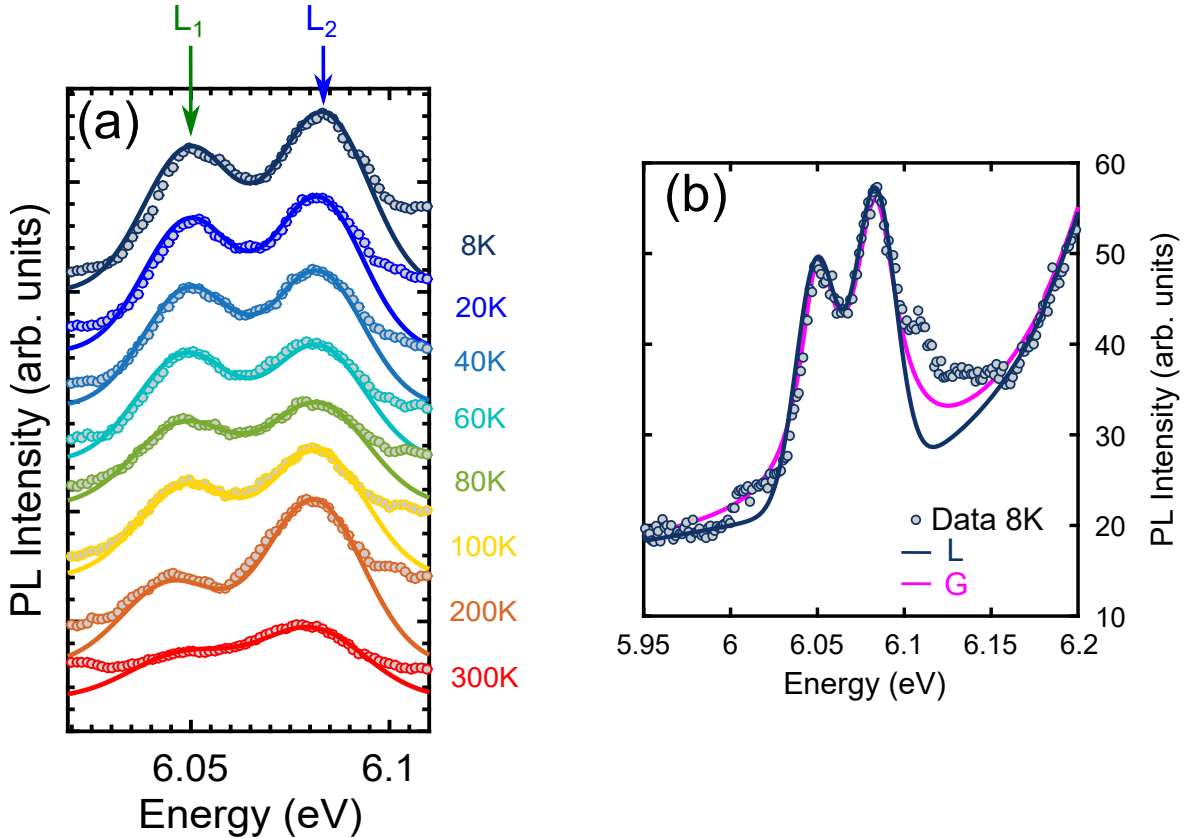


**Figure 3.27: PL spectra in mBN as a function of temperature:** (a) data are presented with open circles and fit with solid lines; all spectra have been corrected for the background arising from laser light scattering, and they are vertically shifted for clarity. (b) PL spectrum in mBN measured at 8K compared to fits given by the sum of 2 Lorentzian functions centered at  $E_1=6.05$  eV and  $E_2=6.08$  eV (L in blue solid line) and by the sum of 2 Gaussian functions centered at  $E_1=6.05$  eV and  $E_2=6.083$  eV (G in magenta solid line)

In our fit, the Gaussian functions have the same linewidth  $\Gamma$  and their amplitudes are defined by  $A_1$  and  $A_2$  respectively. The fitting parameters are adjusted to reproduce our experimental data focusing on the central part of the spectrum and avoiding the spurious contributions on the low and high energy sides. The fits are displayed in solid lines and superposed with the measurements presented in figure 3.27 (a).

The energy positions  $E_1$  and  $E_2$  corresponding to PL lines  $L_1$  and  $L_2$  respectively are extracted from our fits in figure 3.27 (a) and plotted as a function of temperature in figures 3.28 (a) and (b). The energy position of lines  $L_1$  and  $L_2$  shifts similarly toward lower energies ( $L_1$  shifts by 5 meV and  $L_2$  by 4 meV) from 8K to 300K. This energy shift is small in comparison to bulk h-BN, for which the temperature-dependent energy-shift was estimated about 35 meV from 8K to 300K [23] and it indicates that the electron-phonon interaction is modified in mBN with respect to bulk h-BN.

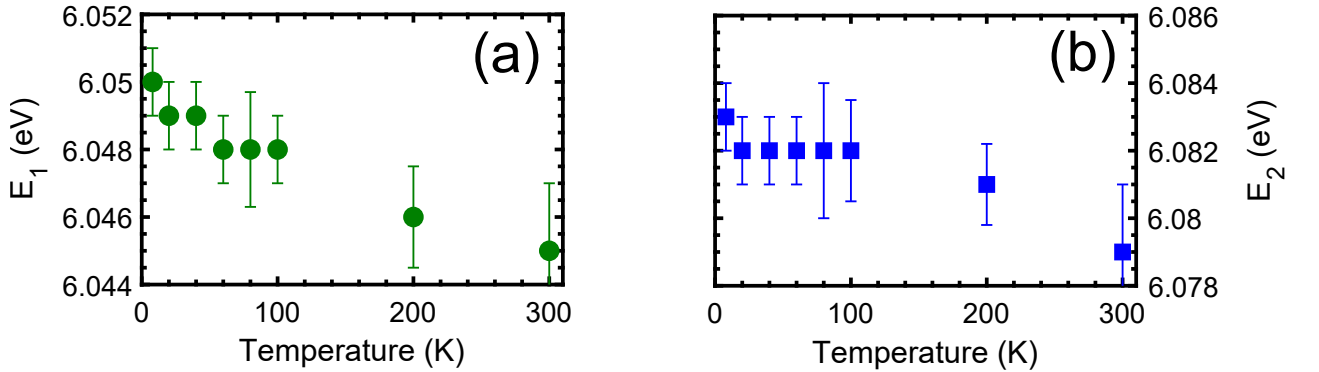


**Figure 3.28: Temperature dependence of the emission in mBN:** (a) spectral position of  $L_1$ ; (b) spectral position of  $L_2$  versus temperature of the sample. Error bars in both figures indicate the uncertainty on the extracted data.

### Temperature dependence of the amplitudes

The extracted amplitudes for both emission lines are displayed in figures 3.29 (a) and (b) as a function of temperature. The data presented in both figures are normalized relatively to the values of  $A_1$  and  $A_2$  at 8K.

The amplitudes of both lines decrease with the temperature: for line  $L_1$  the amplitude decreases by a factor of 3.2, and for  $L_2$  it decreases by a factor of 2.6 from 8K to 300K. Both amplitudes have a comparable variation, except for temperature equal to 200K, we perceive that the extracted parameter corresponding to line  $L_2$  is equal to the one at 8K.

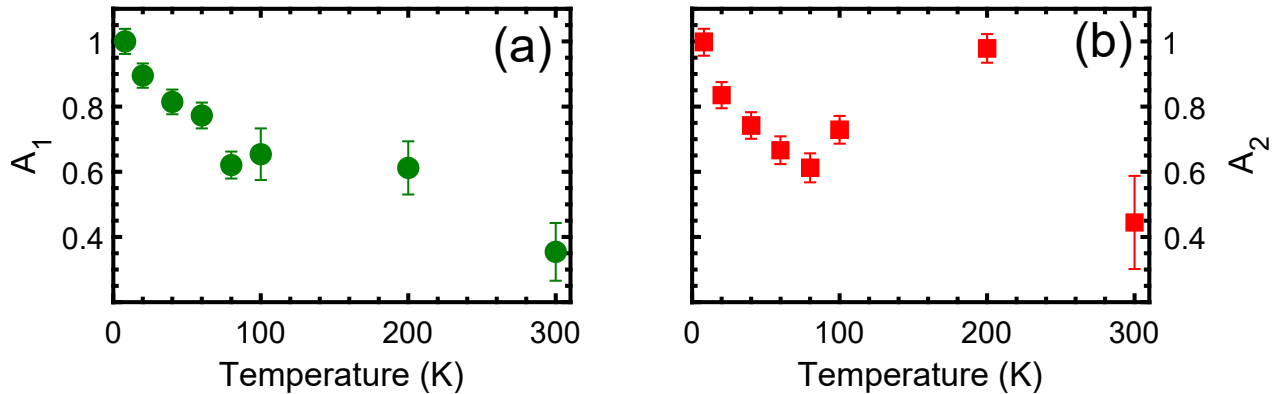


**Figure 3.29: Temperature dependence of the emission in mBN:** (a) normalized amplitude  $A_1$  versus temperature of the sample; (b) normalized amplitude  $A_2$  versus temperature of the sample. Error bars in both figures indicate the uncertainty on the extracted data.

The variation of the PL intensity by a factor of  $\sim 3$  in mBN is slightly smaller than in bulk h-BN, where the intensity decreases by a factor estimated between 4 and 7 from 8K to room temperature [116, 43]. This difference is due to the modification of the interaction with the phonon modes in the case of mBN since the inter-layer phonon modes do not exist anymore for a single h-BN layer. This effect will be demonstrated in the next section 3.4.2.

The emission of light at room temperature in h-BN is due to the high binding energy (in mBN and bulk h-BN), since the thermal energy at 300K will not be able to dissociate the exciton. This effect is of paramount importance for applications of h-BN in the DUV opto-electronic devices operating at room temperature.

### Temperature dependence of the linewidth $\Gamma$

The exciton-phonon coupling in a semiconductor induces a broadening of the excitonic resonance. This phenomenon may overpass the excitonic binding energy and it may dissociate the exciton at room temperature. In bulk h-BN, the exciton-phonon coupling has been identified to be in a strong coupling regime and the thermal broadening is larger than 30 meV between 8K and 300K [61]. This phonon-assisted broadening is dominated by acoustic phonons below 50K, and by optical phonons corresponding to inter-layer breathing modes above 50K. In mBN, the inter-layer breathing mode is absent because of its atomically-thin structure. In this part, we will analyze how the phonon-assisted broadening evolves as a function of temperature in the case of mBN and we compare it to bulk h-BN.

The variation of the linewidth as a function of temperature was extracted from the fits displayed in figure 3.27 (a) and it is displayed in figure 3.30. The linewidth  $\Gamma$  shows an increase

from 32 meV to 38 meV from 8K to room temperature. This means that the temperature causes a thermal broadening of only 6 meV in mBN. This value is much smaller than for bulk h-BN ( $\sim 30$  meV [61]), where the phonon-assisted broadening is mostly dominated at room temperature by the vibrations occurring between the h-BN layers. The decrease in the value of thermal broadening in mBN is due to the absence of inter-layer breathing modes and the limitation of thermal broadening to quasi-elastic acoustic phonon scattering.

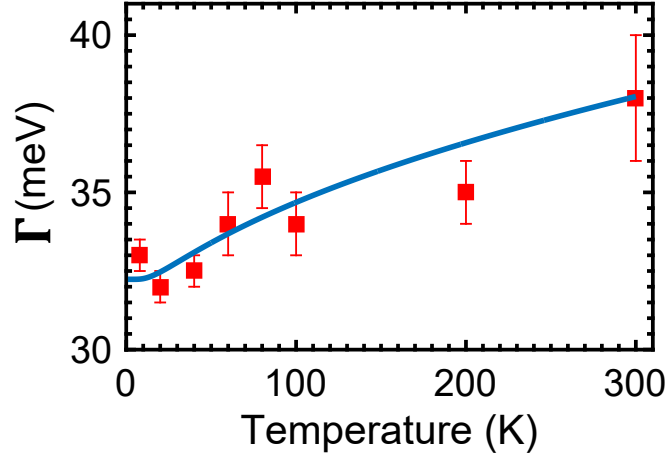


**Figure 3.30: Temperature dependence of the emission in mBN:** variation of full width at half maximum  $\Gamma$  for the lines in the PL doublet as a function of the temperature of the sample (From 8K to 300K); extracted parameters are shown in symbols and the fit is shown in blue solid line.

In order to further analyze the variation of  $\Gamma$  in mBN, we have performed a fit by using the expression of the thermally-induced broadening for the exciton-phonon coupling in a strong coupling regime as used in bulk h-BN [61]. The only difference with Ref. [61] is that the thermal broadening is calculated by taking into account only the contribution of acoustic phonon scattering [117, 118] given by:

$$\Gamma_a^2 = S_A E_A \coth \frac{E_A}{2k_B T} \quad (3.1)$$

As we are using Gaussian functions, then the convolution of two Gaussian of widths  $\Delta_1$  and  $\Delta_2$  takes  $\sqrt{\Delta_1^2 + \Delta_2^2}$  as a width. The expression used in our fit in figure 3.30 is given by:

$$\Gamma = \sqrt{\Gamma_0^2 + \Gamma_a^2} = \sqrt{\Gamma_0^2 + S_A E_A \coth \frac{E_A}{2k_B T}} \quad (3.2)$$

with  $\Gamma_0$  the broadening in the limit of zero temperature  $\Gamma_0=32$  meV. The mean energy for quasi elastic scattering by acoustic phonons  $E_A$  is taken to be equal to 4 meV.  $S_A=8$  meV

being the coupling strength to acoustic phonons and its value is corrected by a factor of 1.7 compared to bulk h-BN.

The comparison between the thermal broadening in mBN and bulk h-BN reveals three important differences:

- (i) In the case of mBN, there is no need for an additional term due to optical phonons in order to reproduce our data. As mentioned previously, these phonons correspond to the inter-layer breathing mode in bulk h-BN, for which the broadening becomes dominant for temperatures above 50K. This contribution is absent in mBN.
- (ii)  $\Gamma_0$  accounts for the linewidth at zero-temperature. It originates from inhomogeneous broadening in addition to the finite radiative broadening.  $\Gamma_0$  is absent for bulk h-BN because the linewidth is only controlled by phonon broadening, while in mBN this term dominates over the thermal broadening and reduces the visibility of the square root temperature dependence of the phonon broadening observed in bulk h-BN.
- (iii) The broadening due to acoustic phonons is slightly higher in mBN than in bulk h-BN ( $S_A$  is higher by a factor of 1.7 in mBN compared to bulk h-BN). This may originate from the increase of the exciton binding energy and consequently the reduction of the excitonic Bohr radius in mBN.

#### 3.4.3 Secondary reflectance minimum at 5.98 eV in mBN

In the previous sections of this chapter, we presented the reflectance spectrum of mBN measured on three different samples. The presence of a minimum at 6.1 eV was the same for the three different samples. In parallel, the presence of a secondary minimum at 5.98 eV was dependent on the growth conditions and its visibility was not the same in the three samples. Here, we discuss the possible origins of this secondary minimum.

In the first chapter of this manuscript, we presented the excitonic states of single mBN layer following the approach of Ando on carbon nanotubes [42]. Taking into account the valley and spin degrees of freedom, there are 16 different states, for which 4 correspond to singlet states and 12 to triplet states.

In a perfect crystal, singlet states are optically allowed while triplet states are optically inactive due to the forbidden spin transitions. The observation of a brightened triplet state requires some symmetry-breaking mechanism that affects the selection rules and allows transitions from triplet states. In carbon nanotubes, it was demonstrated that the presence of defects and distortions efficiently brightens the forbidden triplet states by mixing the singlet and triplet states [119, 120].

The energy splitting between the two minima in reflectance of about 130 meV lies in the same

energy range as what was reported on the brightening of triplet states in carbon nanotubes [119, 120]. In analogy to the case of carbon nanotubes, the origin of the minimum at 5.98 eV may also be interpreted as being the result of a defect-induced brightening of the triplet dark exciton.

We have previously shown that the visibility of the secondary minimum decreases from sample N<sub>1</sub> and N<sub>6</sub> to sample N<sub>2</sub> when changing the growth conditions. The thickness of these samples increases progressively from slightly below one monolayer (sample N<sub>1</sub>) to slightly above one monolayer (samples N<sub>6</sub> and N<sub>2</sub>). This increase in the thickness was accompanied by an increase in the density of defects and of 3D clusters (section 3.2) on the mBN surface. Nevertheless, the variation of the samples growth conditions reduced the visibility of the peak in reflectance spectra of samples N<sub>6</sub> and N<sub>2</sub>. This may be due to different levels of growth-induced residual doping, which are known to play a key role in transition metal dichalcogenides [121] and also in carbon nanotubes [122]. Consequently, an alternative interpretation can be adopted for the minimum at 5.98 eV as being the absorption of a trion.

A trion is a three-particle bound state consisting of two electrons and a hole (negative trion), or one electron and two holes (positive trion). Trions have been observed in atomically thin two-dimensional (2D) transition-metal dichalcogenide semiconductors [123, 121]. The ratio of trion to exciton binding energies is about 10% in monolayer transition metal dichalcogenides [121]. If we assume that this ratio in mBN is similar to the value found in monolayer transition metal dichalcogenides, one could interpret the red-shifted peak in reflectance spectrum as being the absorption of a trion state.

The observation of a secondary minimum in reflectance measurements raises the question of its appearance in the PL spectrum. We highlighted the presence of a weak emission line in the PL spectrum at around 5.98 eV (figure 3.14, page 68), this emission line is in resonance with the secondary minimum in reflectance (see figure 3.26 (b)). Consequently, the emission line at 5.98 eV could be signature for the radiative recombination of a brightened triplet exciton or trion.

We note that the PL line at 5.98 eV is very weak compared to what we observe in reflectance. In PL spectroscopy, the carrier relaxation time is the parameter that plays a key role in the intensity of the PL signal, while in reflectance the oscillator strength is the only relevant parameter. In order to get an intense PL signal from the triplet state or trion, the transition rate or the inter-system crossing rate should compete with the radiative recombination of the singlet. In the next section we will give theoretical interpretation of the reflectance spectra which will provide us with information on the radiative recombination dynamics in mBN.

### 3.4.4 Quantitative modeling of the lineshape fitting of the reflectance in mBN

In this section, we fit our reflectance data using a full quantized approach in order to estimate the radiative efficiency in mBN.

The model we use here is based on the work done on 2D TMDs materials [124, 125, 126] in order to fit reflectance measurements from 2D thin layers.

**Reflection coefficient:** We consider a normally incident plane wave on mBN deposited on a HOPG substrate. The system is assumed to be translationally invariant in the  $xy$  plane, with the incident wave propagating along the  $z$  axis. A fully quantized treatment is considered for both the excitons and the electric field. The amplitude of the reflection coefficient is given by (details of the calculations are given in appendix C):

$$r = r_0 - (1 + r_0)^2 \times L(\omega - \omega_0) \quad (3.3)$$

where  $L(\omega - \omega_0)$  is defined by:

$$L(\omega - \omega_0) = \frac{\frac{i\gamma_r}{2}}{\delta + \text{Im}(r_0)\frac{\gamma_r}{2} + i\frac{\Gamma}{2}} \quad (3.4)$$

with  $\delta = \omega - \omega_0$  and  $\Gamma = 2\gamma_d + \gamma_{nr} + \gamma_r(1 + \text{Re}(r_0))$ . The first term in equation 3.3 corresponds to the response of the substrate and the second term is the response of mBN.  $r_0$  denotes the complex reflection coefficient of the HOPG substrate without mBN layer.  $\gamma_r$  denotes the radiative decay rate of the exciton at the frequency  $\omega_0$ ,  $\gamma_d$  the dephasing rate and  $\gamma_{nr}$  the non-radiative decay rate.

This model permits us to evaluate the minimal value of the radiative rate of the exciton transition  $\gamma_r$  in mBN. Let us evaluate the radiative efficiency by the usual expression:

$$\eta = \frac{\gamma_r}{\gamma_r + \gamma_{nr}} \quad (3.5)$$

We then re-write  $L(\omega - \omega_0)$  as:

$$L(\omega - \omega_0) = \frac{\frac{i\gamma_r}{\Gamma}}{\frac{2}{\Gamma}\delta + \text{Im}(r_0)\frac{\gamma_r}{\Gamma} + i} \quad (3.6)$$

We have:

$$\gamma_{nr} + \gamma_r \leq \Gamma \quad (3.7)$$

$$(3.8)$$

with  $\Gamma = 2\gamma_d + \gamma_{nr} + \gamma_r(1 + \text{Re}(r_0))$  and  $(1 + \text{Re}(r_0)) > 0$ . Then,

$$\begin{aligned} \Leftrightarrow \frac{\gamma_r}{\Gamma} &\leq \frac{\gamma_r}{\gamma_{nr} + \gamma_r} \leq 1 \\ \Leftrightarrow \frac{\gamma_r}{\Gamma} &\leq \eta \leq 1 \end{aligned} \quad (3.9)$$

Our calculations will allow us to evaluate a lower bound of the radiative efficiency. In the following, we rename  $\frac{\gamma_r}{\Gamma}$  as  $\eta_{min}$ . Therefore, we have two independent fitting parameters  $\Gamma$  and  $\eta_{min}$ .

**Inhomogeneous broadening:** In order to account for the inhomogeneous broadening, we consider a Gaussian distribution of  $\omega$ :

$$G(\omega - \Omega) = \frac{1}{\sigma\sqrt{\pi}} e^{-\left(\frac{\omega - \Omega}{\sigma}\right)^2} \quad (3.10)$$

with  $\sigma$  the width of the Gaussian function and  $\Omega$  the distribution center. The convolution of  $L(\omega)$  (equation 3.3) with the Gaussian  $G(\omega - \Omega)$  gives the response of the sample. The convolution is given by:

$$(L * G)(\omega) = \int_{-\infty}^{+\infty} L(\omega - \omega_0) G(\omega_0 - \Omega) d\omega_0 \quad (3.11)$$

The total reflectance is then given by:

$$R = \left| r_0(\omega) + (1 + r_0(\omega))^2 L * G(\omega) \right|^2 \quad (3.12)$$

### Fit of the reflectance data with a single Gaussian distribution of oscillators

We start by fitting the reflectance spectrum presented in figure 3.23 and corresponding to sample N<sub>1</sub> grown for 3 hours at  $T_B = 1875^\circ\text{C}$ . In figures 3.31 (a), (b) and (c), we display our calculations using a single Gaussian distribution of oscillators. Three different cases are displayed in the panels of figures 3.31. The measured data are displayed in blue symbols and our fit in red solid lines.

As a first step, we examine the case with a very weak inhomogeneous broadening  $\hbar\Gamma \gg \sigma$ . For this case, if  $\eta_{min}=0\%$  no contrast can be observed and R is given by the response of HOPG while for  $\eta_{min} = 100\%$  our fit gives 0% reflectance at 6.1 eV. In order to improve our fit, we have to decrease the value of  $\eta_{min}$ . In panel (a), we display the result for  $\eta_{min}=30 \pm 1\%$ , with  $\sigma=1$  meV and  $\hbar\Gamma=145 \pm 5$  meV. The panel (a) shows that with a response determined only by homogeneous broadening, the oscillator (1) at 6.12 eV has a radiative efficiency of at least 30%.

From the other side, reflectance lines are much larger than PL lines (Figure 3.23 b): this is due to the presence of inhomogeneous broadening in the reflectance response in mBN. We

### 3.4. INTERPRETATION

---

thus increase the inhomogeneous broadening in our fit. In panel (b) we take homogeneous and inhomogeneous broadenings more or less equally ( $\sigma = 60 \pm 2$  meV and  $\hbar\Gamma = 50 \pm 2$  meV):  $\eta_{min}$  takes a value of  $59 \pm 2\%$ .

In order to increase  $\sigma$ , we have to increase  $\eta_{min}$ . For a maximal value of  $\eta_{min} = 100\%$  (panel (c)),  $\sigma$  takes a maximal value of  $74 \pm 4$  meV. For this fit  $\hbar\Gamma = 30 \pm 1$  meV, this value is very close to the linewidth of PL lines (32 meV).

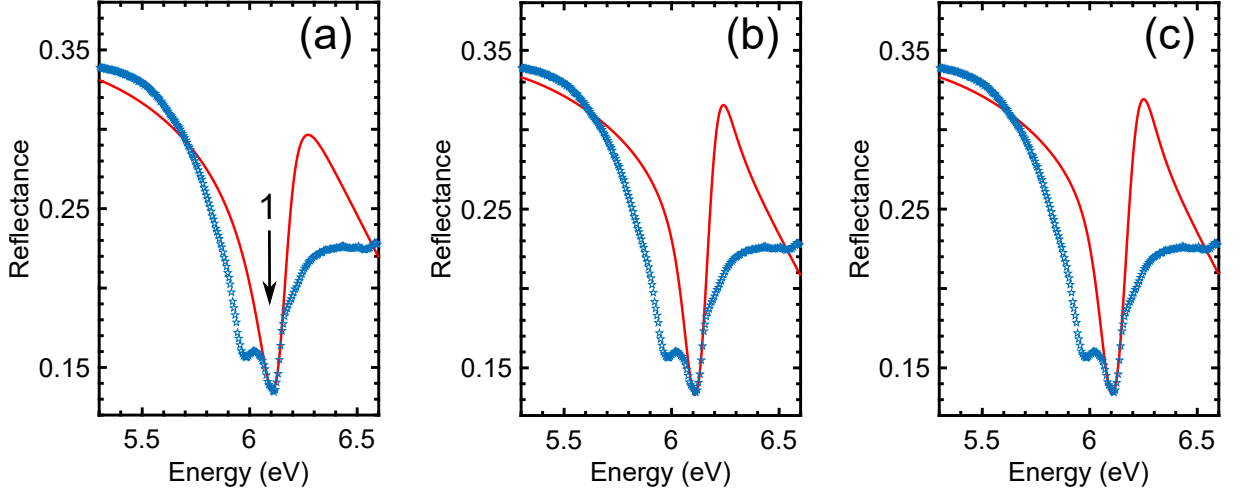


**Figure 3.31: Fit of the reflectance spectrum in mBN taking into account one oscillator at 6.12 eV:** Our data are plotted in blue symbols and compared to the red solid line which displays the calculated data; (a) with negligible inhomogeneous broadening  $\sigma=1$  meV, homogeneous broadening  $\hbar\Gamma = 145 \pm 5$  meV and  $\eta_{min} = 30 \pm 1\%$ ; (b) homogeneous and inhomogeneous broadening are very close :  $\sigma = 60 \pm 2$  meV,  $\hbar\Gamma = 50 \pm 2$  meV and  $\eta_{min} = 59 \pm 2\%$ ; (c) inhomogeneous broadening  $\sigma = 74 \pm 4$  meV, homogeneous broadening  $\hbar\Gamma = 30 \pm 1$  meV and  $\eta_{min} = 100\%$ .

### Fit of the reflectance data with two Gaussian distributions of oscillators

As it was shown previously, our reflectance spectra present a secondary minimum at 5.98 eV and its visibility is dependent on the growth conditions. In order to account the contribution of oscillator (2) at 5.98 eV in the reflectance spectrum of sample N<sub>1</sub>, we consider the sum of two Gaussian functions  $G_1$  and  $G_2$  centered at  $\Omega_1 = 6.12$  eV and  $\Omega_2 = 5.98$  eV. By taking the same value  $\sigma$  for the two Gaussian functions, we now have 3 fitting parameters  $\Gamma$ ,  $\eta_{min}^{(1)}$  and  $\eta_{min}^{(2)}$ .

As in the previous section, we examine the case with a very weak inhomogeneous broadening (figure 3.32 (a)). The response of the sample is dominated by homogeneous broadening ( $\hbar\Gamma = 150 \pm 5$  meV  $\gg \sigma = 1$  meV). The contrast in our fit is given now by the two values of  $\eta_{min}^{(1)}$  and  $\eta_{min}^{(2)}$ . In order to get a curve that fits the doublet present in our data,  $\eta_{min}^{(1)}$  and  $\eta_{min}^{(2)}$  take the values  $35 \pm 1 \%$  and  $14 \pm 1 \%$ , respectively.

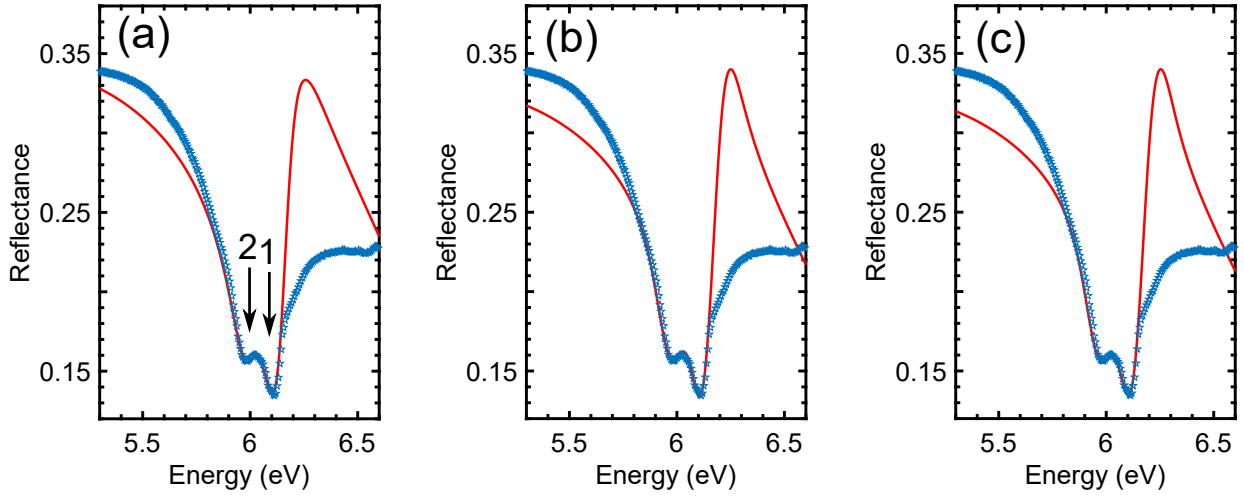


**Figure 3.32: Fit of the reflectance spectrum in mBN taking into account two oscillators at 6.12 and 5.98 eV:** Our data are plotted in blue symbols and compared to the red solid line which displays the calculated data; (a) inhomogeneous broadening  $\sigma=1$  meV  $\ll$  homogeneous broadening  $\hbar\Gamma = 150 \pm 5$  meV,  $\eta_{min}^{(1)} = 35 \pm 1\%$  and  $\eta_{min}^{(2)} = 14 \pm 1\%$ ; (b) homogeneous and inhomogeneous broadening are equivalent :  $\sigma = 66 \pm 2$  meV  $\approx \hbar\Gamma = 60 \pm 1$  meV,  $\eta_{min}^{(1)} = 65 \pm 1\%$  and  $\eta_{min}^{(2)} = 30 \pm 1\%$ ; (c) inhomogeneous broadening  $\sigma = 75 \pm 2$  meV  $>$  homogeneous broadening  $\hbar\Gamma = 36 \pm 1.5$  meV,  $\eta_{min}^{(1)} = 100\%$  and  $\eta_{min}^{(2)} = 48 \pm 2\%$ .

As before, in order to account for inhomogeneous broadening in our fit, we have to increase the value of  $\sigma$ . In order to improve our fits, we increase  $\eta_{min}^{(1)}$  and  $\eta_{min}^{(2)}$  with the increase of  $\sigma$ . In panel (b) of figure 3.32 we take homogeneous and inhomogeneous broadenings more or less equivalent ( $\sigma = 66 \pm 2$  meV,  $\hbar\Gamma = 60 \pm 1$  meV). For this case the minimal bounds of  $\eta$  take the values  $65 \pm 1\%$  and  $30 \pm 1\%$  for oscillators (1) and (2), respectively.

The maximal value of inhomogeneous broadening is given when  $\eta_{min}^{(1)}$  is maximal *i.e.* 100%. For this case  $\sigma = 75 \pm 2$  meV,  $\hbar\Gamma = 36 \pm 1.5$  meV and  $\eta_{min}^{(2)} = 48 \pm 2\%$ .

Based on these fits, we point out firstly that the radiative efficiency given by oscillator (2) is about half the contribution of oscillator (1) in the three cases discussed here. Secondly, for the maximal value of the inhomogeneous broadening,  $\hbar\Gamma$  takes a value comparable to the width of the PL lines (even if we consider 1 or 2 oscillators).

By considering two different oscillators centered at 5.98 eV and 6.12 eV, our fits reproduce perfectly our data for the spectral range between 5.7 and 6.17 eV. On the high energy side ( $> 6.17$  eV), our fits do not overlap with our measured data and give a reflectance level higher by a factor 1.5 compared to our measured data. Consequently, it is difficult to evaluate the real value of inhomogeneous broadening by our fits.

Whatever the contribution of inhomogeneous broadening in our reflectance data,  $\eta_{min}^{(1)}$  takes a value of at least 30% in order to reproduce the high contrast in our reflectance spectra. The radiative decay rate  $\hbar\gamma_r^{(1)}$  can be estimated between 35 and 55 meV. In MoSe<sub>2</sub> monolayers,

radiative decay rate is evaluated to be about 4-7 meV [127, 124]. This means that in mBN, the radiative decay rate is at least higher by a factor of  $\sim 8$  than in MoSe<sub>2</sub>. Finally, the radiative decay rate  $\hbar\gamma_r^{(2)}$  is lower than  $\hbar\gamma_r^{(1)}$  and is estimated about  $\sim 18$ -20 meV.

### Fit of the reflectance data with more Gaussian functions

In order to improve our fit on the high energy side (above 6.17 eV), we added to our model two additional distributions (3) and (4) centered at 6.29 eV and 6.39 eV. The fitting parameters for distributions (3) and (4) are chosen in a way to not affect the fitting parameters for distributions (1) and (2). The results are displayed in figure 3.33 (red solid line) and compared to our data (blue symbols). The comparison between both curves shows that the addition of (3) and (4) improves the fit by decreasing the level of reflectance from 35% (figures 3.32) to 27%, for the energies higher than 6.17 eV. However, this is still not sufficient to fit perfectly our data in this spectral range. Furthermore, the interpretation of these oscillators will not be conclusive since their physical origin is unknown. Their addition to our model shows only that they could provide a better fit to our data for energies  $> 6.17$  eV without any relevant information about physics in mBN for this energy range, except for the presence of additional electronic transitions.

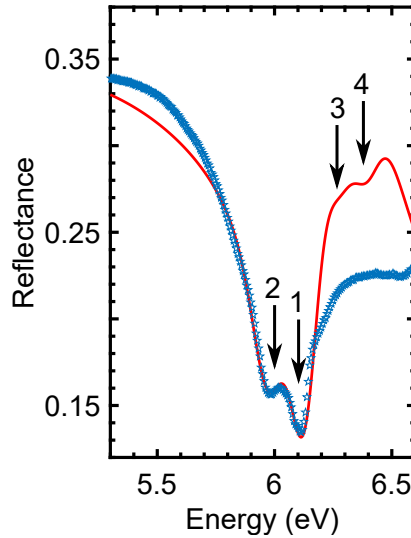


**Figure 3.33: Fit of the reflectance spectrum in mBN taking into account 4 Gaussian distributions centered at  $\Omega_1 = 6.12$  eV,  $\Omega_2 = 5.98$  eV,  $\Omega_3 = 6.29$  eV and  $\Omega_4 = 6.39$  eV: inhomogeneous broadening  $\sigma = 76 \pm 2$  meV  $\gg$  homogeneous broadening  $\hbar\Gamma = 35 \pm 1$  meV,  $\eta_{min}^{(1)} = 100\%$ ,  $\eta_{min}^{(2)} = 50 \pm 2\%$ ,  $\eta_{min}^{(3)} = 30 \pm 2\%$  and  $\eta_{min}^{(4)} = 20\%$ .**

### Fit of the reflectance spectra for other mBN samples

In this section, we present a quantitative analysis for the reflectance spectra measured on samples  $N_2$  and  $N_6$ . We fit the corresponding spectra following the same procedure as described previously for sample  $N_1$  (Figure 3.32). The comparison between the radiative decay rates of three different samples will provide us more information about the radiative efficiency of oscillators (1) and (2), more particularly we will estimate  $\hbar\gamma_r^{(1)}$  and  $\hbar\gamma_r^{(2)}$  in samples  $N_2$  and  $N_6$ . Our fits are presented in figure 3.34 in black solid lines for sample  $N_6$  (a-b) and for sample  $N_2$  (c-d).

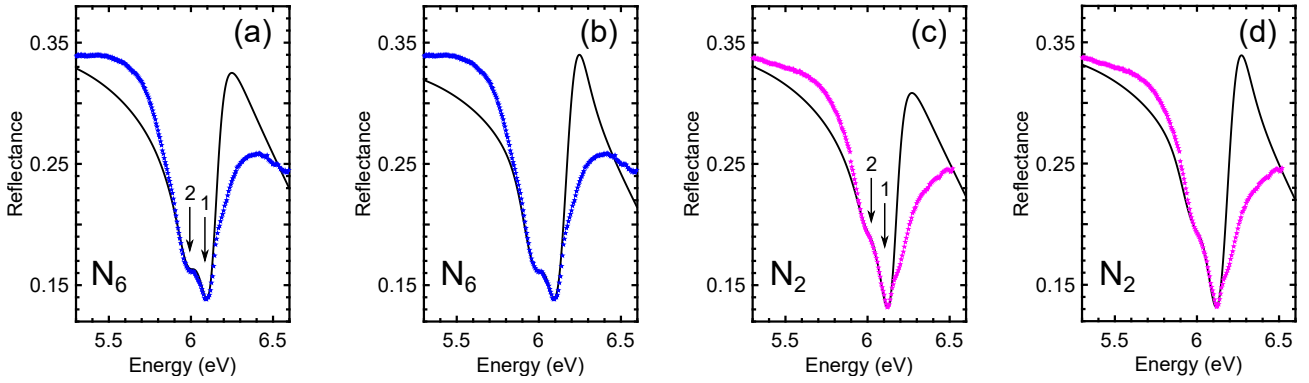


**Figure 3.34: Reflectance spectrum in monolayer Boron nitride for samples  $N_2$  and  $N_6$ :** (a) Sample  $N_6$ : inhomogeneous broadening  $\sigma = 1$  meV, homogeneous broadening  $\hbar\Gamma = 160 \pm 5$  meV,  $\eta_{min}^{(1)} = 33 \pm 1\%$ ,  $\eta_{min}^{(2)} = 11 \pm 1\%$ ; (b) Sample  $N_6$ : inhomogeneous broadening  $\sigma = 76 \pm 2$  meV, homogeneous broadening  $\hbar\Gamma = 150 \pm 5$  meV,  $\eta_{min}^{(1)} = 100\%$ ,  $\eta_{min}^{(2)} = 44 \pm 2\%$ ; (c) Sample  $N_2$ : inhomogeneous broadening  $\sigma = 1$  meV, homogeneous broadening  $\hbar\Gamma = 150 \pm 5$  meV,  $\eta_{min}^{(1)} = 32 \pm 1\%$ ,  $\eta_{min}^{(2)} = 5 \pm 1\%$ ; (d) Sample  $N_2$ : inhomogeneous broadening  $\sigma = 78 \pm 2$  meV, homogeneous broadening  $\hbar\Gamma = 36 \pm 1$  meV,  $\eta_{min}^{(1)} = 100\%$ ,  $\eta_{min}^{(2)} = 26 \pm 2\%$ .

In sample  $N_6$ ,  $\hbar\gamma_r^{(1)}$  varies between  $\sim 35$  and  $53$  meV and  $\hbar\gamma_r^{(2)}$  is about  $\sim 16$ - $18$  meV. In sample  $N_2$ ,  $\hbar\gamma_r^{(1)}$  varies between  $\sim 35$  and  $50$  meV and  $\hbar\gamma_r^{(2)}$  is about  $\sim 7$ - $10$  meV. The comparison between the three samples  $N_1$ ,  $N_2$  and  $N_6$  shows that the radiative efficiency for oscillator (1) (at 6.12 eV) takes comparable values in the three samples and does not depend on the growth conditions.  $\eta_{min}^{(2)}$  is lower than  $\eta_{min}^{(1)}$  in all the three samples and it depends on the growth conditions. Its contribution is weaker in the reflectance spectrum of sample  $N_2$ . Unfortunately, no conclusive information about the origin of the secondary minimum at 5.98 eV could be obtained whether it is due to an absorption of a trion or a brightened triplet exciton.

## 3.5 Conclusion

In this chapter, we demonstrated the existence of a direct transition at 6.1 eV in mBN revealing a band gap crossover from indirect to direct in the h-BN bulk/mBN system. This crossover is similar to many 2D materials like MoS<sub>2</sub>, MoSe<sub>2</sub>, etc...

For that project, we used an original strategy relying on the scalable growth of mBN layer by MBE on HOPG substrate which allowed us to perform macro-PL and reflectance in the DUV. Our strategy did not follow the methods usually used in literature for 2D materials. The growth of the mBN samples was performed in Nottingham, by controlling the growth time  $t_g$ , the temperature of the boron source  $T_B$  and the growth temperature  $T_G$ . It was demonstrated that the B:N ratio affects the morphology of the grown samples and its increase results in the increase of 3D clusters of the growth surface. In order to get a monolayer coverage with a low density of 3D clusters, h-BN has to be grown in a N-rich environment. By the control of the growth parameters, our collaborators in Nottingham have achieved the growth of a single mBN layer with a thickness of  $3.5\text{\AA}$  on a large scale HOPG surface ( $10 \times 10\text{ mm}^2$ ).

Both PL and reflectance measurements have been performed on the mBN layers. PL spectroscopy has revealed the emission of a doublet at 6.05 eV and 6.08 eV. This doublet is a unique feature and it has never been detected before. Reflectance measurements have shown the presence of a highly contrasted minimum centered at 6.11 eV in resonance with the PL doublet. Both reflectance and PL spectra demonstrated the presence of a direct optical transition at 6.1 eV in mBN.

The excitation process in mBN is very different from bulk h-BN, it is conditioned by a selective excitation. The photo-excitation in mBN is assisted by  $2LA(M)$  phonon overtones which provide a pathway allowing to excite mBN. This condition affected the form of the PL spectrum due to resonant Raman lines. Our results demonstrated that both excitation and recombination processes are very different in mBN and in bulk h-BN.

The existence of a doublet rather than a singlet in PL emission spectrum of a direct gap material was not expected. Nevertheless, the optical response of direct-gap 2D materials involves two transitions: a direct transition resulting from the exciton states in the same K valley, and an indirect transition resulting from excitons with electron and hole in two different valleys. Such transitions are phonon-assisted. In mBN, phonon-assisted transitions could involve ZA phonons at the K point.

Temperature dependent experiments were performed in order to analyze the exciton-phonon interaction in mBN. PL measurements demonstrated a 6 meV thermal-broadening. This value

---

is much smaller than the one observed in bulk h-BN. It comes from the absence of the inter-layer vibrating mode in mBN because of its atomically-thin structure thus reducing the efficiency of phonon-assisted broadening.

Finally, we provided a quantitative interpretation of the reflectance spectra using a model that allowed us to estimate the radiative efficiency for the optical transitions involved in mBN. The radiative efficiency of the direct exciton at 6.1 eV was estimated to be at least 30% and the radiative broadening to be between 35 and 55 meV. This value is about 10 times higher than in other 2D materials.

Moreover, reflectance spectra revealed the presence of a secondary minimum at 5.98 eV. The visibility of this minimum was dependent on the growth conditions. We interpreted its origins to be extrinsic and due to either a trion absorption or to the brightening of a triplet dark-exciton in mBN. The radiative efficiency of this transition was estimated to be lower than the one at 6.1 eV and it was dependent on the growth conditions. Our quantitative analysis allowed us to estimate a radiative broadening varying from 7 meV to 20 meV for this excitonic state.

---

# GENERAL CONCLUSION

The exfoliation of graphene by Novoselov and Geim in 2004 has opened a new field of research on heterostructures of layered semiconductor compounds, with the generic name of 2D materials. The properties of these materials range from a zero-gap in graphene and finite gaps in the visible range in TMDs to the deep UV in h-BN. h-BN is highly demanded by the 2D material's community for its interesting properties to encapsulate and protect other materials from their environment or for passivizing their surfaces. Moreover, its captivating optical properties in the deep-ultraviolet make it a promising material for UV lighting. However, the fundamental properties leading to these interesting properties are not fully understood yet. Within this thesis we studied the optical properties of mBN and we demonstrated a bandgap cross-over from indirect to direct when scaling the BN size from the bulk to the monolayer (mBN).

At the beginning of this thesis, our objective was to study several important points related to the emission processes in mBN: is the bandgap in mBN direct or not? What is the energy of the fundamental gap in mBN? How does the emission spectrum in mBN compare to the one in bulk h-BN? How does the emission spectrum vary with the number of layers and how the electron-phonon coupling will be modified for thin layers?

In order to bring quantitative answers to these questions, we built a reflectance setup in the deep-ultraviolet that allowed us to perform photoluminescence and reflectivity measurements to unravel the optical response in mBN.

Our samples were grown in Nottingham University in the group of Prof. S. Novikov. These samples have been studied by Variable Angle Spectroscopic Ellipsometry and Atomic Force Microscopy measurements performed in Nottingham. These measurements demonstrated that the morphology of the grown mBN layers is strongly dependent on the growth parameters and that in order to get the growth of high quality mBN on HOPG substrates, one has to grow h-BN in a N-rich environment, for a growth time equivalent of 3 hours and a growth temperature of 1390°C. The growth of large scale ( $10\times 10\text{mm}^2$ ) mBN on HOPG was achieved with MBE in Nottingham. This achievement allowed us to perform macro-photoluminescence and reflectance measurements in deep UV in order to study the optical properties in mBN.

We have measured the emission spectrum from mBN using our macro-PL setup. It showed the presence of a broad band emission centered at 5.5 eV related to defects in h-BN, in addition to the emission of a PL doublet at 6.05 and 6.08 eV which was detected for the first time in our mBN samples. This doublet is a unique feature related to emission process in mBN. Later, we studied the dependence of the PL spectrum on the excitation energy. In order to excite mBN optically, a resonant excitation of phonon modes was required and the optical pumping was performed with a detuning between excitation and detection that is given by the energy of 2LA(M) phonons. These results showed that the excitation process in mBN is very different

---

from that in bulk h-BN and that it is conditioned by the excitation wavelength/energy. The emission of a doublet was only measured from samples with a thickness around one monolayer and this emission totally disappeared from the emission spectra measured on thicker samples.

We performed reflectance spectroscopy in our mBN samples. The spectra revealed the presence of a highly contrasted minimum centered at 6.1 eV with the presence of a secondary minimum less contrasted on the low energy side (at 5.98 eV). The minimum at 6.1 eV was present and well contrasted in all the spectra measured from different samples having a thickness of one monolayer, whatever the growth conditions are, while the visibility of the secondary minimum at 5.98 eV was dependent on these growth conditions. The resonance between the PL doublet emission and the reflectance minimum revealed the presence of a direct gap at 6.1 eV in mBN.

Temperature dependent PL measurements demonstrated that the thermal broadening in mBN was smaller than in bulk h-BN and that is driven only by the acoustic phonons. This is due to the absence of the interlayer breathing mode in atomically-thin h-BN monolayers.

We interpreted the emission of a doublet in mBN as being the result of one direct optical transition (6.08 eV) with the recombination of a direct exciton with both electron and hole sitting in the same valley, and an indirect optical transition (6.05 eV) resulting from the recombination of a momentum dark-exciton with electron and hole in different valleys.

The secondary minimum in reflectance spectra at 5.98 eV was interpreted of extrinsic origin. It most probably originates from a brightening of a triplet dark exciton or a trion.

A quantitative analyze has been performed in order to estimate the radiative efficiency in mBN. Our calculations revealed a minimal value of 30% for the radiative efficiency of the direct exciton with a radiative broadening of about 20 meV. This value is 8 times higher than the one estimated in other monolayers of 2D TMDs materials.

During this thesis, several aspects were addressed without being presented in this manuscript.

- Photoluminescence and reflectance measurements have been performed on samples with sub-monolayer thicknesses (partial covering of the substrate). The goal of these measurements was to understand the strain effect that could be caused by the substrate on the bandgap of monolayer boron nitride (Appendix D).
- Reflectance measurements have been performed on bulk h-BN crystals in order to investigate the direct excitons in bulk h-BN (at K and H points of the first BZ) that are lying at energies close to the fundamental gap (along MK). The interpretation of these results is work in progress (Appendix A).

---

h-BN is a promising material for a broad range of applications. In this PhD study we have highlighted key advances including the growth of monolayer BN on a large scale using MBE and the fundamental properties of its direct gap. This progress constitutes an important step towards future studies on h-BN. From the technological point of view, the growth of mBN using MBE sets the basis for complementary studies in order to obtain a stacking of continuous monolayers grown on a large scale. A long-term objective would be the growth of wide gap semiconductors with van-der-Waals heterostructures for developing compact solid-state devices. From the fundamental point of view, we discussed the optical properties of the direct gap in monolayer BN while many other properties still have to be explored. The origin of the additional lines observed in the PL spectrum remains to be elucidated. Besides the monolayer, a particular interest is to examine the optical properties of h-BN as a function of the number of layers and the effect of Moiré superlattices on the opto-electronic properties.





---

# REFLECTIVITY OF BULK h-BN

In this appendix we present complementary reflectivity measurements performed during this PhD work on bulk h-BN crystals. These results are not discussed in the chapters of the manuscript since the interpretation of these measurements is not established yet.

This appendix is split into four parts: in section A.1 we present the motivation for these measurements. In section A.2 we compare reflectance measurements on h-BN crystals from different growth sources. In section A.3 we compare reflectance and PL measurements for bulk h-BN. And finally we discuss temperature-dependent reflectance measurements.

## A.1 Motivation

We previously highlighted the presence of direct excitons ( $dX$ ) in bulk h-BN at K and H points of the first BZ. The energies of these excitons are calculated to be close to the one of indirect exciton ( $iX$ ): about 6.1 eV for direct excitons versus 5.95 eV for indirect one in the 2-particle representation (chapter 1, section 1.2).

In order to study the properties of the energy levels higher than the fundamental gap, one has to use a technique which probes excited energy levels that can contribute to transitions higher in energy than the fundamental exciton. As it was explained within chapter 2, the PL spectroscopy probes the relaxation dynamics of charge carriers for a system brought out of equilibrium after laser excitation. Consequently it only investigates the lowest energy states of the excited crystal. h-BN has an indirect fundamental gap (chapter 1, section 1.2) *i.e.* the fundamental exciton (at 5.95 eV) is the one probed by PL spectroscopy. The optical properties of  $iX$  have been largely studied before my thesis and have been summarized in chapter 1. However, the comparison between energies of  $dX$  and  $iX$  in bulk h-BN is not known with high precision yet.

Reflectance technique allows to probe high energy states in bulk h-BN, more particularly the direct excitons lying at  $\sim 6.1$  eV. It investigates the dielectric function of a material at the thermodynamic equilibrium. All the optical transitions involving fundamental and excited energy states contribute to the dielectric constant of the material. The dielectric constant permits to probe rapid variations of the light matter interaction at allowed direct energy transitions.

We note that few papers reported previously the reflectance spectra of h-BN and the understanding of the physics related to excitonic states has not been completed yet. In 1984, Hoffman *et al.* measured the reflectance spectrum of pyrolytic boron nitride in the energy range 0.05-10 eV (figure A.1 (a)) at room temperature. In their work they calculated a direct band gap at  $5.2 \pm 0.2$  eV [128]. However at that time h-BN was only available in powder form and the growth of high quality crystals was not achievable. In 2009, K. Watanabe and T. Taniguchi [129] performed reflectance measurements on high quality h-BN crystals at a cryogenic temperature 8K (figure A.1 b) however the contribution of the excitons close to the gap has not been understood.

In this appendix we show reflectance measurements performed on high quality h-BN crystals in order to resolve this issue and understand the contribution of  $dX$  and  $iX$  to the optical response of bulk h-BN. The reflectance setup that we used in order to perform our measurements was described in chapter 2, figure 2.4.

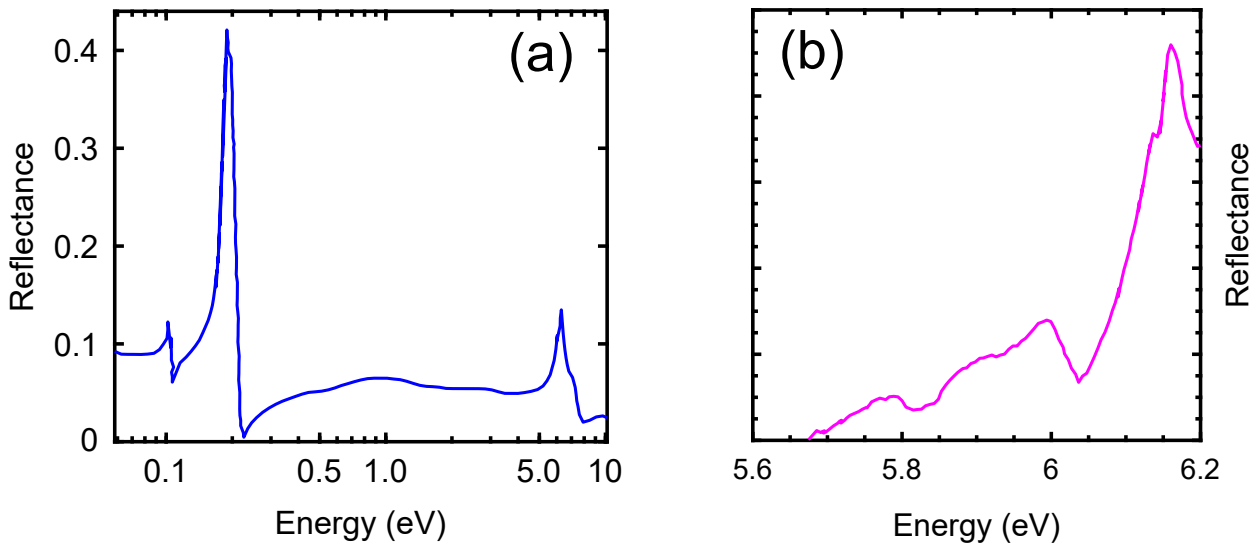


**Figure A.1: Reflectance of BN:** (a) Reflectance spectrum measured from pyrolytic BN at room temperature. These data are taken from Ref. [128]; (b) Reflectance measurements from high quality h-BN at 8K. These data are taken from Ref. [129].

## A.2 Reflectance spectra from two different h-BN crystals

In order to perform reflectance measurements on bulk h-BN, we firstly used h-BN crystals coming from HQ-graphene company. Our measurements on these crystals have been performed at a cryogenic temperature of 8K and using our deuterium lamp (see chapter 2, pages 28-31)

as a light source. The reflectance spectrum that we measured from this crystal is presented in figure A.2 (a). It shows a reflectance level that varies between 2 and 7 % for the spectral range between 5.4 and 7 eV. The spectrum shows a large band centered at 6.2 eV with a FWHM of about 370 meV to which are superimposed 3 features: a weak line at 6 eV, a well contrasted maximum at 6.135 eV, and a line at 6.3 eV. The maximum at 6.135 eV gives a maximal reflectance of 8% for this h-BN crystal. We note that the form of the spectrum for the spectral range between 5.6 and 6.2 eV is very similar to what was observed by K. Watanabe and T. Taniguchi in 2009 (figure A.1 b).

As it was shown in chapter 2, section 2.2.2, large h-BN crystals ( $\sim 3$  cm in total size, with domain made of single crystals with 3 mm size) were grown by our collaborators at the Kansas State University (KSU). The studies performed on these samples such as PL and Raman spectroscopy showed intense PL signal coming from the intrinsic phonon replicas (the ratio between defect-related PL signal at 5.5 eV and intrinsic LO/TO phonon lines is less than 1) and narrow Raman lines ( $\sim 7.8$  cm $^{-1}$ ) which indicate that the quality of these samples is higher than the ones from HQgraphene company [16, 17, 23, 82, 83]. We measured the reflectance spectra from samples K1 and K2 which are described in table 2.2, page 46. The form of the reflectance spectra measured on K2 are very similar to what was measured from the sample coming from HQgraphene company. Here we present only the spectrum corresponding to sample K1 (figure A.2 b). This spectrum has been measured using the Xenon-plasma light source which provides a spot size of  $100 \times 100 \mu m$  (5 times smaller than the one provided by Deuterium light source: see chapter 2, page 29). This spot size is smaller than the relative size of domains of single crystals supplied to us by prof. J. H. Edgar from KSU. The conditions provided by the spot size of the Xenon-plasma light source and the crystal size allowed us to measure reflectance spectra from a single h-BN crystal with better resolution.

The reflectance spectrum measured from sample K1 shows a reflectance level that varies between 6 and 55 % for the spectral range between 5.4 and 7 eV. The spectrum shows a large band centered at 6.2 eV with a FWHM of about 460 meV, superimposed by five relative maxima at 6.02 eV, 6.05 eV, 6.11 eV, 6.14 eV and 6.3 eV. The one at 6.14 eV gives a maximal reflectance level of 55%.

The comparison between both spectra in panels (a) and (b) shows firstly that the overall form of the spectra is more or less the same in both cases, while the one plotted in (b) presents fine structures that were hidden in the spectrum plotted in (a). Moreover, it shows that the sample K1 coming from Kansas State University reflects efficiently the light with one order of magnitude higher than the one coming from HQgraphene company. This comparison highlights the improvement achieved on our experimental setup which will allow us to understand the physics lying behind these resolved fine structures and the optical properties of h-BN for

energies higher than the fundamental gap. This improvement is due to the high quality of our samples and to the spot size provided by our Xenon-plasma light source.

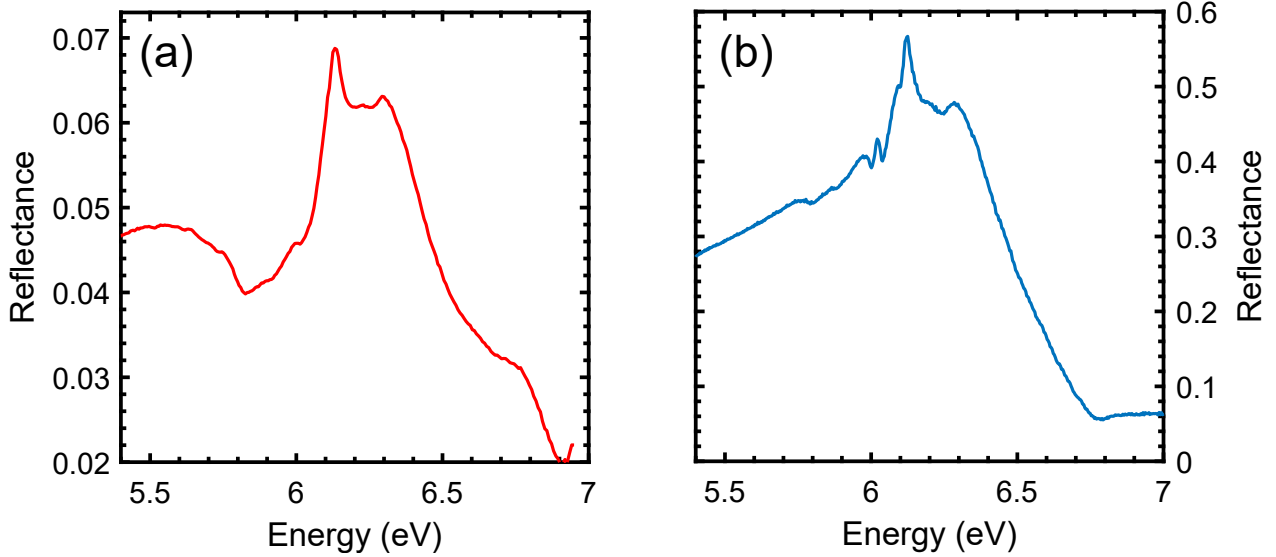


**Figure A.2: Reflectivity of bulk h-BN** (a) Reflectivity spectrum measured from bulk h-BN crystal from HQgraphene company at 8K using a Deuterium lamp as a light source; (b) Reflectivity spectrum measured from bulk h-BN crystal from Kansas University at 8K using a Xenon-plasma light source. Both spectra are normalized following the procedure described in chapter 2, section 2.1.1 using the same reference mirror.

### A.3 Reflectance versus emission in bulk h-BN

As we discussed in chapter 3, page 83, for direct optical transitions absorption and luminescence processes are in resonance. For indirect optical transitions, the phonon-assisted absorption and phonon-assisted emission are processes spectrally mirrored with respect to the indirect exciton ( $iX$ ) and are thus occurring at different energies (A.3 (b)). In figure A.3 (a), we compare the PL (red line) and reflectance (green line) spectra from bulk h-BN (K1 sample). In order to identify a possible mirror effect between PL and reflectance for the indirect transition at 5.95 eV (highlighted by a vertical dashed line), we have plotted the mirror of the PL spectrum with respect to the  $iX$  energy in blue line.

The comparison between the red and green curves shows that the weak modulations appearing in the reflectance spectrum at around 5.77 eV and 5.87 eV respectively correspond to phonon replicas in the PL spectrum given by LO/TO and LA/TA modes. These modulations correspond to light absorption process in bulk h-BN and they appear in our reflectance spectrum. These modulations correspond to light absorption process in bulk h-BN and they appear in our reflectance spectrum. More important, the comparison between the blue and green curves

shows that the energy positions of the relative maxima at 6.02 eV, 6.05 eV, 6.11 eV and 6.14 eV correspond to the mirror image of the phonon replicas due to TA, LA, TO and LO phonons in PL (blue line). We indicate them by horizontal dotted arrows. This comparison shows that we can identify both phonon emission and absorption processes from our reflectance spectrum measured on sample K1. Both processes are assisted by LO/TO and LA/TA phonon modes. Figure A.3 (a) highlights the contribution of the indirect exciton ( $iX$ ) to the reflectance spectrum of bulk h-BN. However, this comparison does not permit us to quantify in terms of intrinsic numbers the contribution of direct excitons to the reflectance spectrum of bulk h-BN except its resonance energy since  $dX$  are not investigated in the PL spectrum (red and blue curves).

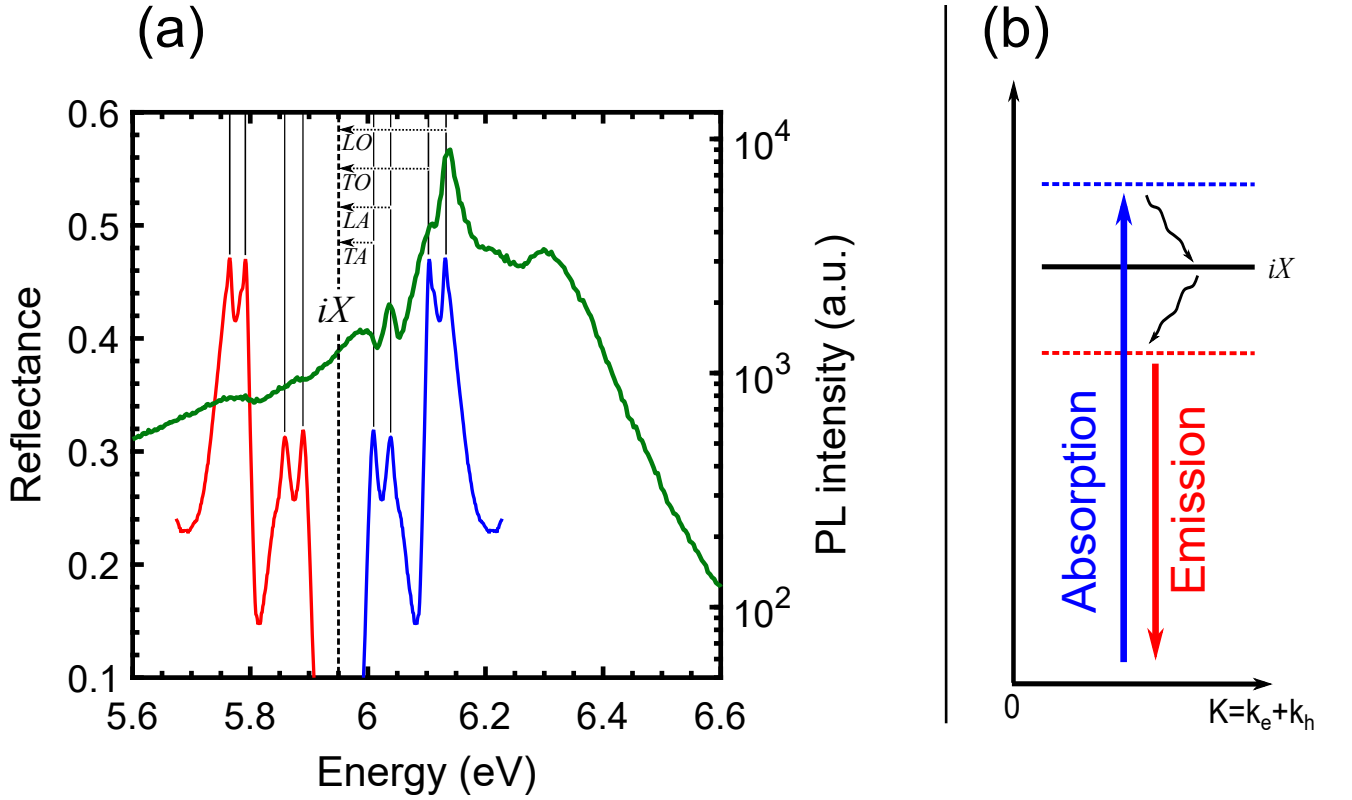


**Figure A.3: Reflectance versus PL in bulk h-BN** (a) Comparison between reflectance and PL (red line) spectra measured from bulk h-BN at 8K. The vertical dashed line at 5.95 eV presents the energy position of the fundamental indirect exciton ( $iX$ ) in bulk h-BN. The blue spectrum shows the mirror of the PL spectrum with respect to the  $iX$  energy. The phonon assisted transitions of  $iX$  are indicated by horizontal dotted arrows. TA, LA, TO and LO indicate the modes of emitted phonons in reflectivity; (b) Schematic representation highlighting the mirror effect between absorption (blue arrow) and emission (red arrow) processes assisted by phonon emission (black zigzag arrows). The blue and red dashed lines indicate the virtual levels of the phonon-assisted absorption and emission processes respectively. The solid line indicates the excitonic level of  $iX$ .

The understanding of the contribution of direct excitons to our reflectance spectrum has to be complemented by theoretical calculations that investigate the dielectric function in bulk h-BN for energies higher than the fundamental gap. The interpretation of our reflectance measurements is in progress in order to fully understand the origins of the large band observed in our measurements and the contribution of  $dX$  to the optical response.

## A.4 Temperature-dependent measurements

In this part, we present temperature-dependent measurements of reflectivity in bulk h-BN. Figure A.4 (a) summarizes our reflectance measurements performed from 8K to room temperature on sample K1.

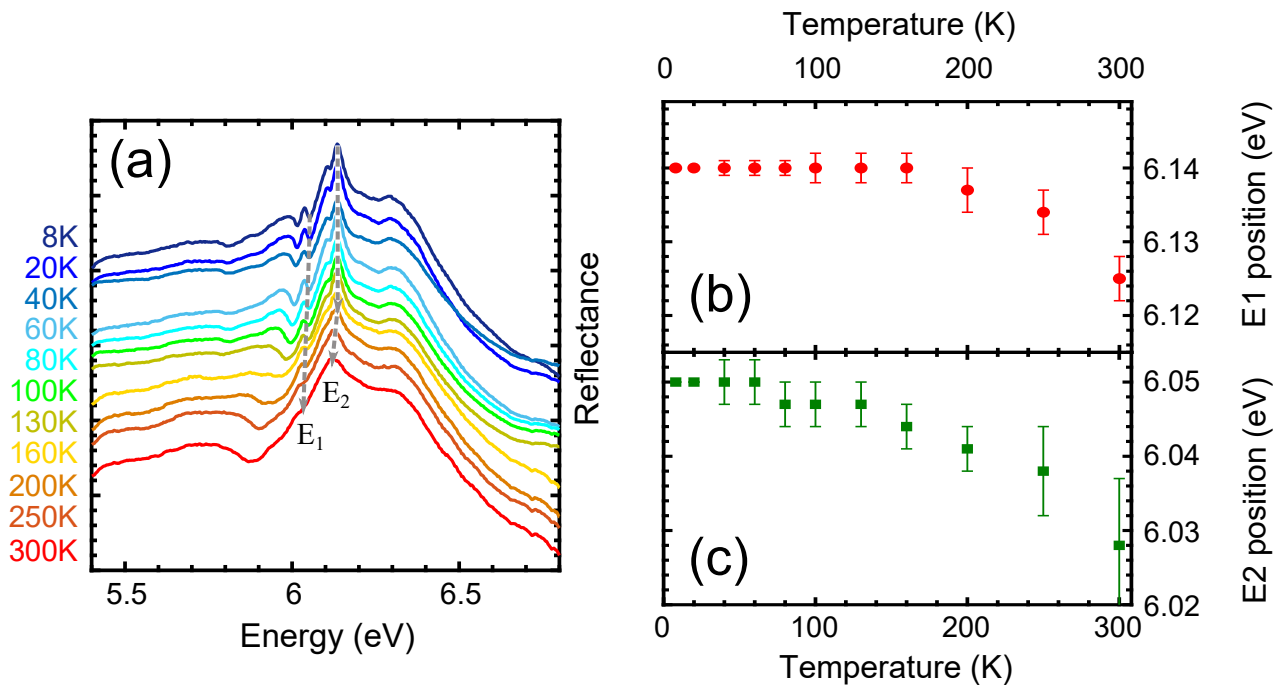


**Figure A.4: Reflectance spectra in bulk h-BN as a function of temperature** (a) Reflectance for different temperatures of the sample. For each spectrum we indicate the temperature on the left side; (b) Variation of the energy position  $E_1$  indicated in panel (a); (c) Variation of the energy position  $E_2$  indicated in panel (a).

The comparison between the plotted curves shows that increasing the temperature produces a broadening of the fine structures, in parallel with the broadening of the large band centered at 6.2 eV. The FWHM of the band at 6.2 eV increases about 160 meV from 8K to room temperature. This broadening is accompanied by a shift of the relative maxima toward lower energies. In figures A.4 (b) and (c) we show the variation of the energy positions of lines  $E_1$  and  $E_2$  highlighted in panel (a). Panels (b) and (c) show that the energies of these two lines decrease in the same way with the increase of temperature.  $E_1$  shifts by about 22 meV towards

lower energies and  $E_2$  red-shifts by about 15 meV from 8K to 300K. Our estimation is in the same order of what was observed in PL [23].

## A.5 Conclusion

In this appendix we provided reflectance measurements performed on h-BN crystals. We firstly presented measured data from samples coming from two different growth sources: Kansas University and HQgraphene company. The one coming from HQgraphene company presented a reflectance spectrum very similar to what was reported previously in the Literature. The one coming from Kansas State University (sample K1) showed a reflectance spectrum with a rich fine structure that led us to identify the phonon-assisted transitions of the  $iX$  lying at 5.95 eV. This improvement in the experimental setup is related to two effects: firstly the size and the quality of the samples grown in Kansas State University. Secondly the size of the spot provided by the Xenon-plasma light source is smaller than the size of a single crystal in our sample. We finally provided temperature-dependent measurements from 8K to room temperature.

The interpretation of our reflectance data is still work in progress in order to elucidate in details the physics lying behind the large reflectance band centered at 6.2 eV and the contribution of direct exciton to these reflectance measurements.



## T-DEPENDENCE OF REFLECTANCE MEASUREMENTS IN MBN

In this appendix we present temperature-dependence of reflectance measurements that we performed on sample N<sub>2</sub>. The measurements were realized in a nitrogen environment, by varying the temperature of the sample from 8K to room temperature (300 K). The light source utilized was Deuterium lamp. These measurements are displayed in figure B.1 for a spectral range between 5.7 and 6.6 eV. The spectra are vertically shifted for clarity.

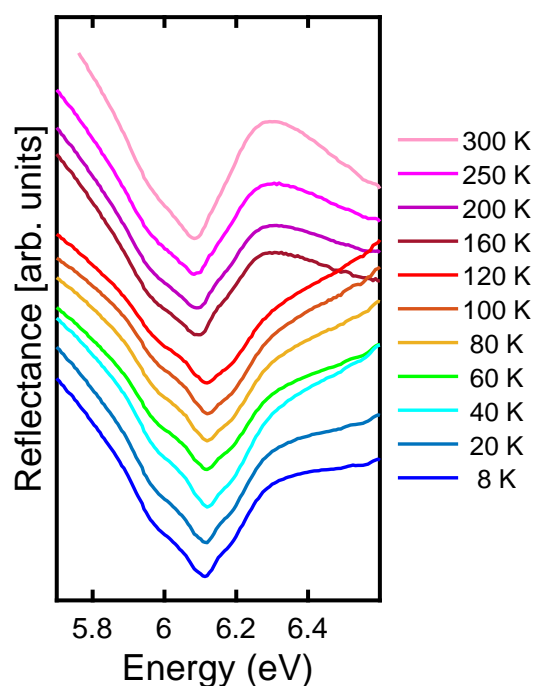


**Figure B.1: Temperature dependence of reflectance in mBN:** All spectra are vertically shifted for clarity. These measurements were performed on sample N<sub>2</sub>.

These measurements do not provide us any additional information on intrinsic physics in mBN due to the large width of the reflectance lines.





## THEORETICAL MODEL USED TO FIT OUR REFLECTANCE DATA: QUANTUM APPROACH

In this appendix, we reproduce the theoretical model developed in order to calculate reflectance for MoSe<sub>2</sub> single layer encapsulated in hexagonal boron nitride. Their results are given in Ref.[130, 124]. They use exfoliated h-BN and MoSe<sub>2</sub> monolayers deposited on SiO<sub>2</sub>/Si substrates.

In their model they consider a normally incident plane wave reflecting on the MoSe<sub>2</sub> monolayers embedded between dielectric layers. The system is considered to be invariant in the xy plane and the incident wave to be propagating along the z axis.

Within the Born-Markov approximation, the positive part of the electric field evolves as:

$$E^+(z, t) = E_0^+(z, t) + \frac{k_0^2}{\epsilon_0} G(z) P_{2D}^+(t). \quad (\text{C.1})$$

$E_0^+(z, t)$  being the free evolution of the electric field without MoSe<sub>2</sub> layer;  $k_0$  is the free space wave-number of the incident field;  $G(z)$  is the electromagnetic Green's function. It is calculated from the transfer matrix techniques.  $P_{2D}^+(t)$  is the two-dimensional polarization of the TMD monolayer with  $P_{2D}^+ = \wp c$  with  $\wp$  being the dipole moment of the exciton transition and  $c$  the exciton annihilation operator given by the master equation as:

$$\begin{aligned} \frac{d}{dt} \langle c|c \rangle &= i(\delta - \Delta + i\tilde{\gamma}) \langle c|c \rangle + i\wp E_0^+ \\ \frac{d}{dt} \langle c^*|c^* \rangle &= -\gamma \langle c^*|c^* \rangle + i\wp E_0^+ \langle c^*|c^* \rangle - i\wp E_0^- \langle c|c \rangle \end{aligned} \quad (\text{C.2})$$

$\delta = \omega - \omega_0$ ;  $\Delta = \alpha\gamma_r k_0 \text{Re}[G(0)]$  (it is equal to null in the vacuum);  $\gamma_r$  denotes the radiative decay rate of the excitons in free space and it is given by:  $\gamma_r = \frac{k_0 \wp^2}{\epsilon_0}$ . The radiative rate is modified by the substrate and it becomes:  $2\gamma_r k_0 \text{Im}[G(0)]$  (in the vacuum  $G(0) = \frac{i}{2k_0}$ ).

At the position  $z=0$  (at the MoSe<sub>2</sub> layer), the electric field is given by:

$$E_r^+ = r_0 E_{in}^+ + \frac{k_0^2}{\epsilon_0} G(0) \wp \langle c|c \rangle \quad (\text{C.3})$$

$r_0$  denotes the complex reflection coefficient of the entire stack of dielectric layers without the MoSe<sub>2</sub> layer. From the equation C.2 they can get  $\langle c|c \rangle = -\frac{\wp E_0^+}{\delta - \Delta + i\tilde{\gamma}}$  and  $\tilde{\gamma} = \gamma_d + \frac{\gamma}{2} =$

$$\gamma_d + \frac{\gamma_{nr}}{2} + \gamma_r k_0 \text{Im}[G(0)],$$

where  $\gamma_{nr}$  denotes the non-radiative decay rate, and  $\gamma_d$  corresponds to the pure dephasing rate between the layers.

We define  $\Gamma = 2\tilde{\gamma} = 2\gamma_d + \gamma_{nr} + 2\gamma_r \text{Im}[G(0)]$ . Replacing these quantities in equation C.3 one gets:

$$\begin{aligned} E_r^+ &= r_0 E_{in}^+ + \frac{k_0^2}{\epsilon_0} G(0) \wp \left( -\frac{\wp E_0^+}{\delta - \Delta + i\tilde{\gamma}} \right) \\ E_r^+ &= r_0 E_{in}^+ - k_0 G(0) \frac{k_0 \wp^2}{\epsilon_0} \frac{E_0^+}{\delta - \Delta + i\tilde{\gamma}} \\ \Rightarrow \frac{E_r^+}{E_{in}^+} &= r_0 - k_0 G(0) \gamma_r \frac{1}{\delta - \Delta + i\tilde{\gamma}} \frac{E_0^+}{E_{in}^+} \end{aligned}$$

$$\text{At } z=0: E_0^+ = (1 + r_0) E_{in}^+ \text{ and } G(0) = \frac{i}{2k_0} (1 + r_0)$$

$$\begin{aligned} \Rightarrow \frac{E_r^+}{E_{in}^+} &= r_0 - \frac{i}{2} (1 + r_0) \frac{\gamma_r}{\delta - \Delta + i\tilde{\gamma}} (1 + r_0) \\ \frac{E_r^+}{E_{in}^+} &= r_0 - (1 + r_0)^2 \frac{\frac{i\gamma_r}{2}}{\delta - \Delta + i\tilde{\gamma}} \end{aligned} \quad (\text{C.4})$$

Finally,

$$\begin{aligned} \tilde{\gamma} &= \gamma_d + \frac{\gamma_{nr}}{2} + \gamma_r k_0 \text{Im}[G(0)] \\ \tilde{\gamma} &= \gamma_d + \frac{\gamma_{nr}}{2} + \gamma_r k_0 \frac{1 + \text{Re}(r_0)}{2k_0} \\ \tilde{\gamma} &= \gamma_d + \frac{\gamma_{nr}}{2} + \frac{\gamma_r}{2} (1 + \text{Re}(r_0)) \end{aligned} \quad (\text{C.5})$$

and for  $\alpha = 1$

$$\begin{aligned} \Delta &= \alpha \gamma_r k_0 \text{Re}[G(0)] \\ \Delta &= \alpha \gamma_r k_0 \left( \frac{\text{Im}(r_0)}{2k_0} \right) \\ \Delta &= \frac{\gamma_r}{2} \text{Im}(r_0) \end{aligned} \quad (\text{C.6})$$

Replacing now equations C.7 and C.6 in C.4 one gets

$$\begin{aligned} r &= \frac{E_r^+}{E_{in}^+} = r_0 - (1 + r_0)^2 \frac{\frac{i\gamma_r}{2}}{\delta - \frac{\gamma_r}{2} \text{Im}(r_0) + i(\gamma_d + \frac{\gamma_{nr}}{2} + \frac{\gamma_r}{2} (1 + \text{Re}(r_0)))} \\ \Rightarrow R = |r|^2 &= \left| r_0 - (1 + r_0)^2 \frac{\frac{i\gamma_r}{2}}{\delta - \text{Im}(r_0) \frac{\gamma_r}{2} + i\frac{\Gamma}{2}} \right|^2 \end{aligned} \quad (\text{C.7})$$

In comparison with their interpretation, we consider in our case a system presenting a single mBN layer grown by MBE on HOPG substrate.  $r_0$  denotes then the complex reflection

---

coefficient of the HOPG in our system and it is given by the real and imaginary parts of the dielectric function of HOPG.

Equation C.7 gives two separated terms: the first one denotes the optical response given by the substrate *i.e.* HOPG, and the second term the response of the mBN layer.

$\gamma_d$  in our case denotes the dephasing rate of the exciton at the interface between the mBN and HOPG.



---

# EPITAXIAL h-BN WITH SUB-MONOLAYER THICKNESS

In this appendix we present PL and reflectance measurements performed during my PhD thesis on h-BN samples with sub-monolayer thicknesses grown by MBE on HOPG substrates. These measurements are in the continuity of our work done on mBN that have been discussed in chapter 3 of this manuscript. The interpretation of the measurements presented in this appendix is not completed yet.

This appendix is split into four parts: in section D.1 we present the growth conditions of our samples on which we performed our optical measurements. In section D.2 we present AFM measurements performed in Nottingham University in order to characterize the morphology of the grown samples. In section D.3 we present PL measurements performed on these samples. Finally we show reflectance measurements (section D.3.2).

## D.1 Motivation

In the continuity of chapter 3 on epitaxial monolayer BN, we present in this appendix PL and reflectance measurements on epitaxial h-BN samples grown by MBE with thicknesses below one monolayer. The growth method of these samples was presented and discussed in chapter 2 (section 2.2.1). The control of the thickness of the deposited h-BN layers was discussed in chapter 3, section 3.2. In this appendix, the thickness of deposited h-BN is controlled by the variation of the boron cell temperature  $T_B$ . We demonstrated in chapter 3 (section 3.2.1) that, in order to achieve a monolayer thickness,  $T_B$  has to be maintained at  $1875^\circ\text{C}$ , with growth time  $t_g=3$  h and  $T_G=1390^\circ\text{C}$ . For temperatures  $T_B$  higher than  $1875^\circ\text{C}$ , the thickness of the deposited h-BN increases and the layers become polycrystalline. PL measurements on these samples demonstrated that the increase of  $T_B$  induces an increase in the intensity of the PL signal related to defects in h-BN (figure 3.20). The emission doublet at 6.05 and 6.08 eV is only present on samples with thickness of 1 ML and this emission disappears for thicker samples. Here, in this appendix we examine the optical response of samples grown by MBE with thicknesses lower than one monolayer. These samples are grown for  $T_B$  lower than  $1875^\circ\text{C}$ . The goal of this work is to study the effect of the possible strain in the heteroepitaxy

of h-BN on HOPG substrate: when the grown domains are small, the strain due to the lattice mismatch with the substrate is higher, and when the domains are large and achieve coalescence in a monolayer, we expect a reduced strain due to the formation of relaxed h-BN domains. Since the lattice parameter of graphene is smaller than the one of h-BN ( $a_G \approx 2.42 \text{ \AA}$  vs  $a_{h-BN} \approx 2.46 \text{ \AA}$ ) we expect a compressive strain of h-BN domains grown on the surface of HOPG.

## D.2 Morphology of the samples

As it was discussed in chapter 3 (section 3.2.1), the growth of high-quality h-BN by MBE requires that the temperature of the source effusion cell ( $T_B$ ) is higher than  $1800^\circ\text{C}$ . Here, the samples have been grown for different boron cell temperature ( $T_B$ ) between  $1800^\circ\text{C}$  and  $1875^\circ\text{C}$  in order to grow high quality h-BN layers with a thickness less than one monolayer. Four different h-BN samples have been grown on HOPG substrates. The growth temperature ( $T_G$ ) was fixed at  $1390^\circ\text{C}$  for a growth time ( $t_g$ ) of 3 h and a Nitrogen flow rate of 2 sccm.  $T_B$  was the only parameter that changes in the growth conditions from one sample to another, with the following values:  $1800^\circ\text{C}$ ,  $1825^\circ\text{C}$ ,  $1850^\circ\text{C}$  and  $1875^\circ\text{C}$ .

The surface morphology of the grown samples was studied using AFM, in Nottingham University. The data were acquired in tapping AFM mode at ambient conditions. These measurements are presented in figure D.1 as a function of  $T_B$ . The upper row presents height images and the bottom one shows their corresponding phase images. Similarly to before, the bright spots in height images correspond to the thickest regions and the dark ones to the thinnest regions. In phase images, it is the reverse case.

For  $T_B=1800^\circ\text{C}$ , figures D.1 (a) and (e) show that h-BN hexagonal domains are grown along the HOPG step edges. As we mentioned previously in chapter 3, at the HOPG step edges the nucleation density is higher than on the HOPG plates. The uncovered HOPG surface appears white in (e). For this sample the surface coverage appears dominated by uncovered HOPG. When  $T_B$  is increased to  $1825^\circ\text{C}$  and  $1850^\circ\text{C}$  (figures D.1 (b), (c), (d) and (f)), the h-BN layers start to coalesce on the HOPG plates in order to form a complete monolayer. The comparison between phase images of samples  $N_8$  and  $N_9$  with sample  $N_7$  shows that the h-BN coverage is comparable in  $N_8$  and  $N_9$  and it is higher than in  $N_7$ . The increase in h-BN coverage for  $N_8$  and  $N_9$  is accompanied by the appearance of bright spots in the height images (b and c). These bright spots are along HOPG step edges. These spots do not appear in figure D.1 (a) for  $T_B=1800^\circ\text{C}$ .

When  $T_B$  is increased to  $1875^\circ\text{C}$ , the surface coverage corresponds to a complete monolayer as it is shown in the phase image (h): no identifiable white regions appear on the surface of this grown sample. In the height image (d) one can identify a surface with a high density of bright spots along the HOPG step edges in comparison with the other grown samples. The morphology of the four grown samples show rather flat h-BN domains deposited on the surface of HOPG. Bright spots start to appear more abundantly on the grown surface when  $T_B$  increases to values higher than  $1875^\circ\text{C}$ . These bright spots correspond to 3D clusters that originate from the step edges where the nucleation density is higher than the one at HOPG plates and from the excess of Boron on the growth surface as we already explained it in chapter 3.

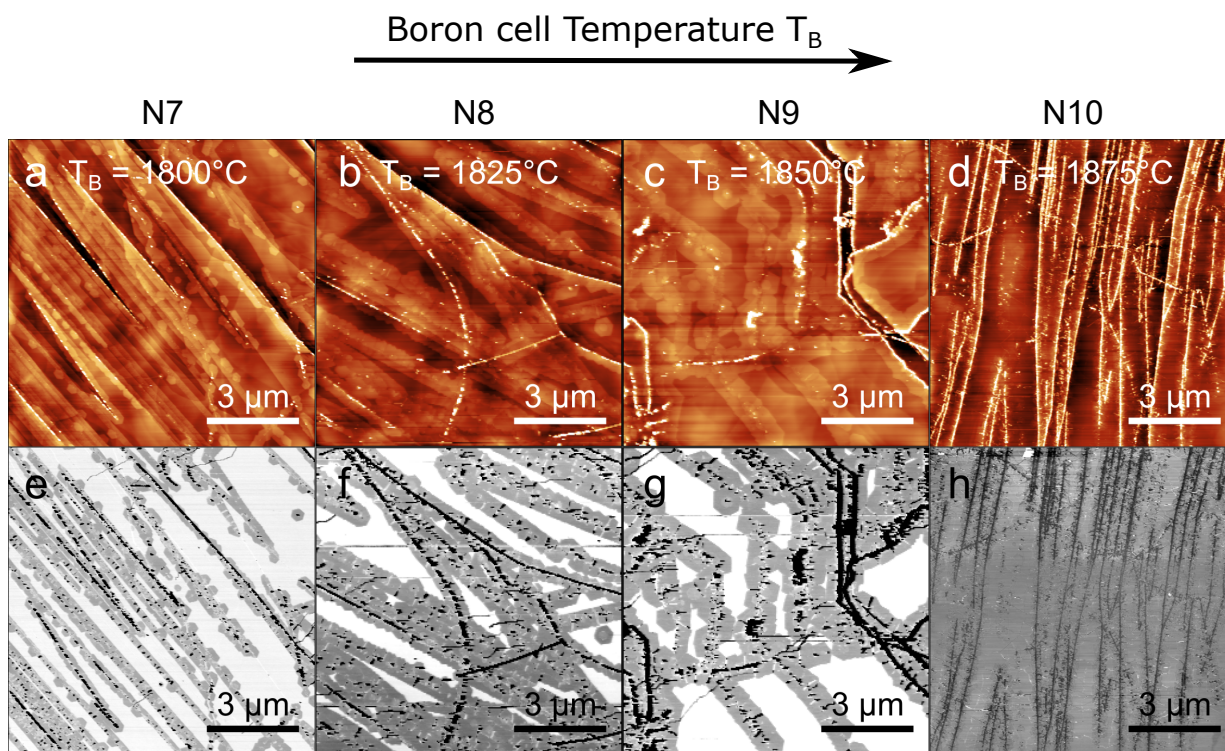


**Figure D.1:** Tapping-mode AFM images measured under ambient conditions on h-BN samples grown by MBE on HOPG substrates for increasing boron cell temperatures: the boron cell temperature increases from left to right; (a-d) are topographic height-channel images showing the evolution of the surface morphology with the increase of the boron cell temperature; (e-h) phase images corresponding to the height ones shown in (a-d). The growth parameters of these samples are given in table D.1 below.

In table D.1, we summarize the growth parameters of h-BN samples that are presented in figure D.1 with their coverage as it appears in AFM images.

Sample	$T_G$	$T_B$	$t_g$	Coverage thickness
N7	1390°C	1800°C	3 hrs	$\leq$ monolayer
N8	1390°C	1825°C	3 hrs	$\leq$ monolayer
N9	1390°C	1850°C	3 hrs	$\leq$ monolayer
N10	1390°C	1875°C	3 hrs	$\sim$ monolayer

**Table D.1:** Growth parameters of the h-BN samples grown by Molecular Beam Epitaxy under ultra-high vacuum conditions in Nottingham University and the estimated thickness of each sample.

## D.3 Experimental results

In this section we present our experimental measurements on h-BN samples with sub-monolayer thicknesses grown by MBE. We will present our PL measurements on the four samples and later the corresponding reflectance measurements, in order to study the influence of the strain given by the substrate on the opto-electronic properties of mBN.

### D.3.1 PL measurements

In order to study the optical properties of the different samples presented in figure D.1, we first performed PL measurements using our experimental setup that was presented in chapter 2 (section 2.1.2). The PL spectra have been recorded in the same conditions, at a cryogenic temperature 8K. The excitation energies for each spectrum are given in the caption of figure D.2 (a). The four recorded spectra are plotted in a linear scale in figures D.2 (a) and (b) after subtraction of the laser diffusion.

In Figure D.1 (a) we plot the recorded spectra for a spectral range between 5.2 and 6.2 eV. This figure shows that the PL signal recorded from samples N9 and N10 exhibit a broad band emission centered at 5.5 eV and a PL doublet at 6.05 and 6.1 eV. For samples N8 and N7 we observe that the PL spectra present only emission lines around the energies of the PL doublet and that the emission of a broad band at 5.5 eV disappears from the PL spectra of these two samples. The comparison between the four recorded spectra shows that the intensity of the PL signal increases with the increase of  $T_B$ . This effect was already observed in chapter 3 (figure 3.20). Moreover, the PL intensity at 5.5 eV increases in an abrupt way from N9 to N10: the PL intensity at 5.5 eV in N10 is higher than in N9 by a factor of 50. These results are in agreement with the AFM images, for which we observe that the density of bright spots on the grown surface increases. In sample N7 no bright spots appear on the surface.

In order to analyze the variation of the PL signal at the energies of the doublet as a

function of the different samples, we re-plot the four spectra in figure D.2 (b) for a narrower spectral range (between 5.9 and 6.13 eV). The spectra are vertically shifted for clarity. For each spectrum we indicate the energy position of the corresponding Raman line by vertical arrows:  $E_{RRS}=E_{exc}-2\Delta$ , with  $\Delta=159$  meV (chapter 3, section 3.3.1). The comparison between the four spectra shows that with the decrease of  $T_B$ , the intensity of the PL doublet decreases. The intensity of the emission line at 6.05 eV decreases and this emission disappears from the emission spectrum of N7. The emission line at 6.1 eV shows that its intensity depends on the sample, it corresponds to PL in the spectrum recorded from N10, while it corresponds to RRS in the spectra measured from N9, N8 and N7.

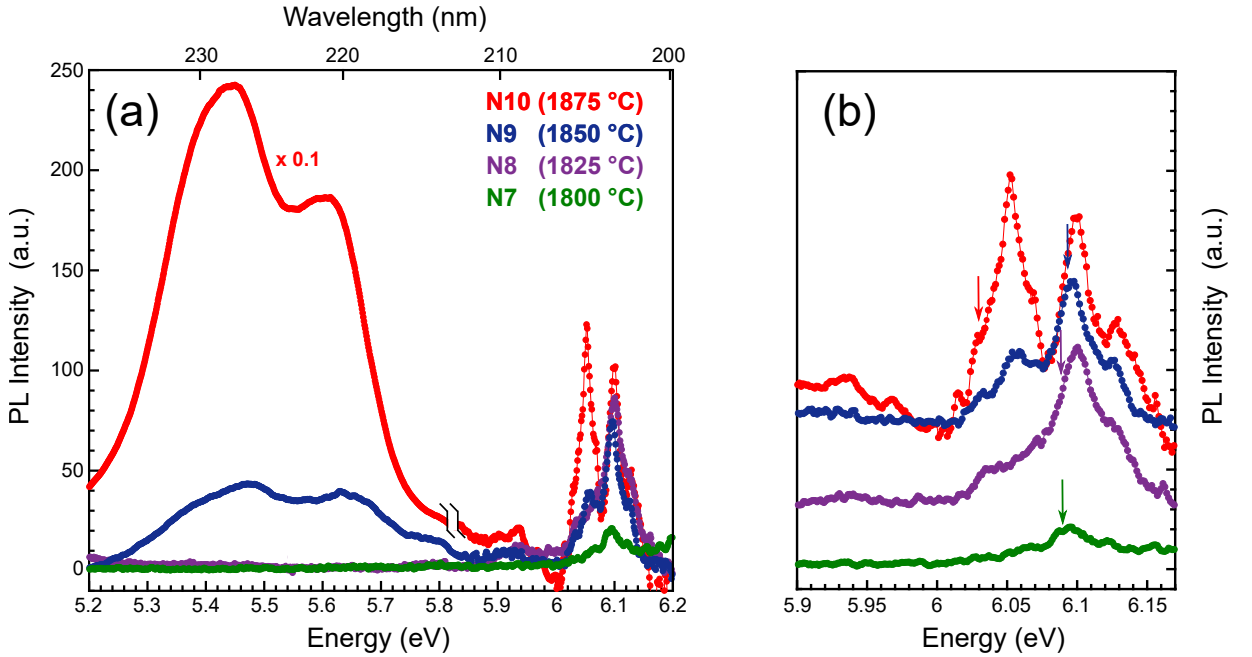


**Figure D.2: Photoluminescence spectroscopy of h-BN epilayers measured at 8K:** (a) PL data plotted in a linear scale after subtraction of the laser diffusion. The excitation energies are  $E_{exc}$ : 6.407 eV (193.5 nm), 6.407 eV (193.5 nm), 6.413 eV (193.3 nm) and 6.351 eV (195.2 nm) for N7, N8, N9 and N10 respectively; (b) same Data as (a) plotted in the spectral range from 5.9 to 6.17 eV; the spectra are vertically shifted. The vertical arrows correspond to:  $E_{exc} - 2\Delta$ , with  $\Delta=159$  meV. The samples are grown with four different MBE boron source temperatures  $T_B$  : N7 :1800°C, N8: 1825°C, N9:1850°C, N10: 1875°C. The surface morphology of these samples is presented in figure D.1.

The PL spectra recorded on these samples exhibit an energy splitting of about 45 meV between the two PL lines of the doublet (samples N9 and N10). This energy splitting is larger than what we measured on our previous samples (N1: 34 meV, see figure 3.25), on which we performed the measurements detailed in chapter 3. Moreover, for sample N1 that was grown under the same conditions as sample N10, the PL signal showed an intensity of the PL doublet higher than the one of defects in h-BN at 5.5 eV. In N10 the intensity of the 5.5 eV band

predominates.

### D.3.2 Reflectance measurements

In this section, we present reflectance measurements performed on the four samples presented previously. The four measured reflectance spectra are presented in figure D.3 (a). We normalized them with respect to the maximum at 5 eV.

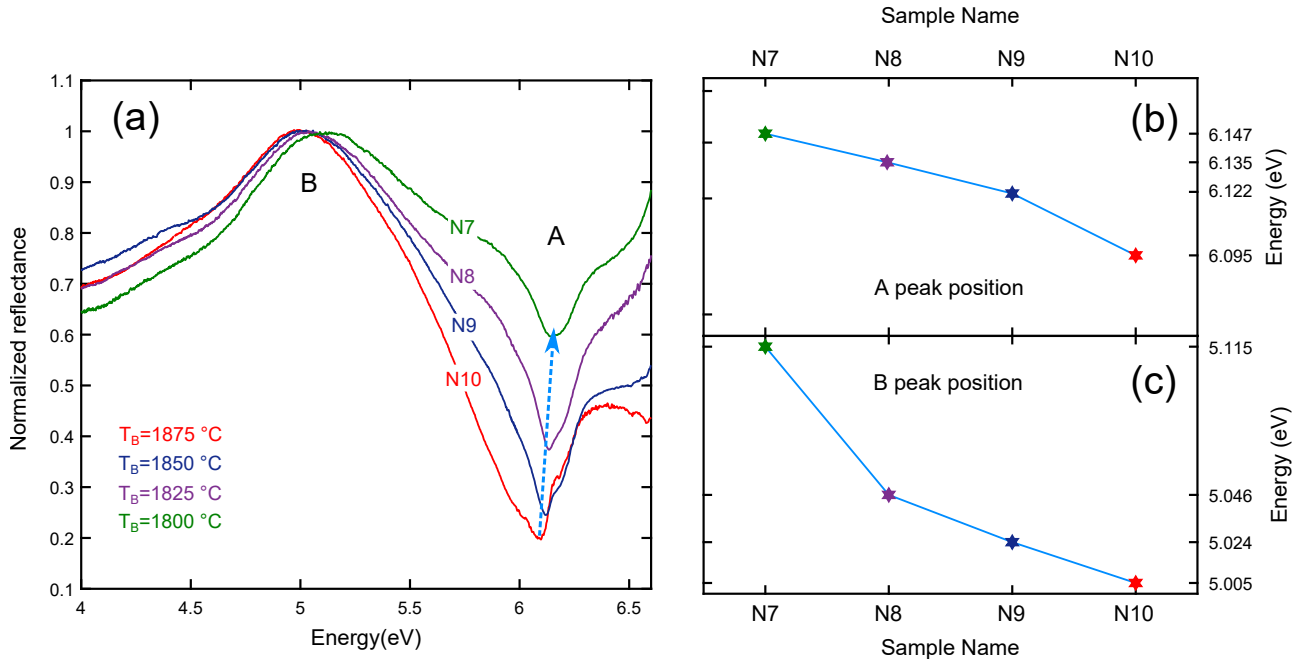


**Figure D.3:** DUV reflectance spectra for several h-BN epilayers samples measured at 8 K, obtained for different MBE boron cell temperatures  $T_B$ : (a)  $T_B=1800^\circ\text{C}$ ,  $1825^\circ\text{C}$ ,  $1850^\circ\text{C}$  and  $1875^\circ\text{C}$  and a growth time  $t_g$ : 3 hours; (b) variation of the A peak position in reflectance spectra presented in (a) as a function of  $T_B$ ; (c) variation of the B peak position in reflectance spectra presented in (a) as a function of  $T_B$ . The surface morphology of these samples is presented in figure D.1.

The four reflectance spectra show a smooth variation between 4 and 5.2 eV, with an increase of the reflectance level by a factor of  $\sim 1.5$  between 4 and 5 eV. For energies higher than 5 eV, we observe pronounced dips around 6.1 eV, similarly to what was observed in chapter 3 (figure 3.24) on the other mBN samples (N1, N2 and N6). The comparison between the four spectra shows that the contrast observed in the reflectance dip between 5 and 6.1 eV depends on the sample. This contrast decreases from  $\sim 5$  in sample N10, to  $\sim 4$  in N9,  $\sim 3$  in N8 to about 2 in N7. This decrease in contrast is related to the h-BN coverage on the HOPG surface. The decrease in contrast is accompanied by an energy shift toward higher energies between N10 and N7 for the dip around 6 eV (labeled A). Additionally to a shift towards higher energies for the maximum around 5 eV (labeled B). The energy shift of the maxima B and minima A

for each sample are given in figures D.3 (b) and (c), respectively. They both shift similarly: the minimum A shifts by about 52 meV from N10 to N7 (figure D.3 (b)) and the maximum B shifts about 110 meV from N10 to N7 (figure D.3 (c)).

## D.4 Conclusion

In this appendix we provided AFM images on h-BN samples grown by MBE on HOPG substrates. The coverage of the h-BN was varying from one monolayer to below monolayer. Our samples have been studied using PL and reflectance spectroscopy.

PL measurements showed the presence of a large emission band centered at 5.5 eV for samples N10 and N9 and which corresponds to defects in h-BN. This emission was observed in parallel to the emission of the PL doublet at 6.05 and 6.1 eV and which corresponds to the recombination of the direct exciton in mBN. The emission of this PL doublet was observed on the PL spectra measured from N9 and N10, except that the intensity of the PL signal at these energies was dependent of the h-BN coverage. For samples N8 and N7 only RRS signal is recorded at these energies.

Reflectance measurements showed the presence of a minimum around 6.1 eV corresponding to direct gap in mBN. The contrast given by the minimum depends on the samples and more importantly the energy of the minima changes with the h-BN coverage. This change may be the first evidence of a dependence of the band gap energy with the strain given by the HOPG substrate.



---

# REFERENCES

- [1] K. S. Novoselov. Electric Field Effect in Atomically Thin Carbon Films. *Science*, 306 (5696):666–669, October 2004. ISSN 0036-8075, 1095-9203. doi: 10.1126/science.1102896. URL <http://www.sciencemag.org/cgi/doi/10.1126/science.1102896>.
- [2] Kin Fai Mak, Changgu Lee, James Hone, Jie Shan, and Tony F. Heinz. Atomically Thin MoS<sub>2</sub>: A New Direct-Gap Semiconductor. *Physical Review Letters*, 105(13):136805, September 2010. ISSN 0031-9007, 1079-7114. doi: 10.1103/PhysRevLett.105.136805. URL <https://link.aps.org/doi/10.1103/PhysRevLett.105.136805>.
- [3] Wei-Ting Hsu, Li-Syuan Lu, Dean Wang, Jing-Kai Huang, Ming-Yang Li, Tay-Rong Chang, Yi-Chia Chou, Zhen-Yu Juang, Horng-Tay Jeng, Lain-Jong Li, and Wen-Hao Chang. Evidence of indirect gap in monolayer WSe<sub>2</sub>. *Nature Communications*, 8 (1):929, December 2017. ISSN 2041-1723. doi: 10.1038/s41467-017-01012-6. URL <http://www.nature.com/articles/s41467-017-01012-6>.
- [4] Effectiveness of 222-nm ultraviolet light on disinfecting SARS-CoV-2 surface contamination, Elsevier Enhanced Reader.
- [5] Myungsoo Kim, Emiliano Pallecchi, Ruijing Ge, Xiaohan Wu, Guillaume Ducournau, Jack C. Lee, Henri Happy, and Deji Akinwande. Analogue switches made from boron nitride monolayers for application in 5G and terahertz communication systems. *Nature Electronics*, 3(8):479–485, August 2020. ISSN 2520-1131. doi: 10.1038/s41928-020-0416-x. URL <https://www.nature.com/articles/s41928-020-0416-x>. Number: 8 Publisher: Nature Publishing Group.
- [6] M. E. Turiansky, A. Alkauskas, and C. G. Van de Walle. Spinning up quantum defects in 2D materials. *Nature Materials*, 19(5):487–489, May 2020. ISSN 1476-4660. doi: 10.1038/s41563-020-0668-x. URL <https://www.nature.com/articles/s41563-020-0668-x>. Number: 5 Publisher: Nature Publishing Group.
- [7] Naifu Zhang, Yanpeng Song, Kaiyao Zhou, and Wenjun Wang. Enhanced performance of solar-blind photodetector of hexagonal boron nitride with bottom-contact electrodes. *AIP Advances*, 10(8):085013, August 2020. doi: 10.1063/5.0010182. URL <https://aip.scitation.org/doi/10.1063/5.0010182>. Publisher: American Institute of Physics.
- [8] Fulvio Paleari, Thomas Galvani, Hakim Amara, François Ducastelle, Alejandro Molina-Sánchez, and Ludger Wirtz. Excitons in few-layer hexagonal boron nitride: Davydov splitting and surface localization. *2D Materials*, 5(4):045017, August 2018. ISSN 2053-1583. doi: 10.1088/2053-1583/aad586. URL <http://stacks.iop.org/2053-1583/5/i=4/a=045017?key=crossref.d4ed3c3461abd8c6f845f8038fdb2ec>.

- [9] Darshana Wickramaratne, Leigh Weston, and Chris G. Van de Walle. Monolayer to Bulk Properties of Hexagonal Boron Nitride. *The Journal of Physical Chemistry C*, 122(44): 25524–25529, November 2018. ISSN 1932-7447, 1932-7455. doi: 10.1021/acs.jpcc.8b09087. URL <https://pubs.acs.org/doi/10.1021/acs.jpcc.8b09087>.
- [10] W.H. Balmain. XLVI. *Observations on the formation of compounds of boron and silicon with nitrogen and certain metals.* *The London, Edinburgh, and Dublin Philosophical Magazine and Journal of Science*, 21(138):270–277, October 1842. ISSN 1941-5966, 1941-5974. doi: 10.1080/14786444208621545. URL <https://www.tandfonline.com/doi/full/10.1080/14786444208621545>.
- [11] Kenji Watanabe, Takashi Taniguchi, and Hisao Kanda. Direct-bandgap properties and evidence for ultraviolet lasing of hexagonal boron nitride single crystal. *Nature Materials*, 3(6):404–409, June 2004. ISSN 1476-4660. doi: 10.1038/nmat1134. URL <https://doi.org/10.1038/nmat1134>.
- [12] Kenji Watanabe, Takashi Taniguchi, and Hisao Kanda. Ultraviolet luminescence spectra of boron nitride single crystals grown under high pressure and high temperature. *physica status solidi (a)*, 201(11):2561–2565, 2004. ISSN 1521-396X. doi: 10.1002/pssa.200405188. URL <https://onlinelibrary.wiley.com/doi/abs/10.1002/pssa.200405188>. eprint: <https://onlinelibrary.wiley.com/doi/pdf/10.1002/pssa.200405188>.
- [13] Y. Kubota, K. Watanabe, O. Tsuda, and T. Taniguchi. Deep Ultraviolet Light-Emitting Hexagonal Boron Nitride Synthesized at Atmospheric Pressure. *Science*, 317(5840): 932–934, August 2007. ISSN 0036-8075, 1095-9203. doi: 10.1126/science.1144216. URL <https://www.sciencemag.org/lookup/doi/10.1126/science.1144216>.
- [14] N.D. Zhigadlo. Crystal growth of hexagonal boron nitride (hBN) from Mg–B–N solvent system under high pressure. *Journal of Crystal Growth*, 402:308–311, September 2014. ISSN 00220248. doi: 10.1016/j.jcrysgro.2014.06.038. URL <https://linkinghub.elsevier.com/retrieve/pii/S0022024814004229>.
- [15] Song Liu, Rui He, Zhipeng Ye, Xiaozhang Du, Jingyu Lin, Hongxing Jiang, Bin Liu, and James H. Edgar. Large-Scale Growth of High-Quality Hexagonal Boron Nitride Crystals at Atmospheric Pressure from an Fe–Cr Flux. *Crystal Growth & Design*, 17(9):4932–4935, September 2017. ISSN 1528-7483. doi: 10.1021/acs.cgd.7b00871. URL <https://doi.org/10.1021/acs.cgd.7b00871>. Publisher: American Chemical Society.
- [16] Jiahan Li, Christine Elias, Gaihua Ye, Dylan Evans, Song Liu, Rui He, Guillaume Cassabois, Bernard Gil, Pierre Valvin, Bin Liu, and James H. Edgar. Single crystal growth of monoisotopic hexagonal boron nitride from a Fe–Cr flux. *Journal of Materials Chemistry*

- C*, 8(29):9931–9935, 2020. ISSN 2050-7526, 2050-7534. doi: 10.1039/D0TC02143A. URL <http://xlink.rsc.org/?DOI=D0TC02143A>.
- [17] Jiahan Li, Chao Yuan, Christine Elias, Junyong Wang, Xiaotian Zhang, Gaihua Ye, Chaoran Huang, Martin Kuball, Goki Eda, Joan M. Redwing, Rui He, Guillaume Cassabois, Bernard Gil, Pierre Valvin, Thomas Pelini, Bin Liu, and James H. Edgar. Hexagonal Boron Nitride Single Crystal Growth from Solution with a Temperature Gradient. *Chemistry of Materials*, 32(12):5066–5072, June 2020. ISSN 0897-4756, 1520-5002. doi: 10.1021/acs.chemmater.0c00830. URL <https://pubs.acs.org/doi/10.1021/acs.chemmater.0c00830>.
- [18] O. HASSEL. *Norske geol. Tidsskr.*, 9(266), March 1926.
- [19] R. S. Pease. (1): Crystal structure of boron nitride, *Nature*, may 6, 1950 vol. 165; (2): An X-ray study of boron nitride. *Acta Crystallographica*, 5(3):356–361, 1952. ISSN 0365-110X. doi: 10.1107/S0365110X52001064. URL <https://onlinelibrary.wiley.com/doi/abs/10.1107/S0365110X52001064>.
- [20] R. Geick, C. H. Perry, and G. Rupprecht. Normal Modes in Hexagonal Boron Nitride. *Physical Review*, 146(2):543–547, June 1966. ISSN 0031-899X. doi: 10.1103/PhysRev.146.543. URL <https://link.aps.org/doi/10.1103/PhysRev.146.543>.
- [21] E. Doni and G. Pastori Parravicini. Energy bands and optical properties of hexagonal boron nitride and graphite. *Il Nuovo Cimento B (1965-1970)*, 64(1):117–144, November 1969. ISSN 1826-9877. doi: 10.1007/BF02710286. URL <https://doi.org/10.1007/BF02710286>.
- [22] R. J. Nemanich, S. A. Solin, and Richard M. Martin. Light scattering study of boron nitride microcrystals. *Physical Review B*, 23(12):6348–6356, June 1981. ISSN 0163-1829. doi: 10.1103/PhysRevB.23.6348. URL <https://link.aps.org/doi/10.1103/PhysRevB.23.6348>.
- [23] T. Q. P. Vuong, S. Liu, A. Van der Lee, R. Cuscó, L. Artús, T. Michel, P. Valvin, J. H. Edgar, G. Cassabois, and B. Gil. Isotope engineering of van der Waals interactions in hexagonal boron nitride. *Nature Materials*, 17(2):152–158, February 2018. ISSN 1476-1122, 1476-4660. doi: 10.1038/nmat5048. URL <http://www.nature.com/articles/nmat5048>.
- [24] X. Blase, Angel Rubio, Steven G. Louie, and Marvin L. Cohen. Quasiparticle band structure of bulk hexagonal boron nitride and related systems. *Physical Review B*, 51(11):6868–6875, March 1995. ISSN 0163-1829, 1095-3795. doi: 10.1103/PhysRevB.51.6868. URL <https://link.aps.org/doi/10.1103/PhysRevB.51.6868>.

- [25] Thomas Galvani, Fulvio Paleari, Henrique P. C. Miranda, Alejandro Molina-Sánchez, Ludger Wirtz, Sylvain Latil, Hakim Amara, and François Ducastelle. Excitons in boron nitride single layer. *Physical Review B*, 94(12):125303, September 2016. doi: 10.1103/PhysRevB.94.125303. URL <https://link.aps.org/doi/10.1103/PhysRevB.94.125303>. Publisher: American Physical Society.
- [26] A. Nagashima, N. Tejima, Y. Gamou, T. Kawai, and C. Oshima. Electronic dispersion relations of monolayer hexagonal boron nitride formed on the Ni(111) surface. *Physical Review B*, 51(7):4606–4613, February 1995. ISSN 0163-1829, 1095-3795. doi: 10.1103/PhysRevB.51.4606. URL <https://link.aps.org/doi/10.1103/PhysRevB.51.4606>.
- [27] A. Nagashima, N. Tejima, Y. Gamou, T. Kawai, and C. Oshima. Electronic Structure of Monolayer Hexagonal Boron Nitride Physisorbed on Metal Surfaces. *Physical Review Letters*, 75(21):3918–3921, November 1995. ISSN 0031-9007, 1079-7114. doi: 10.1103/PhysRevLett.75.3918. URL <https://link.aps.org/doi/10.1103/PhysRevLett.75.3918>.
- [28] D. Usachov, V. K. Adamchuk, D. Haberer, A. Grüneis, H. Sachdev, A. B. Preobrajenski, C. Laubschat, and D. V. Vyalikh. Quasifreestanding single-layer hexagonal boron nitride as a substrate for graphene synthesis. *Physical Review B*, 82(7):075415, August 2010. ISSN 1098-0121, 1550-235X. doi: 10.1103/PhysRevB.82.075415. URL <https://link.aps.org/doi/10.1103/PhysRevB.82.075415>.
- [29] A. Catellani, M. Posternak, A. Baldereschi, H. J. F. Jansen, and A. J. Freeman. Electronic interlayer states in hexagonal boron nitride. *Physical Review B*, 32(10):6997–6999, November 1985. ISSN 0163-1829. doi: 10.1103/PhysRevB.32.6997. URL <https://link.aps.org/doi/10.1103/PhysRevB.32.6997>.
- [30] A. Catellani, M. Posternak, A. Baldereschi, and A. J. Freeman. Bulk and surface electronic structure of hexagonal boron nitride. *Physical Review B*, 36(11):6105–6111, October 1987. ISSN 0163-1829. doi: 10.1103/PhysRevB.36.6105. URL <https://link.aps.org/doi/10.1103/PhysRevB.36.6105>.
- [31] Ludger Wirtz, Andrea Marini, Myrta Gruning, and Angel Rubio. Excitonic effects in optical absorption and electron-energy loss spectra of hexagonal boron nitride. page 5.
- [32] B. Arnaud, S. Lebègue, P. Rabiller, and M. Alouani. Huge Excitonic Effects in Layered Hexagonal Boron Nitride. *Physical Review Letters*, 96(2):026402, January 2006. ISSN 0031-9007, 1079-7114. doi: 10.1103/PhysRevLett.96.026402. URL <https://link.aps.org/doi/10.1103/PhysRevLett.96.026402>.
- [33] Ludger Wirtz, Andrea Marini, and Angel Rubio. Excitons in Boron Nitride Nanotubes: Dimensionality Effects. *Physical Review Letters*, 96(12):126104, March 2006. ISSN

- 0031-9007, 1079-7114. doi: 10.1103/PhysRevLett.96.126104. URL <https://link.aps.org/doi/10.1103/PhysRevLett.96.126104>.
- [34] Giorgia Fugallo, Matteo Aramini, Jaakko Koskelo, Kenji Watanabe, Takashi Taniguchi, Mikko Hakala, Simo Huotari, Matteo Gatti, and Francesco Sottile. Exciton energy-momentum map of hexagonal boron nitride. *Physical Review B*, 92(16):165122, October 2015. ISSN 1098-0121, 1550-235X. doi: 10.1103/PhysRevB.92.165122. URL <https://link.aps.org/doi/10.1103/PhysRevB.92.165122>.
- [35] John Vinson, Terrence Jach, Matthias Müller, Rainer Unterumsberger, and Burkhard Beckhoff. Resonant x-ray emission of hexagonal boron nitride. *Physical Review B*, 96(20):205116, November 2017. ISSN 2469-9950, 2469-9969. doi: 10.1103/PhysRevB.96.205116. URL <https://link.aps.org/doi/10.1103/PhysRevB.96.205116>.
- [36] Lorenzo Sponza, Hakim Amara, Claudio Attaccalite, Sylvain Latil, Thomas Galvani, Fulvio Paleari, Ludger Wirtz, and François Ducastelle. Direct and indirect excitons in boron nitride polymorphs: A story of atomic configuration and electronic correlation. *Physical Review B*, 98(12):125206, September 2018. ISSN 2469-9950, 2469-9969. doi: 10.1103/PhysRevB.98.125206. URL <https://link.aps.org/doi/10.1103/PhysRevB.98.125206>.
- [37] Jaakko Koskelo, Giorgia Fugallo, Mikko Hakala, Matteo Gatti, Francesco Sottile, and Pierluigi Cudazzo. Excitons in van der Waals materials: From monolayer to bulk hexagonal boron nitride. *Physical Review B*, 95(3):035125, January 2017. ISSN 2469-9950, 2469-9969. doi: 10.1103/PhysRevB.95.035125. URL <https://link.aps.org/doi/10.1103/PhysRevB.95.035125>.
- [38] Hugo Henck, Debora Pierucci, Giorgia Fugallo, José Avila, Guillaume Cassabois, Yannick J. Dappe, Mathieu G. Silly, Chaoyu Chen, Bernard Gil, Matteo Gatti, Francesco Sottile, Fausto Sirotti, Maria C. Asensio, and Abdelkarim Ouerghi. Direct observation of the band structure in bulk hexagonal boron nitride. *Physical Review B*, 95(8):085410, February 2017. ISSN 2469-9950, 2469-9969. doi: 10.1103/PhysRevB.95.085410. URL <https://link.aps.org/doi/10.1103/PhysRevB.95.085410>.
- [39] Peter Y. Yu and Manuel Cardona. *Fundamentals of semiconductors: physics and materials properties ; with 52 tables and 116 problems*. Springer, Berlin, 3., rev. and enl. ed., 3, corr. print edition, 2005. ISBN 978-3-540-25470-6. OCLC: 254608096.
- [40] Claus F. Klingshirn. *Semiconductor Optics*. Advanced Texts in Physics. Springer-Verlag, Berlin Heidelberg, 2 edition, 2005. ISBN 978-3-540-26846-8. doi: 10.1007/b138175. URL <https://www.springer.com/gp/book/9783540268468>.

- [41] Tsuneya Ando. Effects of Valley Mixing and Exchange on Excitons in Carbon Nanotubes with Aharonov–Bohm Flux. *Journal of the Physical Society of Japan*, 75(2):024707, February 2006. ISSN 0031-9015, 1347-4073. doi: 10.1143/JPSJ.75.024707. URL <https://journals.jps.jp/doi/10.1143/JPSJ.75.024707>.
- [42] Tsuneya Ando and Seiji Uryu. Theory of excitons in carbon nanotubes. *physica status solidi c*, 6(1):173–180, 2009. ISSN 1610-1642. doi: 10.1002/pssc.200879805. URL <https://onlinelibrary.wiley.com/doi/abs/10.1002/pssc.200879805>.
- [43] Léonard Schué, Lorenzo Sponza, Alexandre Plaud, Hakima Bensalah, Kenji Watanabe, Takashi Taniguchi, François Ducastelle, Annick Loiseau, and Julien Barjon. Bright Luminescence from Indirect and Strongly Bound Excitons in h-BN. *Physical Review Letters*, 122(6):067401, February 2019. ISSN 0031-9007, 1079-7114. doi: 10.1103/PhysRevLett.122.067401. URL <https://link.aps.org/doi/10.1103/PhysRevLett.122.067401>.
- [44] R. Schuster, C. Habenicht, M. Ahmad, M. Knupfer, and B. Büchner. Direct observation of the lowest indirect exciton state in the bulk of hexagonal boron nitride. *Physical Review B*, 97(4):041201, January 2018. ISSN 2469-9950, 2469-9969. doi: 10.1103/PhysRevB.97.041201. URL <https://link.aps.org/doi/10.1103/PhysRevB.97.041201>.
- [45] G. Cassabois, P. Valvin, and B. Gil. Hexagonal boron nitride is an indirect bandgap semiconductor. *Nature Photonics*, 10(4):262–266, April 2016. ISSN 1749-4885, 1749-4893. doi: 10.1038/nphoton.2015.277. URL <http://www.nature.com/articles/nphoton.2015.277>.
- [46] E. Rokuta, Y. Hasegawa, K. Suzuki, Y. Gamou, C. Oshima, and A. Nagashima. Phonon Dispersion of an Epitaxial Monolayer Film of Hexagonal Boron Nitride on Ni(111). *Physical Review Letters*, 79(23):4609–4612, December 1997. ISSN 0031-9007, 1079-7114. doi: 10.1103/PhysRevLett.79.4609. URL <https://link.aps.org/doi/10.1103/PhysRevLett.79.4609>.
- [47] D. Sánchez-Portal and E. Hernández. Vibrational properties of single-wall nanotubes and monolayers of hexagonal BN. *Physical Review B*, 66(23):235415, December 2002. doi: 10.1103/PhysRevB.66.235415. URL <https://link.aps.org/doi/10.1103/PhysRevB.66.235415>. Publisher: American Physical Society.
- [48] Ludger Wirtz, Angel Rubio, Raul Arenal de la Concha, and Annick Loiseau. *Ab initio* calculations of the lattice dynamics of boron nitride nanotubes. *Physical Review B*, 68(4):045425, July 2003. ISSN 0163-1829, 1095-3795. doi: 10.1103/PhysRevB.68.045425. URL <https://link.aps.org/doi/10.1103/PhysRevB.68.045425>.

- [49] J. Kulda, H. Kainzmaier, D. Strauch, B. Dorner, M. Lorenzen, and M. Krisch. Overbending of the longitudinal optical phonon branch in diamond as evidenced by inelastic neutron and x-ray scattering. *Physical Review B*, 66(24):241202, December 2002. ISSN 0163-1829, 1095-3795. doi: 10.1103/PhysRevB.66.241202. URL <https://link.aps.org/doi/10.1103/PhysRevB.66.241202>.
- [50] Roman V. Gorbachev, Ibtisam Riaz, Rahul R. Nair, Rashid Jalil, Liam Britnell, Branson D. Belle, Ernie W. Hill, Kostya S. Novoselov, Kenji Watanabe, Takashi Taniguchi, Andre K. Geim, and Peter Blake. Hunting for Monolayer Boron Nitride: Optical and Raman Signatures. *Small*, 7(4):465–468, February 2011. ISSN 16136810. doi: 10.1002/smll.201001628. URL <http://doi.wiley.com/10.1002/smll.201001628>.
- [51] Qiran Cai, Declan Scullion, Aleksey Falin, Kenji Watanabe, Takashi Taniguchi, Ying Chen, Elton J. G. Santos, and Lu Hua Li. Raman signature and phonon dispersion of atomically thin boron nitride. *Nanoscale*, 9(9):3059–3067, 2017. ISSN 2040-3364, 2040-3372. doi: 10.1039/C6NR09312D. URL <http://xlink.rsc.org/?DOI=C6NR09312D>.
- [52] R. Geick, C. H. Perry, and G. Rupprecht. Normal Modes in Hexagonal Boron Nitride. *Physical Review*, 146(2):543–547, June 1966. ISSN 0031-899X. doi: 10.1103/PhysRev.146.543. URL <https://link.aps.org/doi/10.1103/PhysRev.146.543>.
- [53] Ramon Cuscó, Bernard Gil, Guillaume Cassabois, and Luis Artús. Temperature dependence of Raman-active phonons and anharmonic interactions in layered hexagonal BN. *Physical Review B*, 94(15):155435, October 2016. ISSN 2469-9950, 2469-9969. doi: 10.1103/PhysRevB.94.155435. URL <https://link.aps.org/doi/10.1103/PhysRevB.94.155435>.
- [54] G. Kern, G. Kresse, and J. Hafner. *Ab initio* calculation of the lattice dynamics and phase diagram of boron nitride. *Physical Review B*, 59(13):8551–8559, April 1999. ISSN 0163-1829, 1095-3795. doi: 10.1103/PhysRevB.59.8551. URL <https://link.aps.org/doi/10.1103/PhysRevB.59.8551>.
- [55] K. H. Michel and B. Verberck. Phonon dispersions and piezoelectricity in bulk and multilayers of hexagonal boron nitride. *Physical Review B*, 83(11):115328, March 2011. ISSN 1098-0121, 1550-235X. doi: 10.1103/PhysRevB.83.115328. URL <https://link.aps.org/doi/10.1103/PhysRevB.83.115328>.
- [56] J. Serrano, F. J. Manjón, A. H. Romero, A. Ivanov, M. Cardona, R. Lauck, A. Bosak, and M. Krisch. Phonon dispersion relations of zinc oxide: Inelastic neutron scattering and *ab initio* calculations. *Physical Review B*, 81(17):174304, May 2010. ISSN 1098-0121, 1550-235X. doi: 10.1103/PhysRevB.81.174304. URL <https://link.aps.org/doi/10.1103/PhysRevB.81.174304>.

- [57] T. Kuzuba, K. Era, T. Ishii, and T. Sato. A low frequency Raman-active vibration of hexagonal boron nitride. *Solid State Communications*, 25(11):863–865, March 1978. ISSN 0038-1098. doi: 10.1016/0038-1098(78)90288-0. URL <http://www.sciencedirect.com/science/article/pii/0038109878902880>.
- [58] P. H. Tan, W. P. Han, W. J. Zhao, Z. H. Wu, K. Chang, H. Wang, Y. F. Wang, N. Bonini, N. Marzari, G. Savini, A. Lombardo, and A. C. Ferrari. The Shear Mode of Multi-Layer Graphene. *Nature Materials*, 11(4):294–300, April 2012. ISSN 1476-1122, 1476-4660. doi: 10.1038/nmat3245. URL <http://arxiv.org/abs/1106.1146>. arXiv: 1106.1146.
- [59] G. Cassabois, P. Valvin, and B. Gil. Hexagonal boron nitride is an indirect bandgap semiconductor. *Nature Photonics*, 10:262, January 2016. URL <https://doi.org/10.1038/nphoton.2015.277>.
- [60] Phuong Vuong. Optical spectroscopy of boron nitride heterostructures, PhD thesis. October 2018, Université de Montpellier.
- [61] T. Q. P. Vuong, G. Cassabois, P. Valvin, S. Liu, J. H. Edgar, and B. Gil. Exciton-phonon interaction in the strong-coupling regime in hexagonal boron nitride. *Physical Review B*, 95(20):201202, May 2017. ISSN 2469-9950, 2469-9969. doi: 10.1103/PhysRevB.95.201202. URL <http://link.aps.org/doi/10.1103/PhysRevB.95.201202>.
- [62] X. Z. Du, J. Li, J. Y. Lin, and H. X. Jiang. The origin of deep-level impurity transitions in hexagonal boron nitride. *Applied Physics Letters*, 106(2):021110, January 2015. ISSN 0003-6951, 1077-3118. doi: 10.1063/1.4905908. URL <http://aip.scitation.org/doi/10.1063/1.4905908>.
- [63] G. Cassabois, P. Valvin, and B. Gil. Intervalley scattering in hexagonal boron nitride. *Physical Review B*, 93(3):035207, January 2016. ISSN 2469-9950, 2469-9969. doi: 10.1103/PhysRevB.93.035207. URL <https://link.aps.org/doi/10.1103/PhysRevB.93.035207>.
- [64] Romain Bourrellier, Michele Amato, Luiz Henrique Galvão Tizei, Christine Giorgetti, Alexandre Gloter, Malcolm I. Heggie, Katia March, Odile Stéphan, Lucia Reining, Mathieu Kociak, and Alberto Zobelli. Nanometric Resolved Luminescence in h-BN Flakes: Excitons and Stacking Order. *ACS Photonics*, 1(9):857–862, September 2014. ISSN 2330-4022, 2330-4022. doi: 10.1021/ph500141j. URL <http://pubs.acs.org/doi/10.1021/ph500141j>.
- [65] Monochromator 2016. URL <http://monochromator.us/mono2016.html>.
- [66] Aleksandra B Djuris̃ic and E Herbert Li. Optical properties of graphite. *J. Appl. Phys.*, 85(10):8, 1999.

- [67] T Q P Vuong, G Cassabois, P Valvin, E Rousseau, A Summerfield, C J Mellor, Y Cho, T S Cheng, J D Albar, L Eaves, C T Foxon, P H Beton, S V Novikov, and B Gil. Deep ultraviolet emission in hexagonal boron nitride grown by high-temperature molecular beam epitaxy. *2D Materials*, 4(2):021023, March 2017. ISSN 2053-1583. doi: 10.1088/2053-1583/aa604a. URL <http://stacks.iop.org/2053-1583/4/i=2/a=021023?key=crossref.8ddd039e25fd4753674ef27dbb3e15ba>.
- [68] Debora Pierucci, Jihene Zribi, Hugo Henck, Julien Chaste, Mathieu G. Silly, François Bertran, Patrick Le Fevre, Bernard Gil, Alex Summerfield, Peter H. Beton, Sergei V. Novikov, Guillaume Cassabois, Julien E. Rault, and Abdelkarim Ouerghi. Van der Waals epitaxy of two-dimensional single-layer h-BN on graphite by molecular beam epitaxy: Electronic properties and band structure. *Applied Physics Letters*, 112(25):253102, June 2018. ISSN 0003-6951, 1077-3118. doi: 10.1063/1.5029220. URL <http://aip.scitation.org/doi/10.1063/1.5029220>.
- [69] Song Liu, Rui He, Zhipeng Ye, Xiaozhang Du, Jingyu Lin, Hongxing Jiang, Bin Liu, and James H. Edgar. Large-Scale Growth of High-Quality Hexagonal Boron Nitride Crystals at Atmospheric Pressure from an Fe–Cr Flux, August 2017. URL <https://pubs.acs.org/doi/pdf/10.1021/acs.cgd.7b00871>. Archive Location: world Library Catalog: pubs.acs.org Publisher: American Chemical Society.
- [70] Tim Hoffman. Optimization and characterization of bulk hexagonal boron nitride single crystals grown by the nickel-chromium flux method, PhD thesis. August 2016, Kansas State University.
- [71] Sivabrata Sahu and G. C. Rout. Band gap opening in graphene: a short theoretical study. *International Nano Letters*, 7(2):81–89, June 2017. ISSN 2008-9295, 2228-5326. doi: 10.1007/s40089-017-0203-5. URL <http://link.springer.com/10.1007/s40089-017-0203-5>.
- [72] J.-C. Charlier, P. C. Eklund, J. Zhu, and A. C. Ferrari. Electron and Phonon Properties of Graphene: Their Relationship with Carbon Nanotubes. In Claus E. Ascheron, Adelheid H. Duhm, Ado Jorio, Gene Dresselhaus, and Mildred S. Dresselhaus, editors, *Carbon Nanotubes*, volume 111, pages 673–709. Springer Berlin Heidelberg, Berlin, Heidelberg, 2007. ISBN 978-3-540-72864-1 978-3-540-72865-8. doi: 10.1007/978-3-540-72865-8\_21. URL [http://link.springer.com/10.1007/978-3-540-72865-8\\_21](http://link.springer.com/10.1007/978-3-540-72865-8_21). Series Title: Topics in Applied Physics.
- [73] Deep Jariwala, Vinod K. Sangwan, Lincoln J. Lauhon, Tobin J. Marks, and Mark C. Hersam. Emerging Device Applications for Semiconducting Two-Dimensional Transition Metal Dichalcogenides. *ACS Nano*, 8(2):1102–1120, February 2014. ISSN 1936-0851. doi:

- 10.1021/nn500064s. URL <https://doi.org/10.1021/nn500064s>. Publisher: American Chemical Society.
- [74] Kin Fai Mak and Jie Shan. Photonics and optoelectronics of 2D semiconductor transition metal dichalcogenides. *Nature Photonics*, 10(4):216–226, April 2016. ISSN 1749-4893. doi: 10.1038/nphoton.2015.282. URL <https://www.nature.com/articles/nphoton.2015.282>. Number: 4 Publisher: Nature Publishing Group.
- [75] Fengnian Xia, Han Wang, Di Xiao, Madan Dubey, and Ashwin Ramasubramaniam. Two-dimensional material nanophotonics. *Nature Photonics*, 8(12):899–907, December 2014. ISSN 1749-4885, 1749-4893. doi: 10.1038/nphoton.2014.271. URL <http://www.nature.com/articles/nphoton.2014.271>.
- [76] Gang Wang, Alexey Chernikov, Mikhail M. Glazov, Tony F. Heinz, Xavier Marie, Thierry Amand, and Bernhard Urbaszek. Colloquium: Excitons in atomically thin transition metal dichalcogenides. *Reviews of Modern Physics*, 90(2):021001, April 2018. doi: 10.1103/RevModPhys.90.021001. URL <https://link.aps.org/doi/10.1103/RevModPhys.90.021001>. Publisher: American Physical Society.
- [77] Andrea Splendiani, Liang Sun, Yuanbo Zhang, Tianshu Li, Jonghwan Kim, Chi-Yung Chim, Giulia Galli, and Feng Wang. Emerging Photoluminescence in Monolayer MoS<sub>2</sub>. *Nano Letters*, 10(4):1271–1275, April 2010. ISSN 1530-6984. doi: 10.1021/nl903868w. URL <https://doi.org/10.1021/nl903868w>. Publisher: American Chemical Society.
- [78] S. Demirci, N. Avazli, E. Durgun, and S. Cahangirov. Structural and electronic properties of monolayer group III monochalcogenides. *Physical Review B*, 95(11):115409, March 2017. doi: 10.1103/PhysRevB.95.115409. URL <https://link.aps.org/doi/10.1103/PhysRevB.95.115409>. Publisher: American Physical Society.
- [79] Xufan Li, Ming-Wei Lin, Alexander A. Puretzky, Juan C. Idrobo, Cheng Ma, Miaofang Chi, Mina Yoon, Christopher M. Rouleau, Ivan I. Kravchenko, David B. Geohegan, and Kai Xiao. Controlled Vapor Phase Growth of Single Crystalline, Two-Dimensional GaSe Crystals with High Photoresponse. *Scientific Reports*, 4(1):5497, May 2015. ISSN 2045-2322. doi: 10.1038/srep05497. URL <http://www.nature.com/articles/srep05497>.
- [80] Zeineb Ben Aziza, Viktor Zólyomi, Hugo Henck, Debora Pierucci, Mathieu G. Silly, José Avila, Samuel J. Magorrian, Julien Chaste, Chaoyu Chen, Mina Yoon, Kai Xiao, Fausto Sirotti, Maria C. Asensio, Emmanuel Lhuillier, Mahmoud Eddrief, Vladimir I. Fal’ko, and Abdelkarim Ouerghi. Valence band inversion and spin-orbit effects in the electronic structure of monolayer GaSe. *Physical Review B*, 98(11):115405, September 2018. ISSN 2469-9950, 2469-9969. doi: 10.1103/PhysRevB.98.115405. URL <https://link.aps.org/doi/10.1103/PhysRevB.98.115405>.

- 
- [81] Thomas Pelini. Optical properties of point defects in hexagonal boron nitride, PhD thesis. December 2019, Université de Montpellier.
- [82] T. Pelini, C. Elias, R. Page, L. Xue, S. Liu, J. Li, J. H. Edgar, A. Dréau, V. Jacques, P. Valvin, B. Gil, and G. Cassabois. Shallow and deep levels in carbon-doped hexagonal boron nitride crystals. *Physical Review Materials*, 3(9):094001, September 2019. ISSN 2475-9953. doi: 10.1103/PhysRevMaterials.3.094001. URL <https://link.aps.org/doi/10.1103/PhysRevMaterials.3.094001>.
- [83] Pierre Valvin, Thomas Pelini, Guillaume Cassabois, Alberto Zobelli, Jiahua Li, James H. Edgar, and Bernard Gil. Deep ultraviolet hyperspectral cryomicroscopy in boron nitride: Photoluminescence in crystals with an ultra-low defect density. *AIP Advances*, 10(7):075025, July 2020. ISSN 2158-3226. doi: 10.1063/5.0013121. URL <http://aip.scitation.org/doi/10.1063/5.0013121>.
- [84] Léonard Schué, Bruno Berini, Andreas C. Betz, Bernard Plaçais, François Ducastelle, Julien Barjon, and Annick Loiseau. Dimensionality effects on the luminescence properties of hBN. *Nanoscale*, 8(13):6986–6993, 2016. ISSN 2040-3364, 2040-3372. doi: 10.1039/C6NR01253A. URL <http://xlink.rsc.org/?DOI=C6NR01253A>.
- [85] Haolin Wang, Yajuan Zhao, Yong Xie, Xiaohua Ma, and Xingwang Zhang. Recent progress in synthesis of two-dimensional hexagonal boron nitride. *Journal of Semiconductors*, 38(3):031003, March 2017. ISSN 1674-4926. doi: 10.1088/1674-4926/38/3/031003. URL <https://doi.org/10.1088/1674-4926/38/3/031003>. Publisher: IOP Publishing.
- [86] David Arto Laleyan, Kelsey Mengle, Songrui Zhao, Yongjie Wang, Emmanouil Kioupakis, and Zetian Mi. Effect of growth temperature on the structural and optical properties of few-layer hexagonal boron nitride by molecular beam epitaxy. *Optics Express*, 26(18):23031, September 2018. ISSN 1094-4087. doi: 10.1364/OE.26.023031. URL <https://www.osapublishing.org/abstract.cfm?URI=oe-26-18-23031>.
- [87] Carlo M. Orofeo, Satoru Suzuki, Hiroyuki Kageshima, and Hiroki Hibino. Growth and low-energy electron microscopy characterization of monolayer hexagonal boron nitride on epitaxial cobalt. *Nano Research*, 6(5):335–347, May 2013. ISSN 1998-0124, 1998-0000. doi: 10.1007/s12274-013-0310-1. URL <http://link.springer.com/10.1007/s12274-013-0310-1>.
- [88] Min Wang, Sung Kyu Jang, Won-Jun Jang, Minwoo Kim, Seong-Yong Park, Sang-Woo Kim, Se-Jong Kahng, Jae-Young Choi, Rodney S. Ruoff, Young Jae Song, and Sungjoo Lee. A Platform for Large-Scale Graphene Electronics – CVD Growth of Single-Layer Graphene on CVD-Grown Hexagonal Boron Nitride.

- Advanced Materials*, 25(19):2746–2752, 2013. ISSN 1521-4095. doi: 10.1002/adma.201204904. URL <https://onlinelibrary.wiley.com/doi/abs/10.1002/adma.201204904>. eprint: <https://onlinelibrary.wiley.com/doi/pdf/10.1002/adma.201204904>.
- [89] Joo Song Lee, Soo Ho Choi, Seok Joon Yun, Yong In Kim, Stephen Boandoh, Ji-Hoon Park, Bong Gyu Shin, Hayoung Ko, Seung Hee Lee, Young-Min Kim, Young Hee Lee, Ki Kang Kim, and Soo Min Kim. Wafer-scale single-crystal hexagonal boron nitride film via self-collimated grain formation. page 6, 2018.
- [90] Ki Kang Kim, Allen Hsu, Xiaoting Jia, Soo Min Kim, Yumeng Shi, Mario Hofmann, Daniel Nezich, Joaquin F. Rodriguez-Nieva, Mildred Dresselhaus, Tomas Palacios, and Jing Kong. Synthesis of Monolayer Hexagonal Boron Nitride on Cu Foil Using Chemical Vapor Deposition. *Nano Letters*, 12(1):161–166, January 2012. ISSN 1530-6984, 1530-6992. doi: 10.1021/nl203249a. URL <https://pubs.acs.org/doi/10.1021/nl203249a>.
- [91] Yijing Stehle, Harry M. Meyer, Raymond R. Unocic, Michelle Kidder, Georgios Polyzos, Panos G. Datskos, Roderick Jackson, Sergei N. Smirnov, and Ivan V. Vlassiuk. Synthesis of Hexagonal Boron Nitride Monolayer: Control of Nucleation and Crystal Morphology. *Chemistry of Materials*, 27(23):8041–8047, December 2015. ISSN 0897-4756. doi: 10.1021/acs.chemmater.5b03607. URL <https://doi.org/10.1021/acs.chemmater.5b03607>. Publisher: American Chemical Society.
- [92] Guangyuan Lu, Tianru Wu, Qinghong Yuan, Huishan Wang, Haomin Wang, Feng Ding, Xiaoming Xie, and Mianheng Jiang. Synthesis of large single-crystal hexagonal boron nitride grains on Cu–Ni alloy. *Nature Communications*, 6(1):6160, May 2015. ISSN 2041-1723. doi: 10.1038/ncomms7160. URL <http://www.nature.com/articles/ncomms7160>.
- [93] Lifeng Wang, Bin Wu, Jisi Chen, Hongtao Liu, Pingan Hu, and Yunqi Liu. Monolayer Hexagonal Boron Nitride Films with Large Domain Size and Clean Interface for Enhancing the Mobility of Graphene-Based Field-Effect Transistors. *Advanced Materials*, 26(10):1559–1564, 2014. ISSN 1521-4095. doi: 10.1002/adma.201304937. URL <https://onlinelibrary.wiley.com/doi/abs/10.1002/adma.201304937>. eprint: <https://onlinelibrary.wiley.com/doi/pdf/10.1002/adma.201304937>.
- [94] Li Wang, Xiaozhi Xu, Leining Zhang, Ruixi Qiao, Muhong Wu, Zhichang Wang, Shuai Zhang, Jing Liang, Zhihong Zhang, Zhibin Zhang, Wang Chen, Xuedong Xie, Junyu Zong, Yuwei Shan, Yi Guo, Marc Willinger, Hui Wu, Qunyang Li, Wenlong Wang, Peng Gao, Shiwei Wu, Yi Zhang, Ying Jiang, Dapeng Yu, Enge Wang, Xuedong Bai, Zhu-Jun Wang, Feng Ding, and Kaihui Liu. Epitaxial growth of a 100-square-centimetre

- single-crystal hexagonal boron nitride monolayer on copper. *Nature*, 570(7759):91–95, June 2019. ISSN 0028-0836, 1476-4687. doi: 10.1038/s41586-019-1226-z. URL <http://www.nature.com/articles/s41586-019-1226-z>.
- [95] Lei Fu, Yangyong Sun, Nian Wu, Rafael G. Mendes, Linfeng Chen, Zhen Xu, Tao Zhang, Mark H. Rümeli, Bernd Rellinghaus, Darius Pohl, Lin Zhuang, and Lei Fu. Direct Growth of MoS<sub>2</sub>/h-BN Heterostructures *via* a Sulfide-Resistant Alloy. *ACS Nano*, 10(2):2063–2070, February 2016. ISSN 1936-0851, 1936-086X. doi: 10.1021/acsnano.5b06254. URL <https://pubs.acs.org/doi/10.1021/acsnano.5b06254>.
- [96] Jie Yu, Li Qin, Yufeng Hao, Shengyong Kuang, Xuedong Bai, Yat-Ming Chong, Wenjun Zhang, and Enge Wang. Vertically Aligned Boron Nitride Nanosheets: Chemical Vapor Synthesis, Ultraviolet Light Emission, and Superhydrophobicity. *ACS Nano*, 4(1):414–422, January 2010. ISSN 1936-0851. doi: 10.1021/nn901204c. URL <https://doi.org/10.1021/nn901204c>. Publisher: American Chemical Society.
- [97] Li Qin, Jie Yu, Mingyu Li, Fei Liu, and Xuedong Bai. Catalyst-free growth of mono- and few-atomic-layer boron nitride sheets by chemical vapor deposition. *Nanotechnology*, 22(21):215602, March 2011. ISSN 0957-4484. doi: 10.1088/0957-4484/22/21/215602. URL <https://doi.org/10.1088/0957-4484/22/21/215602>. Publisher: IOP Publishing.
- [98] Roland Yingjie Tay, Siu Hon Tsang, Manuela Loeblein, Wai Leong Chow, Guan Chee Loh, Joo Wah Toh, Soon Loong Ang, and Edwin Hang Tong Teo. Direct growth of nanocrystalline hexagonal boron nitride films on dielectric substrates. *Applied Physics Letters*, 106(10):101901, March 2015. ISSN 0003-6951, 1077-3118. doi: 10.1063/1.4914474. URL <http://aip.scitation.org/doi/10.1063/1.4914474>.
- [99] S. Majety, J. Li, W. P. Zhao, B. Huang, S. H. Wei, J. Y. Lin, and H. X. Jiang. Hexagonal boron nitride and 6H-SiC heterostructures. *Applied Physics Letters*, 102(21):213505, May 2013. ISSN 0003-6951, 1077-3118. doi: 10.1063/1.4808365. URL <http://aip.scitation.org/doi/10.1063/1.4808365>.
- [100] X. Z. Du, J. Li, J. Y. Lin, and H. X. Jiang. The origins of near band-edge transitions in hexagonal boron nitride epilayers. *Applied Physics Letters*, 108(5):052106, February 2016. ISSN 0003-6951, 1077-3118. doi: 10.1063/1.4941540. URL <http://aip.scitation.org/doi/10.1063/1.4941540>.
- [101] Kawser Ahmed, Rajendra Dahal, Adam Wertz, James J.-Q. Lu, Yaron Danon, and Ishwara B. Bhat. Effects of sapphire nitridation and growth temperature on the epitaxial growth of hexagonal boron nitride on sapphire. *Materials Research Express*, 4(1):

- 015007, January 2017. ISSN 2053-1591. doi: 10.1088/2053-1591/aa54d5. URL <https://doi.org/10.1088%2F2053-1591%2Faa54d5>. Publisher: IOP Publishing.
- [102] Qingqing Wu, Jianchang Yan, Liang Zhang, Xiang Chen, Tongbo Wei, Yang Li, Zhiqiang Liu, Xuecheng Wei, Yun Zhang, Junxi Wang, and Jinmin Li. Growth mechanism of AlN on hexagonal BN/sapphire substrate by metal–organic chemical vapor deposition. *CrystEngComm*, 19(39):5849–5856, 2017. ISSN 1466-8033. doi: 10.1039/C7CE01064H. URL <http://xlink.rsc.org/?DOI=C7CE01064H>.
- [103] Mikhail Chubarov, Henrik Pedersen, Hans Högberg, Vanya Darakchieva, Jens Jensen, Per O. Å. Persson, and Anne Henry. Epitaxial CVD growth of sp<sup>2</sup>-hybridized boron nitride using aluminum nitride as buffer layer. *physica status solidi (RRL) - Rapid Research Letters*, 5(10-11):397–399, November 2011. ISSN 18626254. doi: 10.1002/pssr.201105410. URL <http://doi.wiley.com/10.1002/pssr.201105410>.
- [104] Tin S. Cheng, Andrew Davies, Alex Summerfield, YongJin Cho, Izabela Cebula, Richard J. A. Hill, Christopher J. Mellor, Andrei N. Khlobystov, Takashi Taniguchi, Kenji Watanabe, Peter H. Beton, C. Thomas Foxon, Laurence Eaves, and Sergei V. Novikov. High temperature MBE of graphene on sapphire and hexagonal boron nitride flakes on sapphire. *Journal of Vacuum Science & Technology B, Nanotechnology and Microelectronics: Materials, Processing, Measurement, and Phenomena*, 34(2):02L101, March 2016. ISSN 2166-2746, 2166-2754. doi: 10.1116/1.4938157. URL <http://avs.scitation.org/doi/10.1116/1.4938157>.
- [105] Ryan Page, Joseph Casamento, Yongjin Cho, Sergei Rouvimov, Huili Grace Xing, and Debdeep Jena. Rotationally aligned hexagonal boron nitride on sapphire by high-temperature molecular beam epitaxy. *Physical Review Materials*, 3(6):064001, June 2019. ISSN 2475-9953. doi: 10.1103/PhysRevMaterials.3.064001. URL <https://link.aps.org/doi/10.1103/PhysRevMaterials.3.064001>.
- [106] R. Dahal, J. Li, S. Majety, B. N. Pantha, X. K. Cao, J. Y. Lin, and H. X. Jiang. Epitaxially grown semiconducting hexagonal boron nitride as a deep ultraviolet photonic material. *Applied Physics Letters*, 98(21):211110, May 2011. ISSN 0003-6951. doi: 10.1063/1.3593958. URL <https://aip.scitation.org/doi/full/10.1063/1.3593958>. Publisher: American Institute of Physics.
- [107] Xin Li, Suresh Sundaram, Youssef El Gmili, Taha Ayari, Renaud Puybaret, Gilles Patriarche, Paul L. Voss, Jean Paul Salvestrini, and Abdallah Ougazzaden. Large-Area Two-Dimensional Layered Hexagonal Boron Nitride Grown on Sapphire by Metalorganic Vapor Phase Epitaxy. *Crystal Growth & Design*, 16(6):3409–3415, June 2016. ISSN 1528-7483, 1528-7505. doi: 10.1021/acs.cgd.6b00398. URL <https://pubs.acs.org/doi/10.1021/acs.cgd.6b00398>.

- [108] Li Song, Lijie Ci, Hao Lu, Pavel B. Sorokin, Chuanhong Jin, Jie Ni, Alexander G. Kvashnin, Dmitry G. Kvashnin, Jun Lou, Boris I. Yakobson, and Pulickel M. Ajayan. Large Scale Growth and Characterization of Atomic Hexagonal Boron Nitride Layers. *Nano Letters*, 10(8):3209–3215, August 2010. ISSN 1530-6984, 1530-6992. doi: 10.1021/nl1022139. URL <https://pubs.acs.org/doi/10.1021/nl1022139>.
- [109] Takahiro Kawamura, Hiroya Hayashi, Takafumi Miki, Yasuyuki Suzuki, Yoshihiro Kangawa, and Koichi Kakimoto. Molecular beam epitaxy growth of GaN under Ga-rich conditions investigated by molecular dynamics simulation. *Japanese Journal of Applied Physics*, 53(5S1):05FL08, April 2014. ISSN 1347-4065. doi: 10.7567/JJAP.53.05FL08. URL <https://iopscience.iop.org/article/10.7567/JJAP.53.05FL08/meta>. Publisher: IOP Publishing.
- [110] T. D. Moustakas, T. Lei, and R. J. Molnar. Growth of GaN by ECR-assisted MBE. In Chris G. Van de Walle, editor, *Wide-Band-Gap Semiconductors*, pages 36–49. Elsevier, Amsterdam, January 1993. ISBN 978-0-444-81573-6. doi: 10.1016/B978-0-444-81573-6.50008-6. URL <http://www.sciencedirect.com/science/article/pii/B9780444815736500086>.
- [111] Tin Cheng, Alex Summerfield, Christopher Mellor, Andrei Khlobystov, Laurence Eaves, C. Foxon, Peter Beton, and Sergei Novikov. High-Temperature Molecular Beam Epitaxy of Hexagonal Boron Nitride with High Active Nitrogen Fluxes. *Materials*, 11(7):1119, June 2018. ISSN 1996-1944. doi: 10.3390/ma11071119. URL <http://www.mdpi.com/1996-1944/11/7/1119>.
- [112] Tin S. Cheng, Alex Summerfield, Christopher J. Mellor, Andrew Davies, Andrei N. Khlobystov, Laurence Eaves, C. Thomas Foxon, Peter H. Beton, and Sergei V. Novikov. High-temperature molecular beam epitaxy of hexagonal boron nitride layers. *Journal of Vacuum Science & Technology B, Nanotechnology and Microelectronics: Materials, Processing, Measurement, and Phenomena*, 36(2):02D103, March 2018. ISSN 2166-2746, 2166-2754. doi: 10.1116/1.5011280. URL <http://avs.scitation.org/doi/10.1116/1.5011280>.
- [113] L. Museur, G. Brasse, A. Pierret, S. Maine, B. Attal-Tretout, F. Ducastelle, A. Loiseau, J. Barjon, K. Watanabe, T. Taniguchi, and A. Kanaev. Exciton optical transitions in a hexagonal boron nitride single crystal. *physica status solidi (RRL) – Rapid Research Letters*, 5(5-6):214–216, 2011. ISSN 1862-6270. doi: 10.1002/pssr.201105190. URL <https://onlinelibrary.wiley.com/doi/abs/10.1002/pssr.201105190>. eprint: <https://onlinelibrary.wiley.com/doi/pdf/10.1002/pssr.201105190>.
- [114] Colin M. Chow, Hongyi Yu, Aaron M. Jones, John R. Schaibley, Michael Koehler, David G. Mandrus, R. Merlin, Wang Yao, and Xiaodong Xu. Phonon-assisted oscillatory

- exciton dynamics in monolayer MoSe<sub>2</sub>. *npj 2D Materials and Applications*, 1(1):33, December 2017. ISSN 2397-7132. doi: 10.1038/s41699-017-0035-1. URL <http://www.nature.com/articles/s41699-017-0035-1>.
- [115] Jessica Lindlau, Cedric Robert, Victor Funk, Jonathan Förste, Michael Förg, Léo Colombier, Andre Neumann, Emmanuel Courtade, Shivangi Shree, Takashi Taniguchi, Kenji Watanabe, Mikhail M. Glazov, Xavier Marie, Bernhard Urbaszek, and Alexander Högele. Identifying optical signatures of momentum-dark excitons in transition metal dichalcogenide monolayers. *arXiv:1710.00988 [cond-mat]*, October 2017. URL <http://arxiv.org/abs/1710.00988>. arXiv: 1710.00988.
- [116] Shigefusa F. Chichibu, Youichi Ishikawa, Hiroko Kominami, and Kazuhiko Hara. Nearly temperature-independent ultraviolet light emission intensity of indirect excitons in hexagonal BN microcrystals. *Journal of Applied Physics*, 123(6):065104, February 2018. ISSN 0021-8979. doi: 10.1063/1.5021788. URL <https://aip.scitation.org/doi/10.1063/1.5021788>. Publisher: American Institute of Physics.
- [117] Yutaka Toyozawa. Theory of Line-Shapes of the Exciton Absorption Bands. *Progress of Theoretical Physics*, 20(1):53–81, July 1958. ISSN 0033-068X. doi: 10.1143/PTP.20.53. URL <https://academic.oup.com/ptp/article-lookup/doi/10.1143/PTP.20.53>.
- [118] Hitoshi Sumi. Exciton-Phonon Interaction in the Coherent Potential Approximation with Application to Optical Spectra. *Journal of the Physical Society of Japan*, 32(3):616–628, March 1972. ISSN 0031-9015, 1347-4073. doi: 10.1143/JPSJ.32.616. URL <http://journals.jps.jp/doi/10.1143/JPSJ.32.616>.
- [119] Hayk Harutyunyan, Tobias Gokus, Alexander A. Green, Mark C. Hersam, Maria Allegrini, and Achim Hartschuh. Defect-Induced Photoluminescence from Dark Excitonic States in Individual Single-Walled Carbon Nanotubes, March 2009. URL <https://pubs.acs.org/doi/pdf/10.1021/nl9002798>. Archive Location: world Library Catalog: pubs.acs.org Publisher: American Chemical Society.
- [120] Phys. Rev. Lett. 105, 157403 (2010) - Brightening of Triplet Dark Excitons by Atomic Hydrogen Adsorption in Single-Walled Carbon Nanotubes Observed by Photoluminescence Spectroscopy, . URL <https://journals.aps.org/prl/abstract/10.1103/PhysRevLett.105.157403>.
- [121] Kin Fai Mak, Keliang He, Changgu Lee, Gwan Hyoung Lee, James Hone, Tony F. Heinz, and Jie Shan. Tightly bound trions in monolayer MoS<sub>2</sub>. *Nature Materials*, 12(3):207–211, March 2013. ISSN 1476-1122, 1476-4660. doi: 10.1038/nmat3505. URL <http://www.nature.com/articles/nmat3505>.

- [122] Phys. Rev. Lett. 106, 037404 (2011) - Observation of Charged Excitons in Hole-Doped Carbon Nanotubes Using Photoluminescence and Absorption Spectroscopy, . URL <https://journals.aps.org/prl/abstract/10.1103/PhysRevLett.106.037404>.
- [123] Jason S. Ross, Sanfeng Wu, Hongyi Yu, Nirmal J. Ghimire, Aaron M. Jones, Grant Aivazian, Jiaqiang Yan, David G. Mandrus, Di Xiao, Wang Yao, and Xiaodong Xu. Electrical control of neutral and charged excitons in a monolayer semiconductor. *Nature Communications*, 4(1):1474, June 2013. ISSN 2041-1723. doi: 10.1038/ncomms2498. URL <http://www.nature.com/articles/ncomms2498>.
- [124] Giovanni Scuri, You Zhou, Alexander A. High, Dominik S. Wild, Chi Shu, Kristiaan De Greve, Luis A. Jauregui, Takashi Taniguchi, Kenji Watanabe, Philip Kim, Mikhail D. Lukin, and Hongkun Park. Large Excitonic Reflectivity of Monolayer  $\text{MoSe}_2$  Encapsulated in Hexagonal Boron Nitride. *Physical Review Letters*, 120(3):037402, January 2018. doi: 10.1103/PhysRevLett.120.037402. URL <https://link.aps.org/doi/10.1103/PhysRevLett.120.037402>. Publisher: American Physical Society.
- [125] Patrick Back, Aroosa Ijaz, Sina Zeytinoglu, Martin Kroner, and Atac Imamoglu. Realization of an atomically thin mirror using monolayer  $\text{MoSe}_2$ . *Physical Review Letters*, 120(3):037401, January 2018. ISSN 0031-9007, 1079-7114. doi: 10.1103/PhysRevLett.120.037401. URL <http://arxiv.org/abs/1705.07317>. arXiv: 1705.07317.
- [126] Phys. Rev. A 96, 031801(R) (2017) - Atomically thin semiconductors as nonlinear mirrors, . URL <https://journals.aps.org/prl/abstract/10.1103/PhysRevA.96.031801>.
- [127] H. H. Fang, B. Han, C. Robert, M. A. Semina, D. Lagarde, E. Courtade, T. Taniguchi, K. Watanabe, T. Amand, B. Urbaszek, M. M. Glazov, and X. Marie. Control of the Exciton Radiative Lifetime in van der Waals Heterostructures. *Physical Review Letters*, 123(6):067401, August 2019. ISSN 0031-9007, 1079-7114. doi: 10.1103/PhysRevLett.123.067401. URL <https://link.aps.org/doi/10.1103/PhysRevLett.123.067401>.
- [128] D. M. Hoffman, G. L. Doll, and P. C. Eklund. Optical properties of pyrolytic boron nitride in the energy range 0.05–10 eV. *Physical Review B*, 30(10):6051–6056, November 1984. ISSN 0163-1829. doi: 10.1103/PhysRevB.30.6051. URL <https://link.aps.org/doi/10.1103/PhysRevB.30.6051>.
- [129] Kenji Watanabe and Takashi Taniguchi. Jahn-Teller effect on exciton states in hexagonal boron nitride single crystal. *Physical Review B*, 79(19):193104, May 2009. ISSN 1098-0121, 1550-235X. doi: 10.1103/PhysRevB.79.193104. URL <https://link.aps.org/doi/10.1103/PhysRevB.79.193104>.

## REFERENCES

---

- [130] Giovanni Scuri, You Zhou, Alexander A. High, Dominik S. Wild, Chi Shu, Kristiaan De Greve, Luis A. Jauregui, Takashi Taniguchi, Kenji Watanabe, Philip Kim, Mikhail D. Lukin, and Hongkun Park. Large Excitonic Reflectivity of Monolayer MoSe<sub>2</sub> Encapsulated in Hexagonal Boron Nitride. *Physical Review Letters*, 120(3):037402, January 2018. ISSN 0031-9007, 1079-7114. doi: 10.1103/PhysRevLett.120.037402. URL <https://link.aps.org/doi/10.1103/PhysRevLett.120.037402>.